Università degli Studi di Ferrara

DOTTORATO DI RICERCA IN "SCIENZE DELL' INGEGNERIA"

CICLO XXVIII

COORDINATORE Prof. Stefano Trillo

Static analysis and delamination of structures in adhesive contact with an elastic half-plane using a coupled FE-BIE model

Settore Scientifico Disciplinare ICAR/09

<table>
<tr><td>Dottorando
Dott. Tezzon Enrico</td><td>Tutore
Prof. Tullini Nerio</td></tr>
</table>

CoTutore
Prof.ssa Ciancio Daniela

Anni 2013/2015

Contents

2 Static analysis of shear flexible beam bonded to orthotropic elastic half-plane

3 Static analysis of layer bonded to elastic half-plane

5 Zero thickness analysis of layer bonded to traditional boundary condition or elastic half-plane

Acknowledgements

It has been an honour and pleasure to be a PhD student of the Ferrara University.

First, my sincere gratitude goes to my supervisor Dr. Prof. Tullini N. who was patient and always willing to help and assist me in all my needs. I thank the members of the Engineering Department of the University of Ferrara as a whole, for providing me with all the necessary facilities for the research.

I would like to thanks my co-supervisor Dr. Prof. Ciancio D. of the School of Civil, Environmental and Mining Engineering of the University of Western Australia, for the support of my PhD study and relative research, and for letting me be a visiting student of her faculty.

I thank my colleagues and friends who were willing to exchange valuable information of mutual interest for the research. I am also very grateful to my English teacher Karen who dedicated time for the grammatical revision of my thesis.

Finally, I would like to express my profound gratitude to my family for providing me with continuous encouragement throughout my years of study.

Thank you

Ferrara 2016   Enrico Tezzon

Preface

The analysis of the contact interaction is a problem of wide importance which has attracted the attention of many scientists and researchers in the mathematical and engineering field. In the geotechnical and civil engineering, focusing on study of shallow foundations, railroad tracks, road pavements, embankments and rock joint. In the mechanical and aeronautical field for delamination of sandwich panel, laminated and composite material. In the electronic and biomedical area for the behaviour of MEMS or NEMS devices.

Interaction of structure and its foundation with soils has been discussed in this thesis. The method for the analysis of soil-structure interaction involving foundation has taken place over many years. One of the earliest and simplest approaches to soil-structure interaction was to represent the resistance of the soil by a distribution of springs. This approach, defined by Winkler, can lead to serious error because of independence, not interaction, and difficulty to establish the real stiffness values of the elements. Furthermore, the model cannot directly take account of substrate layering, and cannot predict lateral displace by a vertical load. To overcoming such shortcoming, the substrate may be treated as an elastic continuum involving the Boussinesq's solution. The inefficacy to determine the continuous behaviour of real support in the Winkler model, as well as the complexity of the continuum model, finding limited practical application in the past, carry out the investigation of the substrate response with other kind of models, such as Filonenko-Borodich, Pasternak, Hetenyi, Kerr, Reissner, Vlasov and Leentiev.

With the improvement of technology, numerical methods have been applied to analyse the interaction of complex problems, such as the finite difference method, finite element method (FEM) and boundary element method (BEM). In particular, the FEM provides a powerful numerical method, even though a large number of elements could be required to model the substrate medium and the computer requirements may not be adequate. To improve the efficiency in the computation, FEM can be combined with BIE boundary integral equation adopting a simple fundamental solution such as Boussineq's one for three-dimensional problem (half-space) or Flamant solution for the response of a half-plane.

The earliest application on soil-foundation interaction, by means of the last mentioned approach, was led by Cheung and Zienkiewicz for structures on infinitely deep soil. The total stiffness of the system may be obtained by inverting the flexibility matrix of soil and adding the stiffness matrix of the foundation. A frame structure interacts with soil through

rigid foundation was considered by Guarracino et al. adopting a mixed variational formulation. In addition, soil-foundation interaction was analysed by treating the Timoshenko beam theory on elastic half-plane by Tullini and Tralli. The same approach has been adopted to study thin-film devices and coating systems axially loaded and bonded to an elastic substrate. The FE.BIE method has also been used to study the buckling of a beam and frame in frictionless contact on half-plane, recently published by Tullini et al.

The aim of this thesis is to develop the present mixed variational formulation analysed by coupling finite element and boundary element (FE-BIE). The one-dimensional or two-dimensional finite elements are described in terms of nodal displacements (and rotation for the beam element), while the substrate is represented in terms of surface tractions through a boundary integral equation that incorporates a suitable Green's function. The formulation has been discussed with the different considerations in each chapter of this thesis.

In the first chapter, the simple and efficient numerical model introduced by Tullini, has been extended in perfect adhesion for stiff and flexible beams. A comparison is made with result in the frictionless contact and thin-film having a vanishing of bending rigidity. Moreover, with simply load condition, an excellent agreement between the numerical analysis and analytical solution available in the literature, is reported. Two examples of soil-structure interaction are analysed providing a competent aspect of this work: a two-bay frame and a culvert with single or multiple cell.

In the second chapter, the contact model of a rigid punch or a beam resting on an orthotropic half-plane has been considered. A significant aspect of the present analysis is applied for reinforcement strip fully adhesive to wood substrate or shallow foundation resting on soil. Moreover, it is shown that the shear deformation plays a crucial role on shear force at beam end.

In the third chapter, the method has been developed involving thin-shell (two-dimensional element) lying on an elastic half-plane. The thin-shell is suitable to represent a very thick foundation which could not be approximated with the one-dimensional element. Furthermore, the model is well suitable to describe the distribution of the tensile force necessary for a geosynthetic reinforcement located between an embankment and subsoil.

Over the last few years, composite materials have substituted the bonding for welding, bolding and riveting in many applications, focusing on the interaction topic. These materials are subject to phenomena called delamination which is related mainly to how they are constructed. The detachment of a composite is generally characterized by weakness of resin glue between adherents. The common defects in adhesively bonded

joints are: porosity caused by gases and volatiles in the adhesive; voids caused by air entrapment during application of the adhesive; crack associated by thermal shrinkage; and incorrect cure because of contaminants or poor mixing. For this reason the thickness, modulus and properties of the adhesive are difficult to regulate and to determine. But this phenomenon does not always occur, sometimes with different properties of material between substrate and reinforcement, the detachment can happen and rupture of less resistant material. In the following last two chapters of the thesis, some numerical analysis by means of the present technique (FE-BIE) are developed with attempting to simulate the delamination phenomenon.

In the fourth chapter, the problem of reinforcement attached to an infinite substrate has been reconsidered under the assumption of no perfect adhesion. Linear behaviour of an adhesive is compared with the close-form of Melan's solution. Besides, a formulation based on "a priori" description of interfacial contact is adopted through non linear analysis. For the sake of simplicity, a fracture process in pure "mode II" along the contact is examined, disregarding the effect of peeling or out-of-plane displacement.

Finally, in the fifth chapter, zero-thickness method is implemented into the coupling FE-BIE model where brittle crack propagation within a laminate substrate is considered. The substrate is modelled into two parts defined respectively by 2D finite elements (thin-shell) and half-plane. The growth of crack is supposed within the substrate portion constituted by FEs, along the mesh line where interface elements are collocated. The interface element is characterized by zero-thickness and setting "a priori" interfacial stress-slip law.

Results relative to beam and frame resting on isotropic or orthotropic half-plane, mentioned in chapter one and two of this thesis, are published in an international journal.

1 Static analysis of shear flexible beams and frames bonded to isotropic elastic half-plane

1.1 Introduction

The interest for contact problems and the analysis of the relevant interface reactions concern natural sciences, such as geology [1], as well as many engineering fields, such as aeronautics and space applications [2], structural strengthening of concrete with FRP composites [3, 4, 5], mechanical engineering [6, 7, 8] and electronics [9].

In the field of structural engineering, the assessment of the soil-structure interaction has been a challenge for a long time [10, 11]. Analytical solutions were restricted to rigid punches or infinite beams resting on isotropic or anisotropic elastic half-space [12, 13, 14]. Hence the adoption of simple soil models; in particular Winkler model, based on the proportionality between pressure and vertical displacements at every point of the contact surface, and the models introduced by Filonenko-Borodish and Pasternak, who assumed the existence of a shear layer lying on the top surface of the Winkler bed of linear springs [10]. Nevertheless, simplified substrate models like these should be restricted to problems in which the effects of transverse interaction between adjacent parts of the soil surface are not significant.

With regard to numerical methods, soil-structure interaction problems were studied with several approaches. In one approach, both the foundation beam and the substrate were described by means of the Finite Element Method (FEM) allowing for complex soil media and surface profiles [10]. However, to ensure vanishing displacements at the boundaries, the substrate mesh has to be extended far away from the loaded area, leading to a very large number of finite elements and to a discouraging computing time. To improve the computational efficiency, infinite elements were used, see [11] and references cited therein. It is worth observing that using classical beam theory and two-dimensional finite elements for the substrate does not allow for the angular continuity at the contact surface. In principle, this problem may be solved by introducing refined two-dimensional continuum elements containing rotational degrees of freedom [15].

In another approach, the behaviour of the soil medium is approximated by a proper soil model. The earliest applications of the elastic half-space model to soil-structure interaction problems were due to Cheung and Zienkiewicz [16], and Cheung and Nag [17], who developed a model for the analysis of beams and plates resting on elastic foundations that

incorporates Boussinesq's solution. Wang et al. [18] extended this procedure to the analysis of rigid pavements. Nevertheless, this method and many others adopting a similar approach (see [10, 11]) implicitly assume that the beam is connected to the substrate at equally spaced points through a finite number of pinned-clamped rigid links. Thus, no angular continuity between beam and substrate can be imposed. Moreover, this approach requires the explicit inversion of the substrate flexibility matrix. Variational formulations including a suitable Green's function of the substrate were first presented in [19, 20]. Bielak and Stephan [21] investigated the bending problem of beams on elastic soil using a Green's function descending from Boussinesq's influence function. In [22], the analysis of frames with rigid footings resting on an isotropic elastic half-space is reported, whereas Bode et al. [23] used Green's functions of the soil for the assessment of the soil-structure interaction in dynamics.

Finally, a particularly advantageous tool for reproducing the response of the elastic half-space is the Boundary Element Method (BEM), because only the boundary of the elastic substrate has to be discretized, see [24] and references cited therein. However, soil tractions are usually considered as nodal reactions in the FE model of the foundation beam and, once again, the rotation continuity between beam and substrate is neglected. In the general formulation of BEM dealing with elastic half-space, Mindlin's fundamental solution is usually adopted to obtain the displacement field due to a point force applied in the interior of a homogeneous three-dimensional elastic solid [25]. The particular problem discussed in the present paper refers to loads applied to the ground surface of a two-dimensional half-space in plane state. Consequently, Flamant' and Cerruti's solutions are the proper fundamental solutions to be used [12, 13].

In the present paper, a coupled Finite Element-Boundary Integral Equation (FE-BIE) model is used for the plane strain or plane stress analysis of beams and frames bonded to a homogeneous, linearly elastic and isotropic two-dimensional half-space. The model makes use of a standard, displacement-based numerical formulation for the beam, coupled with an integral equation for the substrate boundary that includes a suitable Green's function of the substrate. The independent variables of the mixed formulation proposed are beam displacements and rotations, and soil surface tractions in tangential and normal directions. Only the beam in contact with the substrate boundary has to be discretized. In [26], an analogous mixed formulation was used for the analysis of Timoshenko beams in frictionless contact with the substrate, whereas in [27] structural elements with no bending stiffness, such as bars and thin coatings, were investigated. In [28] and [29], using Euler-

Bernoulli and Timoshenko beam theory, respectively, the coupled FE-BIE method was applied to the buckling analysis of beams and frames in frictionless contact with the substrate. To the authors' knowledge, the present proposal to use the FE-BIE model for the plane strain or plane stress static analysis of shear deformable beams and frames in adhesive contact with the substrate represents a new contribution.

Differently from the formulations available in the literature (see for example [10, 16, 17]), the proposed model enforces the angular continuity between foundation beam and half-plane boundary at the node locations. Moreover, the proposed model involves symmetric soil matrices, whereas the classical FEM-BEM approach based on collocation BEM requires an additional computational effort to remedy the lack of symmetry of the BEM coefficient matrix. In the present approach the weakly singular BIE is evaluated analytically, so avoiding singular and hyper-singular integrals, that are the major concern of the classical BEM. Finally, the resolving matrix has dimensions proportional to the number of the foundation beam FEs. Conversely, in the standard FEM, a refined mesh requires a stiffness matrix with dimensions that are several times the square of the number of FEs used for the foundation beam. The advantages outlined result in accurate solutions at low computational cost.

Several numerical examples are presented. For very stiff beams subjected to a point force or moment, comparisons are made with available closed-form solutions to the contact problem of a rigid indenter. For a rigid punch loaded by a bending moment and a foundation beams bonded to the substrate and loaded by a vertical point force, the proposed model exhibits a superior convergence rate with respect to other two standard numerical models: a standard FE model that uses two-dimensional elastic elements to describe the soil and the approach proposed by Cheung in [16, 17]. Moreover, the shear deformations are shown to play a crucial role on both beam displacements and soil surface tractions. Foundation beams loaded by a horizontal point force at midspan or at one end section as well as beams loaded by a bending moment at midspan are considered. Finally, the model is applied to the soil-structure interaction analysis of a two-bay frame and a culvert with single or multiple cell, both subjected to gravity and lateral loads.

1.2   Variational formulation

A beam bonded to a two-dimensional semi-infinite substrate is referred to a Cartesian coordinate system (O; *x, z*), where *x* coincides with the centroidal axis of the beam, and *z* is chosen in the downward transverse direction (Fig. 1.1a). The beam has length *L* and cross-section depth *h*. Thus, the half-plane boundary is located at $z = h/2$. Generalised plane stress or plane strain state can be considered in the present formulation. In the latter case, cross-section breadth *b* is assumed to be unitary for both the beam and the half-plane. Small displacements and infinitesimal strains are adopted in the analysis. Both the beam and the substrate are made of homogeneous, linearly elastic and isotropic materials. In the following, elastic constants E_b, G_b, and ν_b denote longitudinal and transverse elastic moduli, and Poisson's ratio of the beam, respectively, whereas E_s and ν_s represent Young's modulus and Poisson's ratio of the substrate. The centroidal axis of the beam is subjected to distributions of horizontal and vertical loads $p_x(x)$ and $p_z(x)$, and couples $m(x)$ (Fig. 1.1b). Moreover, perfect adhesion is supposed between the beam and the half-plane boundary. This assumption involves the development of both interfacial shear tractions $r_x(x)$ and vertical normal tractions $r_z(x)$ along the contact region (Fig. 1.1b).
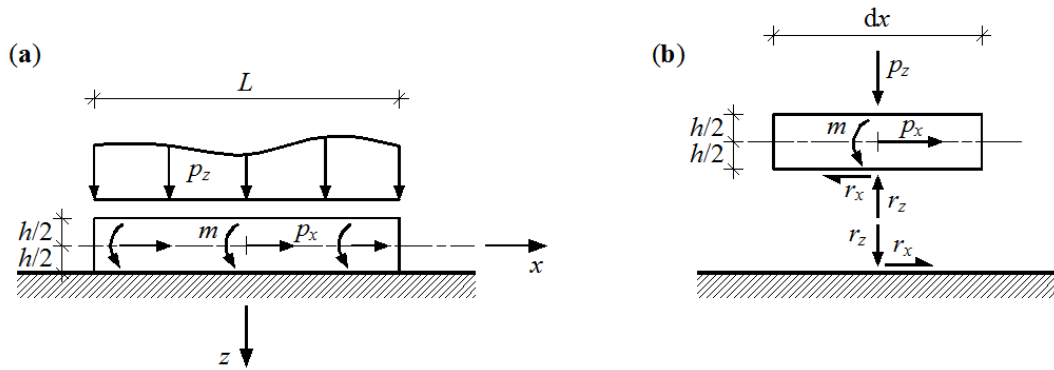
Fig. 1.1. Beam bonded to a two-dimensional half-space (**a**), and free-body diagram (**b**).

1.2.1   Total potential energy for the beam

Assuming positive cross-section rotations φ in counter-clockwise direction, axial and transverse displacements for a Timoshenko beam can be written as:

$$u_{bx}(x, z) = u_{bx,0}(x) + \varphi(x)\, z, \qquad u_{bz}(x, z) = u_z(x), \tag{1.1a, b}$$

where $u_{bx,0}$ and u_z are the axial displacement of the centroidal beam axis and the vertical displacement of both the beam and the half-plane boundary, respectively. The horizontal displacement of the half-plane boundary is given by $u_x(x) = u_{bx,0}(x) + \varphi(x)\,h/2$.

Axial and shear strains in the beam are:

$$\varepsilon_b = u'_{bx,0} + \varphi'\,z\,, \qquad\qquad \gamma_b = u'_z + \varphi\,, \qquad\qquad (1.2\text{a, b})$$

where a prime stands for differentiation with respect to x. Plane state assumption yields the following stress-strain relations:

$$\sigma_b = E_0\,\varepsilon_b, \qquad \tau_b = G_b\,\gamma_b, \qquad\qquad (1.3\text{a, b})$$

where $E_0 = E_b$ or $E_0 = E_b/(1-v_b^2)$ for generalised plane stress or plane strain state, respectively, and $G_b = E_b/[2\,(1+v_b)]$.

The elastic strain energy for a beam of length L is the sum of strain energies $U_{\text{beam},a}$ and $U_{\text{beam},b}$, associated with axial strain (subscript a) and bending and transverse shear strains (subscript b). Using strain components (1.2a,b) and constitutive laws (1.3a,b), $U_{\text{beam},a}$ and $U_{\text{beam},b}$ can be written as:

$$U_{\text{beam}a} = \frac{1}{2}\int_L E_0 A_b (u'_{bx,0})^2\,\mathrm{d}x\,, \qquad\qquad (1.4\text{a})$$

$$U_{\text{beam}b} = \frac{1}{2}\int_L [D_b\,(\varphi')^2 + k_b\,G_b A_b\,(u'_z + \varphi)^2]\,\mathrm{d}x\,. \qquad\qquad (1.4\text{b})$$

where $A_b = bh$ is the cross-sectional area, $D_b = E_0 bh^3/12$ is the flexural rigidity and k_b is the shear correction factor [30, 31]:

$$k_b = \frac{5}{6 - v_b G_b/E_b}\,, \qquad k_b = \frac{5}{6 - v_b(1+v_b)G_b/E_b}\,, \qquad\qquad (1.5)$$

for a plane stress or a plane strain state, respectively.

The total potential energy of the beam, $\Pi_{\text{beam}} = \Pi_{\text{beam},a} + \Pi_{\text{beam},b}$, is obtained from the strain energy contributions and the potential of the external loads, resulting in:

$$\Pi_{\text{beam}a} = U_{\text{beam}a} - b\int_L (p_x - r_x)\,u_{bx,0}\,\mathrm{d}x\,, \qquad\qquad (1.6\text{a})$$

$$\Pi_{\text{beam}b} = U_{\text{beam}b} - b\int_L [(p_z - r_z)\,u_z + (m - r_x\,h/2)\,\varphi]\,\mathrm{d}x\,. \qquad\qquad (1.6\text{b})$$

1.2.2 Total potential energy for the substrate

The solutions to the two-dimensional problem for a homogeneous, linear elastic and isotropic half-plane loaded by a point force normal or tangential to its boundary are referred to as Flamant' and Cerruti's solutions, respectively [12, 13]. In particular, the surface displacement $u_i(x)$, with $i = x, z$, due to a point force $P_i(\hat{x})$ applied to the half-plane boundary can be expressed in closed form as $u_i(x) = g(x, \hat{x}) P_i(\hat{x})$ (Fig. 1.2), where Green's function $g(x, \hat{x})$ is given by the following expression:
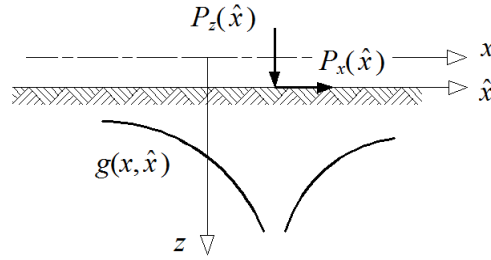
Fig. 1.2. Green's function $g(x, \hat{x})$ related to point forces $P_x(\hat{x})$, $P_z(\hat{x})$ applied to the half-plane boundary.

$$g(x, \hat{x}) = -\frac{2}{\pi E} \ln \frac{|x - \hat{x}|}{d}. \qquad (1.7)$$

In Eq. (1.7), $E = E_s$ or $E = E_s/(1 - v_s^2)$ for a generalised plane stress or plane strain state, respectively, and d represents an arbitrary length related to a rigid-body displacement.

The horizontal and vertical displacements of a point of the half-plane boundary due to the combined action of interfacial shear tractions r_x and normal tractions r_z can be written as [12, 13]:

$$u_x(x) = \int_L g(x, \hat{x}) \, r_x(\hat{x}) \, d\hat{x} - \frac{c}{2E} \left[\int_{x_0}^x r_z(\hat{x}) \, d\hat{x} - \int_x^{x_L} r_z(\hat{x}) \, d\hat{x} \right], \qquad (1.8a)$$

$$u_z(x) = \int_L g(x, \hat{x}) \, r_z(\hat{x}) \, d\hat{x} + \frac{c}{2E} \left[\int_{x_0}^x r_x(\hat{x}) \, d\hat{x} - \int_x^{x_L} r_x(\hat{x}) \, d\hat{x} \right], \qquad (1.8b)$$

where x_0, x_L are the abscissas of the beam end sections, and $c = 1 - v_s$ or $c = (1 - 2 v_s)/(1 - v_s)$ for a generalised plane stress or plane strain state, respectively.

Making use of the theorem of work and energy for exterior domains [32], it is possible to show that total potential energy Π_{soil} for the half-plane equals one half of the work of the external loads [26, 27], i.e.,

$$\Pi_{\text{soil}} = -\frac{b}{2} \int_L (r_x u_x + r_z u_z) \, dx. \qquad (1.9)$$

Substituting Eqs. (1.8a, b) into Eq. (1.9) yields $\Pi_{\text{soil}} = \Pi_{\text{soil},a} + \Pi_{\text{soil},b}$, where

$$\Pi_{\text{soil},a} = -\frac{b}{2}\int_L r_x(x)\,\mathrm{d}x\left\{\int_L g(x,\hat{x})\,r_x(\hat{x})\,\mathrm{d}\hat{x} - \frac{c}{2E}\left[\int_{x_0}^{x} r_z(\hat{x})\,\mathrm{d}\hat{x} - \int_x^{x_L} r_z(\hat{x})\,\mathrm{d}\hat{x}\right]\right\}, \tag{1.10a}$$

$$\Pi_{\text{soil},b} = -\frac{b}{2}\int_L r_z(x)\,\mathrm{d}x\left\{\int_L g(x,\hat{x})\,r_z(\hat{x})\,\mathrm{d}\hat{x} + \frac{c}{2E}\left[\int_{x_0}^{x} r_x(\hat{x})\,\mathrm{d}\hat{x} - \int_x^{x_L} r_x(\hat{x})\,\mathrm{d}\hat{x}\right]\right\}. \tag{1.10b}$$

1.2.3 Total potential energy for the beam-substrate system

Making use of Eqs. (1.6) and (1.10), the total potential energy of the beam-substrate system turns out to be:

$$\Pi = \Pi_{\text{beam}} + \Pi_{\text{soil}} = \Pi_{\text{beam},a} + \Pi_{\text{beam},b} + \Pi_{\text{soil},a} + \Pi_{\text{soil},b}, \tag{1.11}$$

which is a mixed variational formulation with variational functions represented by displacements $u_{bx,0}$, u_z and rotation φ, as well as interfacial shear and normal tractions r_x and r_z along the contact region. It is worth noting that using Green's function given by Eq. (1.7) reduces the domain of integration to the beam length only.

Several particular cases derive from Eq. (1.11). For instance, the frictionless interaction of a Timoshenko beam with the underlying substrate involves null interfacial shear traction r_x along the contact region. Accordingly, the displacement field in Eq. (1.8) reduces to

$$u_x(x) = -\frac{c}{2E}\left[\int_{x_0}^{x} r_z(\hat{x})\,\mathrm{d}\hat{x} - \int_x^{x_L} r_z(\hat{x})\,\mathrm{d}\hat{x}\right], \tag{1.12a}$$

$$u_z(x) = \int_L g(x,\hat{x})\,r_z(\hat{x})\,\mathrm{d}\hat{x}, \tag{1.12b}$$

and the total potential energy in Eq. (1.11) reduces to Eq. (13) reported in [26], where the mixed variational formulation is used to evaluate vertical displacement u_z and rotation φ of the foundation beam, as well as contact pressure r_z.

Pressure r_z may be neglected when the bending stiffness of the beam is small, i.e., the beam is reduced to a thin coating. Consequently, only the interfacial shear traction r_x arises and the displacement field in Eq. (1.8) can be rewritten as

$$u_x(x) = \int_L g(x,\hat{x})\,r_x(\hat{x})\,\mathrm{d}\hat{x}, \tag{1.13a}$$

$$u_z(x) = \frac{c}{2E}\left[\int_{x_0}^{x} r_x(\hat{x})\,\mathrm{d}\hat{x} - \int_x^{x_L} r_x(\hat{x})\,\mathrm{d}\hat{x}\right], \tag{1.13b}$$

Moreover, the total potential energy in Eq. (1.11) reduces to Eq. (6) reported in [27], where the mixed variational formulation is used to evaluate both the axial displacement u_x of the thin coating and the interfacial shear traction r_x.

A stiff beam resting on a soft substrate behaves like a rigid indenter. Thus, the surface displacements are specified by the indenter profile and strain energies $U_{\text{beam},a}$ and $U_{\text{beam},b}$ in Eqs. (1.4) are equal to zero. Therefore, the total potential energy reduces to

$$\Pi = \Pi_{\text{soil},a} + \Pi_{\text{soil},b} - b \int_L \left[(p_x - r_x)\,\overline{u}_x + (p_z - r_z)\,\overline{u}_z + (m - r_x\,h/2)\,\overline{\varphi} \right] \mathrm{d}x \tag{1.14}$$

with $\overline{u}_x$, $\overline{u}_z$, and $\overline{\varphi}$ being the prescribed tangential and normal displacements, and the prescribed rotation, respectively. With reference to the profile of a rigid flat indenter, the prescribed displacements are

$$\overline{u}_x(x) = u_{x,o}, \qquad \overline{u}_z(x) = u_{z,o} - \varphi_o\,x, \qquad \overline{\varphi}(x) = \varphi_o \tag{1.15a, b, c}$$

where $u_{x,o}$, $u_{z,o}$, and φ_o are specified at the origin $x = z = 0$. The variational principle (1.14) can be rewritten as

$$\begin{aligned} \Pi = \Pi_{\text{soil},a} + \Pi_{\text{soil},b} + \\ - b \left\{ u_{x,o} \int_L (p_x - r_x)\,\mathrm{d}x + u_{z,o} \int_L (p_z - r_z)\,\mathrm{d}x + \varphi_o \int_L \left[m - (p_z - r_z)x \right]\mathrm{d}x \right\} \end{aligned} \tag{1.16}$$

It can readily be noted that, in Eq. (1.16), each integral in curly brackets imposes a global equilibrium equation.

With regard to an inextensible thin coating bonded to an elastic substrate, pressure $r_z(x) = 0$ along the contact region, and variational principle (1.14) yields

$$\Pi = -\frac{b}{2} \int_L r_x(x)\,\mathrm{d}x \int_L g(x,\hat{x})\,r_x(\hat{x})\,\mathrm{d}\hat{x} - b \int_L (p_x - r_x)\,\overline{u}_x\,\mathrm{d}x \tag{1.17}$$

Finally, for an indenter in frictionless contact with the substrate, the interfacial shear traction $r_x = 0$ and Eq. (1.14) reduces to

$$\Pi = -\frac{b}{2} \int_L r_z(x)\,\mathrm{d}x \int_L g(x,\hat{x})\,r_z(\hat{x})\,\mathrm{d}\hat{x} - b \int_L \left[(p_z - r_z)\,\overline{u}_z + m\,\overline{\varphi} \right] \mathrm{d}x \tag{1.18}$$

Variational forms similar to Eqs. (1.17) and (1.18) have widely been used to determine contact areas and pressures in contact problems involving rigid punches, see e.g. [19] and references cited therein.

1.3 Finite element model

Both the foundation beam and the substrate boundary are subdivided into FEs. It is worth noting that the mesh of the half-plane boundary can be defined independently of that of the beam, but in the following the same mesh is adopted. The generic ith FE is characterised by initial and end coordinates x_i and x_{i+1}, length $l_i = |x_{i+1} - x_i|$ and dimensionless local coordinate $\xi = x/l_i$. As usual in the FEM, vectors $\mathbf{u}_{xi} = [u_{x,i}, u_{x,i+1}]^T$ and $\mathbf{q}_{zi} = [u_{z,i}, \varphi_i, u_{z,i+1}, \varphi_{i+1}]^T$ of nodal displacements characterise the displacement field within the ith element by means of the following relations:

$$u(\xi) = \mathbf{N}_a(\xi)\,\mathbf{u}_{xi}, \qquad [v(\xi),\,\varphi(\xi)]^T = \mathbf{N}_b(\xi)\,\mathbf{q}_{zi} \tag{1.19}$$

where vector $\mathbf{N}_a(\xi)$ and matrix $\mathbf{N}_b(\xi)$ contain the shape functions. In particular, for the analyses presented in the following, $\mathbf{N}_a(\xi) = [N_{a,1},\ N_{a,2}]$ collects linear Lagrangian functions $N_{a,1} = 1 - \xi$ and $N_{a,2} = \xi$, whereas matrix $\mathbf{N}_b(\xi)$ assembles "modified" Hermitian shape functions [26, 33-36]:

$$N_{b,11} = \left[1 - 3\xi^2 + 2\xi^3 + \phi_i(1-\xi)\right]\Big/(1+\phi_i), \tag{1.20a}$$

$$N_{b,12} = -l_i\,\xi\left[(1-\xi)^2 + \phi_i(1-\xi)/2\right]\Big/(1+\phi_i), \tag{1.20b}$$

$$N_{b,13} = \left[3\xi^2 - 2\xi^3 + \phi_i\xi\right]\Big/(1+\phi_i), \tag{1.20c}$$

$$N_{b,14} = -l_i\,\xi\left[-\xi + \xi^2 - \phi_i(1-\xi)/2\right]\Big/(1+\phi_i), \tag{1.20d}$$

$$N_{b,21} = 6\xi(1-\xi)\big/\left[l_i(1+\phi_i)\right], \tag{1.20e}$$

$$N_{b,22} = \left[1 - 4\xi + 3\xi^2 + \phi_i(1-\xi)\right]\Big/(1+\phi_i), \tag{1.20f}$$

$$N_{b,23} = -6\xi(1-\xi)\big/\left[l_i(1+\phi_i)\right], \tag{1.20g}$$

$$N_{b,24} = \left[-2\xi + 3\xi^2 + \phi_i\xi\right]\Big/(1+\phi_i), \tag{1.20h}$$

where coefficient $\phi_i = 12D_b/(k_b\,G_b\,A_b l_i^2)$. Polynomials (1.20) follow from the exact solution to the homogeneous governing equations of Timoshenko beam theory [33]. Moreover, when shear deformations are negligible, coefficients ϕ_i vanish and polynomials

$N_{b,1j}$ and $N_{b,2j}$ ($j = 1,\ldots,4$) in Eqs. (1.20) reduce to the classical Hermitian polynomials and to their first derivatives, respectively.

Soil reactions for the ith element can be approximated by the expressions:

$$r_x(\xi)= [\boldsymbol{\rho}_a(\xi)]^{\mathrm{T}}\,\mathbf{r}_{xi}, \qquad r_z(\xi)= [\boldsymbol{\rho}_b(\xi)]^{\mathrm{T}}\,\mathbf{r}_{zi}, \qquad\qquad (1.21\text{a, b})$$

where $\mathbf{r}_{xi}$, $\mathbf{r}_{zi}$ denote nodal interfacial shear and normal tractions, respectively, and vectors $\boldsymbol{\rho}_a$, $\boldsymbol{\rho}_b$ collect constant or linear shape functions.

Substituting Eqs. (1.19), (1.21) into variational principle (1.11) and assembling over all elements, the potential energy takes the expression

$$\begin{aligned}
\Pi(\mathbf{u}_x, \mathbf{q}_z, \mathbf{r}_x, \mathbf{r}_z) = {} & \frac{1}{2}\mathbf{u}_x^{\mathrm{T}}\mathbf{K}_a\mathbf{u}_x + \frac{1}{2}\mathbf{q}_z^{\mathrm{T}}\mathbf{K}_b\mathbf{q}_z - \mathbf{u}_x^{\mathrm{T}}\mathbf{f}_x - \mathbf{q}_z^{\mathrm{T}}\mathbf{f}_z + \mathbf{u}_x^{\mathrm{T}}\mathbf{H}_{xx}\mathbf{r}_x + \mathbf{q}_z^{\mathrm{T}}\mathbf{H}_{zz}\mathbf{r}_z + \mathbf{q}_z^{\mathrm{T}}\mathbf{H}_{zx}\mathbf{r}_x \\
& - \frac{1}{2}\mathbf{r}_x^{\mathrm{T}}\mathbf{G}_{xx}\mathbf{r}_x - \frac{1}{2}\mathbf{r}_z^{\mathrm{T}}\mathbf{G}_{zz}\mathbf{r}_z - \frac{1}{2}\mathbf{r}_x^{\mathrm{T}}\mathbf{G}_{xz}\mathbf{r}_z - \frac{1}{2}\mathbf{r}_z^{\mathrm{T}}\mathbf{G}_{zx}\mathbf{r}_x
\end{aligned} \qquad (1.22)$$

where $\mathbf{K}_a$, $\mathbf{K}_b$ are the beam stiffness matrices and $\mathbf{f}_x$, $\mathbf{f}_z$ are the external load vectors, whose components for the ith FE can be written in the usual form:

$$k_{a,ij} = l_i \int_0^1 E_0 A_b(\xi) N'_{a,i}(\xi) N'_{a,j}(\xi)\,\mathrm{d}\xi, \qquad\qquad (1.23\text{a})$$

$$k_{b,ij} = l_i \int_0^1 D_b(\xi)\left[N'_{b,2i}(\xi)N'_{b,2j}(\xi) \; + \right. \qquad\qquad (1.23\text{b})$$

$$\left. \frac{12}{\phi_i l_i^2}\left(N'_{b,1i}(\xi) + N_{b,2i}(\xi)\right)\left(N'_{b,1j}(\xi) + N_{b,2j}(\xi)\right)\right]\mathrm{d}\xi$$

$$f_{x,i} = bl_i \int_0^1 N_{a,i}(\xi)\,p_x(\xi)\,\mathrm{d}\xi, \qquad\qquad (1.24\text{a})$$

$$f_{z,i} = bl_i \int_0^1 N_{b,1i}(\xi)\,p_z(\xi) + N_{b,2i}(\xi)m(\xi)\,\mathrm{d}\xi. \qquad\qquad (1.24\text{b})$$

With regard to the components of matrices $\mathbf{H}_{xx}$, $\mathbf{H}_{zz}$, $\mathbf{H}_{xz}$ appearing in Eq. (1.22), the following expressions hold for the generic FE:

$$h_{xx,ij} = bl_i \int_0^1 N_{a,i}(\xi)\rho_{a,j}(\xi)\mathrm{d}\xi, \qquad\qquad (1.25\text{a})$$

$$h_{zz,ij} = bl_i \int_0^1 N_{b,1i}(\xi)\rho_{b,j}(\xi)\mathrm{d}\xi, \qquad\qquad (1.25\text{b})$$

$$h_{xz,ij} = \frac{bhl_i}{2} \int_0^1 N_{b,2i}(\xi)\rho_{a,j}(\xi)\mathrm{d}\xi. \qquad\qquad (1.25\text{c})$$

Matrices $\mathbf{G}_{xx}$, $\mathbf{G}_{zz}$, $\mathbf{G}_{xz}$, $\mathbf{G}_{zx}$ are fully populated since they take account of the nonlocal relation between beam displacements and surface tractions. The components of these matrices are given by:

$$g_{xx,ij} = b\int_{x_i}^{x_{i+1}} \rho_{a,i}(x)\,\mathrm{d}x \int_{x_j}^{x_{j+1}} g(x,\hat{x})\,\rho_{a,j}(\hat{x})\,\mathrm{d}\hat{x}, \tag{1.26a}$$

$$g_{zz,ij} = b\int_{x_i}^{x_{i+1}} \rho_{b,i}(x)\,\mathrm{d}x \int_{x_j}^{x_{j+1}} g(x,\hat{x})\,\rho_{b,j}(\hat{x})\,\mathrm{d}\hat{x}, \tag{1.26b}$$

$$g_{xz,ij} = -\frac{bc}{2E}\int_{x_i}^{x_{i+1}} \rho_{a,i}(x)\,\mathrm{d}x \left[\int_{x_0}^{x} \rho_{b,j}(\hat{x})\,\mathrm{d}\hat{x} - \int_{x}^{x_L} \rho_{b,j}(\hat{x})\,\mathrm{d}\hat{x}\right], \tag{1.26c}$$

$$g_{zx,ij} = \frac{bc}{2E}\int_{x_i}^{x_{i+1}} \rho_{b,i}(x)\,\mathrm{d}x \left[\int_{x_0}^{x} \rho_{a,j}(\hat{x})\,\mathrm{d}\hat{x} - \int_{x}^{x_L} \rho_{a,j}(\hat{x})\,\mathrm{d}\hat{x}\right]. \tag{1.26d}$$

The integrals in Eqs. (26a, b) are weakly singular, i.e. they always exist in the Cauchy principal value sense and are finite. Moreover, if equal substrate shape functions are adopted, i.e., $\rho_a = \rho_b = \rho$, Eqs. (26a, b) involve symmetric matrices and yield $\mathbf{G}_{xx} = \mathbf{G}_{zz}$, whereas Eqs. (26c, d) imply the condition $\mathbf{G}_{zx} = -\mathbf{G}_{xz}$.

Requiring the total potential energy in Eq. (22) to be stationary, the following system of equations is obtained:

$$\begin{bmatrix} \mathbf{K} & \mathbf{H} \\ \mathbf{H}^{\mathrm{T}} & -\mathbf{G} \end{bmatrix}\begin{Bmatrix} \mathbf{q} \\ \mathbf{r} \end{Bmatrix} = \begin{Bmatrix} \mathbf{f} \\ \mathbf{0} \end{Bmatrix}, \tag{1.27}$$

where

$$\mathbf{K} = \begin{bmatrix} \mathbf{K}_a & \mathbf{0} \\ \mathbf{0} & \mathbf{K}_b \end{bmatrix}, \quad \mathbf{H} = \begin{bmatrix} \mathbf{H}_{xx} & \mathbf{0} \\ \mathbf{H}_{xz} & \mathbf{H}_{zz} \end{bmatrix}, \quad \mathbf{G} = \begin{bmatrix} \mathbf{G}_{xx} & \mathbf{G}_{xz} \\ \mathbf{G}_{zx} & \mathbf{G}_{zz} \end{bmatrix}, \tag{1.28a, b, c}$$

$$\mathbf{q} = \begin{bmatrix} \mathbf{u}_x \\ \mathbf{q}_z \end{bmatrix}, \quad \mathbf{r} = \begin{bmatrix} \mathbf{r}_x \\ \mathbf{r}_z \end{bmatrix}, \quad \mathbf{f} = \begin{bmatrix} \mathbf{f}_x \\ \mathbf{f}_z \end{bmatrix}. \tag{1.29a, b, c}$$

Equation (27) represents the discrete system of equations governing the response of the beam-substrate system. From the numerical point of view, vectors $\mathbf{q}$ and $\mathbf{r}$ are obtained by solving Eq. (27). In particular, the following expressions hold:

$$\mathbf{r} = \mathbf{G}^{-1}\,\mathbf{H}^{\mathrm{T}}\,\mathbf{q}, \qquad (\mathbf{K} + \mathbf{K}_{\mathrm{soil}})\,\mathbf{q} = \mathbf{f}, \tag{1.30a, b}$$

where $\mathbf{K}_{\mathrm{soil}} = \mathbf{H}\,\mathbf{G}^{-1}\,\mathbf{H}^{\mathrm{T}}$ is the stiffness matrix of the substrate. Some general considerations on stability and convergence properties of the proposed mixed FE model are reported in [26, 27], and references cited therein. Furthermore, it is simple to show that

$\mathbf{K}_{\text{soil}}$ is symmetric. In fact, $(\mathbf{K}_{\text{soil}})^\mathrm{T} = (\mathbf{H}\,\mathbf{G}^{-1}\,\mathbf{H}^\mathrm{T})^\mathrm{T} = \mathbf{H}\,\mathbf{G}^{-\mathrm{T}}\,\mathbf{H}^\mathrm{T} = \mathbf{H}\,\mathbf{G}^{-1}\,\mathbf{H}^\mathrm{T} = \mathbf{K}_{\text{soil}}$, since matrix $\mathbf{G}$ is symmetric, as it will be shown in Section 3.2.

It is worth noting that the second row of Eq. (1.27), containing the governing equation of the discrete Galerkin method for the system of Eqs. (1.8a, b), includes the beam rotations due to the substrate tractions. In particular, the compatibility of rotation between foundation beam and soil substrate is enforced by the following term appearing in Eq. (1.6b):

$$-b \int_L \left[r_z\, u_z + r_x\, h/2\, \varphi \right] \mathrm{d}x \tag{1.31}$$

leading to $\mathbf{q}_z^\mathrm{T}\mathbf{H}_{zz}\mathbf{r}_z + \mathbf{q}_z^\mathrm{T}\mathbf{H}_{zx}\mathbf{r}_x$ in Eq. (1.22). Thus, matrices $\mathbf{H}_{zz}$ and $\mathbf{H}_{zx}$ play a key role in enforcing the compatibility of nodal rotations. It is also to be noted that the validity of Eq. (1.30a) does not depend on the presence of a foundation beam. In other words, Eq. (1.30a) may be used to obtain the surface tractions arising from a generic displacement field $\mathbf{q}$ assigned to the half-plane boundary. The particular case of a flat rigid punch perfectly bonded to the substrate will be analysed in Sections 1.3.6 and 1.4.1.

Differently, Cheung and Nag [17], and many others adopting the same approach (see for example [11]), used Eqs. (1.8a, b) to compute the displacements due to piecewise constant soil tractions. This method implicitly assumes that the beam is connected to the substrate at equally spaced points through a finite number of pinned-clamped rigid links; thus, no angular continuity between beam and soil substrate can be imposed. Accordingly, the resulting soil matrix has to be augmented by rows and columns of zeros in correspondence of the nodal rotations. The numerical performance of the approach proposed in [17] is reported in Section 1.4.2.2 for comparison.

Finally, in the case of a structure connected to a foundation beam, Eq. (1.27) can be partitioned as reported in [26, 27]. In particular, denoting with $\mathbf{q}_1$ and $\mathbf{q}_2$ the vectors of nodal displacements referred to the structure only and those shared between structure and foundation beam, respectively, and with $\mathbf{f}_1$ and $\mathbf{f}_2$ the corresponding load vectors, Eq. (1.27) takes the form:

$$\begin{bmatrix} \mathbf{K}_{11} & \mathbf{K}_{12} & \mathbf{0} \\ \mathbf{K}_{21} & \mathbf{K}_{22} & \mathbf{H} \\ \mathbf{0} & \mathbf{H}^\mathrm{T} & -\mathbf{G} \end{bmatrix} \begin{Bmatrix} \mathbf{q}_1 \\ \mathbf{q}_2 \\ \mathbf{r} \end{Bmatrix} = \begin{Bmatrix} \mathbf{f}_1 \\ \mathbf{f}_2 \\ \mathbf{0} \end{Bmatrix} \tag{1.32}$$

1.3.1 Prismatic beam subjected to uniform loads

For the sake of completeness, classical results referred to a prismatic beam subjected to uniform loads $p_x(x)$, $p_z(x)$ and couple $m(x)$ are recalled. Beam stiffness matrices $\mathbf{K}_a$, $\mathbf{K}_b$ and external load vectors $\mathbf{f}_x$, $\mathbf{f}_z$ can be rewritten as

$$\mathbf{K}_a = \frac{E_0 A}{L}\, \widetilde{\mathbf{K}}_a, \quad \mathbf{K}_b = \frac{D_b}{L^3}\, \widetilde{\mathbf{K}}_b, \quad \mathbf{f}_a = b\widetilde{\mathbf{f}}_a, \quad \mathbf{f}_b = b\widetilde{\mathbf{f}}_b \qquad (1.33a, b, c, d)$$

where, by virtue of Eqs. (1.23) and (1.24), the last terms on the right-hand sides are given by:

$$\widetilde{\mathbf{K}}_{a,i} = \frac{L}{l_i}\begin{bmatrix} 1 & -1 \\ -1 & 1 \end{bmatrix}, \quad \widetilde{\mathbf{f}}_{a,i} = \frac{p_x l_i}{2}\begin{bmatrix} 1 \\ 1 \end{bmatrix} \qquad (1.34a, b)$$

$$\widetilde{\mathbf{K}}_{b,i} = \frac{L^3}{(1+\phi_i)l_i^3}\begin{bmatrix} 12 & -6l_i & -12 & -6l_i \\ & (4+\phi_i)l_i^2 & 6l_i & (2-\phi_i)l_i^2 \\ & & 12 & 6l_i \\ \text{symm} & & & (4+\phi_i)l_i^2 \end{bmatrix} \qquad (1.35a)$$

$$\widetilde{\mathbf{f}}_{b,i} = p_z\,[l_i/2,\ -l_i^2/12,\ l_i/2,\ l_i^2/12]^{\mathrm{T}} + m/(1+\phi_i)\,[1,\ l_i\phi_i/2,\ -1,\ l_i\phi_i/2]^{\mathrm{T}} \qquad (1.35b)$$

Assembly of global stiffness matrices $\mathbf{K}_a$, $\mathbf{K}_b$ and load vectors $\mathbf{f}_a$, $\mathbf{f}_b$ from the corresponding element matrices $\mathbf{K}_{ai}$, $\mathbf{K}_{bi}$ and load vectors $\mathbf{f}_{ai}$, $\mathbf{f}_{bi}$ follows the usual procedure. However, possible constraint equations among displacements or rotations of the foundation beam can be included into the total potential energy of the beam-substrate system (Eq. (1.22)) by means of a penalty approach, as illustrated in [28, 29].

1.3.2 Piecewise constant substrate tractions

In the following numerical examples, only piecewise constant functions are used to interpolate $\mathbf{r}_x$ and $\mathbf{r}_z$, i.e., the shape functions for the soil tractions are assumed to be $\rho_a(\xi) = \rho_b(\xi) = 1$. Consequently, matrices $\mathbf{G}_{xx}$, $\mathbf{G}_{zz}$, $\mathbf{G}_{xz}$, $\mathbf{G}_{zx}$ can be written as

$$\mathbf{G}_{xx} = \mathbf{G}_{zz} = \frac{b}{E}\, \widetilde{\mathbf{G}}, \qquad \mathbf{G}_{xz} = \frac{bc}{E}\, \widetilde{\mathbf{G}}_{xz}, \qquad (1.36a, b)$$

where the components of $\widetilde{\mathbf{G}}$ are given by:

$$\widetilde{g}_{ii} = \frac{2l_i^2}{\pi}\left(\frac{3}{2} - \ln l_i\right) \qquad (1.37a)$$

$$\widetilde{g}_{ij} = \frac{2}{\pi} \left[\frac{3}{2} l_i l_j + G(x_{j+1} - x_{i+1}) - \right.$$

$$\left. G(x_{j+1} - x_i) - G(x_j - x_{i+1}) + G(x_j - x_i) \right] \qquad \text{for } i \neq j \tag{1.37b}$$

In the previous equation $G(x) = x^2/2 \, \ln|x|$ and parameter d has been omitted since a rigid-body displacement can be imposed in the post-processing analysis. The components of $\widetilde{\mathbf{G}}_{xz}$ are given by:

$$\widetilde{g}_{xz} = \begin{cases} \widetilde{g}_{xz,ij} = -l_i \, l_j/2 & \text{if } i > j \\ \widetilde{g}_{xz,ii} = 0 & \text{if } i = j \\ \widetilde{g}_{xz,ij} = l_i \, l_j/2 & \text{if } i < j \end{cases} \tag{1.38}$$

implying the property $\mathbf{G}_{xz} = -\mathbf{G}_{xz}^{\mathrm{T}}$. Thus, taking into account that $\mathbf{G}_{zx} = -\mathbf{G}_{xz}$, the relation $\mathbf{G}_{zx} = \mathbf{G}_{xz}^{\mathrm{T}}$ is obtained. Therefore, matrix $\mathbf{G}$ reported in Eq. (1.28c) is symmetric.

With regard to matrix $\mathbf{H} = b\,\widetilde{\mathbf{H}}$, if piecewise constant tractions $\mathbf{r}_x$ and $\mathbf{r}_z$ are assumed, Eqs. (1.25) yield the following components for the ith FE

$$\widetilde{\mathbf{h}}_{xx,i} = l_i/2 \, [1, 1]^{\mathrm{T}} \tag{1.39a}$$

$$\widetilde{\mathbf{h}}_{zz,i} = [l_i/2, \, -l_i^2/12, \, l_i/2, \, l_i^2/12]^{\mathrm{T}} \tag{1.39b}$$

$$\widetilde{\mathbf{h}}_{xz,i} = \frac{h}{2(1+\phi_i)} [1, \, \phi_i l_i/2, \, -1, \, \phi_i l_i/2]^{\mathrm{T}} \tag{1.39c}$$

The ith column of global matrices $\mathbf{H}_{xx}$, $\mathbf{H}_{zz}$ and $\mathbf{H}_{xz}$ contains only the vectors represented by Eqs. (1.39a), (1.39b) and (1.39c), respectively. Therefore, in a mesh with node and element numbers sorted in ascending order and indicating with symbol '×' a nonzero entry, global matrices $\mathbf{H}_{xx}$ and $\mathbf{H}_{zz}$ are populated as follows:

$$\mathbf{H}_{xx} = \begin{bmatrix} \times & & & \\ \times & \times & & \\ & \times & \times & \\ & & \times & \cdots \end{bmatrix}, \qquad \mathbf{H}_{zz} = \begin{bmatrix} \times & & \\ \times & & \\ \times & \times & \\ \times & \times & \\ & \times & \times \\ & \times & \cdots \end{bmatrix}. \tag{1.40a, b}$$

Moreover, matrix $\mathbf{H}_{xz}$ has nonzero entries in the same positions as $\mathbf{H}_{zz}$.

The foundation beam interposed between the substrate and the external load may be ignored if axial and bending beam stiffnesses are small. Consequently, beam matrix $\mathbf{K}$ can

be neglected in Eq. (1.27) and the corresponding equation, $\mathbf{K}_{\text{soil}}\ \mathbf{q}\ =\ \mathbf{f}$, gives the displacements of the soil surface due to assigned load distributions. As shown in [26] for flexible foundation beams in frictionless contact with the substrate, the vertical displacements of the soil surface are well approximated by the analytical solution resulting from the problem of an elastic half-plane loaded by a uniform vertical load p_z. However, Fig. 11d reported in [26] shows that pressure r_z may be affected by oscillations at the ends of the loaded region, similar to Gibbs oscillations in series analysis.

1.3.3 Prismatic beam with piecewise constant surface tractions

Making use of Eqs. (1.33) and (1.36), Eq. (1.27) may be rewritten as follows:

$$\begin{bmatrix} D_b/L^3\,\widetilde{\mathbf{K}} & b\widetilde{\mathbf{H}} \\ b\widetilde{\mathbf{H}}^{\mathrm{T}} & -b/E\,\widetilde{\mathbf{G}} \end{bmatrix}\begin{Bmatrix} \mathbf{q} \\ \mathbf{r} \end{Bmatrix} = \begin{Bmatrix} b\widetilde{\mathbf{f}} \\ \mathbf{0} \end{Bmatrix}, \tag{1.41}$$

where

$$\widetilde{\mathbf{K}} = \begin{bmatrix} \lambda_0^2\,\widetilde{\mathbf{K}}_a & \mathbf{0} \\ \mathbf{0} & \widetilde{\mathbf{K}}_b \end{bmatrix}, \quad \widetilde{\mathbf{H}} = \begin{bmatrix} \widetilde{\mathbf{H}}_{xx} & \mathbf{0} \\ \widetilde{\mathbf{H}}_{xz} & \widetilde{\mathbf{H}}_{zz} \end{bmatrix}, \quad \widetilde{\mathbf{G}} = \begin{bmatrix} \widetilde{\mathbf{G}}_{xx} & c\widetilde{\mathbf{G}}_{xz} \\ c\widetilde{\mathbf{G}}_{xz}^{\mathrm{T}} & \widetilde{\mathbf{G}}_{zz} \end{bmatrix}, \quad \widetilde{\mathbf{f}} = \begin{bmatrix} \widetilde{\mathbf{f}}_x \\ \widetilde{\mathbf{f}}_z \end{bmatrix}, \tag{1.42a, b, c, d}$$

with $\lambda_0 = L/r_g$ and the radius of gyration $r_g = h/\sqrt{12}$. Therefore, solutions (1.30) reduce to

$$\mathbf{r} = E\widetilde{\mathbf{G}}^{-1}\widetilde{\mathbf{H}}^{\mathrm{T}}\mathbf{q}, \qquad D_b/L^3\left[\widetilde{\mathbf{K}} + (\alpha L)^3\,\widetilde{\mathbf{K}}_{\text{soil}}\right]\mathbf{q} = b\widetilde{\mathbf{f}}, \tag{1.43a, b}$$

being $\widetilde{\mathbf{K}}_{\text{soil}} = \widetilde{\mathbf{H}}\widetilde{\mathbf{G}}^{-1}\widetilde{\mathbf{H}}^{\mathrm{T}}$ the nondimensional stiffness matrix of the substrate and

$$\alpha L = \sqrt[3]{b\,E\,L^3/D_b}\,. \tag{1.44}$$

According to references [14, 26, 37], parameter αL governs the static response of the beam-substrate system. Low values of αL characterise short beams stiffer than soil, whereas high values of αL correspond to slender beams on a relatively stiff soil. It is worth noting that a different parameter characterises the elastic response of a thin coating bonded to an elastic substrate. This parameter takes the following form [27, 38]:

$$\beta L = b\,E\,L/(E_0\,A_b), \tag{1.45}$$

yielding the relationship $(\alpha L)^3 = (\beta L)\,\lambda_0^2$.

As stated above, mesh sizes of beam and substrate boundary can be defined independently of one another, and shape functions different from those of Eqs. (1.20) may

be adopted as well. For example, in [27] quadratic Lagrangian bar elements including one or two equal substrate elements are used. In [26] beam-substrate matrices obtained using four equal soil elements for each beam element are reported.

1.3.4   Beam in frictionless contact with the substrate

For a beam resting in frictionless contact on an elastic half-plane, $\mathbf{r}_x = \mathbf{f}_x = \mathbf{0}$, and Eq. (1.27) reduces to the following expression:

$$
\begin{bmatrix} \mathbf{K}_b & \mathbf{H}_{zz} \\ \mathbf{H}_{zz}^{\mathrm{T}} & -\mathbf{G}_{zz} \end{bmatrix} \begin{Bmatrix} \mathbf{q}_z \\ \mathbf{r}_z \end{Bmatrix} = \begin{Bmatrix} \mathbf{f}_z \\ \mathbf{0} \end{Bmatrix}
\tag{1.46}
$$

coinciding with Eq. (26) reported in [26]. In particular, the second row of Eq. (1.46) contains the governing equation of the discrete Galerkin method for Eq. (1.12b), and relates beam rotations to vertical reactions. Differently, in [16] a collocation method is proposed to solve Eq. (1.12b), but no angular continuity between the foundation beam and the substrate is ensured. Accordingly, static condensation was applied to beam matrix $\mathbf{K}_b$, so as to cancel out rows and columns corresponding to the nodal rotations.

The horizontal displacements at the substrate boundary may be obtained by making use of a Galerkin solution to Eq. (1.12a), written in the form:

$$
\int_L r_z(x)\, u_x(x)\, \mathrm{d}x = -\frac{c}{2E} \int_L r_z(x)\, \mathrm{d}x \left[\int_{x_0}^{x} r_z(\hat{x})\, \mathrm{d}\hat{x} - \int_{x}^{x_L} r_z(\hat{x})\, \mathrm{d}\hat{x} \right].
\tag{1.47}
$$

The previous equation may be solved numerically using a piecewise constant discretization of both normal reactions r_z, see Eq. (1.21b), and horizontal displacements, i.e.,

$$
u_x(\xi) = [\boldsymbol{\rho}_a(\xi)]^{\mathrm{T}}\, \mathbf{u}_{xi},
\tag{1.48}
$$

leading to the following expression:

$$
diag(l_1, \cdots, l_n)\, \mathbf{u}_x = \frac{c}{E}\, \widetilde{\mathbf{G}}_{xz} \mathbf{r}_z.
\tag{1.49}
$$

1.3.5   Thin coating bonded to the substrate

With regard to a bar with zero bending stiffness (i.e., a thin coating) bonded to an elastic half-plane and having the centroidal axis coinciding with the substrate boundary, $\mathbf{r}_z = \mathbf{f}_z = \mathbf{0}$, $D_b = 0$, and Eq. (1.27) reduces to the following expression (see Eq. (14) reported in [27]):

$$\begin{bmatrix} \mathbf{K}_a & \mathbf{H}_{xx} \\ \mathbf{H}_{xx}^{\mathrm{T}} & -\mathbf{G}_{xx} \end{bmatrix} \begin{Bmatrix} \mathbf{q}_x \\ \mathbf{r}_x \end{Bmatrix} = \begin{Bmatrix} \mathbf{f}_x \\ \mathbf{0} \end{Bmatrix} \qquad (1.50)$$

The vertical displacements at the substrate boundary may be obtained by making use of a Galerkin solution to Eq. (1.13b), written in the form:

$$\int_L r_x(x)\, u_z(x)\, \mathrm{d}x = \frac{c}{2E} \int_L r_x(x)\, \mathrm{d}x \left[\int_{x_0}^{x} r_x(\hat{x})\, \mathrm{d}\hat{x} - \int_{x}^{x_L} r_x(\hat{x})\, \mathrm{d}\hat{x} \right]. \qquad (1.51)$$

The previous equation may be solved numerically using a piecewise constant discretization of both tangential reactions r_x, see Eq. (1.21a), and vertical displacements, i.e.,

$$v(\xi) = [\boldsymbol{\rho}_a(\xi)]^{\mathrm{T}}\, \mathbf{u}_{zi}, \qquad (1.52)$$

leading to the following expression:

$$diag(l_1, \cdots, l_n)\, \mathbf{u}_z = \frac{c}{E} \widetilde{\mathbf{G}}_{zx} \mathbf{r}_x. \qquad (1.53)$$

1.3.6 Rigid flat punch with piecewise constant surface tractions

Eq. (1.15) shows that vector $\mathbf{q}_o = [u_{x,o}, u_{z,o}, \varphi_o]^{\mathrm{T}}$, collecting the displacements prescribed at the origin, governs the displacement field generated by a rigid flat punch. Thus, substituting Eqs. (1.21) into variational principle (1.16), assembling over all substrate elements, and requiring the potential energy to be stationary, the following system of equations is obtained

$$\begin{bmatrix} \mathbf{0} & \mathbf{H}_o \\ \mathbf{H}_o^{\mathrm{T}} & -\mathbf{G} \end{bmatrix} \begin{Bmatrix} \mathbf{q}_o \\ \mathbf{r} \end{Bmatrix} = \begin{Bmatrix} \mathbf{f}_o \\ \mathbf{0} \end{Bmatrix}, \qquad (1.54)$$

where

$$\mathbf{H}_o = \begin{bmatrix} \mathbf{h}_{o,xx}^{\mathrm{T}} & \mathbf{0} \\ \mathbf{0} & \mathbf{h}_{o,zz}^{\mathrm{T}} \\ \mathbf{0} & \mathbf{h}_{o,\varphi z}^{\mathrm{T}} \end{bmatrix}, \quad \mathbf{f}_o = \begin{bmatrix} P_{x,o} \\ P_{z,o} \\ M_o \end{bmatrix}, \qquad (1.55\text{a, b})$$

vector $\mathbf{f}_o$ collects the three external load resultants

$$P_{x,o} = \int_L p_x\, \mathrm{d}x, \qquad P_{z,o} = \int_L p_z\, \mathrm{d}x, \qquad M_o = \int_L (m - p_z x)\, \mathrm{d}x, \qquad (1.56\text{a, b, c})$$

whereas vectors $\mathbf{h}_{o,xx}$, $\mathbf{h}_{o,zz}$, $\mathbf{h}_{o,\varphi z}$ have the following components

17

$$h_{o,xx,i} = bl_i \int_0^1 \rho_{a,i}(\xi)\,\mathrm{d}\xi, \quad h_{o,zz,i} = bl_i \int_0^1 \rho_{b,i}(\xi)\,\mathrm{d}\xi, \quad h_{o,\varphi z,i} = -b \int_{x_i}^{x_{i+1}} \rho_{b,i}(x)x\,\mathrm{d}x \quad (1.57a, b, c)$$

Assuming constant functions $\rho_{a,i} = \rho_{b,i} = 1$, Eqs. (1.57) reduces to

$$h_{o,xx,i} = h_{o,zz,i} = bl_i, \qquad h_{o,\varphi z,i} = -bl_i \frac{x_i + x_{i+1}}{2}. \qquad (1.58a, b, c,)$$

The first relation of Eq. (1.54), $\mathbf{H}_o\,\mathbf{q}_o = \mathbf{f}_o$, imposes compatibility conditions between $\mathbf{q}_o$ and $\mathbf{f}_o$, whereas the second relation, $\mathbf{G}\,\mathbf{r} = \mathbf{H}_o{}^{\mathrm{T}}\,\mathbf{q}_o$, represents the governing equation of the discrete Galerkin method for the system of equations (1.8a, b), with displacements prescribed by Eqs. (1.15a, b). Moreover, the solutions to Eq. (1.54):

$$\mathbf{r} = \mathbf{G}^{-1}\,\mathbf{H}_o^{\mathrm{T}}\,\mathbf{q}_o, \qquad \mathbf{K}_o\,\mathbf{q}_o = \mathbf{f}_o, \qquad\qquad (1.59a, b)$$

are similar to Eqs. (1.30a, b), with the only difference that the stiffness matrix of the substrate, $\mathbf{K}_o = \mathbf{H}_o\,\mathbf{G}^{-1}\,\mathbf{H}_o{}^{\mathrm{T}}$, is a 3-by-3 matrix.

For an inextensible thin coating bonded to an elastic substrate, pressure $r_z = 0$ along the contact region, the variational principle of Eq. (1.17) applies, and in Eq. (1.54) the following relations hold: $\mathbf{G} = \mathbf{G}_{xx}$, $\mathbf{H}_o = \mathbf{h}^{\mathrm{T}}_{o,xx}$, $\mathbf{q}_o = u_{x,o}$, $\mathbf{r} = \mathbf{r}_x$, $\mathbf{f}_o = P_{x,o}$. Consequently, Eqs. (1.59) reduce to

$$\mathbf{G}_{xx}\,\mathbf{r}_x = u_{x,o}\,\mathbf{h}_{o,xx}, \qquad\qquad u_{x,o} = P_{x,o}/k_{o,xx}, \qquad\qquad (1.60a, b)$$

where $k_{o,xx} = \mathbf{h}^{\mathrm{T}}_{o,xx}\,\mathbf{G}^{-1}_{xx}\,\mathbf{h}_{o,xx}$, and Eq. (1.60a) represents the governing equation of the discrete Galerkin method for first kind integral equations with a logarithmic kernel, see [39, 40] and references cited therein. As shown in [27], a thin coating bonded to a substrate behaves like an inextensible stiffener for $\beta L < 0.5$.

For the contact of a frictionless indenter, interfacial shear traction $r_x = 0$, the variational principle of Eq. (1.18) applies, and Eq. (1.54) reduces to

$$\begin{bmatrix} 0 & 0 & \mathbf{h}^{\mathrm{T}}_{o,zz} \\ 0 & 0 & \mathbf{h}^{\mathrm{T}}_{o,\varphi z} \\ \mathbf{h}_{o,zz} & \mathbf{h}_{o,\varphi z} & \mathbf{G}_{zz} \end{bmatrix} \begin{Bmatrix} u_{z,o} \\ \varphi_o \\ \mathbf{r}_z \end{Bmatrix} = \begin{Bmatrix} P_{z,o} \\ M_o \\ \mathbf{0} \end{Bmatrix} \qquad\qquad (1.61)$$

As shown in [26], a foundation beam in frictionless contact with the substrate behaves like a rigid punch for $\alpha L < 1$.

1.3.7 Prismatic beam-column with a rigid foundation placed at the bottom

For a prismatic beam-column element with the bottom node connected with the upper side of a rigid foundation beam of height h (node i in Fig. 1.3), a classical transformation matrix $\mathbf{T}$ has to be adopted to impose the kinematical constraints between the degrees of freedom at node i and those at the substrate boundary (node o in Fig. 1.3):

$$
\mathbf{q}_i = \mathbf{T}\mathbf{q}_{i,o} \quad \Leftrightarrow \quad
\begin{bmatrix}
u_{x,i} \\
u_{x,i+1} \\
u_{z,i} \\
\varphi_i \\
u_{z,i+1} \\
\varphi_{i+1}
\end{bmatrix}
=
\begin{bmatrix}
1 & & & -h & & \\
& 1 & & & & \\
& & 1 & & & \\
& & & 1 & & \\
& & & & 1 & \\
& & & & & 1
\end{bmatrix}
\begin{bmatrix}
u_{x,o} \\
u_{x,i+1} \\
u_{z,o} \\
\varphi_o \\
u_{z,i+1} \\
\varphi_{i+1}
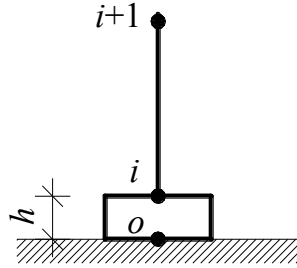\end{bmatrix},
\tag{1.62}
$$

Fig. 1.3. Rigid footing placed on the half-plane boundary and connected to a beam-column.

where unspecified entries in Eq. (1.62) are set equal to zero. The corresponding stiffness matrix and load vector for the ith element undergo the usual transformation rule, i.e., $\mathbf{K}_{i,o} = \mathbf{T}^{\mathrm{T}}\mathbf{K}_i\,\mathbf{T}$ and $\mathbf{f}_{i,o} = \mathbf{T}^{\mathrm{T}}\mathbf{f}_i$, whereas matrix $\mathbf{H}_i$ of the element must be modified as

$$
\mathbf{H}_i =
\begin{bmatrix}
\mathbf{h}_{o,xx}^{\mathrm{T}} & \mathbf{0} \\
\mathbf{0} & \mathbf{0} \\
\mathbf{0} & \mathbf{h}_{o,zz}^{\mathrm{T}} \\
\mathbf{0} & \mathbf{h}_{o,\varphi z}^{\mathrm{T}} \\
\mathbf{0} & \mathbf{0} \\
\mathbf{0} & \mathbf{0}
\end{bmatrix}.
\tag{1.63}
$$

1.4 Numerical Examples

1.4.1 Rigid punch

Accuracy and convergence properties of the proposed coupled FE-BIE formulation are first evaluated with regard to the rotation of a rigid punch of length L, bonded to an elastic half-plane and subjected to a horizontal force P_x or to a bending moment M. Analytical

solutions to these problems are available in the literature. In particular, the punch rotation can be written in closed form as [13]:

$$\varphi_P = \frac{(\kappa+1)\ln\kappa}{G(\pi^2+\ln^2\kappa)L}P_x \tag{1.64a}$$

$$\varphi_M = \frac{\pi(\kappa+1)}{2G(\pi^2+\ln^2\kappa)L^2}M \tag{1.64b}$$

for the case of horizontal force P_x, and for that of bending moment M, respectively. In the previous equations, $\kappa = (3-\nu_s)/(1+\nu_s)$ for generalised plane stress state and $\kappa = 3-4\nu_s$ for generalised plane strain state, and $G = E_s/[2\,(1+\nu_s)]$.

For comparison purposes, both uniform and graded meshes are considered. Coordinate x_j of the generic jth node of the mesh is then given by:

$$x_j = \begin{cases} \dfrac{1}{2}\left[\left(\dfrac{2j}{n_{el}}\right)^{\beta_{exp}} - 1\right] & \text{if } 0 \le j \le n_{el}/2 \\ -x_{n_{el}-j} & \text{if } n_{el}/2 < j \le n_{el} \end{cases} \tag{1.65}$$

with n_{el} being the total number of FEs in the mesh and β_{exp} the so-called grading exponent [41]. A uniform mesh is obtained by assuming $\beta_{exp} = 1$.

Figure 1.4a shows relative error $e_{P\varphi} = |P_x/\varphi_P - P_x/\varphi_o|/(P_x/\varphi_P)$ versus n_{el} for $\beta_{exp} = 1, 2, 3$, where φ_o is the punch rotation obtained from the present analysis when the punch is subjected to force P_x. Analogously, Fig. 1.4b shows relative error $e_{M\varphi} = |M/\varphi_M - M/\varphi_o|/(M/\varphi_M)$ versus n_{el} for $\beta_{exp} = 1, 2, 3$, where φ_o is the punch rotation obtained from the present analysis when the punch is subjected to moment M. In evaluating φ_P and φ_M from Eqs. (1.64), $\kappa = 2.333$ is assumed. In Figs. (1.4a, b), relative errors decrease at a rate $n_{el}^{-1.0}$ for uniform mesh ($\beta_{exp} = 1$), and at higher rates, equal to $n_{el}^{-2.0}$ and $n_{el}^{-2.8}$, for graded mesh with $\beta_{exp} = 2$ and 3. In particular, for a uniform mesh with n_{el} greater than 32, relative error $e_{P\varphi}$ is less than 1%, but the same error can be obtained with graded meshes having $n_{el} \ge 8$. Furthermore, relative error $e_{M\varphi}$ is equal to 0.8% for a uniform mesh with $n_{el} = 64$, and $e_{M\varphi}$ reduces to 0.4% for $\beta_{exp} = 2$ and $n_{el} = 16$, or to 0.5% for $\beta_{exp} = 3$ and $n_{el} = 8$.
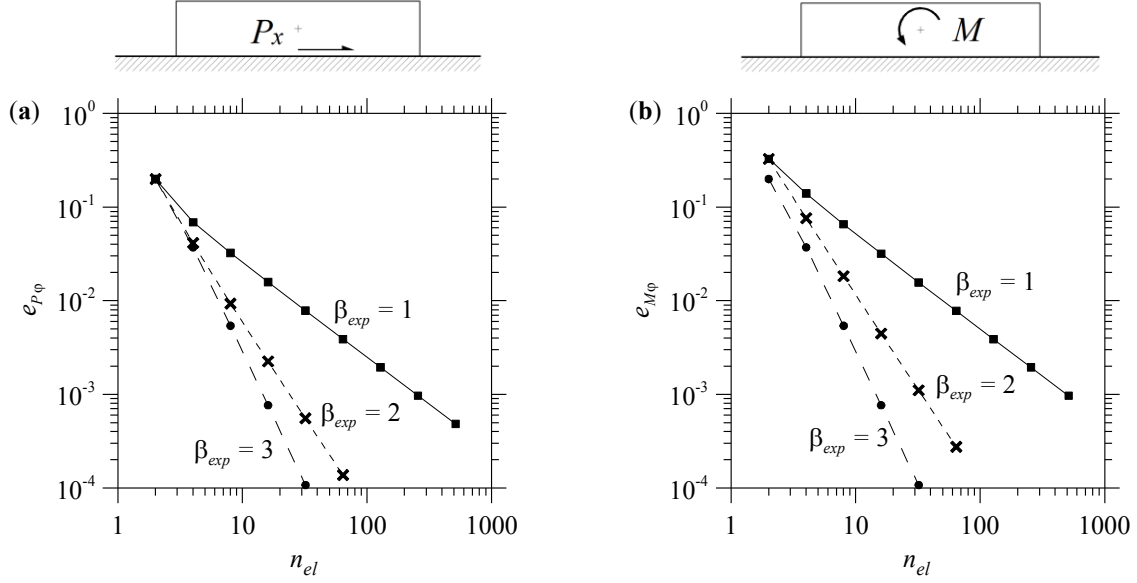
Fig. 1.4. Rigid punch subjected to a horizontal force P_x or a bending moment M. Relative errors $e_{P\varphi} = |P_x/\varphi_P - P_x/\varphi_o|/(P_x/\varphi_P)$ **(a)** and $e_{M\varphi} = |M/\varphi_M - M/\varphi_o|/(M/\varphi_M)$ **(b)** versus n_{el} for uniform ($\beta_{exp} = 1$) and graded mesh ($\beta_{exp} = 2, 3$). φ_P and φ_M are the closed-form rotations (1.64a) and (1.64b), and φ_o is the rotation obtained from the proposed formulation.

Interfacial shear and normal tractions $r_x(x)$ and $r_z(x)$ for a rigid flat punch loaded by a horizontal force P_x and a vertical force P_z are given by Abramov's formulas [12, 13]:

$$r_x(x) = \frac{P_x\, c(x) + P_z\, s(x)}{2\pi\sqrt{(L/2)^2 - x^2}} \qquad (1.66a)$$

$$r_z(x) = \frac{-P_x\, s(x) + P_z\, c(x)}{2\pi\sqrt{(L/2)^2 - x^2}} \qquad (1.66b)$$

where $c(x) = \dfrac{1+\kappa}{\sqrt{\kappa}}\cos\left(\dfrac{\ln\kappa}{2\pi}\ln\dfrac{L/2+x}{L/2-x}\right)$, $s(x) = \dfrac{1+\kappa}{\sqrt{\kappa}}\sin\left(\dfrac{\ln\kappa}{2\pi}\ln\dfrac{L/2+x}{L/2-x}\right)$ and κ takes

the alternative expressions reported above. It is possible to show that the tractions obtained from Eqs. (1.66a, b) fluctuate, in sign an infinite number of times, as x tends to $L/2$ [12]. However, for $P_x = 0$ and $\nu_s = 0.2$, surface tractions become negative for the first time when $x = +0.499996\ L$, which is so close to the edge of the punch that usual continuum mechanics hypothesis does not hold anymore.

In the case of a rigid flat punch subjected to a bending moment M, surface tractions $r_x(x)$ and $r_z(x)$ may be written in closed form as [12, 13]:

$$r_x(x) = \frac{M\left[\pi\, x\, s(x) - L(\ln \kappa)\, c(x)/2\right]}{(\pi^2 + \ln^2 \kappa)(L/2)^2 \sqrt{(L/2)^2 - x^2}}$$

(1.67a)

$$r_z(x) = \frac{M\left[\pi\, x\, c(x) + L(\ln \kappa)\, s(x)/2\right]}{(\pi^2 + \ln^2 \kappa)(L/2)^2 \sqrt{(L/2)^2 - x^2}}$$

(1.67b)

with c, s and κ being obtained from the previously reported expressions.

The results in terms of surface tractions r_x and r_z obtained from the proposed FE-BIE formulation using a uniform mesh with $n_{el} = 512$ substantially coincide with the analytical solutions of Eqs. (1.66) and (1.67). To evaluate the accuracy of numerical solutions obtained using a coarser FE discretization, horizontal and vertical reactions r_x and r_z between a rigid punch subjected to a vertical force P_z and the substrate are estimated by means of a graded mesh with $n_{el} = 8$ and $\beta_{exp} = 2$. The results are reported in nondimensional form in Fig. 1.5 versus the relative position x/L along the punch, where they are compared with the reference solutions corresponding to $n_{el} = 512$ and $\beta_{exp} = 1$. Analytical solutions deriving from Eqs. (1.66) are not reported in the figures because they are indistinguishable from the uniform mesh solutions. Analogous comparisons are presented in Fig. 1.6 for the case of a horizontal force P_x and in Fig. 1.7 for the case of a bending moment M. In all cases, the coarse graded mesh with $n_{el} = 8$ and $\beta_{exp} = 2$ proves to approximate the reference solutions very well.
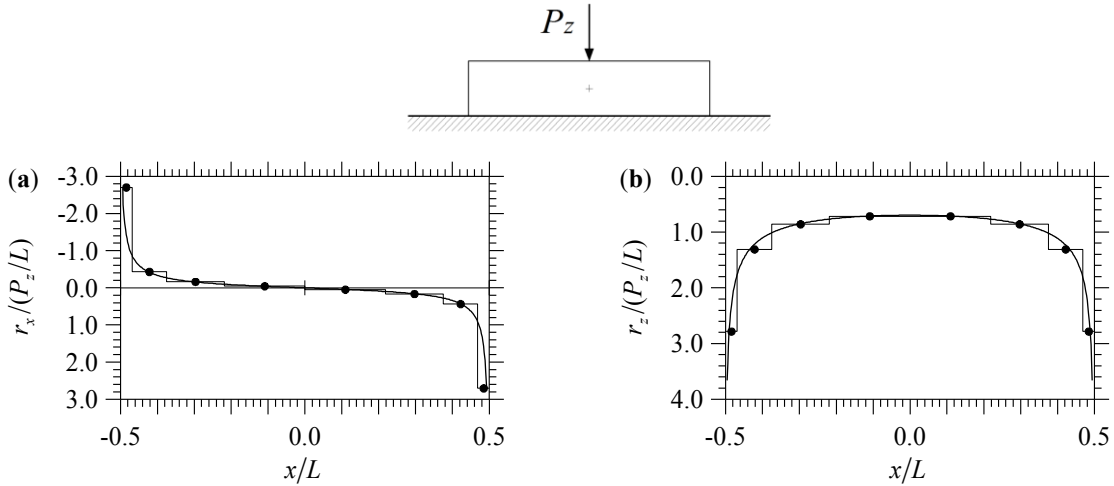

Fig. 1.5. Rigid punch loaded by a vertical point force P_z at midspan. Nondimensional tangential (**a**) and normal (**b**) reactions versus x/L obtained using a uniform mesh with $n_{el} = 512$ (thick solid line) and a graded mesh with $n_{el} = 8$, $\beta_{exp} = 2$ (thin solid line with symbol).
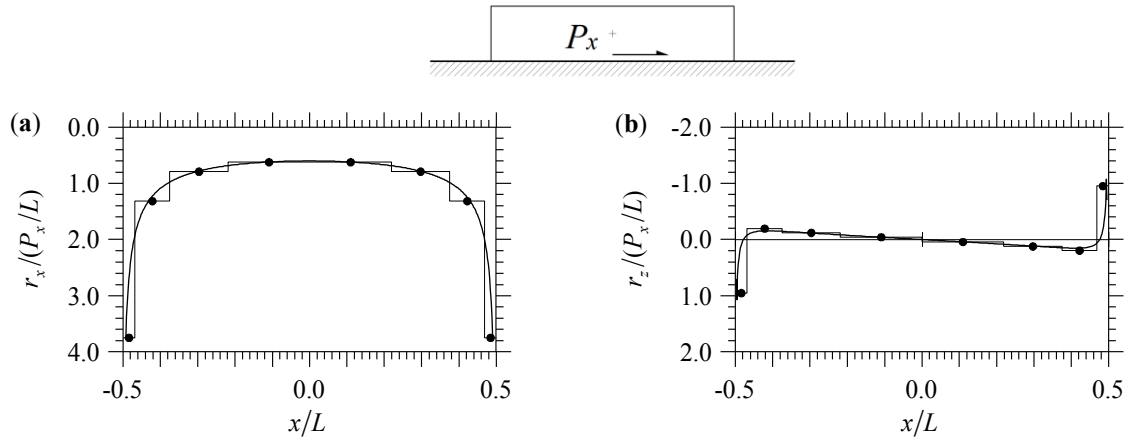
Fig. 1.6. Rigid punch loaded by a horizontal point force P_x at midspan. Nondimensional tangential (**a**) and normal (**b**) reactions versus x/L obtained using a uniform mesh with $n_{el} = 512$ (thick solid line) and a graded mesh with $n_{el} = 8$, $\beta_{exp} = 2$ (thin solid line with symbol).

Fig. 1.7. Rigid punch loaded by a bending moment M at midspan. Nondimensional tangential (**a**) and normal (**b**) reactions versus x/L obtained using a uniform mesh with $n_{el} = 512$ (thick solid line) and a graded mesh with $n_{el} = 8$, $\beta_{exp} = 2$ (thin solid line with symbol).
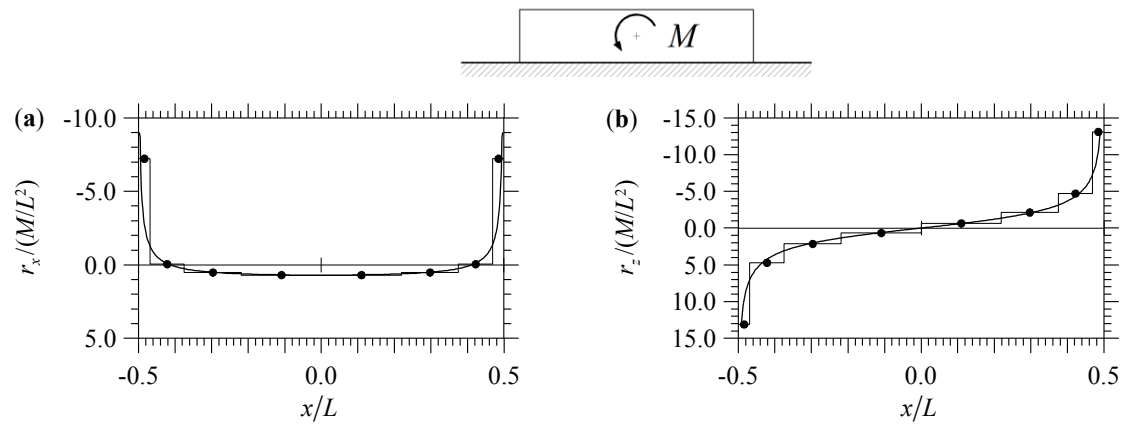
1.4.1.1 Reactions at the end of the rigid punch

The study of stress singularity factor, which was investigated by a thin coating [27] or that could be also analysed in frictionless condition, can not be examined in perfect adhesion because of the nature of tractions which fluctuate in sign an infinite number of times toward the ends [12].

On the other hand, interfacial reactions at the ends of the rigid punch in perfect adhesion, assuming different Poisson's coefficient of the substrate (ν_s), has been investigated. Using 256 logarithmically spaced elements, where, with reference to positive axis, a number of 27 elements are used in the interval $[10^{-4}; 0.1]/L$, 27 into $[0.1; 0.4]/L$ and 72 into $[0.4; 0.5\text{-}10^{-9}]/L$, shear and normal reactions are calculated under the action of a vertical or horizontal concentrated force, Fig. 1.8a-b and c-d, respectively. Moreover, the

normal stress singularity factor K_I in the frictionless condition (dashed line in Fig. 1.8b) and the shear stress singularity factor K_{II} of the thin coating (dashed line in Fig. 1.8c) are reported and defined as

$$K_I = \lim_{x \to L/2} \sqrt{2\pi(L/2 - x)} \, r_z(x) \tag{1.68a}$$

$$K_{II} = \lim_{x \to L/2} \sqrt{2\pi(L/2 - x)} \, r_x(x) \tag{1.68b}$$

The present numerical analysis (in thick solid line) and the analytic solution until $(1/2 - x/L) = 10^{-15}$ (in thin solid line) show an oscillation and its length depend on the value of ν_s. It is worth noting that the analysis at the ends reaches the atomic nucleus scale if the length of beam is assumed equal to 1 meter, vanishing so the condition of a continuum body.
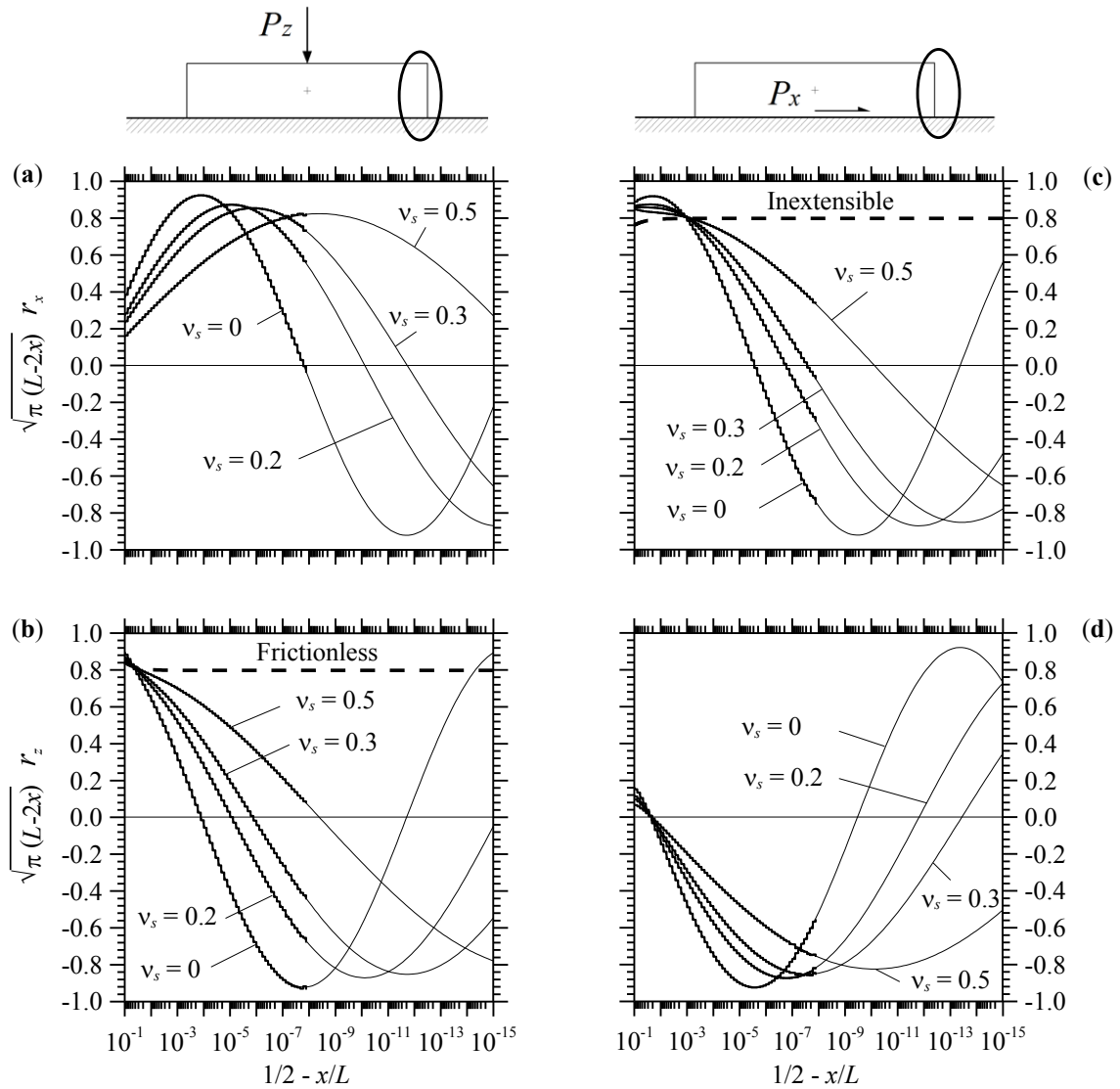

Fig. 1.8. Rigid punch loaded by a vertical P_z or horizontal P_x point force at midspan, shear (**a**, **c**) and normal (**b**, **d**) reactions. Normal K_I and shear K_{II} stress singularity factor (dashed line in (**b**, **c**)) in frictionless contact and for the inextensible bar, respectively.

1.4.2 Beam loaded by point force or moment

In this section, a beam with $L/h = 10$ resting on an elastic substrate having $c = 0.8$ is considered. Correspondingly, $\nu_s = 0.20$ or $\nu_s = 0.167$ for a generalised plane stress or plane strain state, respectively. In all examples presented, unless otherwise specified, a uniform mesh of $n_{el} = 512$ beam elements is used, and the same discretization is applied to the substrate boundary. Moreover, the plotted values of horizontal and vertical displacements u_x and u_z refer to the substrate boundary. In some case, for comparison, horizontal displacements $u_{bx,0}$ of the beam at $z = 0$ are reported in the plots.

1.4.2.1 Beam loaded by a vertical point force P_z at midspan

The case of a beam with $\alpha L = 10$ perfectly bonded to an elastic half-plane and loaded by a vertical point force P_z at midspan is considered first. Dimensionless displacements and reactions along the substrate boundary are reported in Fig. 1.9 for both an Euler-Bernoulli beam ($\phi = 0$, thick solid line) and a Timoshenko beam ($\phi = 0.3$, thin solid line). In particular, the corresponding plots of horizontal displacements u_x (Fig. 1.9a) clearly indicate that the beam-substrate systems tend to stretch in the neighbourhood of the loaded cross-section, and to contract far away from it. When the horizontal displacements are evaluated along the beam axis, a completely different behaviour is observed. For example, for the Euler-Bernoulli beam a contraction of the whole beam axis is obtained, i.e., $u_{bx,0} > 0$ for $x/L < 0$ and $u_{bx,0} < 0$ for $x/L > 0$ (dash-dot line in Fig. 1.9a). Therefore, for perfect adhesion, u_x turns out to be strongly influenced by the contribution of term $\varphi\, h/2$. Moreover, the significant discrepancy in the responses of Euler-Bernoulli and Timoshenko beams emphasizes the crucial role played by the shear deformations. This feature is even more evident from the plot of tangential reactions r_x (Fig. 1.9b), which is continuous for the shear-rigid beam, but shows a discontinuity at midspan for the shear-flexible beam. With regard to vertical displacements u_z (Fig. 1.9c), a wedge-shaped plot is obtained for the Timoshenko beam, showing a maximum deflection 56% larger than the Euler-Bernoulli beam. At the same section, the Timoshenko beam shows a singularity in normal reactions r_z (Fig. 1.9d). This aspect was already noted in [26]. Furthermore, it is worth observing that, at the beam end sections, the normal reactions for the two beams take opposite sign.

For comparison, the results obtained for the Euler-Bernoulli beam ($\phi = 0$) in frictionless contact with the substrate are also reported in Fig. 1.9 (dashed line). In particular, differently from the perfectly bonded beam, the frictionless condition yields contraction

along the whole beam-substrate interface (Fig. 1.9a). Moreover, as expected, $r_x = 0$ everywhere (Fig. 1.9b). With regard to vertical displacements u_z (Fig. 1.9c), for the beam in frictionless contact a maximum increase of 47% is obtained with respect to the perfect adhesion case. Finally, vertical reactions r_z (Fig. 1.9d) obtained for the Euler-Bernoulli beam do not seem to depend appreciably on the contact condition, with the exception of the cross-sections lying in the range $|x/L| > 0.40$.

The comparison between perfect adhesion and frictionless contact condition is re-proposed in Fig. 1.10 for a more flexible Euler-Bernoulli beam with $\alpha L = 100$. In this case, the two different contact conditions lead to substantially coincident results in terms of displacements u_x (Fig. 1.10a). With regard to tangential reactions r_x (Fig. 1.10b) for the beam in perfect adhesion, only the cross-sections lying in the range $-0.18 \leq x/L \leq 0.18$ show $r_x \neq 0$, whereas, as is obvious, for the beam in frictionless contact $r_x = 0$ everywhere. The beam responses in terms of u_z (Fig. 1.10c) and r_z (Fig. 1.10d) show larger values for the frictionless contact case only in proximity of the loaded cross-section. With regard to displacements u_x, an intermediate behaviour between those shown in Fig. 1.9a ($\alpha L = 10$) and in Fig. 1.10a ($\alpha L = 100$) is illustrated in Fig. 1.11a for $\alpha L = 40$.
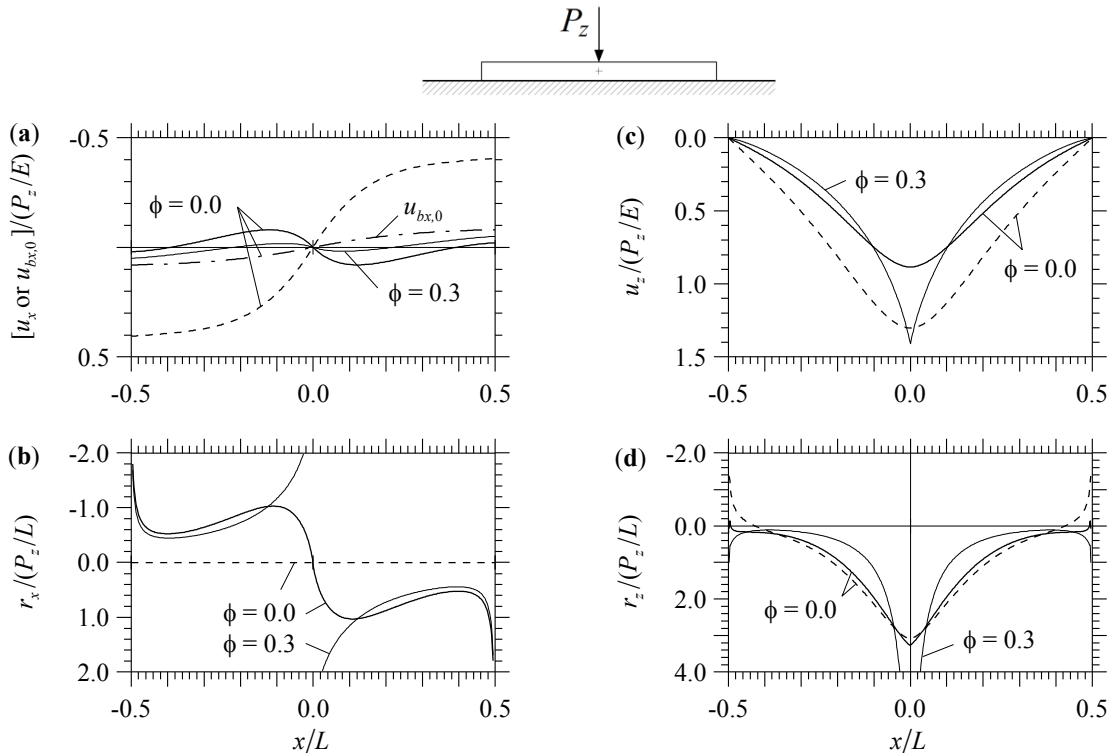
Fig. 1.9. Beam ($L/h=10$, $\alpha L=10$) loaded by a vertical point force P_z at midspan. Nondimensional values of u_x (**a**), r_x (**b**), u_z (**c**), and r_z (**d**) versus x/L for perfect adhesion with $\phi = 0.0$ and 0.3 (thick and thin solid line), and for frictionless contact with $\phi = 0.0$ (dashed line). Horizontal displacement $u_{bx,0}$ (dash-dot line in **a**) is referred to the centreline of the beam in perfect adhesion with $\phi = 0.0$.
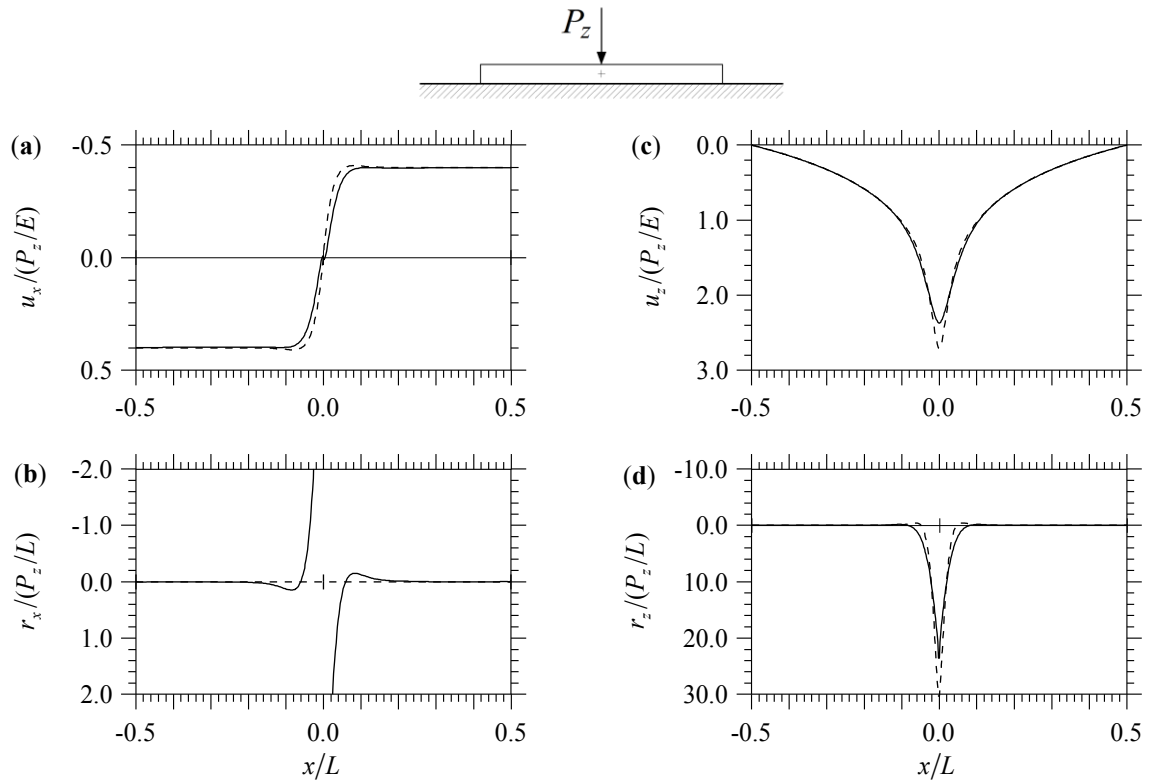
Fig. 1.10. Euler-Bernoulli beam (L/h=10, αL=100, ϕ = 0.0) loaded by a vertical point force P_z at midspan. Nondimensional values of u_x (**a**), r_x (**b**), u_z (**c**), and r_z (**d**) versus x/L for perfect adhesion (solid line) and frictionless contact (dashed line).
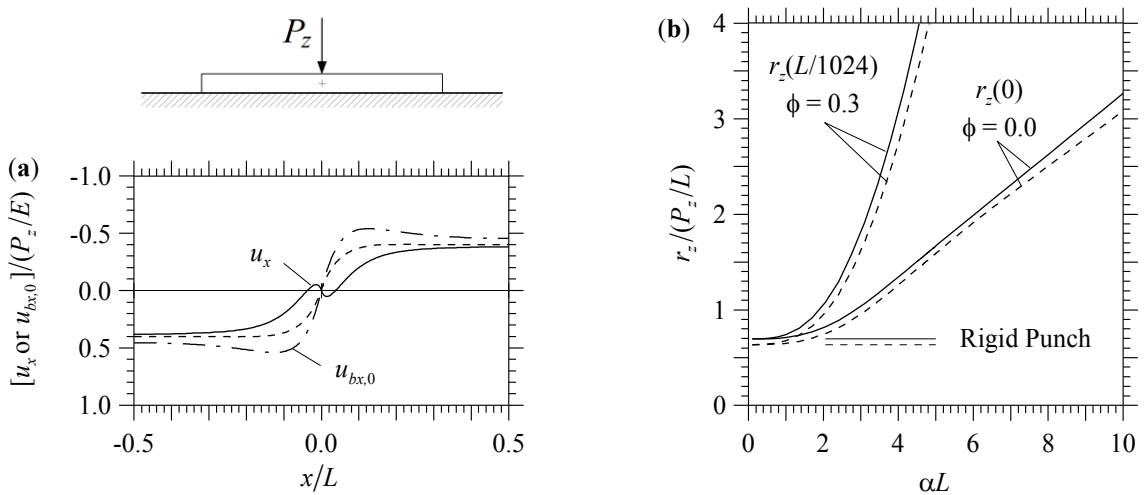
Fig. 1.11. Beam (L/h=10) loaded by a vertical point force P_z at midspan, comparison between perfect adhesion (thick solid line) and frictionless contact (dashed line). Nondimensional values of u_x versus x/L obtained for αL=40 and ϕ = 0.0 (**a**); and nondimensional values of r_z at or in proximity of midspan versus αL obtained for ϕ = 0.0 and 0.3 (**b**). Horizontal displacement $u_{bx,0}$ (dash-dot line in **a**) is referred to the beam centreline.

27

In particular, for the perfectly bonded beam, a contraction at the beam-substrate interface is observed with the exception of a very narrow region centred on the loaded cross-section, where a stretching occurs (solid line in Fig. 1.11a). Note that, differently from what is observed in Fig. 1.9a, displacements $u_{bx,0}$ at the centreline of the perfectly bonded beam (dash-dot line in Fig. 1.11a) are always larger than displacements u_x obtained for the beam in frictionless contact (dashed line in Fig. 1.11a).

The influence of the shear deformations on the normal reaction in proximity of the loaded cross-section is then analysed for different values of αL. In particular, an Euler-Bernoulli beam ($\phi = 0$) and a Timoshenko beam with $\phi = 0.3$ are considered. An accurate description of the normal reactions is searched for using a uniform mesh of 1024 elements. Reported in Fig. 1.11b are reactions $r_z(0)$ and $r_z(L/1024)$ versus αL for the Euler-Bernoulli and the Timoshenko beam, respectively. Note that for the shear-flexible beam, showing a singularity in the normal reaction at $x = 0$ (Fig. 1.9d), one of the nodes closest to the beam centroid, located at $x = L/1024$, is chosen. The figure shows the numerical solutions for both perfect adhesion (thick solid lines) and frictionless contact (thick dashed lines). It can be noted that for $\alpha L \leq 1$ the normal reactions for the two beams asymptotically tend to those of the rigid punch (thin solid and dashed lines). For larger values of αL, the normal reaction for the Timoshenko beam is significantly larger than that for the Euler-Bernoulli beam.

1.4.2.2 Comparison with other numerical formulations

With the purpose to evaluate the numerical performance of the present analysis, a beam perfectly bonded to an elastic half-plane is also analysed using two traditional numerical methods: a standard FE model that uses two-dimensional elastic elements to describe the soil and the approach proposed in [16, 17].

With regard to the two-dimensional FE model, the soil is modelled by means of quadrilateral elements in plane state. Three different square soil meshes are compared, showing total width equal to $8L$ (Fig. 1.12a), $16L$ (Fig. 1.12b) and $32L$ (not shown graphically because of the very large dimensions), with L being the beam span length. In the following, these meshes are referred to as FEM 8L, FEM 16L and FEM 32L, respectively. For all cases, at the boundaries, the displacements in the normal direction are fixed.
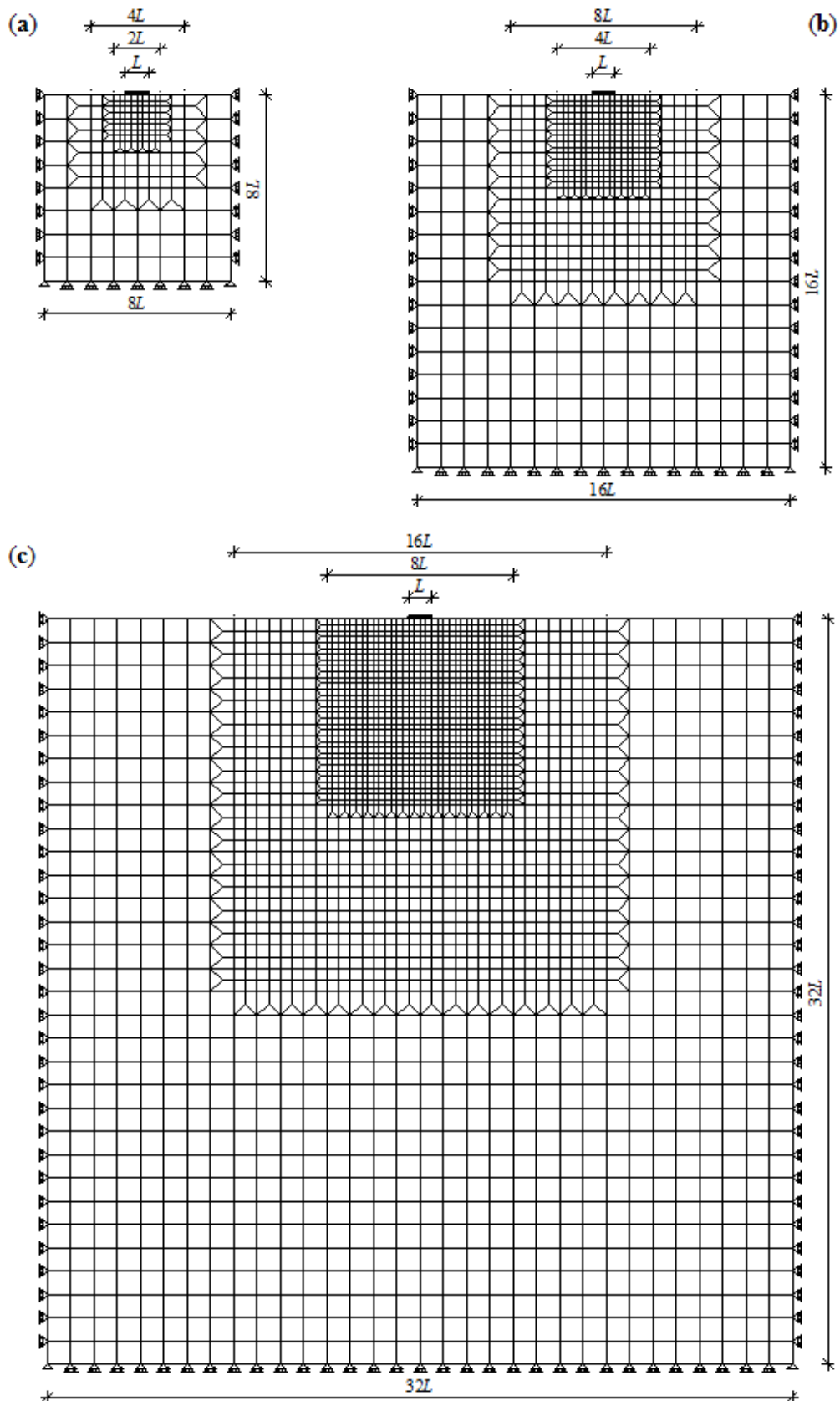
Fig. 1.12. Meshes adopted for the two-dimensional FE models with a foundation beam subdivided into 4 equal FEs. Models with mesh dimension 8*L* (FEM 8L) (**a**) and 16*L* (FEM 16L) (**b**), and 32*L* (FEM 32L) (**c**).
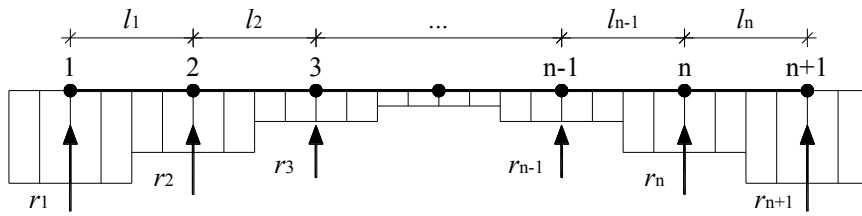
Fig 1.13. Piecewise constant pressure elements adopted in [17].
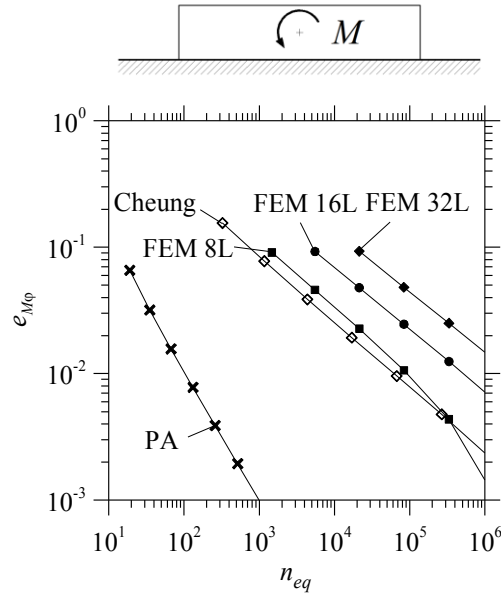
Fig. 1.14. Rigid punch subjected to a bending moment M. Relative errors $e_{M\varphi} = |M/\varphi_M - M/\varphi_o|/(M/\varphi_M)$ versus number of equation n_{eq}, with φ_o representing the rotation obtained from the generic numerical model, and φ_M being the closed-form rotation provided by Eq. (1.64b).
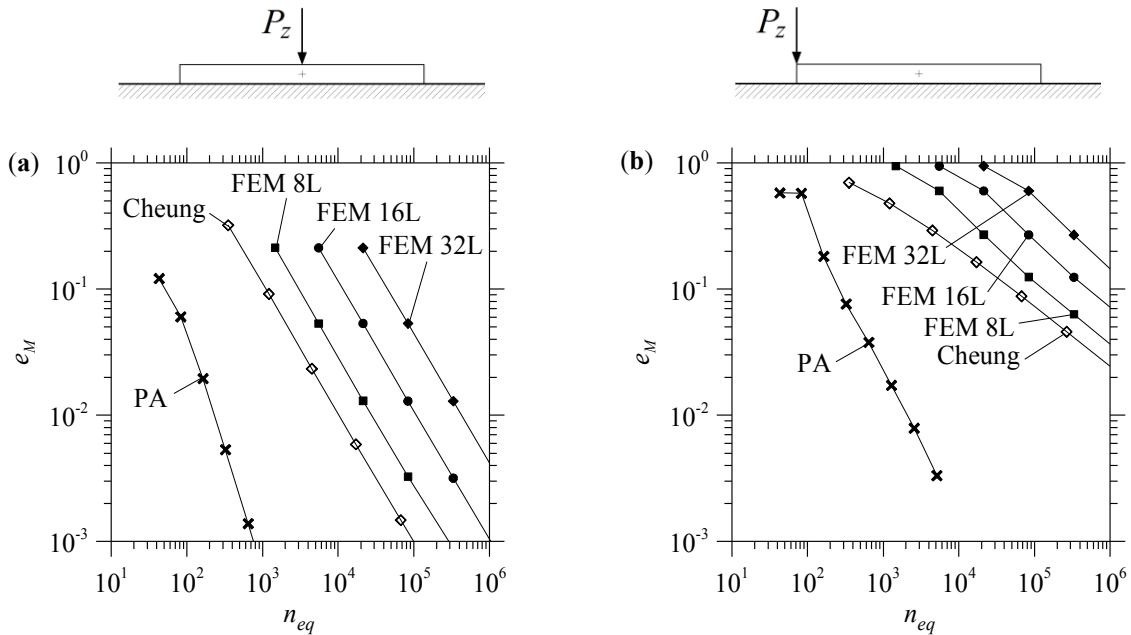
Fig. 1.15. Euler-Bernoulli beam (L/h=10, αL=20) subjected to a vertical force P_z at midspan (**a**) and at one end section (**b**). Relative errors $e_M = |M_{max} - M_{ref}|/|M_{ref}|$ in terms of the maximum bending moment versus number of equation n_{eq} for the present analysis (PA), Cheung's solution [17] and meshes FEM 8L, FEM 16L and FEM 32L.

Since for a relatively slender beam non-negligible horizontal displacements are to be expected for most of the beam length (see for example Figs. 1.10a for $\alpha L = 100$ and Fig. 1.11a for $\alpha L = 40$), FEM 16L and FEM 32L meshes were introduced with the aim to provide a more accurate description of the beam horizontal displacement. Two nested square meshes, showing widths equal to $4L$ and $2L$ for FEM 8L, to $8L$ and $4L$ for FEM 16L, and, finally, to $16L$ and $8L$ for FEM 32L, are built close to the foundation beam. Each edge of the quadrilateral elements of the smaller mesh has the same size of the beam elements. In Figs. 1.12, the case of the foundation beam subdivided into 4 beam FEs is shown for meshes FEM 8L and FEM 16L. The adopted meshes allow for the accurate solution to the soil-structure interaction problem with a number of FEs lower than that required by a simpler uniform mesh of quadrilateral elements.

With regard to the approach proposed in [17], a piecewise constant pressure having resultants applied to the nodes of the beam elements is adopted (Fig. 1.13). It is worth noting that a half of the end constant pressures lie ostside the foundation beam. Inserting piecewise constant surface tractions into Eq. (1.8) yields the following expressions for the nodal displacements:

$$\mathbf{u}_x = \mathbf{G}_{C,xx}\,\mathbf{r}_x + c\,\mathbf{G}_{C,xz}\,\mathbf{r}_z \tag{1.69a}$$

$$\mathbf{u}_z = \mathbf{G}_{C,zz}\,\mathbf{r}_z + c\,\mathbf{G}_{C,zx}\,\mathbf{r}_x \tag{1.69b}$$

where

$$g_{C,xx,ij} = -\frac{1}{\pi E}\left[\left[(x_j - x_i) + l_i/2\right]\ln\left(\frac{(x_j - x_i) + l_i/2}{l_i/2}\right)^2 - \right.$$

$$\left. \left[(x_j - x_i) - l_i/2\right]\ln\left(\frac{(x_j - x_i) - l_i/2}{l_i/2}\right)^2 \right] \tag{1.70}$$

corresponds to the classical solution due to a uniform distribution of surface tractions [12] and

$$g_{C,xz,ij} = \frac{1}{E}\begin{cases} -l/2 & \text{if } i > j \\ 0 & \text{if } i = j \\ l/2 & \text{if } i < j \end{cases} \tag{1.71}$$

With arguments similar to those reported in Section 3.2, the relations $\mathbf{G}_{C,zz} = \mathbf{G}_{C,xx}$ and $\mathbf{G}_{C,zx} = \mathbf{G}_{C,xz}^{\mathrm{T}}$ hold. Thus, the following matrix expression of Eqs. (1.69a, b) is obtained:

$$
\begin{bmatrix} \mathbf{u}_x \\ \mathbf{u}_z \end{bmatrix} = \begin{bmatrix} \mathbf{G}_{C,xx} & c\,\mathbf{G}_{C,xz} \\ c\,\mathbf{G}_{C,xz}^{\mathrm{T}} & \mathbf{G}_{C,zz} \end{bmatrix} \begin{bmatrix} \mathbf{r}_x \\ \mathbf{r}_z \end{bmatrix} = \mathbf{G}_{\mathrm{C}}\,\mathbf{r}
\tag{1.72}
$$

Differently from Eq. (1.27), the nodal rotations do not appear in Eq. (1.72); thus, nodal rotations of the beam are independent of those resulting in the substrate boundary due to the surface tractions. Accordingly, the resulting soil matrix $\mathbf{K}_{C,\mathrm{soil}}$ coincides with $\mathbf{G}_{\mathrm{C}}^{-1}$ as far as nodal displacements are concerned and has rows and columns of zeros in correspondence of the nodal rotations. Finally, the soil-structure interaction problem can be solved by replacing $\mathbf{K}_{\mathrm{soil}}$ with $\mathbf{K}_{C,\mathrm{soil}}$ in Eq. (1.30b).

In the case of beams, indicating with n_{el} the number of beam FEs, the number of equations, n_{eq}, associated with the present analysis (PA) is given by $n_{eq}^{(\mathrm{PA})} = 5\,n_{el} + 3$. Moreover, the number of equations associated with meshes FEM 8L, FEM 16L and FEM 32L is given by $n_{eq}^{(8\mathrm{L})} = 20.1\,n_{el}^2$, $n_{eq}^{(16\mathrm{L})} = 80.4\,n_{el}^2$ and $n_{eq}^{(32\mathrm{L})} = 321.6\,n_{el}^2$, respectively (note that, for meshes FEM 8L and FEM 16, the case for $n_{el} = 4$ is depicted in Fig. 1.12). Finally, with regard to the approach proposed in [16, 17], a matrix inversion is required, which is computationally equivalent to the solution to $2\,(n_{el} + 1)$ systems of $2\,(n_{el} + 1)$ algebraic equations. Therefore, such an approach gives rise to a number of equations $n_{eq}^{(\mathrm{C})} = 3\,(n_{el} + 1) + 4\,(n_{el} + 1)^2$. In the case of a rigid punch, the number of equations associated with the present analysis reduces to $n_{eq}^{(\mathrm{PA})} = 2\,n_{el} + 3$.

Because no exact solution to the adhesive contact problem for flexible beams is available in the literature, the convergence properties of the proposed formulation are preliminarily compared with those exhibited by the other formulations for the case of a rigid flat punch. To this aim, the FE-BIE model reduces to the form presented in Section 3.6, whereas, in the FE models and in the approach proposed in [17], the (flexible) beam elements are replaced with (rigid) FEs characterised by a parameter $\alpha L = 0.5$. As already abovementioned (Section 4.1), an analytical solution to such a problem exists, and the proposed formulation is capable to recover this solution accurately (Fig. 1.4).

With the purpose of a convergence test, a rigid flat punch subjected to a bending moment M is considered. For each of the numerical models compared, a series of mesh refinements is obtained by letting n_{el} progressively take the values 8, 16, 32, 64, 128, 254, 512 and 1024. The analytical solution in terms of rotation, i.e., Eq. (1.64b), is used as reference solution for the test. The test results are reported in Fig. 1.14 in terms of relative error $e_{M\varphi} = |M/\varphi_M - M/\varphi_o|/(M/\varphi_M)$ versus number of equations n_{eq}, with φ_o and

φ_M indicating the rotations provided by the generic numerical formulation and by Eq. (1.64b), respectively. It can readily be observed that, in the log-log representation of Fig. 1.14, all models, though with different slopes, converge almost linearly to the exact solution, as is testified by the progressive reductions of error $e_{M\varphi}$ with n_{eq}. However, the proposed FE-BIE model exhibits a convergence rate larger than twice those shown by the other models. In other words, at equal accuracy in the numerical solution, the proposed model is computationally more efficient. This feature justifies the use of the proposed model as the reference in the numerical examples presented below.

A further comparison of the various formulations is then carried out with reference to an Euler-Bernoulli beam with $\alpha L = 20$ and $L/h = 10$, and subjected to a point force P_z at midspan or at one end section is chosen. For each of the numerical models compared, a series of mesh refinements is obtained by letting n_{el} take the same values as for the case of the rigid punch just investigated. The numerical solution obtained with the present analysis by discretizing the beam with 4096 equal FEs is used as reference solution for the comparison.

The test results are reported in Fig. 1.15 in terms of relative error $e_M = |M_{max} - M_{ref}|/|M_{ref}|$ versus the number of equations n_{eq}, where M_{max} indicates the maximum bending moment in the beam obtained from the various models for a generic discretization, and M_{ref} represents the maximum bending moment corresponding to the reference solution. In particular, for P_z acting at midspan (Fig. 1.15a) $M_{ref} = + 0.02323\ P_z L$ (sagging bending moment with tension in bottom fibres), whereas for P_z acting at the beam end section (Fig. 1.15b) $M_{ref} = - 0.01567\ P_z L$ (hogging bending moment with tension in top fibres).

It can readily be observed from Fig. 1.15 that, at equal n_{eq}, the solution provided by the proposed model is significantly more accurate and presents higher convergence rate than the other formulations. However, it is to be recognised that the number of elements n_{el}, rather than the number of equations n_{eq}, is a more representative parameter to compare the convergence properties of the numerical models. Therefore, some further remarks are presented by assuming the same number of beam elements, though remembering that at equal n_{el} the computing time of the present formulation is noticeably lower than that required by the other numerical models. For example, for the beam with P_z acting at midspan (Fig. 1.15a), assuming $n_{el} = 32$ yields $e_M = 2.0\%$, 2.3% and 1.3% for the present analysis (PA), Cheung's solution [17] and all two-dimensional FE models, respectively. For the beam with P_z applied to one end beam section (Fig. 1.15b), a mesh refinement is required to obtain errors of the same order of magnitude as the previous case. Then,

assuming $n_{el} = 256$ yields $e_M = 1.7\%$, 4.6% and 3.0% for the present analysis (PA), Cheung's solution [17] and mesh FEM 8L, respectively.

Table 1.1 reports constant C and exponent λ of convergence rate $C n_{eq}^{-\lambda}$ for the curves shown in Figs. 1.15a, b (Euler-Bernoulli beam). The present analysis yields an exponent λ larger than 1.95 times the exponents provided by the other formulations. The parameters of the convergence rate for a Timoshenko beam with $\phi = 0.3$ are also reported in Table 1.1. In particular, for P_z acting at midspan, the present analysis yields an exponent λ that is 1.93 times the other exponents. For the same Timoshenko beam, an error $e_M = 1.8\%$ is obtained from the present analysis with $n_{el} = 128$. Because of the portions of the piecewise constant pressure lying beyond the beam end sections (Fig. 1.13), Cheung's solution [17] gives the same relative error as the present analysis with $n_{el} = 256$. The two-dimensional FE models provide $e_M = 2.1\%$ with $n_{el} = 128$. Moreover, for a Timoshenko beam with P_z applied to one end section, the present analysis yields $e_M = 2.1\%$ with $n_{el} = 512$ and a value of the exponent λ that is 2.7 times larger than the other exponents (Table 1.1). To obtain the same numerical error with the other methods, more than 2,048 equal beam FEs are to be used.

In conclusion, the present model can be considered effective to solve beam-soil problems, and a number $n_{el} = 512$ of equal beam FEs gives accurate solutions for all cases reported in the following.
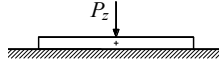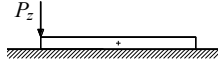
Euler-Bernoulli	C	λ	C	λ
PA	504	1.99	56	1.13
Cheung	124	1.02	16	0.47
FEM 8L	251	0.98	44	0.51
FEM 16L	1404	1.02	139	0.55
FEM 32L	5514	1.02	390	0.57
Timoshenko	C	λ	C	λ
PA	205	1.47	105	1.07
Cheung	217	0.76	8	0.34
FEM 8L	102	0.67	10	0.34
FEM 16L	77	0.58	12	0.31
FEM 32L	90	0.53	17	0.31

Table 1.1. Euler-Bernoulli and Timoshenko ($\phi = 0.3$) beams ($L/h=10$, $\alpha L=20$) subjected to a vertical force P_z at midspan and at one end section. Parameters of the convergence rate expression $C n_{eq}^{-\lambda}$ for relative error e_M in terms of the maximum bending moment. Comparison between present analysis (PA), Cheung's solution [17] and two-dimensional FE models.

1.4.2.3 Beam loaded by a horizontal point force P_x at midspan or at one end section

When a beam bonded to an elastic substrate is subjected to a horizontal force P_x, the solution to the beam-substrate interaction problem does not appreciably depend on parameter ϕ, and the distinction between Euler-Bernoulli and Timoshenko theories becomes negligible. The comparison between a beam showing $\alpha L = 10$ and a bar with equal cross-section but zero bending stiffness, corresponding to $\beta L = 0.83$, is reported in Fig. 1.16 for the horizontal force acting at midspan. In particular, neglecting the beam bending stiffness yields an overall reduction of horizontal displacements (Fig. 1.16a), that attains approximately 30% in correspondence of the centroidal cross-section. Nevertheless, with regard to horizontal reactions r_x (Fig. 1.16b), the influence of the bending stiffness proves not to be particularly significant. This is also true for u_z (Fig. 1.16c), with the exception of the two beam regions $|x/L| > 0.30$, where differences in the vertical displacements up to approximately 20% are observed at the beam end sections. The normal reactions (Fig. 1.16d) for the beam show a discontinuity at $x = 0$, whereas for zero bending stiffness, r_z is equal to zero everywhere. Analogous considerations hold when the horizontal force is assumed to act at one end section (Fig. 1.17), with the exception that the horizontal displacements of the bar are larger than those of the beam for $x/L > 0.4$ (Fig. 1.17a).

Fig. 1.16. Beam with $L/h = 10$, $\alpha L = 10$ (solid line) and thin coating with $\beta L = 0.83$ (dashed line) in perfect adhesion to a half-plane, loaded by a horizontal point force P_x at midspan. Nondimensional values of u_x (**a**), r_x (**b**), u_z (**c**), and r_z (**d**) versus x/L.
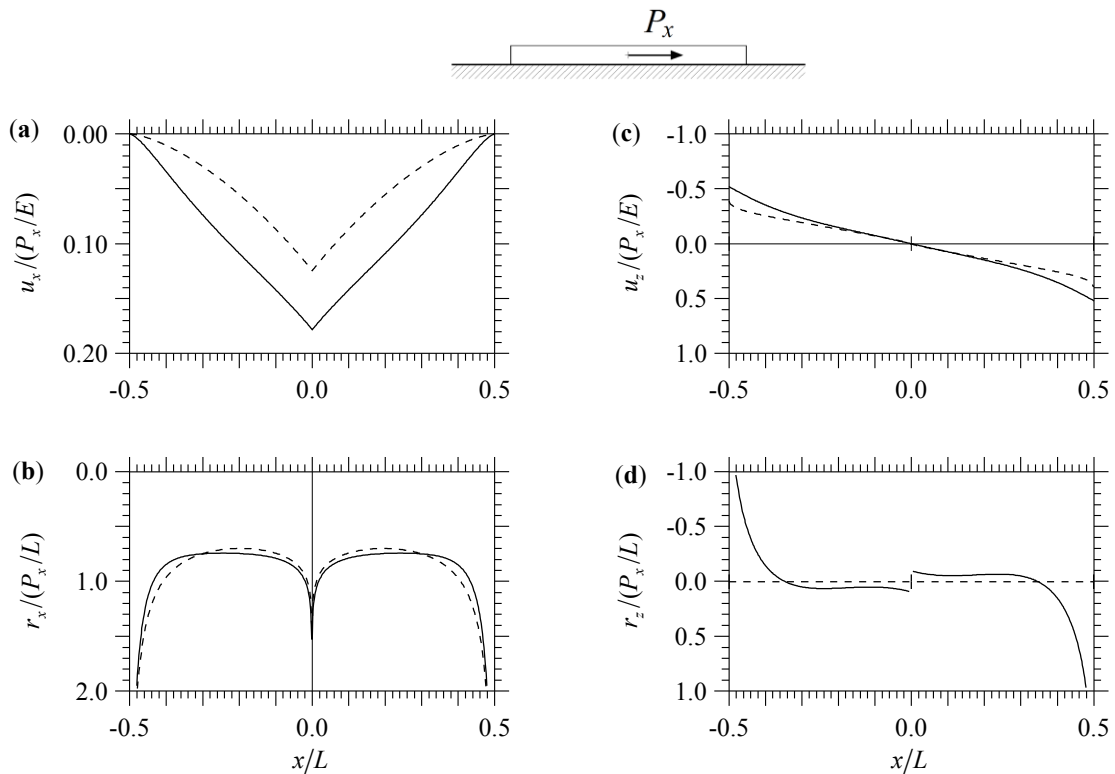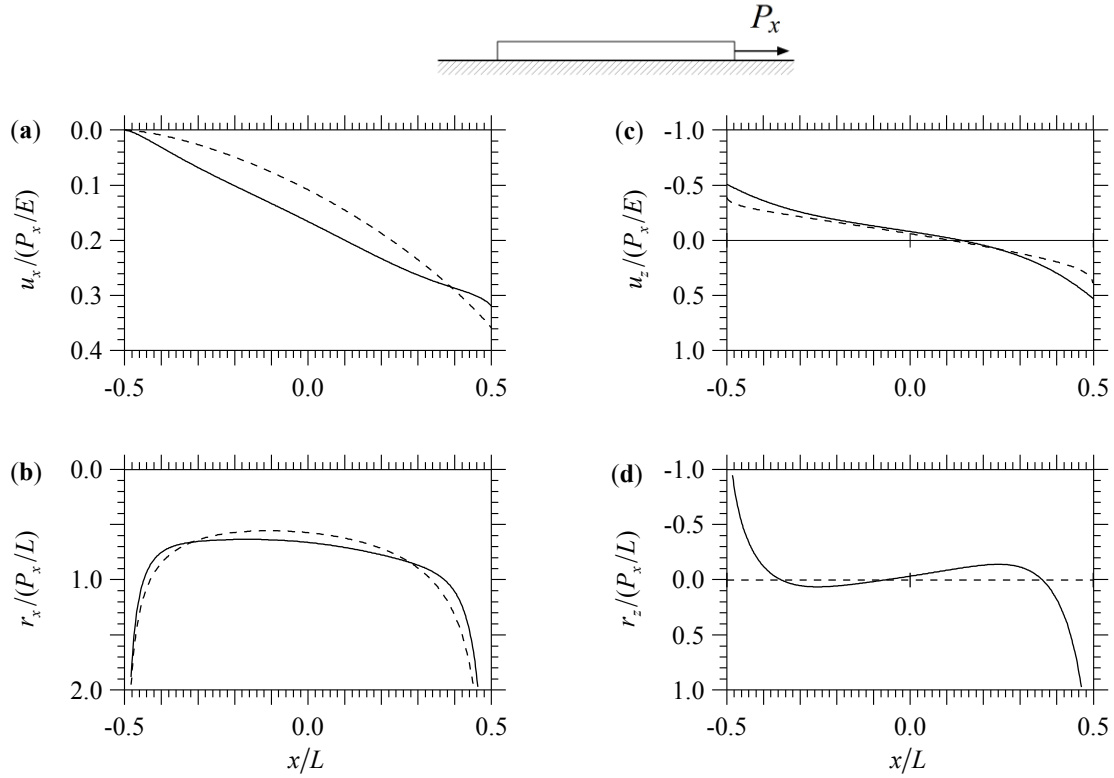
Fig. 1.17. Beam with $L/h = 10$, $\alpha L = 10$ (solid line) and thin coating with $\beta L = 0.83$ (dashed line) in perfect adhesion to a half-plane, loaded by a horizontal point force P_x at one end section. Nondimensional values of u_x (**a**), r_x (**b**), u_z (**c**), and r_z (**d**) versus x/L.

1.4.2.4 Beam loaded by a bending moment M at midspan

The case of an Euler-Bernoulli beam ($\phi = 0$) and a Timoshenko beam with $\phi = 0.3$, both showing $\alpha L = 10$ and perfectly bonded to an elastic half-plane, is investigated (Fig. 1.18). Horizontal displacements u_x (Fig. 1.18a) for the shear-flexible beam (thin solid line) noticeably exceed those for the shear-rigid beam (thick solid line). In particular, at $x = 0$ the value of u_x attained from the Timoshenko beam is approximately 60% larger than that computed for the Euler-Bernoulli beam. The dash-dot line in Fig. 1.18a refers to the horizontal displacements at the centreline of the perfectly bonded Euler-Bernoulli beam. In particular, for $-0.18 \leq x/L \leq 0.18$, $u_{bx,0}$ takes significantly lower absolute values, and even opposite sign, with respect to displacements u_x evaluated at the substrate boundary. Hence, the strong relevance of term $\varphi\, h/2$ is confirmed. Although the shear deformations have significant influence on displacements u_x, tangential reactions r_x for the Timoshenko beam coincide almost everywhere with those computed for the Euler-Bernoulli beam (Fig. 1.18b). Moreover, differently from the case of vertical load P_z (Fig. 1.9c, d), normal displacements (Fig. 1.18c) and reactions (Fig. 1.18d) for the Timoshenko beam are lower than the corresponding quantities for the Euler-Bernoulli beam for all cross-sections

located in the range $-0.4 \leq x/L \leq 0.4$. Only in proximity of the beam end sections, i.e., for $|x/L| > 0.4$, the shear deformations lead to higher displacements and reactions along the x-axis.
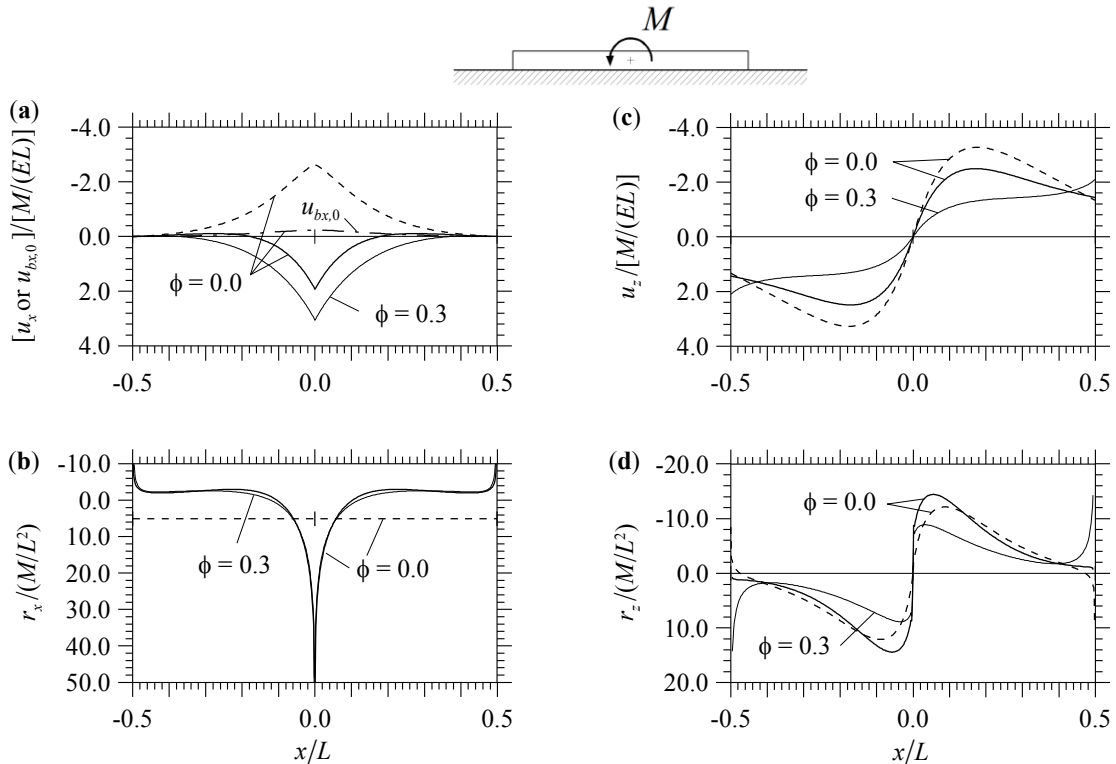

Fig. 1.18. Beam (L/h=10, αL=10) loaded by a bending moment M at midspan. Nondimensional values of u_x (**a**), r_x (**b**), u_z (**c**), and r_z (**d**) versus x/L for perfect adhesion with $\phi = 0.0$ and 0.3 (thick and thin solid line), and for frictionless contact with $\phi = 0.0$ (dashed line). Horizontal displacement $u_{bx,0}$ (dash-dot line in (**a**)) is referred to the centreline of the perfectly bonded beam with $\phi = 0.0$.
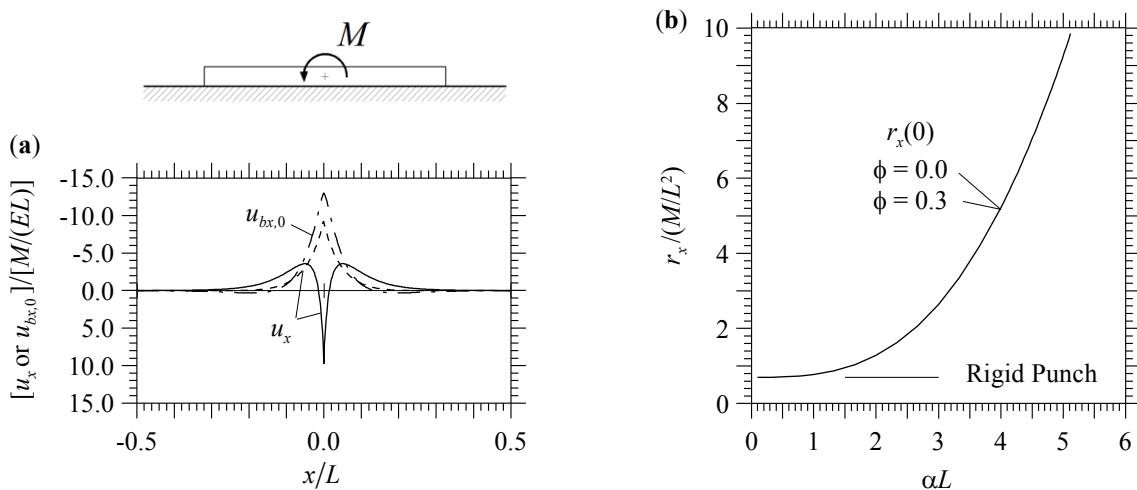
Fig. 1.19. Beam (L/h=10) loaded by a bending moment M at midspan, comparison between perfect adhesion (solid line) and frictionless contact (dashed line). Nondimensional values of u_x versus x/L obtained for αL=40 and $\phi = 0.0$ (**a**); and nondimensional values of r_x at midspan versus αL obtained for $\phi = 0.0$ and 0.3 (**b**). Horizontal displacement $u_{bx,0}$ (dash-dot line in (**a**)) is referred to the beam centreline.

37

For comparison, the results obtained for an Euler-Bernoulli beam with $\alpha L = 10$ in frictionless contact with the substrate are also presented in Fig. 1.18 (dashed line). A completely different behaviour in terms of horizontal displacements is observed with respect to the Euler-Bernoulli beam in perfect adhesion. In particular, displacements u_x for the two contact conditions take opposite sign in a large interval of x/L values (Fig. 1.18a). The responses of the shear-rigid beam in terms of normal displacements (Fig. 1.18c) and reactions (Fig. 1.18d) for the two contact conditions are qualitatively similar, even if perfect adhesion leads to lower absolute values of u_z along the whole interface and larger absolute values of r_z for $-0.14 \leq x/L \leq 0.14$.

The horizontal displacements at the substrate boundary for an Euler-Bernoulli beam with $\alpha L = 40$ are reported in Fig. 1.19a for both perfect adhesion (solid line) and frictionless contact (dashed line). Reported in the same figure is the plot of displacements $u_{bx,0}$ evaluated along the centreline of the beam in perfect adhesion (das-dot line). The example confirms that the contact condition has a noteworthy influence on the horizontal displacements. Moreover, near the midspan of the beam in perfect adhesion, displacements $u_{bx,0}$ take not only opposite sign with respect to displacements u_x, but also larger absolute values. Then, the role played by the beam cross-section rotation, already highlighted for $\alpha L = 10$ in Fig. 1.18a, becomes crucial for more flexible beams.

The tangential reaction at midspan for an Euler-Bernoulli and a Timoshenko beam bonded to an elastic substrate is plotted in Fig. 1.19b versus αL. These results follow from numerical models based on a uniform mesh of 1024 FEs. Note that, in this case, the shear deformations do not influence the beam response (an analogous consideration can also be made by observing in Fig. 1.18b the curves for the perfectly bonded Euler-Bernoulli and Timoshenko beams in proximity of $x/L = 0$). The behaviour of a rigid punch is substantially re-obtained for $\alpha L \leq 1$.

1.4.2.5 Reactions at the midpoint or one end of a beam loaded at midspan

The substrate reactions in the area of the end and close to the load section of a beam under the action of a point force or a couple at midspan, have been investigated. A Timoshenko beam with $\phi = 0.3$ in perfect adhesion, assuming the stiffness parameter of beam-substrate system equal to $\alpha L = 10$ or 20, has been analysed. Moreover, tangential and normal reactions at the end of a rigid punch ($\alpha L = 0$) are reported. A suitable mesh refinement is implemented by a number of logarithmically spaced FEs, equal to 238.

Firstly, the case of a vertical point force applied at midspan has been studied, Fig. 1.20, generating 54 logarithmically spaced elements in the interval $[10^{-7}; 0.1]/L$, 9 into $[0.1; 0.4]/L$ and 54 into $[0.4; 0.5\text{-}10^{-7}]/L$. The numerical analysis, at the load section, shows the tangential reaction r_x tending to a constant that depends on αL value, Fig. 1.20a. Whereas, a singularity behaviour is shown in the normal reaction, Fig. 1.20b. At the beam end, the interfacial reactions fluctuate in sign an infinite number of times Fig. 1.20c and d. That oscillation is observed in the normal reaction until $(1/2 - x/L) = 10^{-6}$, while it is necessary to increase the refinement mesh for the tangential one.

Owing to instability numerical, the case with a horizontal force P_x or a bending moment M at the midpoint, Figs. 1.21 or 1.22, is analysed with logarithmically spaced elements in the following way.
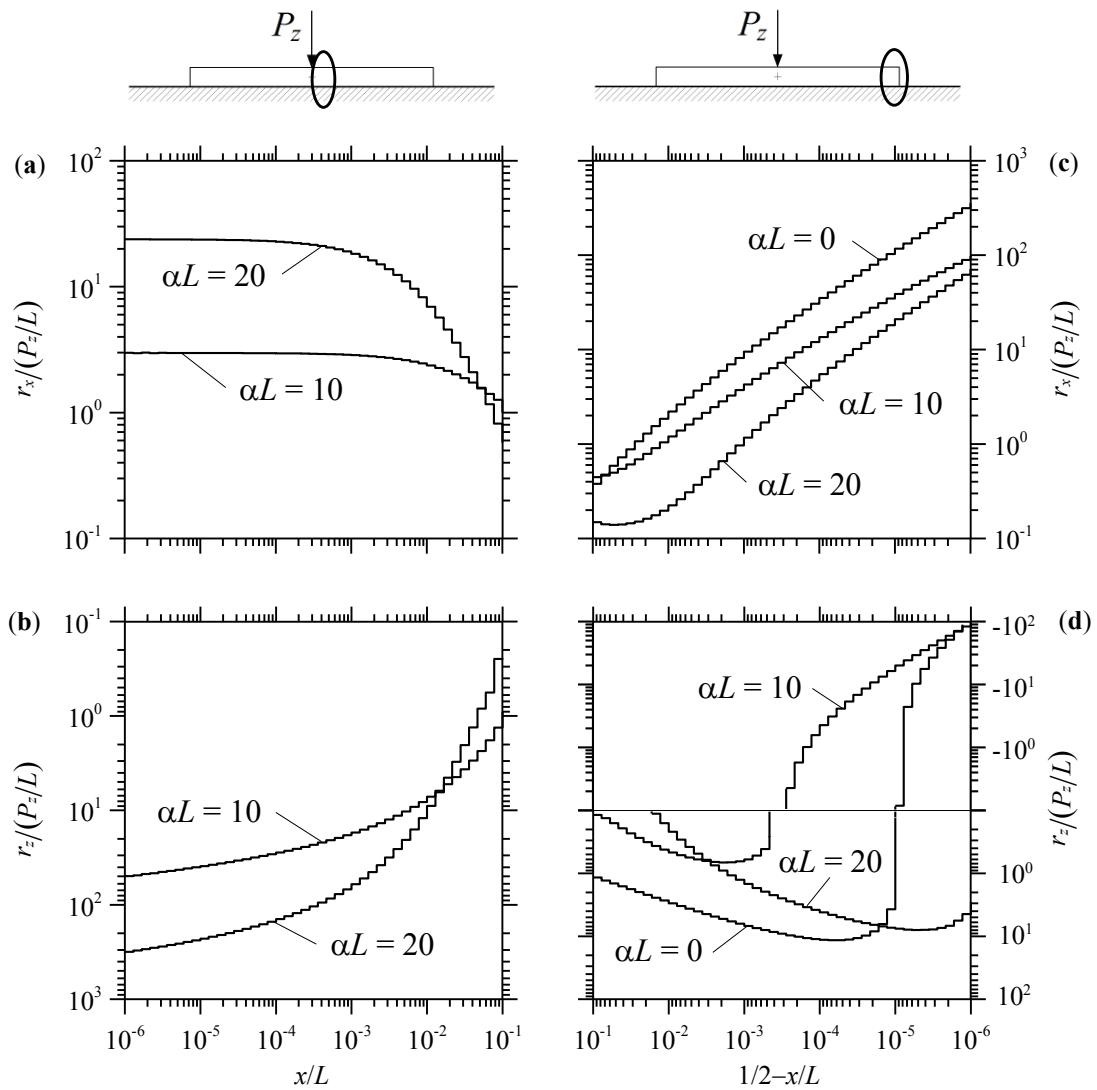

Fig. 1.20. Beam ($\phi = 0.3$) loaded by a vertical point force P_z at midspan, assuming $\alpha L = 10$ and 20. Nondimensional substrate reaction r_x, r_z at the load section (**a**, **b**) and beam end (**c**, **d**). The parameter $\alpha L = 0$ represents the rigid punch.
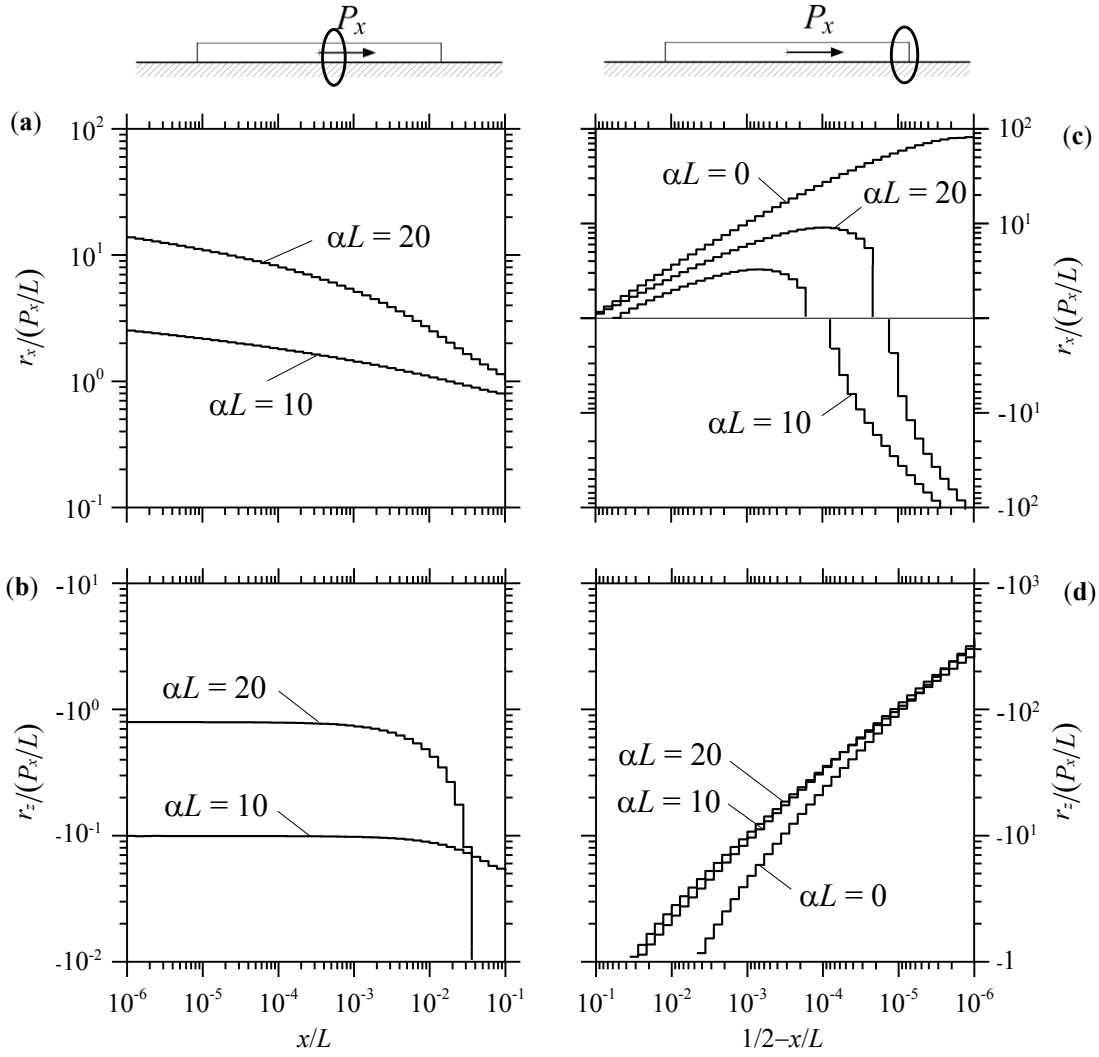
Fig. 1.21. Beam (ϕ = 0.3) loaded by a horizontal point force P_x at midspan, assuming αL = 10 and 20. Nondimensional substrate reaction r_x, r_z at the load section (**a**, **b**) and beam end (**c**, **d**). The parameter αL = 0 represents the rigid punch.

The representation of behaviour at the beam end are used 36 elements in the interval $[10^{-7};$ 0.1]/L, 27 into [0.1; 0.4]/L and 54 into [0.4; 0.5-10^{-7}]/L, whereas behaviour at the load section are used 54 elements in the interval $[10^{-7}; 0.1]/L$ and 19 ones into [0.4; 0.5]/L.

For the beam subjected to the horizontal force in perfect adhesion with the substrate, a raise of tangential reaction and constant normal reaction occur at midspan, Fig. 1.21a-b. Such behaviour is opposite at that found in the previously load case (Fig. 1.20a-b). Nevertheless, both substrate reactions (r_x, r_z) at the beam end fluctuate in sign. It is evident for the tangential reaction up to (1/2 - x/L) = 10^{-6}, Fig. 1.21c, but not remarked for the normal one, Fig. 1.21d.
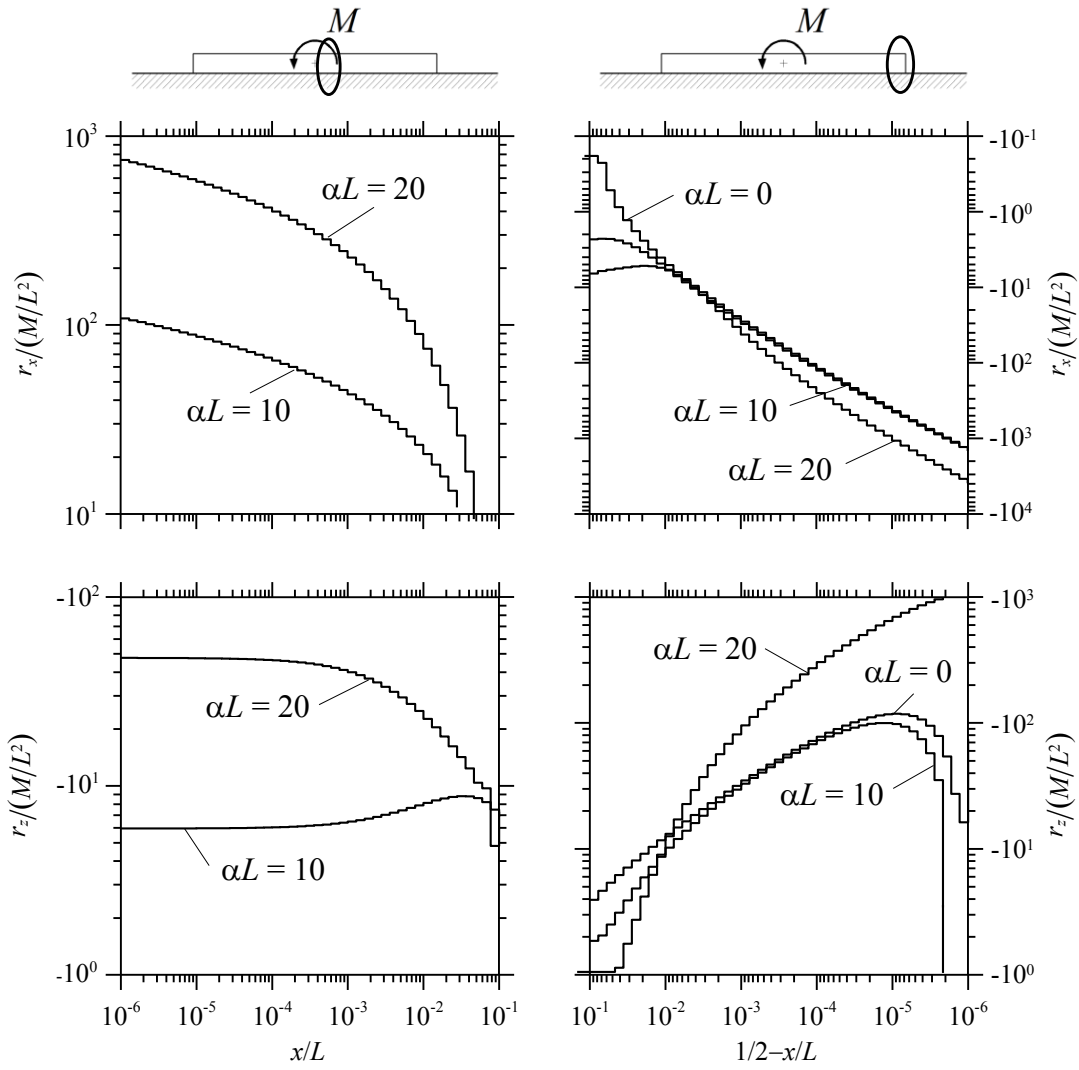
Fig. 1.22. Beam ($\phi = 0.3$) loaded by a bending moment M at midspan, assuming $\alpha L = 10$ and 20. Nondimensional substrate reaction r_x, r_z at the load section (**a**, **b**) and beam end (**c**, **d**). The parameter $\alpha L = 0$ represents the rigid punch.

Finally, for the beam subjected to the bending moment M, the numerical analysis shows an increase of tangential reaction and a constant value of normal one at the load section, Fig. 1.22a and b, respectively. According to reactions at the beam end, the mesh refinement assumed until $(1/2 - x/L) = 10^{-6}$ is not enough to show how both interfacial reactions fluctuate in sign an infinite number of time.

1.4.3 Plane strain analysis of a two-bay frame resting on an isotropic elastic substrate

The present example is aimed at assessing the soil-structure interaction for the realistic case of a double-cell box culvert or tunnel (Fig. 1.23a), that is a very common structural typology usually made of reinforced concrete. The foundation structures and the upper slab with net span length 6.00 m, both showing thickness $h = 1.20$ m, as well as the three 1 m-thick abutments, are cast-in-place members. Across the largest span, left and intermediate abutments support 1.5 m-high precast I-beams with 2 m spacing, mutually connected at the top through a 0.2 m-thick continuous slab. The resulting ribbed slab has a self-weight of 15 (kN/m)/m and second moment of area $I = 0.34$ m^4/m. To obtain monolithic connections between precast beams and abutments, suitable cast-in-place joints are provided at the beam supports. Then, the generic cross-section of the double-cell tunnel is reduced to the plane frame shown in Fig. 1.23b, having a uniform out-of-plane dimension $b = 1$ m and span lengths $L1 = 14.50$ m and $L2 = 7.00$ m. Foundation R1 is modelled as a 1.2 m-high rigid punch bonded to an isotropic, elastic half-plane, and discretized using a graded mesh with $n_{el} = 8$ and $\beta_{exp} = 2$. Because of the larger flexibility in comparison with R1, foundation F2 is modelled using a uniform mesh of $n_{el} = 20$ Euler-Bernoulli beam FEs in perfect adhesion with the substrate. According to Fig. 1.3 and the transformation rule reported in Section 3.5, column B1 is connected at the base to the top node of punch R1, resulting in a column height $H1 = 7.20$ m. Conversely, according with the formulation presented in Section 3.3, the FE-BIE elements used for foundation beam F2 have the centreline placed at a distance $h/2 = 0.6$ m from the substrate boundary, leading columns B4 and B5 to have a total height $H2 = 7.80$ m. For both the rigid punch and the foundation beam, one single soil element is used for each FE. Euler-Bernoulli beam FEs are used for members B1 to B5. A series of preliminary tests confirmed that the numerical model described ensures convergent solutions.

A plane strain analysis is conducted by assuming $E_s = 30$ MPa and $\nu_s = 0.3$ for the substrate and $E_b/(1-\nu_b^2) = 30$ GPa for all structural elements. In particular, the two load cases shown in Fig. 1.23c are considered, i.e., the self-weight and a horizontal load p_x uniformly distributed along beams B2 and B3. This load can be viewed as a hypothetic seismic action of magnitude approximately equal to 20% of the structural self-weight.

Reported in Fig. 1.24a are the deformed shapes of the frame corresponding to the self-weight (solid line) and to the lateral load (dashed line) separately acting from one another.
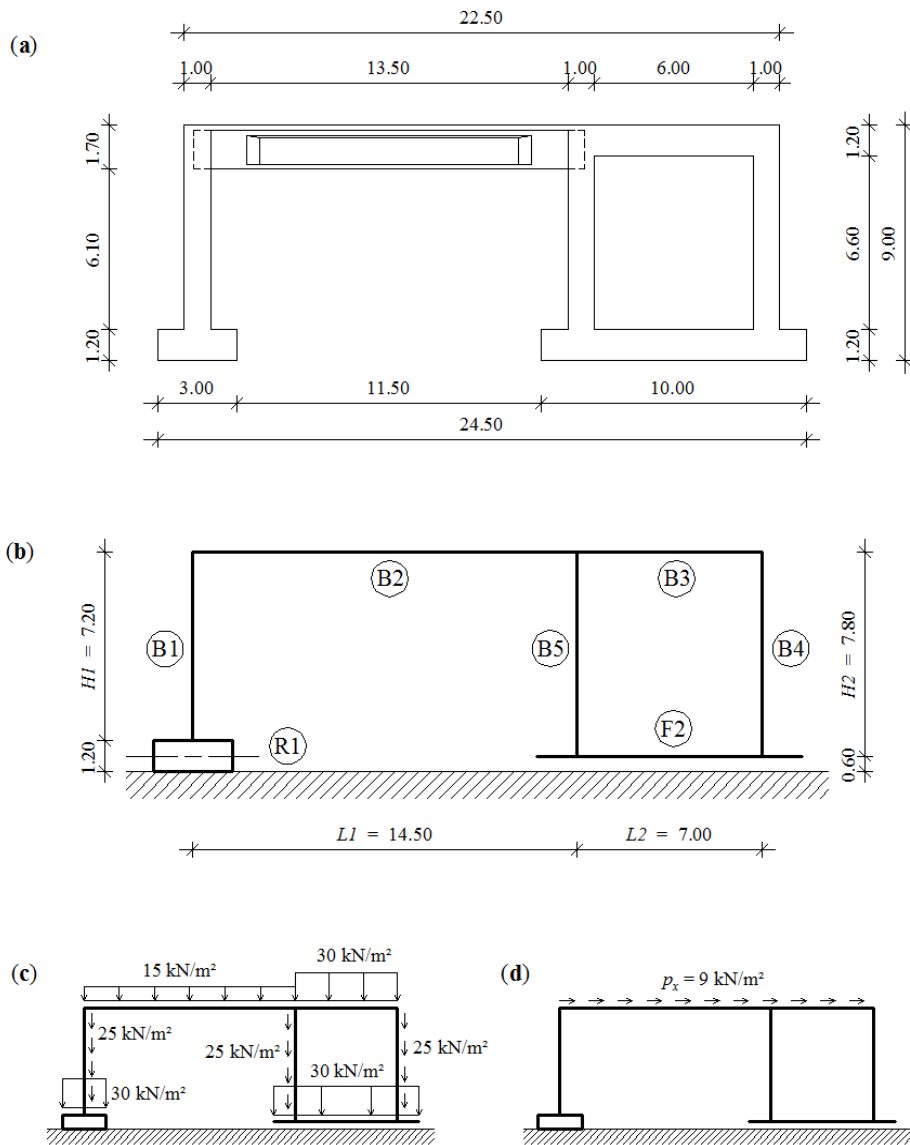
Fig. 1.23. Cross-section geometry of the double-cell tunnel investigated (**a**); corresponding two-bay frame analysed under plane strain assumption (**b**) and load cases considered (**c, d**).

In the same figure, the undeformed shape is reported for comparison (dash-dot line). The maximum vertical deflection is observed in correspondence of the right-hand section of foundation beam F2 and is approximately 11 mm for both load cases. The frame lateral deflection due to the horizontal force is about 7 mm. Tangential and normal reactions underneath foundations R1 and F2 are reported in Fig. 1.24b and Fig. 1.24c, respectively, for the two load cases. The maximum reactions are obtained for the frame subjected to self-weight. With the exception of the end elements of rigid punch R1, where the reactions tend to become excessive because of the foundation stiffness, the values of r_x and r_z

Fig. 1.24. Frame deflections (**a**) and reactions underneath rigid punch and foundation beam (**b**, **c**) for the structure subjected to self-weight (solid line) and lateral load (dashed line). Ratio r_x/r_z for the two load cases acting simultaneously (**d**). Dash-dot line in (**a**) represents the undeformed frame.

obtained for foundations R1 and F2 for the frame subjected to self-weight are substantially comparable. On the other hand, in the presence of the lateral load, the responses of the two foundations in terms of tangential reactions r_x appear to be completely different (dashed lines in Fig. 1.24c). Finally, ratio r_x/r_z obtained when vertical and lateral loads are applied simultaneously is reported in Fig. 1.24d. Note that, with the exception of the end elements of the two foundations, ratio r_x/r_z linearly varies for both R1 and F2, taking values not larger than 0.3.
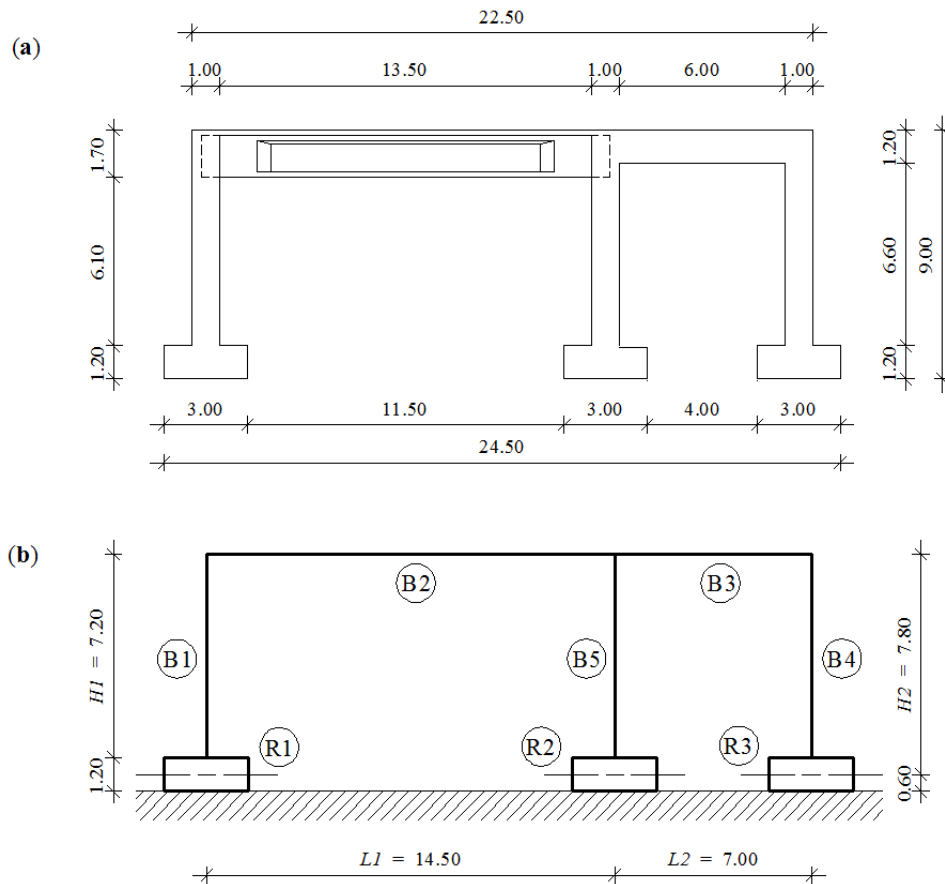
Fig. 1.25. Cross-section geometry of the two-bay frame investigated (**a**), analysis under plane strain assumption with three rigid punch foundation (**b**).

Figure 1.25a reports the same frame structure lying on the same isotropic soil of the previously case but adopting three single foundations with length 3 m each, situated at the abutments. The foundations could be modelled as rigid punch: R1, R2 and R3 of Fig. 1.25b, using a graded mesh with $n_{el} = 8$ and $\beta_{exp} = 2$.

Deformed shapes of the frame corresponding to self-weight (solid line) and to the lateral load (dashed line) are reported in Fig. 1.26a, separately acting from one another. Both load cases, the maximum relative vertical displacement appears in correspondence of the right-hand section of the foundation R3. Note that, the value of relative deflection, due to the horizontal force or self-weight, is approximately equal to that of the previously structure. Tangential and normal reactions, are reported respectively in Fig. 1.26b and c, showing values higher than the case which adopts a continuous foundation. The maximum substrate reaction is found for the frame subjected to self-weight. In particular, at the coordinate $x = 17.5$ m and 21.5 m, the reactions turn out higher than 200 kPa, unlike from those obtained with the continuous beam (F2).
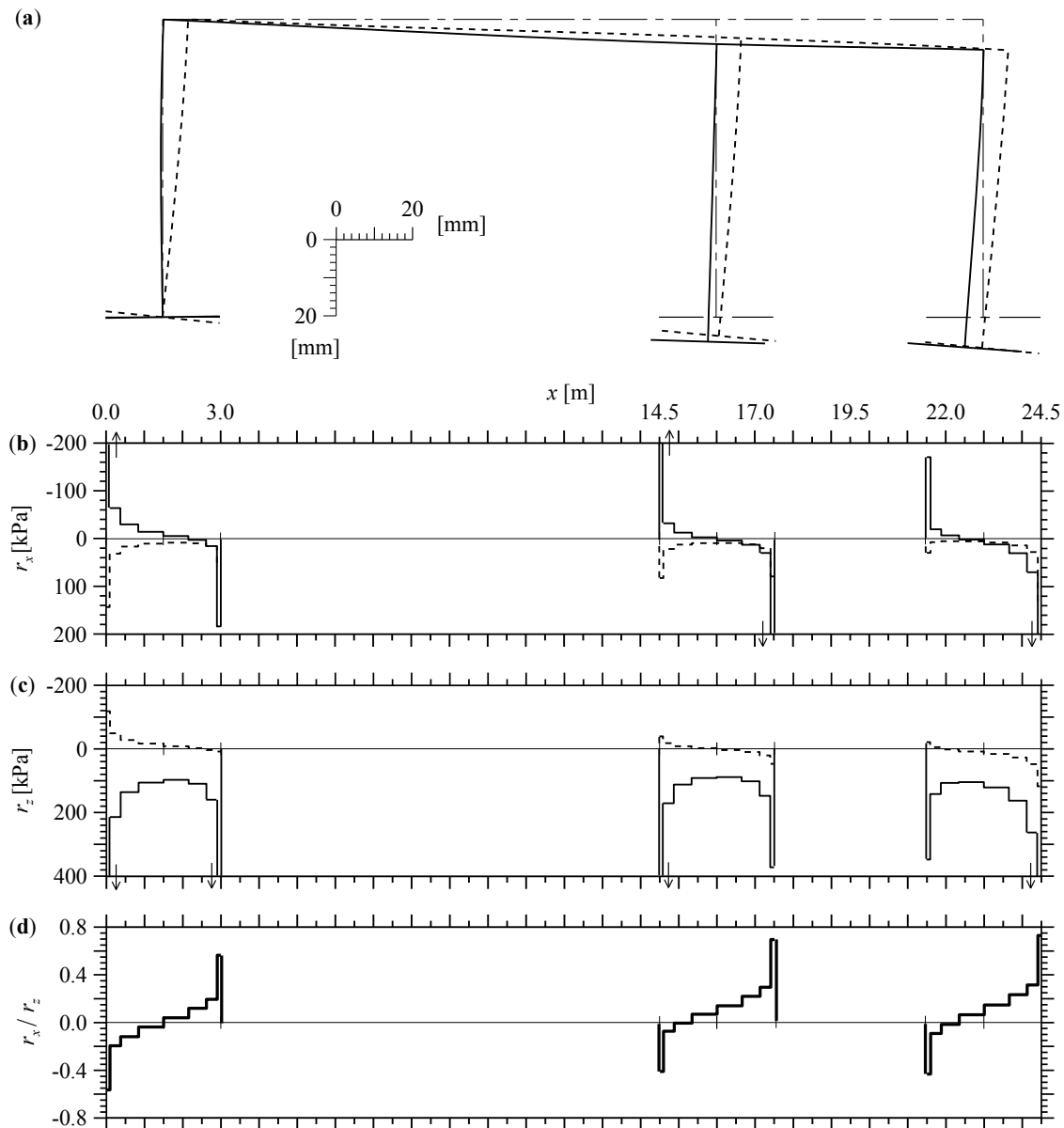
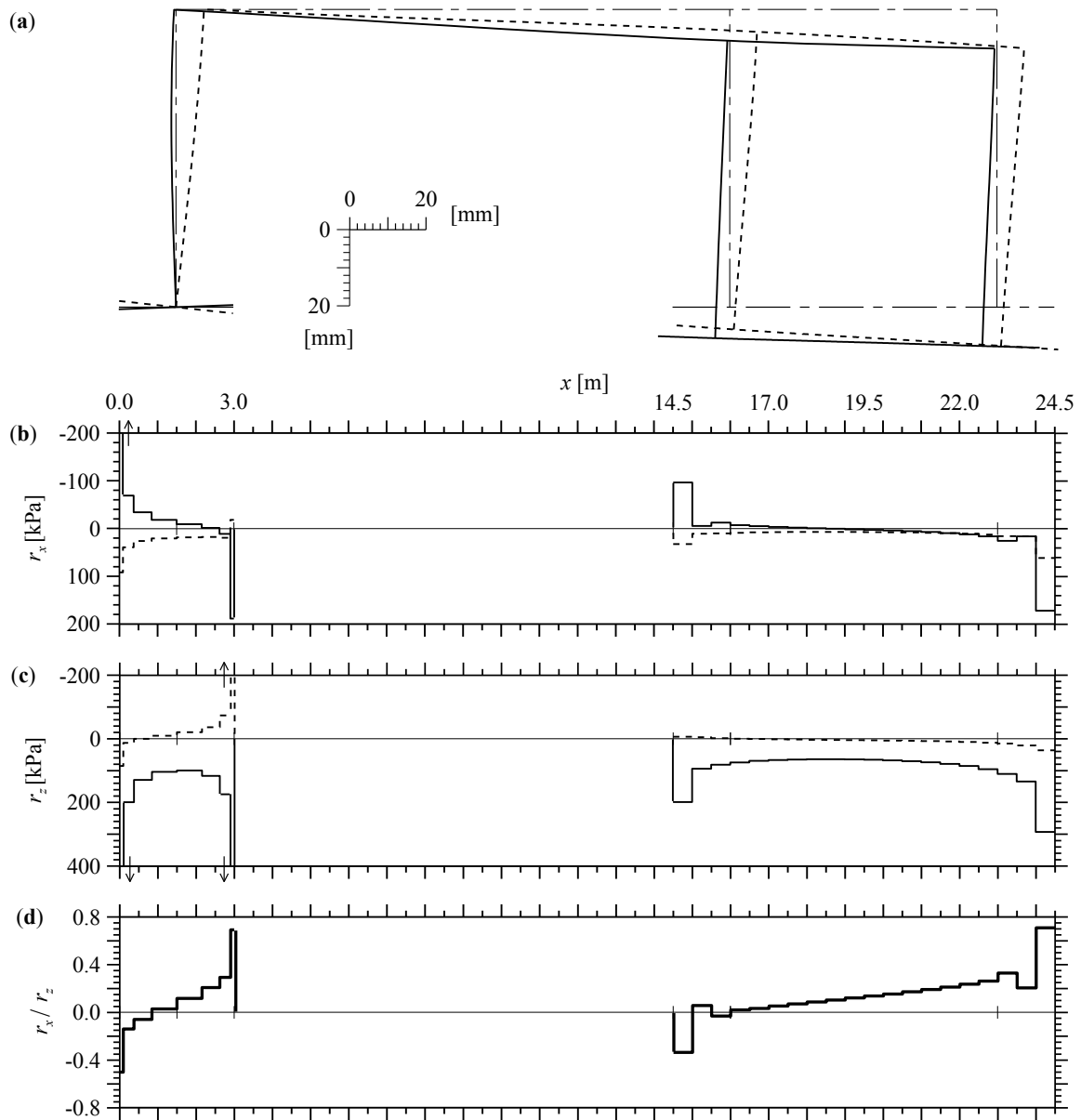Fig. 1.26. Frame deflections (**a**) and reactions underneath rigid punches (**b**, **c**) for the structure subjected to self-weight (solid line) and lateral load (dashed line). Ratio r_x/r_z for the two load cases acting simultaneously (**d**). Dash-dot line in (**a**) represents the undeformed frame.

Finally, the ratio r_x/r_z, which is reported in Fig. 1.26d and determined applying simultaneously vertical and lateral load, overtakes the value of 0.3 in more zones.

1.4.4   Plane strain analysis of a culvert resting on an isotropic elastic substrate

The choice of size, shape and number of cell of a culvert plays a fundamental role to control the flow of water, especially during extreme weather, such as major floods and washouts, determining a significantly cost of project on overall construction.
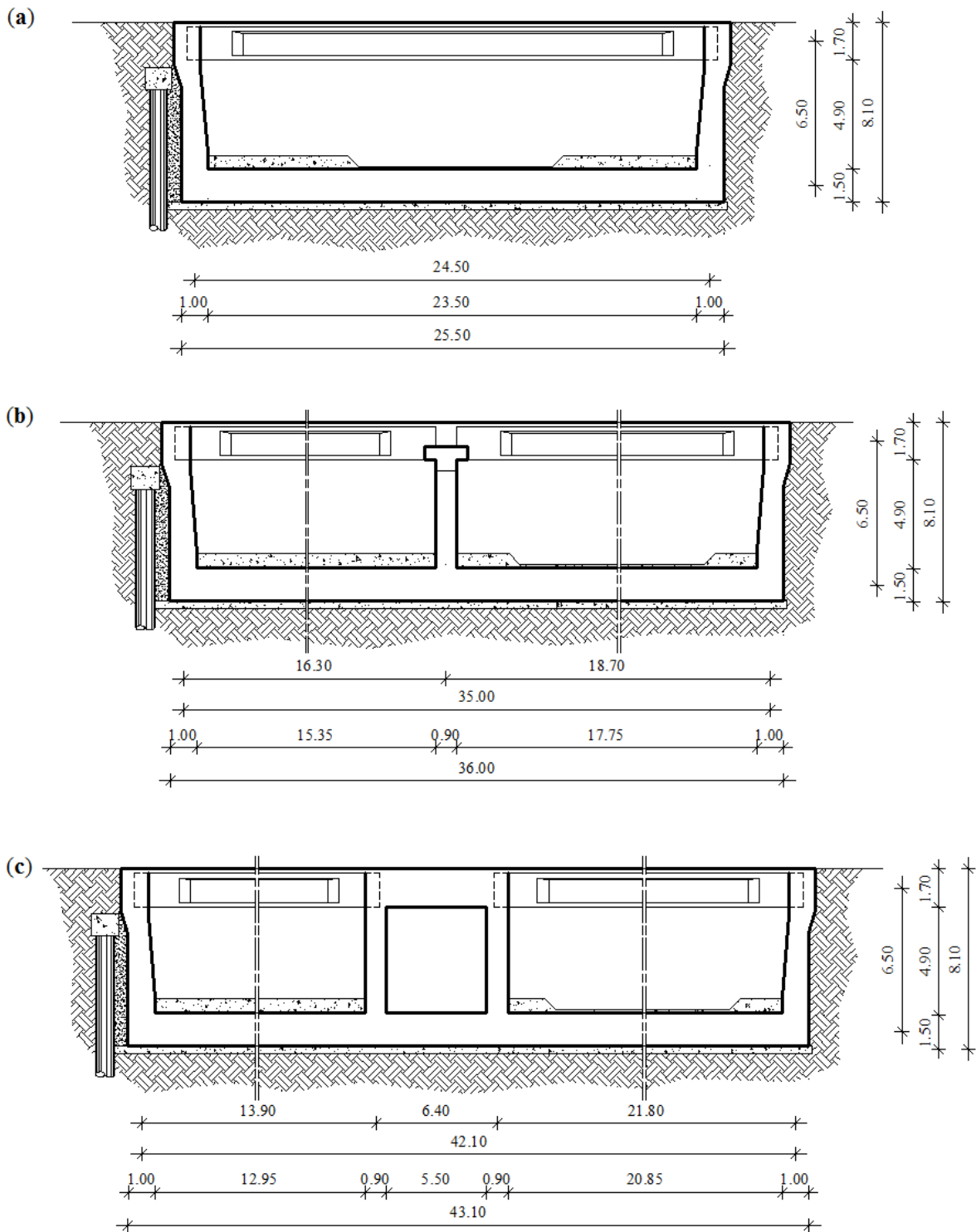
Fig. 1.27. Three cross-sections geometry of a culvert with single (**a**), double (**b**) and triple-cell (**c**).
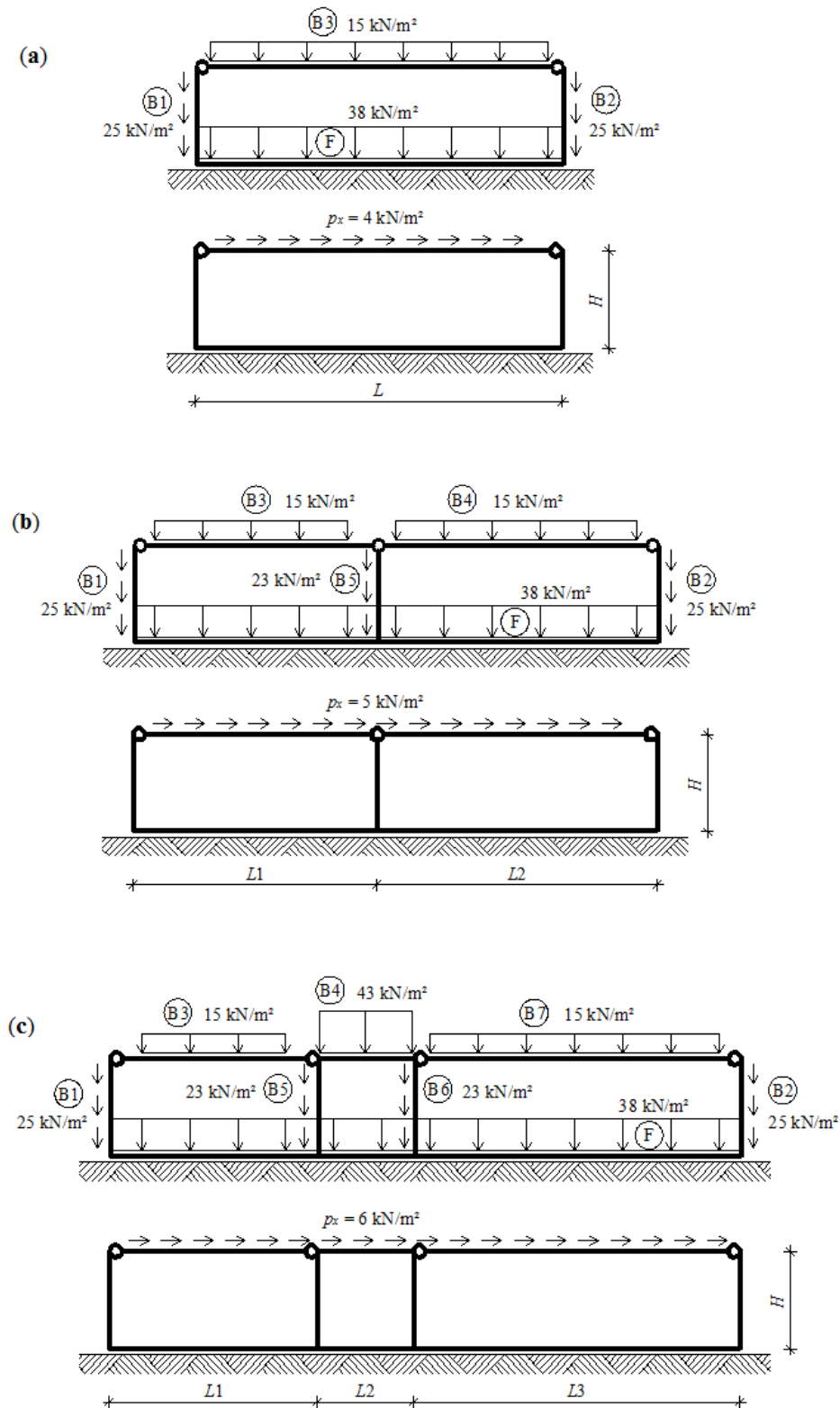
Fig. 1.28. Frame of the culvert under plane strain assumption and load cases considered of single (**a**), double (**b**) and triple-cell (**c**).

In this paragraph, three cross-sections of a rectangular reinforced concrete culvert have been studied by means of the present interaction analysis. In particular, Fig. 1.27 shows the cross-section of the culvert with a single, double and triple cell. The generic cross-section of the tunnel is reduced to a plane frame having out-of-plane dimension b = 1 m, height H = 6.5 m, as shown in Fig. 1.28. The continuous foundation has thickness h = 1.5 m (beam F in Fig. 1.28), where at its extremity are collocated two 1-m thick abutments (beam element B1 and B2 in Fig. 1.28). The self-weight of the foundation is equal to 38 kN/m^2, while for the abutment is equal to 25 kN/m^2. At the top, a ribbed slab high 1.7 m is connected by a precast I-beam and a continuous slab thick 0.2 m. For the analysis, it has been assumed a hinge joint between the ribbed slab and the abutment, as shown in Fig. 1.28. The self-weight of the ribbed slab is equal to 15 kN/m^2. A uniformly distributed horizontal load has been considered along the top of structure to simulate a hypothetic seismic action of magnitude approximately equal to 20% of the total self-weight. For the single box tunnel with length equal to L = 24.5 m, the uniform horizontal load is equal to p_x = 4 kN/m^2.

According to the double cell, the same load per square is present for the foundation, two abutments and ribbed slab (beam element B3 and B4 in Fig. 1.28b). The separation of the two boxes is determined by a concrete wall (beam element B5 in Fig. 1.28b) thick 0.9 m, having self-weight of 23 kN/m^2. The dividing wall separates the two rooms long $L1$ = 16.3 m and $L2$ = 18.7 m respectively. The uniform horizontal load at the top of the double tunnel results p_x = 5 kN/m^2.

The cross-section of culvert with triple cell is obtained by a concrete rectangle box defined by the beam elements B5, B4 and B6, Fig. 1.28c. The dividing walls B5 and B6 have the same thickness of 0.9 m, and the slab B6 is a full section high 1.7 m with self-weight of 43 kN/m^2. While, the beam elements B3 and B7 are ribbed slab with the same self-weigh of 15 kN/m^2. The length of the three cells is equal to $L1$ = 13.9 m, $L2$ = 6.4 m and $L3$ = 21.8 m. The uniform horizontal load of the triple cell is equal to p_x = 6 kN/m^2.

The foundation (beam F) in perfect adhesion with the substrate is modelled using a uniform mesh of n_{el} = 512 Timoshenko beam FEs assuming the shear correction factor k_b = 5/6. Moreover, according to the present formulation in this chapter, elements used for the foundation beam have the centreline at a distance from the substrate boundary of half-height of beam. A plane strain analysis is conducted by assuming a substrate soil with Young's modulus E_s = 30 MPa and Poisson's coefficient v_s = 0.3. While, for the frame is assumed a Young's modulus for the plane strain state equal to $E_b/(1-v_s^2)$ = 30 GPa.

Fig. 1.29. Single-cell frame deflections (**a**) and reactions underneath foundation beam (**b** and **c**) for the structure subjected to self-weight (solid line) and lateral load (dashed line). Ratio r_x/r_z for the two load cases acting simultaneously (**d**). Undeformed frame in dash-dot line (**a**).

Figs. 1.29-1.30-1.31a show deformation shape of the culvert with the three kinds of frames, acting separately the self-weight (solid line) and the lateral load (dashed line). Moreover the undeformed shape is reported (dashed line) for comparison.

The single-cell box has the stiffness parameter of the foundation-soil system equal to αL = 3.8 and the ratio length to height of foundation beam L/h = 16.3. The maximum vertical deflection at the top is approximately 5 mm, while the settlement is about 3 mm between the edge end and the middle of foundation. The double-cell box has the parameter $\alpha L = 5.5$ and the ratio L/h = 23.3. The maximum vertical deflection is 5 mm, while the maximum horizontal deflection is about 6 mm.
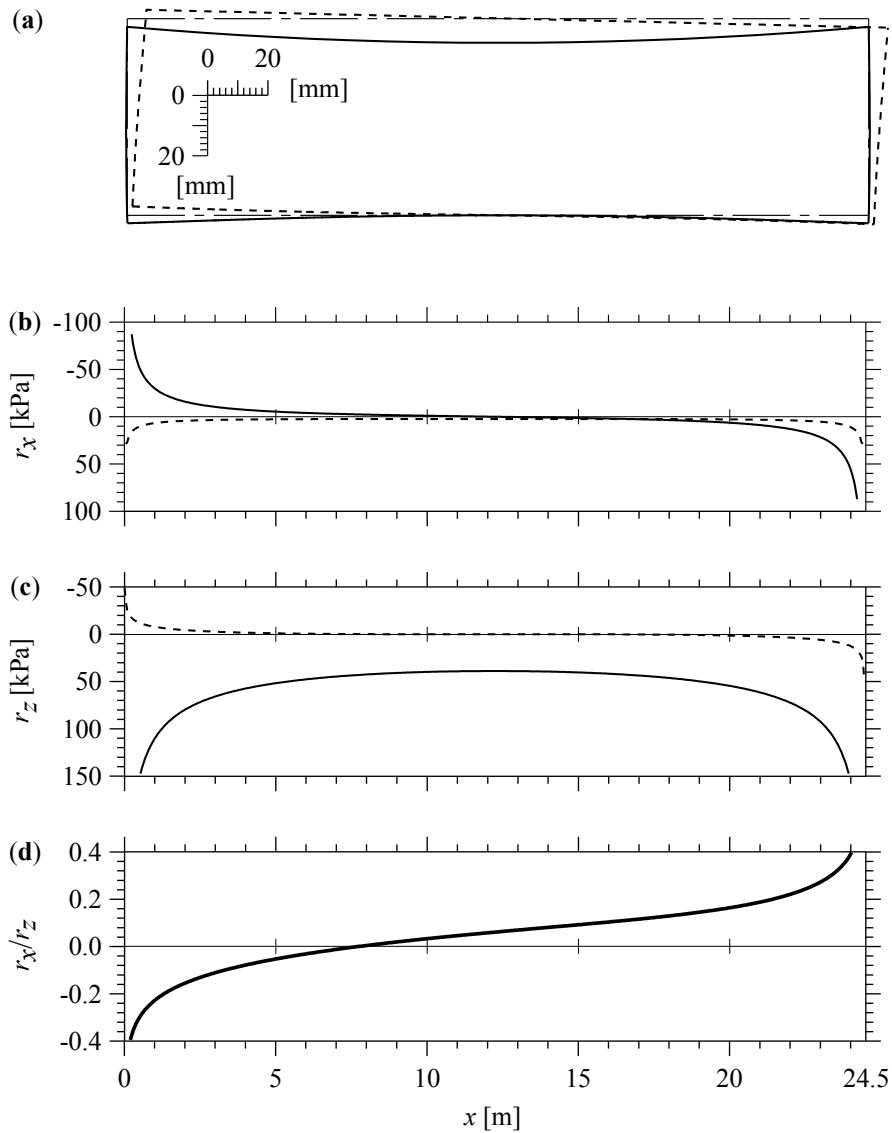
Fig. 1.30. Double-cell frame deflections (**a**) and reactions underneath foundation beam (**b** and **c**) for the structure subjected to self-weight (solid line) and lateral load (dashed line). Ratio r_x/r_z for the two load cases acting simultaneously (**d**). Undeformed frame in dash-dot line (**a**).

The triple-cell box, having αL = 6.6 and L/h = 28.0, shows the highest maximum vertical deflection at the middle cell where it is obtained a displacement of 16 mm. The lateral deflection due to the horizontal load is about 7 mm, rather similar to that of the double-cell structure.

Furthermore, the tangential and normal reactions underneath the foundation F are reported in Figs. 1.29-1.30-1.31b and c, respectively for the culvert subjected to self-weight (solid line) and lateral load (dashed line). Notice that, the both maximum reactions are obtained for the structure subjected to self-weigh.

The ratio r_x/r_z, when self-weight and horizontal load are applied simultaneously, is reported in Figs. 1.29-1.30-1.31d overtaking value of 0.3 at the foundation ends.
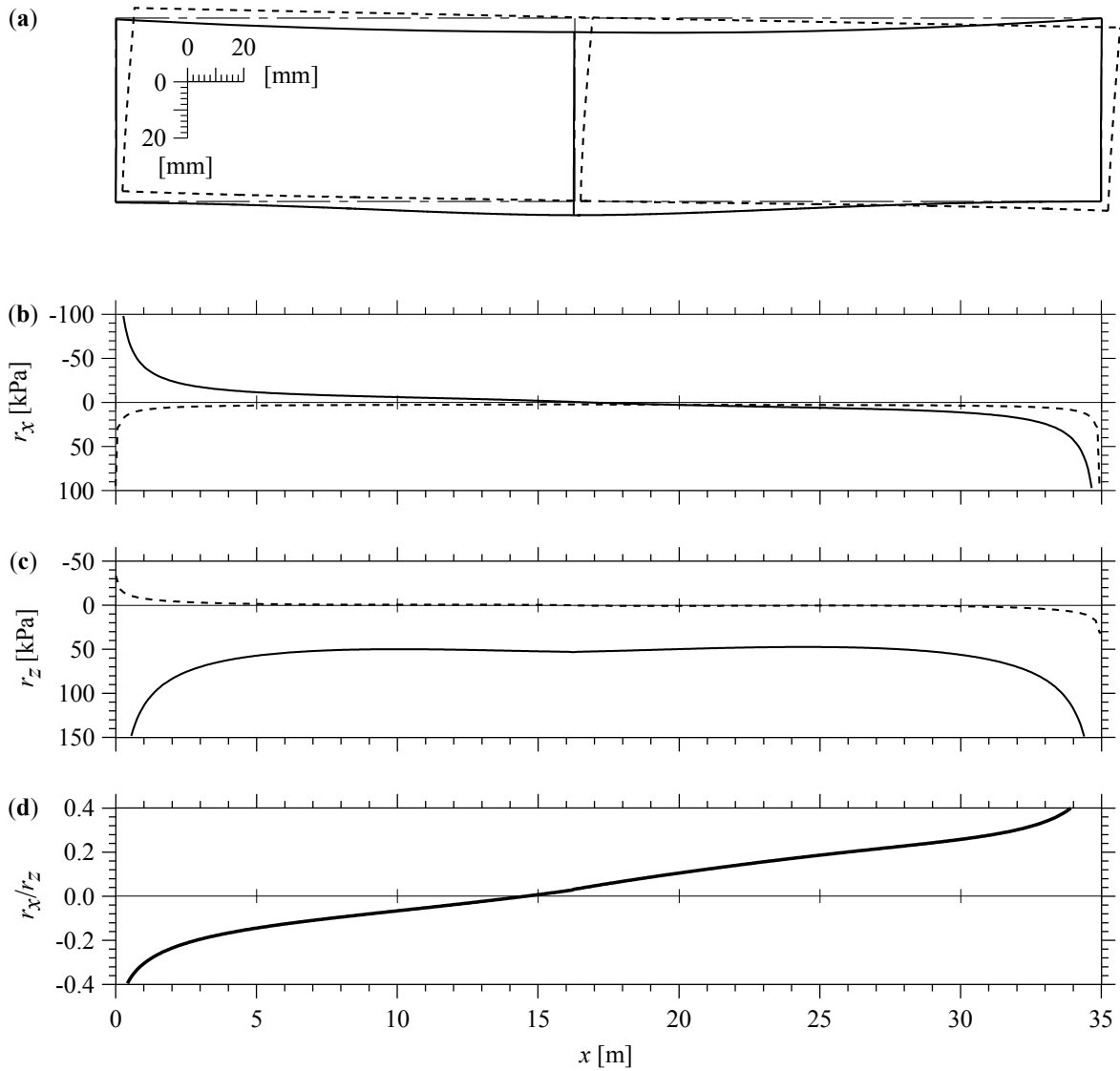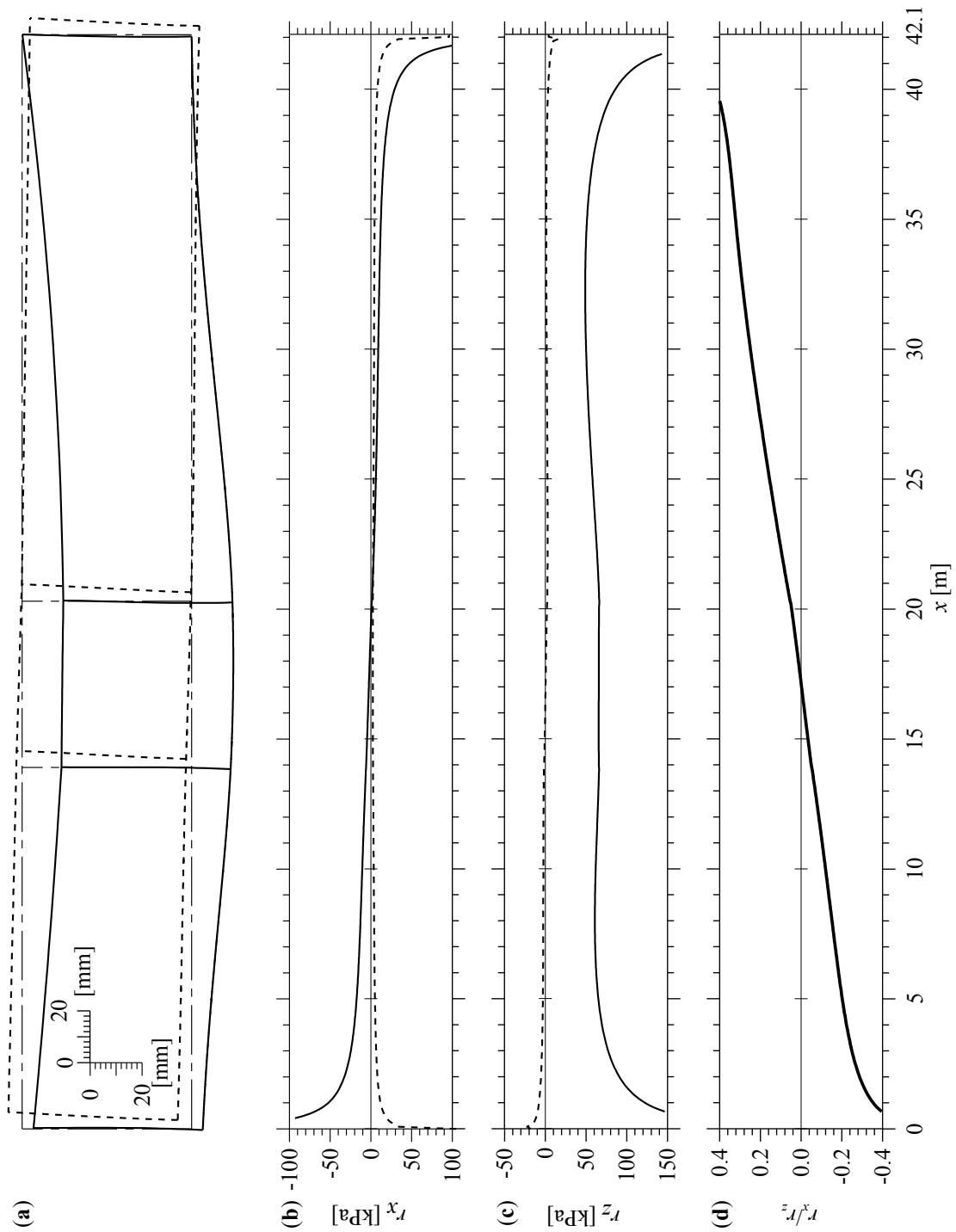
Fig. 1.31. Triple-cell frame deflections (**a**) and reactions underneath foundation beam (**b** and **c**) for the structure subjected to self-weight (solid line) and lateral load (dashed line). Ratio r_x/r_z for the two load cases acting simultaneously (**d**). Undeformed frame in dash-dot line (**a**).

The value of 0.3, which represents coefficient of friction, might be determined assuming an angle friction of the footing-soil for concrete foundation equal to 2/3 of the internal friction angle of soil [42]. Overtaking the coefficient of friction, the perfect adhesion condition is not ensured and should be disregarded.

1.5   Conclusions

A coupled FE-BIE model for the analysis of prismatic beams and frames in perfect adhesion to a homogeneous, linearly elastic and isotropic two-dimensional half-space is proposed. In particular, the classical displacement based FE method is used to describe the response of beams or frames, whereas a BIE approach is used for the substrate boundary, where surface displacements are linked to the applied loads by means of a suitable Green's function. Under the assumption of plane strain or plane stress state, the variational formulation is obtained through the theorem of work and energy for exterior domains, with the independent unknown functions being represented by beam displacements and surface tractions. In the more general case, Timoshenko beam theory is used to account for the effects of the shear deformations. Locking-free cubic and quadratic Hermitian shape functions are selected to interpolate transverse deflection and rotation, respectively, whereas axial displacement is approximated by linear functions. In addition, piecewise constant shape functions are used to describe both tangential and normal surface tractions. If the beam strain energy is ignored, the beam behaves like a rigid punch resting on a two-dimensional half-space. When tangential tractions and external horizontal forces are set equal to zero, the proposed formulation may be applied to the analysis of frictionless contact problems. Finally, by neglecting the beam bending stiffness, the problem of a thin coating bonded to a half-plane is recovered.

A number of numerical examples are presented to show the effectiveness of the proposed formulation in the analysis of the soil-structure interaction. In the case of a rigid punch subjected to point forces or moments, the analytical solutions available in the literature in terms of punch rotation and soil reactions are re-obtained. Moreover, it is shown that good approximations of these solutions are ensured by a coarse, graded mesh of only 8 FEs.

In the case of a beam subjected to a vertical point force or a bending moment at midspan, the shear deformations have a significant influence on both tangential and normal surface displacements and soil reactions. Moreover, the difference between horizontal displacements evaluated along the substrate boundary and the beam axis indicates a noteworthy contribution of the beam section rotation. In addition, the perfect adhesion is shown to dramatically modify the beam response with respect to the condition of frictionless contact. Both for Euler-Bernoulli and Timoshenko beams subjected to vertical point loads, the numerical performance of the proposed model has shown an excellent convergence rate in comparison with those of other standard numerical methods. Finally, if

the beam is subjected to a horizontal point force, the horizontal displacements are completely different from those obtained for a thin coating of equal cross-section, indicating a significant effect of the beam bending stiffness.

The last examples concern the soil-structure interaction analysis for cell box tunnel. Assuming plane strain state, the tunnel cross-section is identified with frame subjected to self-weight and a distributed lateral load. The loads are transferred to the soil by means of a foundation modelled with rigid punch or beam elements in perfect adhesion with the substrate boundary. Rigid punches are discretized by graded mesh, while foundation beams through uniform mesh of FEs. The proposed formulation is shown to be effective in the evaluation of frame deflections and soil reactions.

References

[1]   Helgeson DE, Aydin A. Characteristics of joint propagation across layer interfaces in sedimentary rocks. J Struct Geol 1991; 13(8):897–911.

[2]   Voevodin AA, Zabinski JS. Nanocomposite and nanostructured tribological materials for space applications. Compos Sci Technol 2005; 65(5):741–748.

[3]   Oehlers DJ. Reinforced concrete beam with plates glued to their soffits. J Struct Eng 1992; 118(8):2023–2038.

[4]   Akbar I, Oehlers DJ, Mohamed Ali MS. Derivation of the bond-slip characteristics for FRP plated steel members. J Constr Steel Res 2010; 66(8-9):1047–1056.

[5]   Varastehpour H, Hamelin P. Strengthening of concrete beams using fiber-reinforced plastics. Mater Struct 1997; 30(197):160–166.

[6]   Tsai MY, Morton J. The effect of a spew fillet on adhesive stress distribution in laminated composite single-lap joints. Compos Struct 1995, 32(1-4):123–131.

[7]   Belingardi G, Goglio L, Tarditi A. Investigating the effect of spew and chamfer size on the stresses in metal/plastics adhesive joints. Int J Adhes Adhes 2002, 22(4):273–282.

[8]   Da Silva LFM, Adams RD. Techniques to reduce the peel stresses in adhesive joints with composites. Int J Adhes Adhes 2007, 27(3):227–235.

[9]   Shen YL. Constrained Deformation of Materials, Devices, Heterogeneous Structures and Thermo-Mechanical Modeling. New York: Springer; 2010.

[10]   Selvadurai APS. Elastic analysis of soil-foundation interaction. Developments in Geotechnical Engineering, Elsevier Science; 1979.

[11]   Wang YH, Tham LG, Cheung YK. Beams and plates on elastic foundations: a review. Prog Struct Eng Mater 2005; 7(4):174–182.

[12]   Johnson KL. Contact mechanics. Cambridge: Cambridge University Press; 1985.

[13]   Kachanov ML, Shafiro B, Tsukrov I. Handbook of elasticity solutions. Dordrecht: Kluwer Academic Publishers; 2003.

[14]   Biot MA. Bending of an infinite beam on an elastic foundation. J Appl Mech 1937; 4:A1–A7.

[15]   Felippa CA. A study of optimal membrane triangles with drilling freedoms. Comput Meth Appl Mech Eng 2003; 192(16-18):2125–2168.

[16]   Cheung YK, Zienkiewicz OC. Plates and tanks on elastic foundations - an application of finite element method. Int J Solids Structure 1965; 1(4):451–461.

[17] Cheung YK, Nag DK. Plates and beams on elastic foundation - linear and non-linear behaviour. Geotechnique 1968; 18(2):250–260.

[18] Wang SK, Sargious M, Cheung YK. Advanced analysis of rigid pavements. J Transp Eng-ASCE 1972; 98(1):37–44.

[19] Kikuchi N, Oden J. Contact problems in elasticity. A study of variational inequalities and finite element methods. Philadelphia: SIAM; 1988.

[20] Kikuchi N. Beam bending problems on a Pasternak foundation using reciprocal variational-inequalities. Q Appl Math 1980; 38(1):91–108.

[21] Bielak J, Stephan E. A modified Galerkin procedure for bending of beams on elastic foundations. SIAM J Sci Stat Comput 1983; 4(2):340–352.

[22] Guarracino F, Minutolo V, Nunziante L. A simple analysis of soil-structure interaction by BEM-FEM coupling. Eng Anal Bound Elem 1992; 10(4):283–289.

[23] Bode C, Hirschauer R, Savidis SA. Soil-structure interaction in the time domain using half-space Green's functions. Soil Dyn Earthq Eng 2002; 22(4):283–295.

[24] Ribeiro DB, Paiva JB. An alternative BE–FE formulation for a raft resting on a finite soil layer. Eng Anal Bound Elem 2015; 50:352–359.

[25] Aleynikov S. Spatial Contact Problems in Geotechnics. Boundary-Element Method. Berlin Heidelberg: Springer-Verlag; 2011.

[26] Tullini N, Tralli A. Static analysis of Timoshenko beam resting on elastic half-plane based on the coupling of locking-free finite elements and boundary integral. Comput Mech 2010; 45(2–3):211–225.

[27] Tullini N, Tralli A, Lanzoni L. Interfacial shear stress analysis of bar and thin film bonded to 2D elastic substrate using a coupled FE-BIE method. Finite Elem Anal Des 2012; 55:42–51.

[28] Tullini N, Tralli A, Baraldi D. Stability of slender beams and frames resting on 2D elastic half-space. Arch Appl Mech 2013; 83(3):467–482.

[29] Tullini N, Tralli A, Baraldi D. Buckling of Timoshenko beams in frictionless contact with an elastic half-plane. J Eng Mech 2013; 139(7):824–831.

[30] Cowper GR. The shear coefficient in Timoshenko's beam theory. J Appl Mech ASME 1966; 33:335–340.

[31] Tullini N, Savoia M. Elasticity interior solution for orthotropic strips and the accuracy of beam theories. J Appl Mech ASME 1999; 66(2):368–373.

[32] Gurtin ME, Sternberg E. Theorems in linear elastostatics for exterior domains. Arch Ration Mech Anal 1961; 8:99–119.

[33] Reddy JN. On locking-free shear deformable beam finite elements. Comput Meth Appl Mech Eng 1997; 149(1-4):113–132.

[34] Narayanaswami R, Adelman HM. Inclusion of transverse shear deformation in finite element displacement formulations. AIAA J 1974; 12(11):1613–1614.

[35] Friedman Z, Kosmatka JB. An improved two-node Timoshenko beam finite element. Comput Struct 1993; 47(3):473–481.

[36] Minghini F, Tullini N, Laudiero F. Locking-free finite elements for shear deformable orthotropic thin-walled beams. Int J Numer Methods Eng 2007; 72(7):808–834.

[37] Vesic AB. Bending of beams on isotropic elastic medium. J Eng Mech Div ASCE 1961; 87(EM2):35–53.

[38] Grigolyuk EI, Tolkachev VM. Contact problems in the theory of plates and shells, Moscow: Mir Publishers; 1987.

[39] Hsiao GC, Wendland WL. A finite element method for some integral equations of the first kind. J Math Anal Appl 1977; 58(3):449–481.

[40] Costabel M. Boundary integral operators on Lipschitz domains: Elementary results. SIAM J Math Anal 1988; 19(3):613–626.

[41] Graham IG, McLean W. Anisotropic mesh refinement: the conditioning of Galerkin Boundary element matrices and simple preconditioners. SIAM J Numer Anal 2006, 44(4):1487–1513.

[42] Joseph E. Bowles, Foundation Analysis and Design, McGraw-Hill Companies, 1997.

2 Static analysis of shear flexible beam bonded to orthotropic elastic half-plane

2.1 Introduction

The contact problem of bars, beams and plates bonded to an elastic support is an important issue that has generated much interest in recent years. It has been widely dealt with in areas of aerospace, electronic, marine, transportation and infrastructure. In the framework of civil engineering, this topic has been dealt with in order to study soil-structure interaction problems or to investigate the effect induced by some reinforcements to increase the load-bearing capacity of existing structural elements. The latter application has been considered in Fiber-Reinforced Polymer (FRP) strengthening of concrete, steel or timber structures [1, 2, 3].

The contact problem involved in the indentation of an elastic half-plane has been treated by many authors under the assumptions of frictionless or fully adhesive contact, see [4, 5, 6] and references cited therein. The solution of a line force acting onto an elastic half-space was usually the main tool to study the contact problem. In particular, limiting to orthotropic or transversely isotropic half-plane under normal and tangential loadings acting onto the half-plane boundary, references have to be made to [7-13]. A mechanical application, adopting the contact model of a rigid flat punch or a beam resting on an orthotropic half-plane, has been considered in [14, 15, 16] to study a steel clamping joint attached to a composite truck leaf spring.

Early studies concerning thin films coated on an elastic substrate adopted series approximation method to solve singular integral equations including proper Green's function, see [17, 18] and references cited therein. Series approximation method was also used to study the bending problem of Euler-Bernoulli beams resting on an isotropic half-plane, under the assumptions of frictionless [19] or fully adhesive contact [20]. The influence of shear deformation was considered in [21], where the frictionless contact between a transversely loaded Timoshenko beam and an elastic isotropic layer is analysed.

The mechanical behaviour of single or multi-layered systems subjected to different loading conditions can be straightforwardly assessed by means of the Finite Element Method (FEM) due to its potential and versatility. Nonetheless, FEM undergoes important limitations when applied to film-substrate systems [22]. Indeed, owing to the thinness of the layers typically involved in many thin film-based devices and coated systems, a refined

mesh must be used, thus leading to a computer-time consuming. A proper grid refinement is needed in the neighbourhood of geometric discontinuities also in order to capture properly stress and strain localizations, whose knowledge is an important issue for many engineering issues, ranging from the mechanical behaviour of MEMS and NEMS [23], to the analysis of the punch problem of coated systems prone to crack formations [24, 25]. Moreover, in order to simulate the half-plane, FE meshes should be extended to a region significantly greater than the contact area, with detrimental effect on the time needed to carry out the numerical simulations. Finally, it should be remarked that, by modelling the covers through beam elements and the underlying half-plane by means of classical two-dimensional FEs, the angular continuity between the cover and the substrate cannot be imposed exactly as the connection between the elements occurs at discrete points.

Boundary Element Method (BEM) is a particularly advantageous tool for reproducing the response of an elastic half-plane because only the substrate boundary has to be discretized, see [26] and references cited therein. However, substrate tractions are usually considered as nodal reactions in the FE model of the foundation beam and the rotation continuity between beam and substrate is neglected. Alternatively, BE technique can be used to evaluate the mechanical behaviour of coated systems involving thin layers, as long as the nearly-singular integrals existing in the BE formulations are handled correctly [27, 28]. Nonetheless, beam model can be computationally more efficient than thin layer.

Otherwise, the behaviour of the soil can be approximated by incorporating a proper model for the substrate. As an example, Cheung and Zienkiewicz [29], and Cheung and Nag [30] performed a numerical model in which the deflection of the foundation and, in turn, the corresponding flexibility matrix, involve the fundamental Boussinesq's solution for the elastic half-plane, thus simulating accurately the interaction between loaded beams and plates in contact with an elastic support. However, based on such an approach, the continuity of the slope between the beam and the half-plane boundary cannot be imposed. Indeed, the connection among the beam and the substrate elements is realized by means of a finite number of pinned-clamped rigid links acting at equally spaced points, thus enforcing the continuity of the transversal deflection only. Moreover, the inversion of the substrate flexibility matrix is needed, thus consuming high computer-time.

In the present chapter, a static analysis of beams in plane strain or plane stress condition bonded to a homogeneous, linearly elastic and orthotropic half-plane, with a plane of elastic symmetry parallel to the boundary, is performed by using a coupled Finite Element-Boundary Integral Equation (FE-BIE) model. The proposed approach involves the Green's

function for the half-plane, thus providing a proper relation between the displacement and the interfacial stress fields at the substrate boundary, whereas a standard displacement-based formulation is used for the beam. The mechanical response of the half-plane is represented through a weakly singular integral equation, which solution is given analytically, thus avoiding singular and hyper-singular integrals typically involved in the classical BEM formulation. The independent unknowns of the problem are the displacement and the stress fields at the interface. It is worth noting that only the beam in contact with the substrate boundary has to be discretized. Unlike the numerical analyses available in the literature (e.g. [29, 30]), the proposed approach enforces the angular continuity between foundation beam and half-plane boundary at the node locations. Conversely to the classical FEM-BEM formulations, only symmetric soil matrices are involved in the proposed method, thus avoiding the computational cost due to the lack of symmetry of the BEM coefficient matrix. Note also that, differently to the standard FEM approaches in which a refined mesh requires a stiffness matrix with dimensions that are several times the square of the number of FEs used for the foundation beam, in the present model the resolving matrix has dimensions proportional to the number of the foundation beam FEs. This makes it possible to obtain very accurate solutions with low computational cost, as shown in [25], where a static analysis of both Euler-Bernoulli and Timoshenko beams bonded to an isotropic half-plane has been performed founding an excellent convergence rate as compared with those of other standard numerical methods.

Once the unknowns have been determined, the internal forces on the beam are determined through usual post-processing analysis. Recently, the static analysis of Timoshenko beams in frictionless [31] or fully adhesive contact [32] with an isotropic half-plane has been performed based on a similar mixed formulation (an analogous study concerning bars and thin coatings can be found in [33]). Furthermore, the FE-BIE coupling method has been also used to study the buckling of Euler-Bernoulli [27] and Timoshenko [28] beams in frictionless contact with an elastic support.

Numerical analysis of a beam with different bending rigidity, and loaded by a concentrated vertical force, a horizontal force or a couple at the midspan are considered firstly. In particular, the maximum bending moment of the beam subjected to point vertical load at the midpoint is investigated and compared with analytic solution present in the literature. Secondly, examples of FRP laminate bonded to wood substrate and concrete foundation and resting on soil are treated by assuming beam or membrane theory for the stiffener and concerning the contact condition, perfect adhesion or frictionless contact. A

detached or fully bonded reinforcement subjected to peel force is analysed. Afterwards, a stiffener loaded by horizontal force at one end or subjected to a uniform thermal is investigated. It is shown that the shear force at the beam ends can be significantly affected by shear deformation according to the Timoshenko beam theory. Finally, a shallow foundation loaded by a moment at the midspan is studied as a Timoshenko beam in perfect adhesion as well as in frictionless contact on an elastic orthotropic soil.

2.2   Variational formulation

A shear deformable beam with length L, height h and width b, bonded to an orthotropic semi-infinite substrate in a generalized plane stress or plane strain state is considered. Reference is made to a Cartesian coordinate system (O; x, z) having the x axis coincident with the centroidal axis of the beam and the z axis is downward directed (Fig. 2.1). Distributed horizontal and vertical external loads $p_x(x)$, $p_z(x)$, couple $m(x)$ as well as thermal variation $\Delta T(x)$ act along the beam. The beam is supposed in perfect adhesion with the half-plane. According to this assumption, both interfacial shear and normal tractions, $r_x(x)$ and $r_z(x)$, will occur within the contact region.

Here, a mixed variational principle is used to study the beam-substrate system, including the Green's function for the orthotropic half-plane. The total potential energy of the system Π is given by adding the total potential energy of the beam Π_{beam} to that of the substrate Π_{soil}, i.e., $\Pi = \Pi_{beam} + \Pi_{soil}$. As limit cases, an inextensible thin coating with a vanishing bending rigidity bonded to a half-plane and a beam in frictionless contact with a half-plane are considered in some detail.
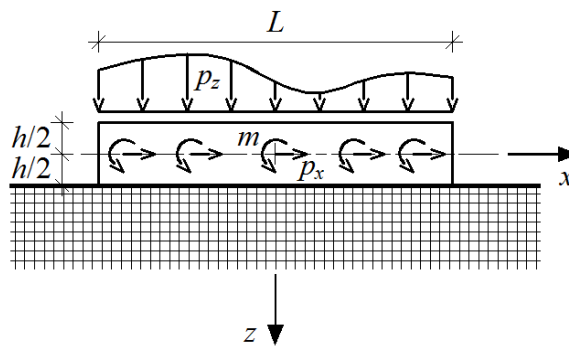

Fig. 2.1. Beam under general loads bonded to an orthotropic half-plane.

2.2.1 Total potential energy for the beam

Assuming positive cross-section rotations φ in counter-clockwise direction, the horizontal and vertical components of the displacement field of the Timoshenko beam can be written as

$$u_{bx}(x,z) = u_{bx,0}(x) + \varphi(x)\,z, \qquad u_{bz}(x,z) = u_z(x), \tag{2.1a,b}$$

where $u_{bx,0}$ is the axial displacement of the centroidal beam axis and u_z is the vertical displacement of both the beam and the half-plane boundary. The horizontal displacement of the lower side of the beam in contact with the half-plane boundary is given by $u_x(x) = u_{bx,0}(x) + \varphi(x)\,h/2$. The corresponding axial and shear strains are

$$\varepsilon_b = u'_{bx,0} + \varphi'\,z, \qquad \gamma_b = u'_z + \varphi, \tag{2.2a,b}$$

where prime represents differentiation with respect to variable x. Plane state assumption yields the following stress-strain relations:

$$\sigma_b = E_0\,\varepsilon_b, \qquad \tau_b = G_b\,\gamma_b, \tag{2.3a,b}$$

where $E_0 = E_{x,b}$ or $E_0 = E_{x,b}/(1-\nu_{xy,b}\nu_{yx,b})$ for generalised plane stress or plane strain state respectively, $E_{x,b}$ is the Young's modulus of the beam along the x-axis, $\nu_{ij,b}$ is the Poisson's coefficient of the beam associated with the pair directions $i, j = x, y, z$, G_b is the shear modulus $G_{xz,b}$ of the beam.

The elastic strain energy of the beam, U_{beam}, can be written as the sum of the axial strain energy $U_{\text{beam},a}$ and the bending-transverse shear strain energy $U_{\text{beam},b}$. By using the strain components (2.2) and the stress-strain relations (2.3), the elastic strain energies $U_{\text{beam},a}$ and $U_{\text{beam},b}$ can be written as:

$$U_{\text{beam}a} = \frac{1}{2}\int_L E_0 A_b (u'_{bx,0} - \alpha_0 \Delta T)^2 \, \mathrm{d}x, \tag{2.4a}$$

$$U_{\text{beam}b} = \frac{1}{2}\int_L [D_b\,(\varphi')^2 + k_b\,G_b A_b\,(u'_z + \varphi)^2]\,\mathrm{d}x, \tag{2.4b}$$

where $A_b = bh$, $D_b = E_0\,bh^3/12$ are the area and the flexural rigidity of the beam, respectively, α_0 is the coefficient of thermal expansion of the beam, k_b is the shear correction factor [36, 37]

$$k_b = \frac{5}{6 - \nu_{xz,b}G_b/E_{x,b}}, \qquad k_b = \frac{5}{6 - (\nu_{xz,b} + \nu_{xy,b}\nu_{yz,b})G_b/E_{x,b}} \tag{2.5a,b}$$

for a plane stress or a plane strain state, respectively.

Finally, the total potential energy of the beam, Π_{beam}, is assessed by adding the axial part $\Pi_{\text{beam},a}$ to the bending component $\Pi_{\text{beam},b}$, which are obtained from the strain energy contributions and the potential energy of the external loads, resulting in

$$\Pi_{\text{beam},a} = U_{\text{beam},a} - b \int_L (p_x - r_x) \, u_{bx,0} \, \mathrm{d}x, \tag{2.6a}$$

$$\Pi_{\text{beam},b} = U_{\text{beam},b} - b \int_L \left[(p_z - r_z) u_z + (m - r_x h/2) \varphi \right] \mathrm{d}x, \tag{2.6b}$$

2.2.2   Total potential energy for the orthotropic substrate

According to Voigt compact notation [6], the stress-strain relationship of a linearly elastic material can be expressed by the Hooke's law $\boldsymbol{\varepsilon} = \mathbf{S} \, \boldsymbol{\sigma}$, where the compliance matrix $\mathbf{S}$ can be written making reference to the canonical base (O; x, z). As known, for an orthotropic body exhibiting three perpendicular planes of elastic symmetry xz, yz, and xz in a plane state, the strain-stress relationship reduces to

$$\begin{bmatrix} \varepsilon_{xx} \\ \varepsilon_{zz} \\ 2\varepsilon_{xz} \end{bmatrix} = \begin{bmatrix} R_{11} & R_{13} & 0 \\ R_{13} & R_{33} & 0 \\ 0 & 0 & R_{55} \end{bmatrix} \begin{bmatrix} \sigma_{xx} \\ \sigma_{zz} \\ \sigma_{xz} \end{bmatrix}, \tag{2.7}$$

where the elastic compliance constants involved in Eq. (2.7) can be written as

$$R_{11} = \frac{1}{E_x}, \qquad R_{33} = \frac{1}{E_z}, \qquad R_{13} = -\frac{\nu_{xz}}{E_x} = -\frac{\nu_{zx}}{E_z}, \qquad R_{55} = \frac{1}{G_{xz}}, \tag{2.8a,b,c,d}$$

$$R_{11} = \frac{1 - \nu_{xy}\nu_{yx}}{E_x}, \qquad R_{33} = \frac{1 - \nu_{zy}\nu_{yz}}{E_z}, \tag{2.9a,b}$$

$$R_{13} = -\frac{\nu_{xz} + \nu_{xy}\nu_{yz}}{E_x} = -\frac{\nu_{zx} + \nu_{yx}\nu_{zy}}{E_z}, \qquad R_{55} = \frac{1}{G_{xz}}. \tag{2.9c,d}$$

for plane stress state, Eq. (2.8), or plane strain state, Eq. (2.9), respectively, where E_i denotes the Young's modulus along the directions $i = x, z$, G_{ij} and ν_{ij} are the shear modulus and Poisson's coefficient, respectively, associated with the pair directions $i, j = x, y, z$. In particular, due to this special kind of material symmetry, $\nu_{ij}/E_i = \nu_{ji}/E_j$.

In the following, three combinations of the elastic compliance constants are used

$$c_1 = \left(\frac{R_{11}}{R_{33}}\right)^{1/4}, \qquad c_2 = \left(2 + \frac{R_{55} + 2R_{13}}{\sqrt{R_{11}R_{33}}}\right)^{1/2}, \qquad c_3 = \left(\frac{R_{11}}{R_{33}}\right)^{1/2} + \frac{R_{13}}{R_{33}}. \qquad (2.10\text{a,b,c})$$

In particular, in plane stress state, making use of Eq. (2.8), Eq. (2.10) reduces to

$$c_1 = \left(\frac{E_z}{E_x}\right)^{1/4}, \quad c_2 = \left(2 + \frac{\sqrt{E_x E_z}}{G_{xz}} - 2\,\nu_{xz}\left(\frac{E_z}{E_x}\right)^{1/2}\right)^{1/2}, \quad c_3 = \left(\frac{E_z}{E_x}\right)^{1/2} - \nu_{zx}, \qquad (2.11\text{a,b,c})$$

while in plane strain state, by substituting Eq. (2.9) into Eq. (2.10), the constants c_1, c_2, c_3 become

$$c_1 = \left(\frac{E_z}{E_x}\frac{1 - \nu_{xy}\nu_{yx}}{1 - \nu_{zy}\nu_{yz}}\right)^{1/4}, \qquad (2.12\text{a})$$

$$c_2 = \left(2 + \sqrt{\frac{E_z}{(1 - \nu_{xy}\nu_{yx})(1 - \nu_{zy}\nu_{yz})}\left(\frac{\sqrt{E_x}}{G_{xz}} - \frac{2(\nu_{xz} + \nu_{xy}\nu_{yz})}{\sqrt{E_x}}\right)}\right)^{1/2}, \qquad (2.12\text{b})$$

$$c_3 = \left(\frac{E_z}{E_x}\frac{1 - \nu_{xy}\nu_{yx}}{1 - \nu_{zy}\nu_{yz}}\right)^{1/2} - \frac{\nu_{zx} + \nu_{yx}\nu_{zy}}{1 - \nu_{zy}\nu_{yz}}. \qquad (2.12\text{c})$$

It is worth remarking that, for an isotropic substrate, the elastic compliance component R_{33} of half-plane in z-direction is equal to $1/E$ and the substrate coefficients are $c_1 = 1$, $c_2 = 2$, $c_3 = c$, where $E = E_{soil}$ and $c = 1 - \nu_{soil}$ or $E = E_{soil}/(1 - v_{soil}^2)$ and $c = (1 - 2\,\nu_{soil})/(1 - \nu_{soil})$ for a generalized plane stress or plane strain state, respectively, with E_{soil} and ν_{soil} being Young's modulus and Poisson ratio of the isotropic substrate.

The solutions to the two-dimensional problem for a homogeneous, linear elastic and orthotropic half-plane loaded by a point force normal or tangential to its boundary are given in [12, 13]. In particular, the surface displacement $u_i(x)$, with $i = x, z$, due to a point force $P_i(\hat{x})$ applied to the half-plane boundary can be expressed in closed form as $u_i(x) = g(x, \hat{x})\, P_i(\hat{x})$, where Green's function $g(x, \hat{x})$ is given by the following expression:

$$g(x, \hat{x}) = -\frac{c_1 c_2}{\pi} R_{33} \ln\frac{|x - \hat{x}|}{d}, \qquad (2.13)$$

being d an arbitrary length related to a rigid-body displacement.

After some cumbersome algebraic manipulation of results reported in [12, 13], the horizontal and vertical displacements of a point of the orthotropic half-plane boundary due to the combined action of tangential and normal tractions can be written as:

$$u_x(x) = c_1^2 \int_L g(x,\hat{x}) \, r_x(\hat{x}) \, \mathrm{d}\hat{x} - \frac{c_3}{2} R_{33} \left[\int_{x_0}^{x} r_z(\hat{x}) \, \mathrm{d}\hat{x} - \int_{x}^{x_L} r_z(\hat{x}) \, \mathrm{d}\hat{x} \right], \qquad (2.14a)$$

$$u_z(x) = \int_L g(x,\hat{x}) \, r_z(\hat{x}) \, \mathrm{d}\hat{x} + \frac{c_3}{2} R_{33} \left[\int_{x_0}^{x} r_x(\hat{x}) \, \mathrm{d}\hat{x} - \int_{x}^{x_L} r_x(\hat{x}) \, \mathrm{d}\hat{x} \right], \quad \text{with } x_0 < x < x_L \qquad (2.14b)$$

where x_0, x_L are the abscissas of the beam ends. Therefore, a combination of only four elastic constants characterises the displacements field (2.14).

Making use of the theorem of work and energy for exterior domains [38], it can be shown that the total potential energy Π_{soil} for the half-plane equals one half of the work of external loads [31, 33, 32], i.e.,

$$\Pi_{\text{soil}} = -\frac{b}{2} \int_L (r_x \, u_x + r_z \, u_z) \, \mathrm{d}x., \qquad (2.15)$$

Substituting Eq. (2.14) into Eq. (2.15) yields $\Pi_{\text{soil}} = \Pi_{\text{soil},a} + \Pi_{\text{soil},b}$, where

$$\Pi_{\text{soil},a} = -\frac{b}{2} \int_L r_x(x) \, \mathrm{d}x \left\{ c_1^2 \int_L g(x,\hat{x}) \, r_x(\hat{x}) \, \mathrm{d}\hat{x} - \frac{c_3}{2} R_{33} \left[\int_{x_0}^{x} r_z(\hat{x}) \, \mathrm{d}\hat{x} - \int_{x}^{x_L} r_z(\hat{x}) \, \mathrm{d}\hat{x} \right] \right\}, \qquad (2.16a)$$

$$\Pi_{\text{soil},b} = -\frac{b}{2} \int_L r_z(x) \, \mathrm{d}x \left\{ \int_L g(x,\hat{x}) \, r_z(\hat{x}) \, \mathrm{d}\hat{x} + \frac{c_3}{2} R_{33} \left[\int_{x_0}^{x} r_x(\hat{x}) \, \mathrm{d}\hat{x} - \int_{x}^{x_L} r_x(\hat{x}) \, \mathrm{d}\hat{x} \right] \right\}. \qquad (2.16b)$$

2.2.3   Total potential energy for the beam-substrate system

The total potential energy of the beam-substrate system $\Pi = \Pi_{\text{beam}} + \Pi_{\text{soil}}$ is a mixed variational formulation with variational functions represented by displacements $u_{bx,0}$, u_z and rotation φ, as well as interfacial shear and normal tractions r_x and r_z along the contact region. It is worth noting that using Green's function given by Eq. (2.13) reduces the domain of integration to the beam length only. For an isotropic substrate, the total potential energy Π reduces to that proposed in [32].

Several particular cases derive from the proposed mixed variational formulation. For instance, a beam in frictionless contact with the underlying substrate involves null interfacial shear traction r_x along the contact region. Accordingly, the displacement field provided by Eq. (2.14) reads

$$u_x(x) = -\frac{c_3}{2} R_{33} \left[\int_{x_0}^{x} r_z(\hat{x}) \, \mathrm{d}\hat{x} - \int_{x}^{x_L} r_z(\hat{x}) \, \mathrm{d}\hat{x} \right], \qquad (2.17a)$$

$$u_z(x) = \int_L g(x,\hat{x}) \, r_z(\hat{x}) \, \mathrm{d}\hat{x}, \qquad (2.17b)$$

and the total potential energy of orthotropic half-plane Π_{soil} becomes

$$\Pi_{\text{soil}} = \Pi_{\text{soil,b}} = -\frac{b}{2}\int_L r_z\, u_z\, \mathrm{d}x = -\frac{b}{2}\int_L r_z(x)\, \mathrm{d}x \int_L g(x,\hat{x})\, r_z(\hat{x})\, \mathrm{d}\hat{x}, . \tag{2.18}$$

The displacement field (2.17) is similar to Eq. (12) reported in [31], where a beam in frictionless contact with an isotropic substrate is considered, except for different values of the Young's modulus and the coefficient c. Therefore, an orthotropic substrate behaves like an isotropic soil having an equivalent Young's modulus $E = 2/(c_1\, c_2\, R_{33})$ and a ratio $c/E = c_3\, R_{33}$, with $c = 2\, c_3/(c_1\, c_2)$. Thus, the FE-BIE methods as well as the results show in [31] can be used. In particular, in the case of a rigid punch resting on an orthotropic half-plane, the normal traction under the punch is the same of that found for the indentation problem of an isotropic half-plane [6]. However, the stress and displacement fields in the half-plane will differ from the one in the case of isotropy.

A beam with a small bending rigidity may be considered as a thin coating where the normal tractions r_z can be neglected. Then, the displacement field (2.14) reduces to

$$u_x(x) = c_1^2 \int_L g(x,\hat{x})\, r_x(\hat{x})\, \mathrm{d}\hat{x}, \tag{2.19a}$$

$$u_z(x) = \frac{c_3}{2} R_{33} \left[\int_{x_0}^{x} r_x(\hat{x})\, \mathrm{d}\hat{x} - \int_{x}^{x_L} r_x(\hat{x})\, \mathrm{d}\hat{x} \right], \tag{2.19b}$$

and the total potential (2.15) becomes

$$\Pi_{\text{soil}} = \Pi_{\text{soil,a}} = -\frac{b}{2}\int_L r_x\, u_x\, \mathrm{d}x = -\frac{b}{2} c_1^2 \int_L r_x(x)\, \mathrm{d}x \int_L g(x,\hat{x})\, r_x(\hat{x})\, \mathrm{d}\hat{x}. \tag{2.20}$$

The displacement field (2.19) is similar to Eq. (13) reported in [33], where a thin coating bonded to an isotropic substrate is studied, except for different values of the Young's modulus and the coefficient c. Therefore, an orthotropic substrate behaves like an isotropic soil having an equivalent Young's modulus $E = 2/(c_1^3\, c_2\, R_{33}) = 2\, c_1/(c_2\, R_{11})$ and a ratio $c/E = c_3\, R_{33}$, with $c = 2\, c_3/(c_1^3\, c_2)$. Therefore, the analyses made in [33] can be employed. In particular, in the case of an inextensible stiffener bonded to an orthotropic half-plane, the interfacial shear tractions r_x are the same of those founded for an isotropy half-plane.

2.3 Finite element model

Both the foundation beam and the substrate boundary are subdivided into FEs sharing the same mesh. Nevertheless, the mesh of the beam could be chosen independently from that used for the half-space boundary. The generic ith FE has a length $l_i = |x_{i+1} - x_i|$ where x_i and x_{i+1} are the initial and end coordinates. Assuming a dimensionless local coordinate $\xi = x/l_i$, the displacements of the centroidal axis of beam can be approximated as

$$u(\xi) = \mathbf{N}_a(\xi)\,\mathbf{u}_{xi}, \qquad [v(\xi),\,\varphi(\xi)]^{\mathrm{T}} = \mathbf{N}_b(\xi)\,\mathbf{q}_{zi}, \qquad (2.21a,b)$$

where $\mathbf{u}_{xi} = [u_{x,i},\ u_{x,i+1}]^{\mathrm{T}}$ and $\mathbf{q}_{zi} = [u_{z,i},\ \varphi_i,\ u_{z,i+1},\ \varphi_{i+1}]^{\mathrm{T}}$ are the vectors of nodal displacements, while $\mathbf{N}_a(\xi) = [N_{a,1},\ N_{a,2}]$ is the vector collecting the linear Lagrangian functions, whereas $\mathbf{N}_b(\xi)$ is the matrix of the "modified" Hermitian shape functions [31, 32, 39, 40]. These latter functions reduce to the classical Hermitian polynomials (and to their first derivatives) when shear deformations are negligible, so resulting in locking-free FEs [41, 42].

The tractions may be approximated as

$$r_x(\xi) = [\boldsymbol{\rho}(\xi)]^{\mathrm{T}}\,\mathbf{r}_{xi}, \qquad r_z(\xi) = [\boldsymbol{\rho}(\xi)]^{\mathrm{T}}\,\mathbf{r}_{zi}, \qquad (2.22a,b)$$

where $\mathbf{r}_{xi},\ \mathbf{r}_{zi}$ denote nodal interfacial shear and normal tractions, respectively, and vector $\boldsymbol{\rho}$ collect constant shape functions, i.e., only piecewise constant functions are used to interpolate $\mathbf{r}_x$ and $\mathbf{r}_z$ and $\boldsymbol{\rho}(\xi)$ is assumed to be unitary along the generic FE.

Substituting Eqs. (2.21) and (2.22) into the variational principle, assembling over all elements and requiring the stationary of the potential energy, the following system of equations is obtained:

$$\begin{bmatrix} \mathbf{K} & \mathbf{H} \\ \mathbf{H}^{\mathrm{T}} & -\mathbf{G} \end{bmatrix} \begin{Bmatrix} \mathbf{q} \\ \mathbf{r} \end{Bmatrix} = \begin{Bmatrix} \mathbf{f} \\ \mathbf{0} \end{Bmatrix}. \qquad (2.23)$$

where $\mathbf{K}$ is the beam stiffness matrix, $\mathbf{f}$ is the external load vector, whose components for the generic FE can be written in the usual form, (see Eqs. (23) and (24) reported in [32] for details), whereas vectors $\mathbf{q} = [\mathbf{u}_x, \mathbf{q}_z]^{\mathrm{T}}$ and $\mathbf{r} = [\mathbf{r}_x, \mathbf{r}_z]^{\mathrm{T}}$ collect the nodal displacements and nodal reactions, respectively. Matrix $\mathbf{H}$ descends by the potential energy of the substrate tractions appearing in Eqs. (2.6a, b) and play a key role as it enforces the compatibility of displacements and rotations between beam and substrate. Finally, substrate matrix $\mathbf{G}$ is fully populated since it accounts for the nonlocal relation between beam displacements and surface tractions, and can be written as

$$\mathbf{G} = -bR_{33}\widetilde{\mathbf{G}} = -bR_{33}\begin{bmatrix} c_1^2\,\widetilde{\mathbf{G}}_{xx} & c_3\,\widetilde{\mathbf{G}}_{xz} \\ c_3\,\widetilde{\mathbf{G}}_{xz}^{\mathrm{T}} & \widetilde{\mathbf{G}}_{zz} \end{bmatrix} \tag{2.24}$$

The components of the matrix $\mathbf{G}$ are given by:

$$\widetilde{g}_{xx,ij} = \widetilde{g}_{zz,ij} = \frac{c_1 c_2}{\pi} \int_{x_i}^{x_{i+1}} \rho_i(x)\,\mathrm{d}x \int_{x_j}^{x_{j+1}} \ln|x - \hat{x}|\,\rho_j(\hat{x})\,\mathrm{d}\hat{x} \tag{2.25a}$$

$$\widetilde{g}_{xz,ij} = \int_{x_i}^{x_{i+1}} \rho_i(x)\,\mathrm{d}x \left[\int_{x_0}^{x} \rho_j(\hat{x})\,\mathrm{d}\hat{x} - \int_{x}^{x_L} \rho_j(\hat{x})\,\mathrm{d}\hat{x} \right] \tag{2.25b}$$

where the contribution due to the arbitrary length d has been omitted since rigid-body displacements can be imposed in post-processing analysis. The integral in Eq. (2.25a) is weakly singular, i.e. it always exists in the Cauchy principal value sense and it is finite. Substituting piecewise constant functions (2.22) in Eq. (2.25a) yields

$$\widetilde{g}_{xx,ii} = \widetilde{g}_{zz,ii} = \frac{c_1 c_2}{\pi}\, l_i^2 \left(\frac{3}{2} - \ln l_i \right), \tag{2.26a}$$

$$\widetilde{g}_{xx,ij} = \widetilde{g}_{zz,ij} \qquad \text{for } i \neq j \tag{2.26c}$$

where $\ \widetilde{g}_{zz,ij} = \dfrac{c_1 c_2}{\pi}\left[\dfrac{3}{2} l_i l_j + G(x_{j+1} - x_{i+1}) - G(x_{j+1} - x_i) - G(x_j - x_{i+1}) + G(x_j - x_i) \right]$

with $G(x) = x2/2\ \ln|x|$, whereas the components of matrix $\widetilde{\mathbf{G}}_{xz}$, Eq. (2.25b), are the following

$$\widetilde{g}_{xz} = \begin{cases} \widetilde{g}_{xz,ij} = -l_i\,l_j/2 & \text{if } i > j \\ \widetilde{g}_{xz,ii} = 0 & \text{if } i = j, \\ \widetilde{g}_{xz,ij} = l_i\,l_j/2 & \text{if } i < j \end{cases} \tag{2.27}$$

For an isotropic half-plane, system of equation (2.24) reduces to Eq. (42c) reported in [32]. For the sake of completeness, classical results referred to a prismatic beam subjected to distributions of loads $p_x(x)$, $p_z(x)$, couple $m(x)$ as well as thermal variation ΔT are recalled. The system of equations (2.23) concerning a prismatic beam bonded to an orthotropic half-plane can be written in dimensionless form as

$$\begin{bmatrix} D_b/L^3\,\widetilde{\mathbf{K}} & b\widetilde{\mathbf{H}} \\ b\widetilde{\mathbf{H}}^{\mathrm{T}} & -bR_{33}\widetilde{\mathbf{G}} \end{bmatrix} \begin{Bmatrix} \mathbf{q} \\ \mathbf{r} \end{Bmatrix} = \begin{Bmatrix} b\widetilde{\mathbf{f}} \\ \mathbf{0} \end{Bmatrix}, \tag{2.28a}$$

and, after some manipulations, as

$$
\left[
\begin{bmatrix}
\dfrac{D_b}{L^3}\begin{bmatrix} \lambda_0^2\,\widetilde{\mathbf{K}}_a & \mathbf{0} \\[4pt] \mathbf{0} & \widetilde{\mathbf{K}}_b \end{bmatrix} & b\begin{bmatrix} \widetilde{\mathbf{H}}_{xx} & \mathbf{0} \\[4pt] \widetilde{\mathbf{H}}_{xz} & \widetilde{\mathbf{H}}_{zz} \end{bmatrix} \\[18pt]
b\begin{bmatrix} \widetilde{\mathbf{H}}_{xx}^{\mathrm{T}} & \widetilde{\mathbf{H}}_{xz}^{\mathrm{T}} \\[4pt] \mathbf{0} & \widetilde{\mathbf{H}}_{zz}^{\mathrm{T}} \end{bmatrix} & -bR_{33}\begin{bmatrix} c_1^2\,\widetilde{\mathbf{G}}_{xx} & c_3\,\widetilde{\mathbf{G}}_{xz} \\[4pt] c_3\,\widetilde{\mathbf{G}}_{xz}^{\mathrm{T}} & \widetilde{\mathbf{G}}_{zz} \end{bmatrix}
\end{bmatrix}
\right]
\left\{
\begin{bmatrix} \mathbf{u}_x \\ \mathbf{q}_z \\ \mathbf{r}_x \\ \mathbf{r}_z \end{bmatrix}
\right\}
=
\left\{
b\begin{bmatrix} \widetilde{\mathbf{f}}_a \\ \widetilde{\mathbf{f}}_b \\ \mathbf{0} \\ \mathbf{0} \end{bmatrix}
\right\}.
\tag{2.28b}
$$

with $\lambda_0 = L/r_g$ and the radius of gyration $r_g = h/\sqrt{12}$. Making use of Eqs. (2.21a, b), the stiffness matrices of the ith FE read

$$
\widetilde{\mathbf{K}}_{a,i} = \frac{L}{l_i}\begin{bmatrix} 1 & -1 \\ -1 & 1 \end{bmatrix},
\tag{2.29a}
$$

$$
\widetilde{\mathbf{K}}_{b,i} = \frac{L^3}{(1+\phi_i)l_i^3}\begin{bmatrix}
12 & -6l_i & -12 & -6l_i \\
 & (4+\phi_i)l_i^2 & 6l_i & (2-\phi_i)l_i^2 \\
 & & 12 & 6l_i \\
\text{sym} & & & (4+\phi_i)l_i^2
\end{bmatrix},
\tag{2.29b}
$$

where the coefficient $\phi_i = 12D_b/(k_bG_bA_bl_i^2)$ accounts for the shear deformation according to the Timoshenko beam theory. The vectors of the external load of the ith FE, due to uniform load distributions $p_x(x)$, $p_z(x)$, $m(x)$ and thermal variation ΔT, is decomposed into the axial and shear-bending components as follows

$$
\widetilde{\mathbf{f}}_{a,i} = \frac{p_x l_i}{2}\begin{bmatrix} 1 \\ 1 \end{bmatrix} + \frac{1}{b}E_0\,A_b\,\alpha_0\,\Delta T\begin{bmatrix} -1 \\ 1 \end{bmatrix},
\tag{2.30a}
$$

$$
\widetilde{\mathbf{f}}_{b,i} = p_z\begin{bmatrix} l_i/2 \\ -l_i^2/12 \\ l_i/2 \\ l_i^2/12 \end{bmatrix} + \frac{m}{(1+\phi_i)}\begin{bmatrix} 1 \\ l_i\phi_i/2 \\ -1 \\ l_i\phi_i/2 \end{bmatrix} + \frac{1}{b}D_b\,\frac{2\alpha_0\,\Delta T}{h}\begin{bmatrix} 0 \\ -1 \\ 0 \\ 1 \end{bmatrix}.
\tag{2.30b}
$$

The components of matrix $\mathbf{H}$ for the generic FE coincide with Eqs. (25) reported in [32]. In particular, the ith FE has the following components

$$
\widetilde{\mathbf{h}}_{xx,i} = \frac{l_i}{2}\begin{bmatrix} 1 \\ 1 \end{bmatrix}, \qquad
\widetilde{\mathbf{h}}_{zz,i} = \begin{bmatrix} l_i/2 \\ -l_i^2/12 \\ l_i/2 \\ l_i^2/12 \end{bmatrix}, \qquad
\widetilde{\mathbf{h}}_{xz,i} = \frac{h}{2(1+\phi_i)}\begin{bmatrix} 1 \\ \phi_i l_i/2 \\ -1 \\ \phi_i l_i/2 \end{bmatrix}.
\tag{2.31a,b,c}
$$

To sum, a representation of the matrix (2.28b) is shown in Fig. 2.2, where the beam is subdivided into two elements (b_1, b_2) bonded to two substrate elements (s_1, s_2) and is subjected to pointwise loads P_x, P_z, C at the beam midspan.

The solutions of Eq. (2.23) reduces to the following equations

$$\mathbf{r} = \frac{1}{R_{33}} \widetilde{\mathbf{G}}^{-1} \widetilde{\mathbf{H}}^{\mathrm{T}} \mathbf{q}, \qquad D_b/L^3 \left[\widetilde{\mathbf{K}} + (\alpha L)^3 \widetilde{\mathbf{K}}_{\mathrm{soil}} \right] \mathbf{q} = b\widetilde{\mathbf{f}}, \qquad (2.32a,b)$$

being $\widetilde{\mathbf{K}}_{\mathrm{soil}} = \widetilde{\mathbf{H}} \widetilde{\mathbf{G}}^{-1} \widetilde{\mathbf{H}}^{\mathrm{T}}$ the dimensionless stiffness matrix of the substrate and

$$\alpha L = \sqrt[3]{b L^3 / (R_{33} D_b)}. \qquad (2.33)$$

According to references [31, 32, 43, 44], parameter αL governs the static response of the beam-substrate system. Low values of αL characterize short beams stiffer than soil, whereas high values of αL correspond to slender beams on a relatively stiff soil. Nonetheless, differently from the isotropic case, the three combinations of the elastic compliance constants (2.10) play a crucial role in the static response. It is worth noting that the elastic response of a thin coating bonded to an elastic substrate is characterized by the parameter $\beta L = bL/(R_{33}E_0 A_b)$, yielding the relationship $(\alpha L)^3 = (\beta L) \lambda_0^2$ [33, 32, 45].
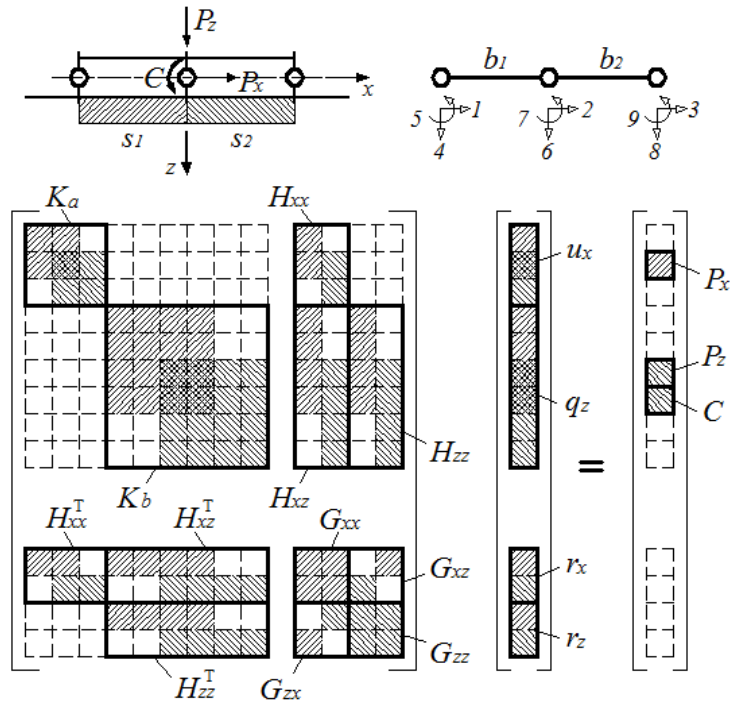
Fig. 2.2. Matrix system of a beam subdivided in two beam elements b_1, b_2, each of which is bonded to a single substrate element s_1, s_2, respectively. External pointwise loads P_x, P_z and couple C applied at the middle.

2.4   Numerical examples

Unless otherwise specified, a number of 512 equal beam FEs have been used. Each beam FE includes one substrate element. The solution of the system, Eq (2.23), provides the displacements along the centroidal beam axis and the interfacial tractions. The plotted values of horizontal interface displacement are obtained by Eq. (2.1a) with $z = h/2$. The axial force N, shear force V and bending moment M along the beam have been calculated by means of post-processing analysis, multiplying the local stiffness matrix of the beam by the displacement vector obtained by the solution of system (2.23).

Firstly, a beam loaded by a vertical force acting downward direction at the midpoint is investigate in perfect adhesion and frictionless contact. In particular, the normal pressure at the midspan as well as the maximum bending moment are studied with regard to the parameter αL. Secondly, a beam or a thin film subjected to a horizontal force at the midpoint is analysed. Moreover, a beam loaded by a couple at the midpoint is considered in perfect adhesion and in frictionless contact. Besides the maximum pressure in proximity the midspan is reported versus αL. The behaviour of the internal shear force of the beam has been focused on all the three load cases. Finally, examples of practical meaning are considered: a GFRP or aluminium reinforcement bonded to an orthotropic wood and concrete foundation resting on an orthotropic soil.

2.4.1   Beam loaded by a point force or a couple at midpoint

The proposed couple FE-BIE formulation are firstly examined with regard to a beam of length L and height h, having ratio $L/h = 10$. Perfect adhesion and frictionless contact are investigated with a Timoshenko beam ($\phi = 0.3$) resting on an orthotropic half-plane, as well as a Euler-Bernoulli beam ($\phi = 0.0$) in perfect adhesion is reported for comparison. The results of the system are obtained in plane stress state, assuming the parameter of the beam-substrate system $\alpha L = 10$, and substrate coefficients $c_1 = 0.56$, $c_2 = 3.08$, $c_3 = 0.3$. The choice of coefficients c is established assuming Young modulus in x-direction ten times more than that in z-direction of the substrate in Chapter 1 ($E_1 = 10\,E_3$). Furthermore, some investigation are studied varying the parameter of relative stiffness system αL from 0 to 10. Although the usual continuum mechanics hypothesis could be not hold anymore when $x/L > +0.4999L$ or $x/L < -0.4999L$, shear force of beam is focussed on at one end, using a logarithmically mesh in the interval $[0.4, 0.5\text{-}10^{-4}]$.

2.4.1.1 Beam loaded by a vertical point force P_z

The case of beam having ratio $L/h = 10$, fully bonded to an elastic orthotropic half-plane and loaded by a vertical point force at midspan is considered firstly, Fig. 2.3. The parameter of the beam-substrate system $\alpha L = 10$, and substrate coefficients $c_1 = 0.56$, $c_2 = 3.08$, $c_3 = 0.3$ are assumed. Dimensionless displacements and reactions along the substrate boundary are obtained by the equation system (Eq. 2.28) and are plotted in Fig. 2.3a-d. Through the post-processing analysis, dimensionless value of axial force, shear force and bending moment of the beam are calculated, Fig. 2.3e, f, g.

The interfacial horizontal displacements u_x are stretched in the area of the load section and contracted far away from it. That is remarkable for the Euler-Bernoulli beam with a length of stretching wider. The stretched displacements tend to disappear when are evaluated toward the centreline of the beam (dashed-dot line in Fig. 2.3a). Nevertheless, for the frictionless contact, u_x does not turn out to be influenced by the contribution of the term $\varphi\, z$, and along throughout contact are only contracted. A wedge-shaped of vertical displacements u_z is obtained in the Timoshenko beam, showing in perfect adhesion a maximum deflections 20% less than in frictionless contact. At the loaded cross-section, a discontinuity in the shear reaction for the perfect adhesion and a singularity in normal reaction for both contacts are shown in the Timoshenko beam theory. Axial force may be calculated in perfect adhesion only, the two beam theories show the same maximum value at the midspan and different shape along the beam. The same maximum shear force is obtained at the midspan, as well. With regard to the bending moment, the Timoshenko beam in perfect adhesion has the maximum value 60% less than that in frictionless.

The influence of normal stress at the midspan is analysed versus values of αL. A uniform mesh of 1024 elements can be used to accurately describe the normal reaction in perfect adhesion and in frictionless contact. Reporting in Fig. 2.4a, reactions $r_z(0)$ and $r_z(L/1024)$ versus αL for the Euler-Bernoulli and Timoshenko beam, respectively. Normal reactions of the two beams with $\alpha L < 1$ tend to those under the rigid punch. It is worth noting that the normal pressure of punch bonded to orthotropic half-plane is the same as in the case of isotropy which illustrated in the Chapter 1. Particular interest is dedicated to shear force at beam end, as shown Fig. 2.4b. Assuming several value of ϕ, it is noted that value of the Timoshenko beam tends to Euler-Bernoulli one with low ϕ, except in the neighbourhood. Moreover, the shear force takes opposite sign with beam having ϕ lower than 10^{-4} and in frictionless contact. That happens even in Euler-Bernoulli beam in perfect adhesion which, however, does not tends to zero.
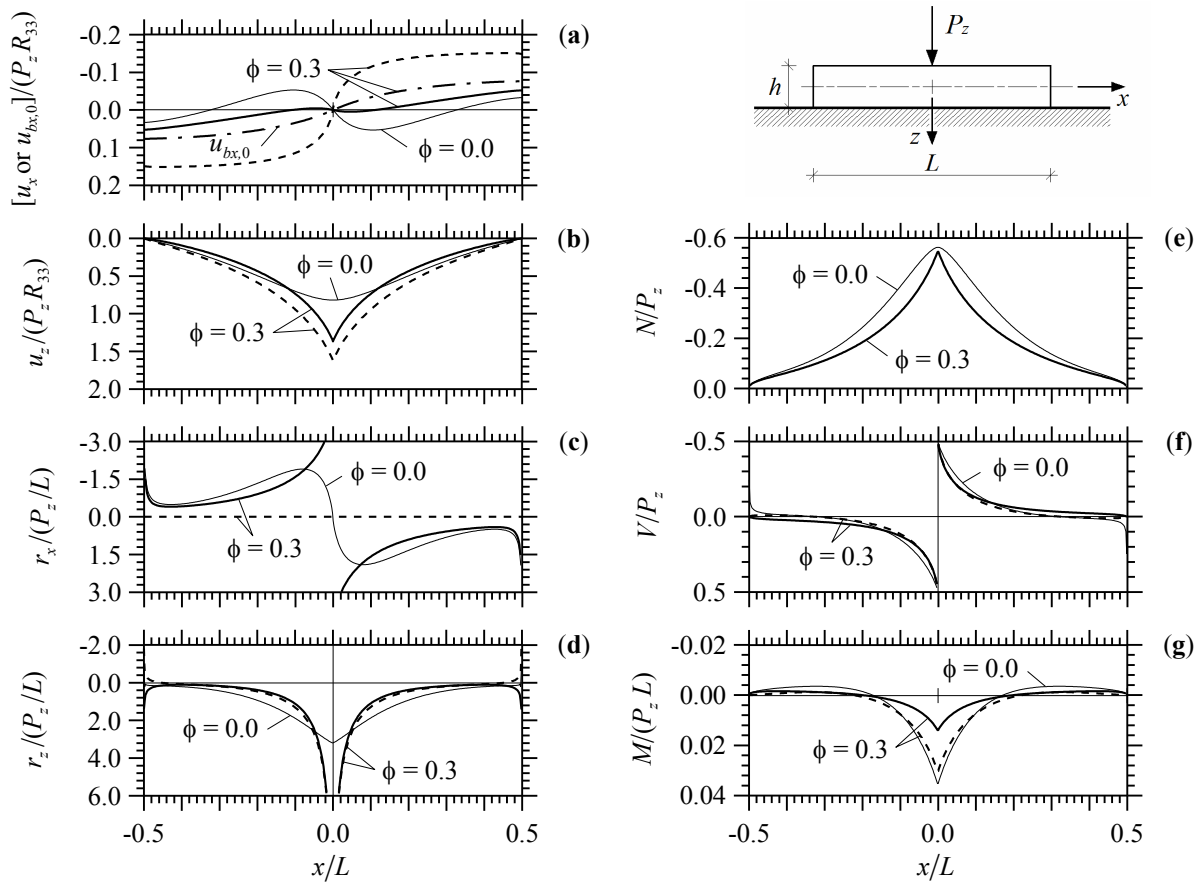
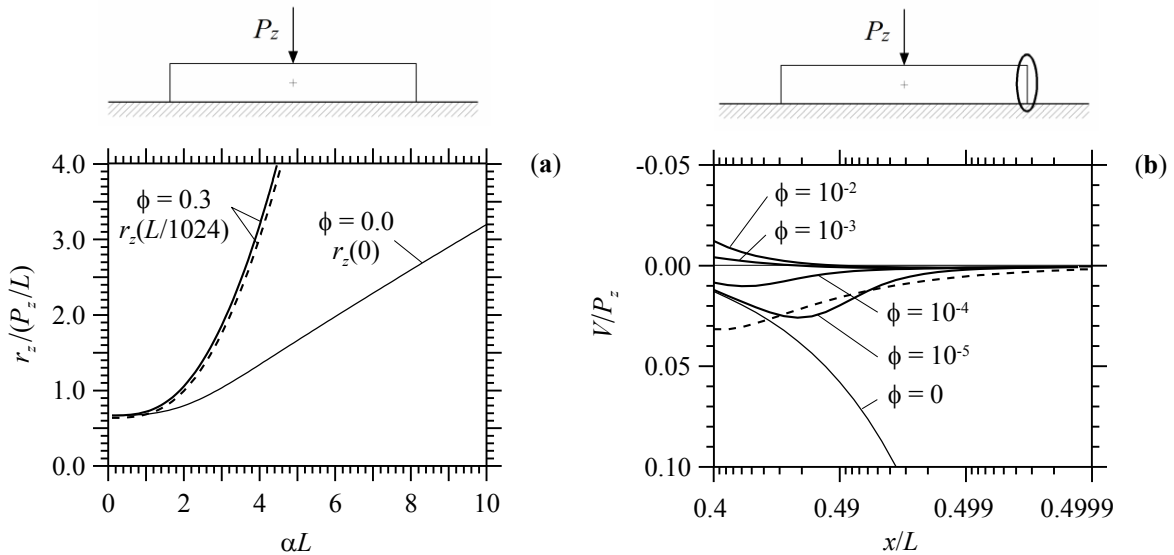Fig. 2.3. Beam ($L/h = 10$, $\alpha L = 10$) loaded by a vertical force P_z at the midpoint, bonded to an orthotropic half-plane ($c_1 = 0.56$; $c_2 = 3.08$; $c_3 = 0.30$). Timoshenko beam ($\phi = 0.3$) in perfect adhesion (thick solid line) and in frictionless contact (thick dashed line). Euler-Bernoulli beam in perfect adhesion (thin solid line). Nondimensional values of u_x (**a**), u_z (**b**), r_x (**c**), r_z (**d**), N (**e**), V (**f**), M (**g**) versus x/L. Horizontal displacement $u_{bx,0}$ (dash-dot line in **a**) refers to the centreline of the Timoshenko beam in perfect adhesion.

Fig. 2.4. Beam ($L/h = 10$) loaded by a vertical force P_z at midspan, bonded to an orthotropic half-plane ($c_1 = 0.56$; $c_2 = 3.08$; $c_3 = 0.30$) in perfect adhesion (solid line) and in frictionless contact (dashed line). Dimensionless pressure r_z at or in proximity the midpoint versus αL for $\phi = 0.0$ and 0.3 (**a**), shear force V at beam end ($\alpha L = 10$) with several value of ϕ (**b**).

74
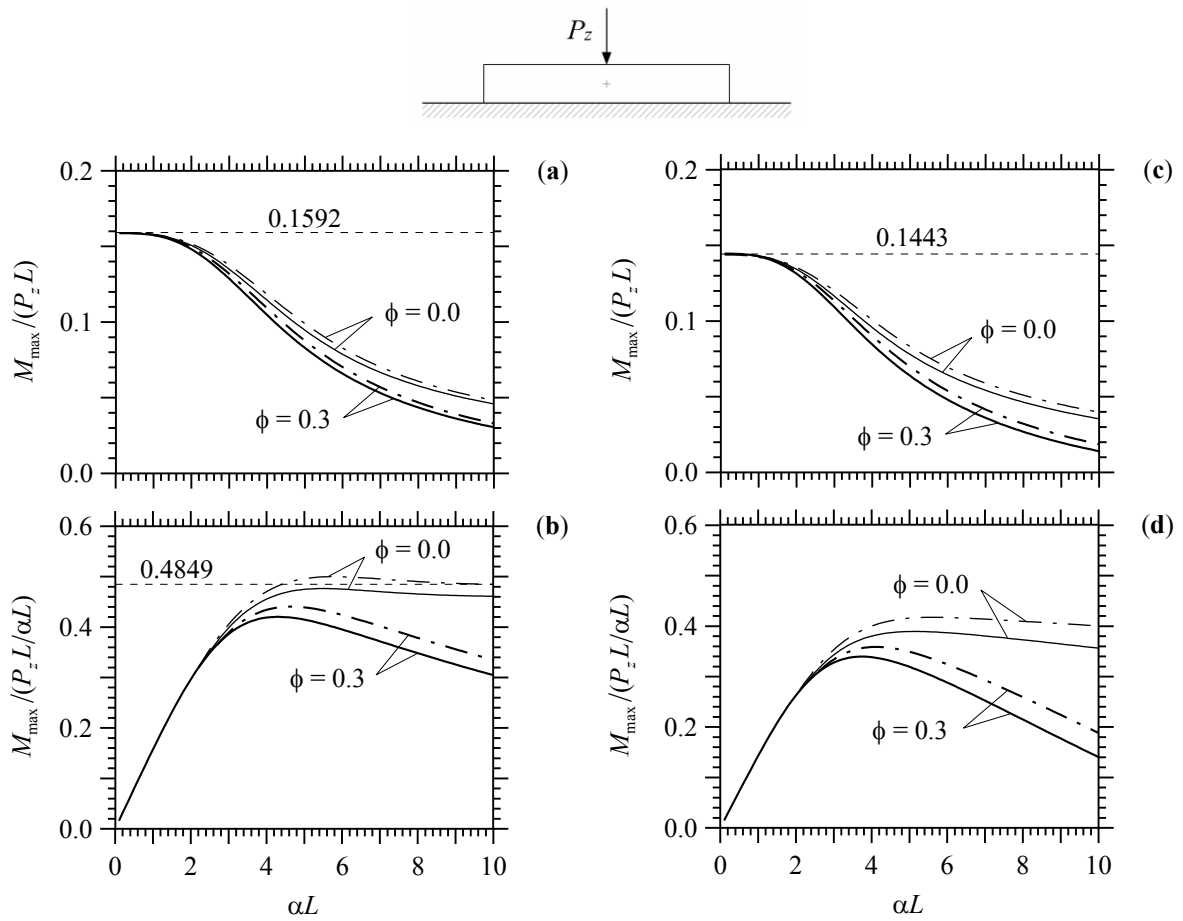
Fig. 2.5. Beam ($L/h = 10$) loaded by a vertical force P_z at the midpoint, bonded to an isotropic half-plane (dash-dot line) and an orthotropic half-plane with $c_1 = 0.56$; $c_2 = 3.08$; $c_3 = 0.30$ (solid line). Bending moment M at the midspan versus αL in frictionless contact (**a,b**) and in perfect adhesion (**c,d**) for $\phi = 0.0$ and $\phi = 0.3$ (thin and thick line respectively).

2.4.1.2 Maximum bending moment of rigid or flexible beam loaded by point force P_z

With regard to the relative stiffness beam-substrate αL, the maximum bending moment of both beam theories, Euler-Bernoulli ($\phi = 0.0$) or Timoshenko ($\phi = 0.03$), loaded by vertical point force P_z at midspan is illustrated in Fig. 2.5. An isotropic (dashed-dot line) or orthotropic (solid line) substrate is investigated with frictionless, Fig. 2.5a, b and perfect contact Fig. 2.5c, d.

In frictionless contact, the maximum bending moment, M_{max}, of a flat rigid indenter loaded by a vertical force P_z, may be calculated by integrating from 0 to $L/2$ the moment induced by the pressure r_z given by Sadowsky [4, 6] with respect to the midspan, namely

$$M_{max} = \int_0^{L/2} r_z \, x \, \mathrm{d}x = \frac{P_z L}{2\pi} \cong 0.1592 \, P_z \, L, \qquad (2.34)$$

where pressure is given by

$$r_z(x) = \frac{P_z}{\pi\sqrt{(L/2)^2 - x^2}}. \tag{2.35}$$

As shown in Fig. 2.5a, the maximum value of the bending moment for $\alpha L \leq 1$ agrees well with that predicted by Sadowsky solution. The magnitude of maximum bending moment decreases as αL increases, hence for flexible or long beams. According to Biot [43], the maximum bending moment of an infinite Euler-Bernoulli beam resting on isotropic substrate in frictionless contact reads

$$M_{max} = \frac{P_z a}{\pi} \int_0^\infty \frac{a}{a^3 + 1}\, da = \frac{2}{3\sqrt{3}} P_z a \cong 0.4849 \frac{P_z L}{\alpha L}, \tag{2.36}$$

where $a = \sqrt[3]{2}\, L/\alpha L$.

It is worth noting from Fig. 2.5b that the maximum bending moment, provided by Eq. (2.36), holds for $\alpha L > 10$. Conversely, for an infinite Timoshenko beam is not possible to obtain a constant value. Assuming an orthotropic substrate having tangential stiffness ten times more than that normal, the maximum bending moment of both beam theories results slightly lower than that in the isotropic case.

For the perfect adhesion condition, the maximum bending moment of a rigid flat punch loaded by a vertical force P_z, acting on an elastic isotropic substrate, could be obtained by integrating the normal and shear tractions given by Abramov [6]:

$$r_z(x) = \frac{1+\kappa}{\sqrt{\kappa}} \frac{P_z}{2\pi\sqrt{(L/2)^2 - x^2}} \cos\left(\frac{\ln\kappa}{2\pi} \ln\frac{L/2 + x}{L/2 - x}\right), \tag{2.37a}$$

$$r_x(x) = \frac{1+\kappa}{\sqrt{\kappa}} \frac{P_z}{2\pi\sqrt{(L/2)^2 - x^2}} \sin\left(\frac{\ln\kappa}{2\pi} \ln\frac{L/2 + x}{L/2 - x}\right), \tag{2.37b}$$

within the contact region $0 \leq x < L/2$ multiplied by their distance from the centroid of the rigid punch, as following

$$M_{max} = \int_0^{L/2} (r_z\, x - r_x\, h/2)\, dx \cong (0.1522 - 0.0795\, h/L)\, P_z\, L \cong 0.1443\, P_z\, L, \tag{2.38}$$

by assuming $L/h = 10$, $\kappa = 2.333$ that is $\kappa = (3 - \nu_s)/(1 + \nu_s)$ or $\kappa = 3 - 4\nu_s$ for a generalized plane stress or strain state with the Poisson coefficient of isotropic substrate ν_s equal to 0.2 or 0.167 respectively. As shown in Fig. 2.5c, Eq. (2.38) holds for both beams (Euler-Bernoulli and Timoshenko) bonded to an elastic isotropic or orthotropic substrate with $\alpha L \leq 1$. Finally, the maximum bending moment of a beam bonded to a substrate in perfect

adhesion is 10% lower than that found for a beam in frictionless contact because of the presence of tangential traction r_x. The analytic solution of M_{max} of infinite beam resting on substrate in perfect adhesion contact is not present in the literature. However, the numerical solution, displayed in Fig. 2.12d, shows a decrease in the maximum value of the bending moment, whereas for a beam in perfect adhesion ($\alpha L = 10$) is approximately 20% less than that found in the frictionless contact condition for both the beam theories.

2.4.1.3 Beam loaded by a horizontal point force P_x

A beam bonded to an elastic orthotropic substrate and subjected to a horizontal point force P_x at midspan and towards positive x-direction is studied in this Section. The comparison between Euler-Bernoulli and Timoshenko theories is investigated, though the solution of beam-substrate system does not significantly depend on parameter ϕ, as it has been mentioned in Chapter 1.

A Beam with $\alpha L = 10$ and a thin film (no bending rigidity) with equal cross-section corresponding to $\beta L = 0.83$, is reported in Fig. 2.6. Dimensionless interfacial displacements and substrate reactions are shown in perfect adhesion for the beam (solid line) and for the thin film (dashed line) versus x/L. The horizontal displacements of the bar (thin film) resting on orthotropic half-plane are reduced with regard to the beam-substrate system and are less than that the isotropic case, Fig. 2.6a. The same happens for vertical displacements, Fig. 2.6b. Furthermore at midspan, shear reaction r_x shows a singularity for the beam and bar, Fig. 2.6c, while normal reaction r_z shows a discontinuity only for the beam, Fig. 2.6d. The normal reactions along the bar are everywhere equal to zero.

The influence of the bending stiffness for axial force N of the beam proves not be particularly significant as shown Fig. 2.6e. Only shear force and bending moment of the beam in perfect adhesion may be calculated by the post-computation analysis, Fig. 2.6f and g respectively. Particular interest is dedicated for the shear force, showing along the beam different results with the choice of ϕ value, Fig. 2.7a. A peak is evident at the loaded point when the beam tends to the Euler-Bernoulli behaviour. Finally, shear force of Timoshenko beam becomes zero toward ends, turning out opposite sign when $\phi \leq 10^{-5}$, Fig. 2.7b.
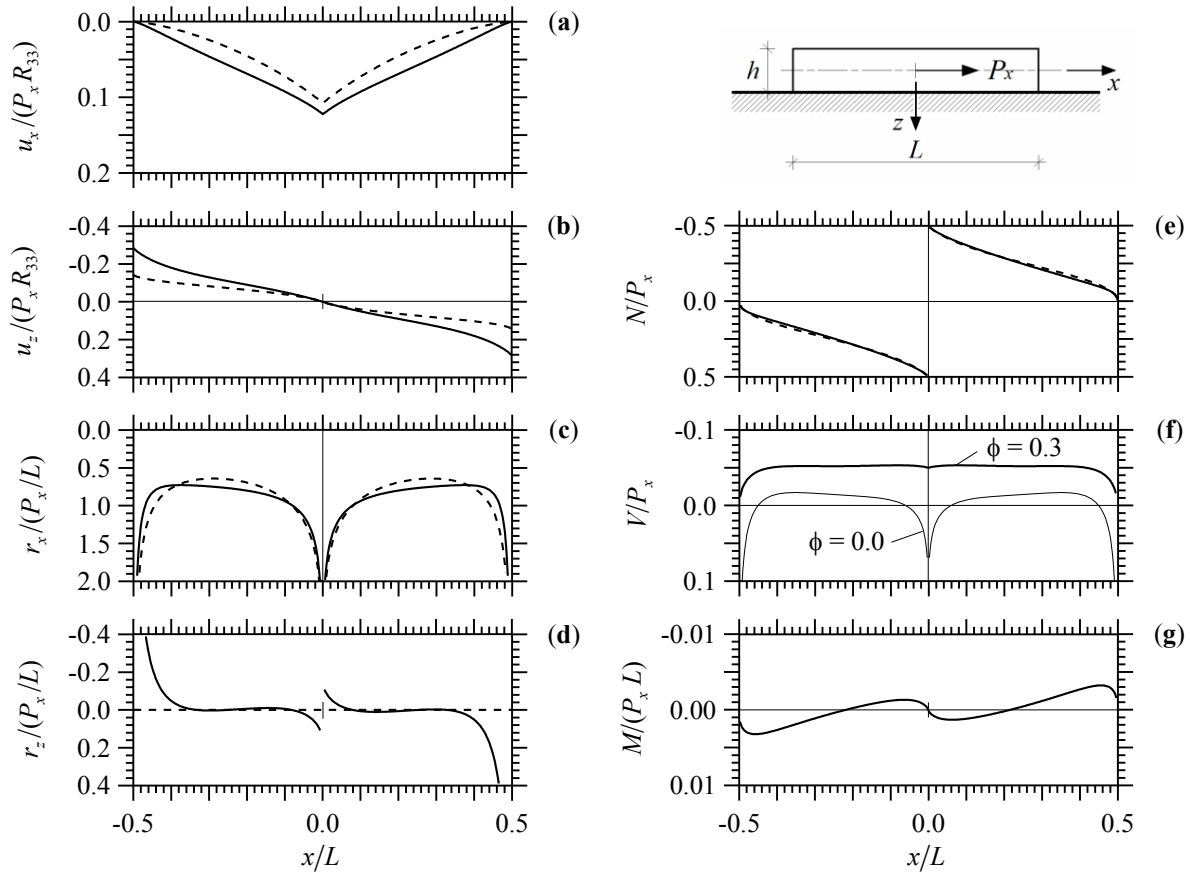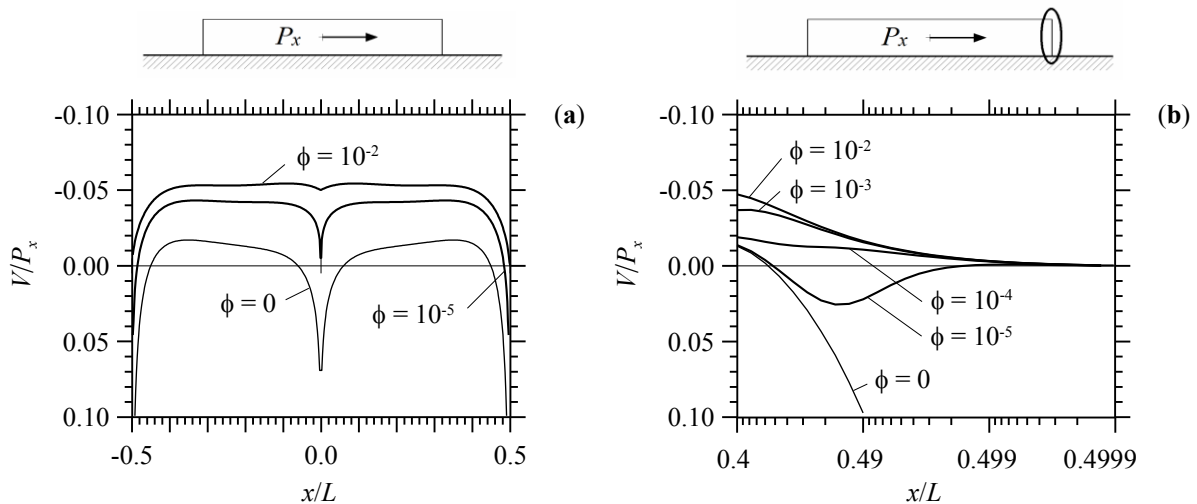
Fig. 2.6. Beam ($L/h = 10$) loaded by a horizontal force P_x at the midpoint, bonded to an orthotropic half-plane ($c_1 = 0.56$; $c_2 = 3.08$; $c_3 = 0.30$). Timoshenko beam ($\phi = 0.3$) in perfect adhesion $\alpha L = 10$ (thick solid line), and thin film $\beta L = 0.83$ (thick dashed line). Euler-Bernoulli beam in perfect adhesion (thin solid line). Dimensionless values of u_x (**a**), u_z (**b**), r_x (**c**), r_z (**d**), N (**e**), V (**f**), M (**g**) versus x/L.

Fig. 2.7. Beam ($L/h = 10$) loaded by a horizontal force P_x at the midpoint, bonded to an orthotropic half-plane ($c_1 = 0.56$; $c_2 = 3.08$; $c_3 = 0.30$) in perfect adhesion $\alpha L = 10$. Dimensionless shear force V along length of beam (**a**) and at one end (**b**) with several value of ϕ.

2.4.1.4 Beam loaded by a couple C

The beam loaded by a counter-clockwise couple C, resting on orthotropic half-plane has been investigated in Fig. 2.8, showing the case with an Euler-Bernoulli beam in perfect adhesion (thin solid line) and a shear-flexible beam having $\phi = 0.3$ in perfect adhesion (thick solid line) and frictionless contact (thick dashed line). When the beam is subjected to a couple at the midspan, horizontal and vertical displacements are symmetrical and antisymmetrical, respectively. Unlike from the case of beam loaded by vertical force.

The horizontal displacements at the surface boundary u_x are opposite sign than those at the centreline of the beam $u_{bx,0}$ (dot-dashed line) in a wide interval of x/L, confirming the strong relevance of term $\varphi\ h/2$, Fig. 2.8a. In the frictionless condition, the horizontal displacements tend always to contract along length L, with values quite similar to those calculated in perfect adhesion at the centreline of beam. The maximum horizontal interface displacement of the Timoshenko beam is approximately 60% higher than that computed with Euler-Bernoulli beam theory. With regard to vertical interface displacements u_z, the results in perfect adhesion are lower than those in frictionless contact, except close to ends, Fig. 2.8b. Although the shear deformations have a significant influence on displacements, tangential tractions r_x coincide with both beam theories, where everywhere is zero in the frictionless case, Fig. 2.8c.

The normal tractions r_z near the loaded point becomes meaningful with respect to influence of the shear beam and typology of contact, Fig. 2.8d. For both beams, axial force is plotted in Fig. 2.8e, shear force in Fig. 2.8f which shows a crucial role, and bending moment in Fig. 2.8g. Moreover, frictionless condition is reported in shear force and bending moment.

Using 1024 equal FEs, Fig. 2.9a shows the maximum pressure r_z at $-L/4 < x^* < 0$ versus the parameter $\alpha L \geq 5$ whereas no maximum pressure is present in the span for smaller values of αL. The normal pressures with Timoshenko beam (thick line) are smaller than those with Euler-Bernoulli beam (thin line). For both beams, the normal pressures in perfect adhesion (solid line) are higher than that in frictionless contact (dashed line). That different increases for flexible Timoshenko beams. Finally, Fig. 2.9b shows the shear force V in perfect adhesion and frictionless contact, following the numerical models based on logarithmically mesh generated in the interval $[0.4, 0.5-10^{-4}]$. Nevertheless the shear force behaviour in the frictionless case does not change significantly, while in perfect adhesion is strongly influence from choice of the shear deformations (ϕ) as already claimed.
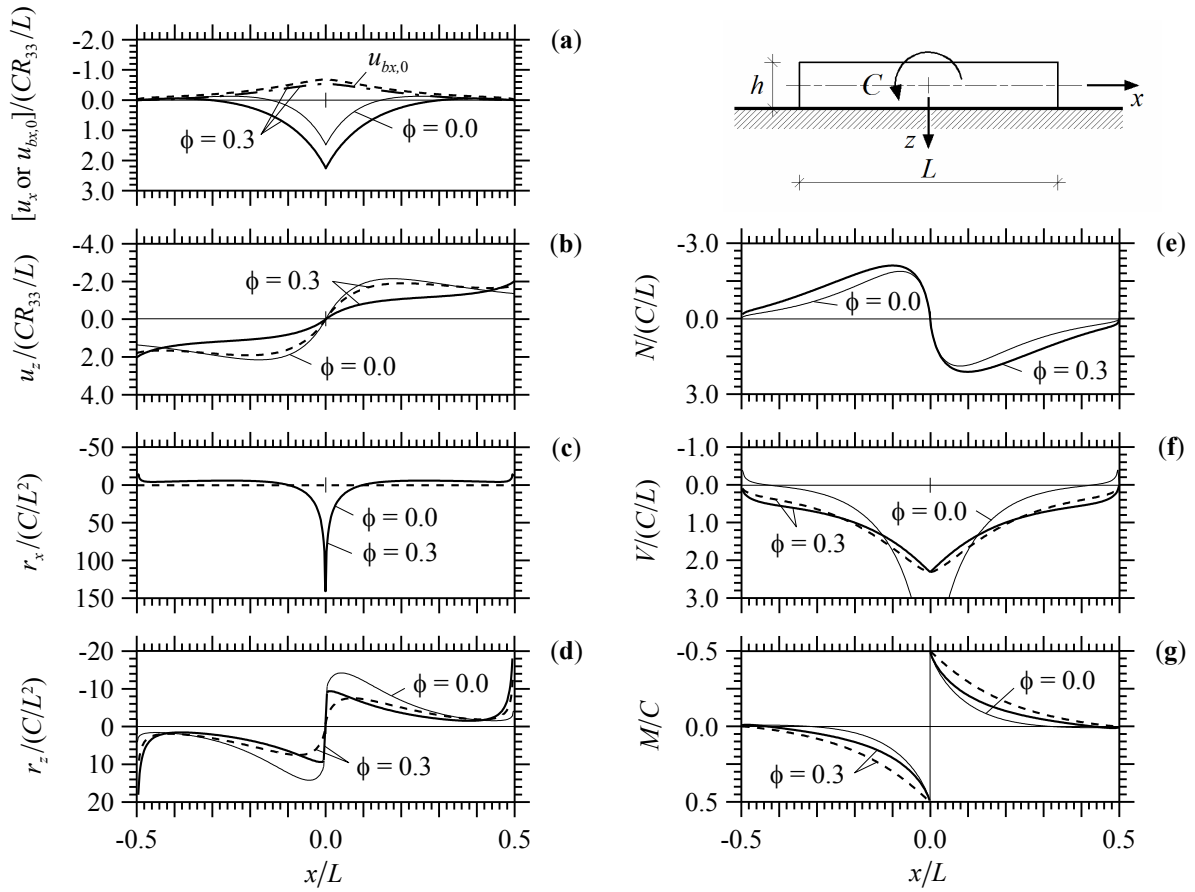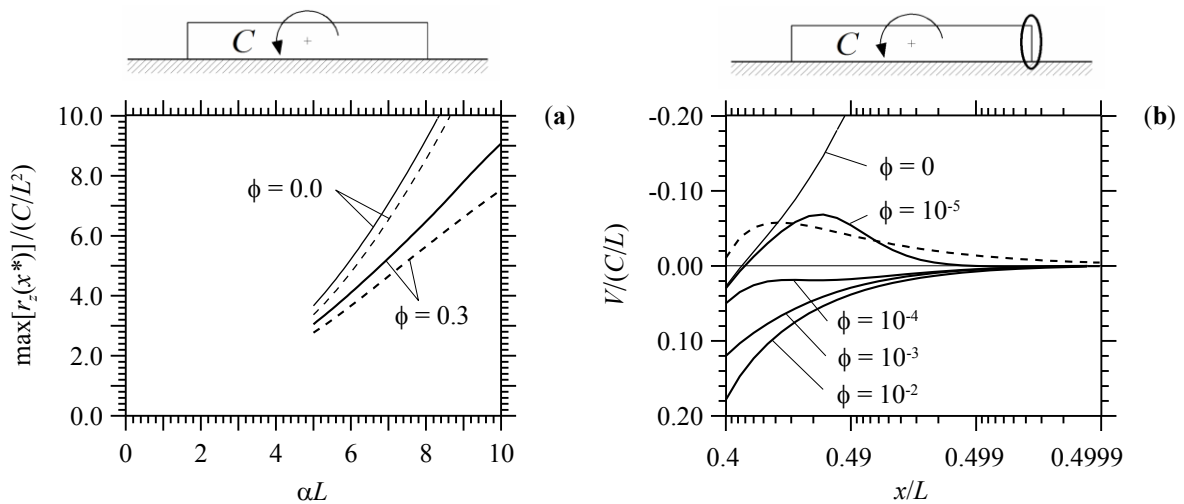
Fig. 2.8. Beam ($L/h = 10$, $\alpha L = 10$) loaded by a counter-clockwise couple C at the midpoint, bonded to an orthotropic half-plane ($c_1 = 0.56$; $c_2 = 3.08$; $c_3 = 0.30$). Timoshenko beam ($\phi = 0.3$) in perfect adhesion (thick solid line) and in frictionless contact (thick dashed line). Euler-Bernoulli beam in perfect adhesion (thin solid line). Dimensionless values of u_x (**a**), u_z (**b**), r_x (**c**), r_z (**d**), N (**e**), V (**f**), M (**g**) versus x/L. Horizontal displacement $u_{bx,0}$ (dash-dot line in **a**) refers to the centreline of the Timoshenko beam in perfect adhesion.

Fig. 2.9. Beam ($L/h = 10$) loaded by a counter-clockwise couple C at the midpoint, bonded to an orthotropic half-plane ($c_1 = 0.56$; $c_2 = 3.08$; $c_3 = 0.30$) in perfect adhesion (solid line) and in frictionless contact (dashed line). Dimensionless maximum pressure r_z at $0.25/L < x^* < 0$ versus αL obtained with $\phi = 0.0$ and 0.3 (**a**), shear force V at beam end ($\alpha L = 10$) with several value of ϕ (**b**).

2.4.2   Practical examples of stiffener-wood and foundation-soil interaction

Examples of practical meaning are considered in plane strain state, unless specified. A glass fibre reinforced polymer (GFRP) stiffener loaded by vertical concentrate force and bonded to a Balsa substrate. A concrete foundation subjected to vertical point force or uniform vertical pressure and resting on orthotropic soil. A peel test of a GFRP wholly bonded or partially detached to a Balsa orthotropic substrate. Subsequently, shear test of a GFRP reinforcement bonded to a wood substrate in perfect adhesion, with or without bending rigidity, and an aluminium reinforcement subjected to an uniform thermal variation, resting on different single wood substrate, are analysed. Finally, a study of a concrete foundation in perfect adhesion and or in frictionless contact subjected to couple at the midspan is investigated. In this case the horizontal displacement $u_{bx,0}$ of the centroidal beam axis has also been reported. The mechanical properties used in these examples have been found in the literature, i.e. wood and plywood [46], rock [47, 48], clay [49, 50] and sand [51, 52]. Elastic moduli and Poisson's coefficients are reported in Table 2.1 for beams (B1, B2, B3) and substrates (S1, S2, S3, S4, S5, S6). The coefficients of the substrate c_1, c_2, c_3 have been determined according to Eqs. (2.11) or (2.12).

	Beam			Substrate					
	GFRP T1	Concrete T2	Alum. T3	Balsa S1	Clay S2	Sand S3	Wood S4	S5	S6
E_1	40	30	70	0.05	0.24	0.18	10	24	5
E_3	10	30	70	4.0	0.12	0.23	1	1	1
E_2	-	-	-	0.2	0.24	0.18	-	-	-
G_{13}	5	12	26	0.15	0.06	0.07	1	2.7	0.3
ν_{13}	0.25	0.2	0.35	0.006	0.14	0.12	0.35	0.06	0.12
ν_{12}	-	-	-	0.165	0.18	0.19	-	-	-
ν_{23}	-	-	-	0.012	0.15	0.12	-	-	-
c_1	-	-	-	2.91	0.84	1.06	0.56	0.45	0.65
c_2	-	-	-	2.24	2.15	2.15	2.22	1.95	2.9
c_3	-	-	-	7.81	0.62	0.93	0.28	0.2	0.4

Table 2.1. Elastic moduli [GPa] and Poisson's coefficients of beams or substrates and coefficients c of half-plane.

2.4.2.1 GFRP stiffener loaded by P_z at midspan and bonded to Balsa substrate

The case of GFRP Timoshenko beam, with $L/h = 10$, $\alpha L = 106.4$ and $\phi = 0.001$, perfectly bonded to an elastic orthotropic half-plane having $c_1 = 2.91$, $c_2 = 2.24$, $c_3 = 7.81$, and loaded

by a vertical point force P_z acting at the midspan is reported in this Section. The adopted elastic modulus and Poisson's coefficients of the beam B1 and substrate S1 are listed in Table 2.1.

Dimensionless displacements and reactions along the substrate boundary are shown in Figs. 2.10a, b, and c, d, respectively. Dimensionless values of the axial force, shear force and bending moment along the beam are shown in Figs. 2.10e, f and g. The cases of a beam in perfect adhesion (solid line) and in frictionless contact (dashed line) are reported. The horizontal displacement u_x corresponding to the frictionless condition produces a contraction of the half-plane surface along the whole interface. Conversely, a different behaviour occurs in the case of a beam in perfect adhesion, owing to the fact that u_x is affected by the contribution of the term $\varphi\ h/2$ also. Indeed, in such a condition, Fig. 2.10a shows a non-monotonic trend for the horizontal displacement which changes its sign into a narrow central region (i.e. $-0.1 < x/L < 0.1$). At the beam ends, the horizontal displacement assumes a value 10 times lower than those found for the frictionless contact. The maximum value of the vertical displacement u_z is achieved at the midpoint ($x/L = 0$) and, in perfect adhesion, it results 20% lower than that found for a beam in perfect contact with the half-plane, as shown in Fig. 2.10b. For a beam in perfect adhesion, the tangential reaction r_x at $x/L = 0$ and at the beam ends exhibits a finite discontinuity, whereas it is equal to zero for a beam in frictionless contact, as reported in Fig. 2.10c. As expected, a singularity of normal reaction r_z at the midspan is found, as shown in Fig. 2.10d. Note also that the peel traction at the beam ends assumes different sign depending upon the contact condition. This aspect was already remarked in [31, 32]. The axial force of the beam in perfect adhesion is shown in Fig. 2.10e. Shear force and bending moment are not significantly affected by the contact condition, as displayed in Figs. 2.10f and g. An accurate description of the shear force is obtained using the beam T1 with $L/h = 40$, see Fig. 2.11. The comparison is made among an Euler-Bernoulli ($\phi = 0$) and two Timoshenko beams ($\phi = 10^{-2}$ and 10^{-5}) in perfect adhesion (solid line) and in frictionless contact (dashed line) versus the dimensionless coordinate x/L. The orthotropic substrate S1 is considered, leading to $\alpha L = 42.5$. Fig. 2.11a show that the shear force of a Timoshenko beam with small value of ϕ is analogous to that of an Euler-Bernoulli beam, except at the beam ends. The response in terms of shear force is analyzed in detail at the beam ends, using a logarithmically spaced mesh in the interval $[0.4, 0.5 - 10^{-4}]$, where a different behaviour between Euler-Bernoulli and Timoshenko beams is found.
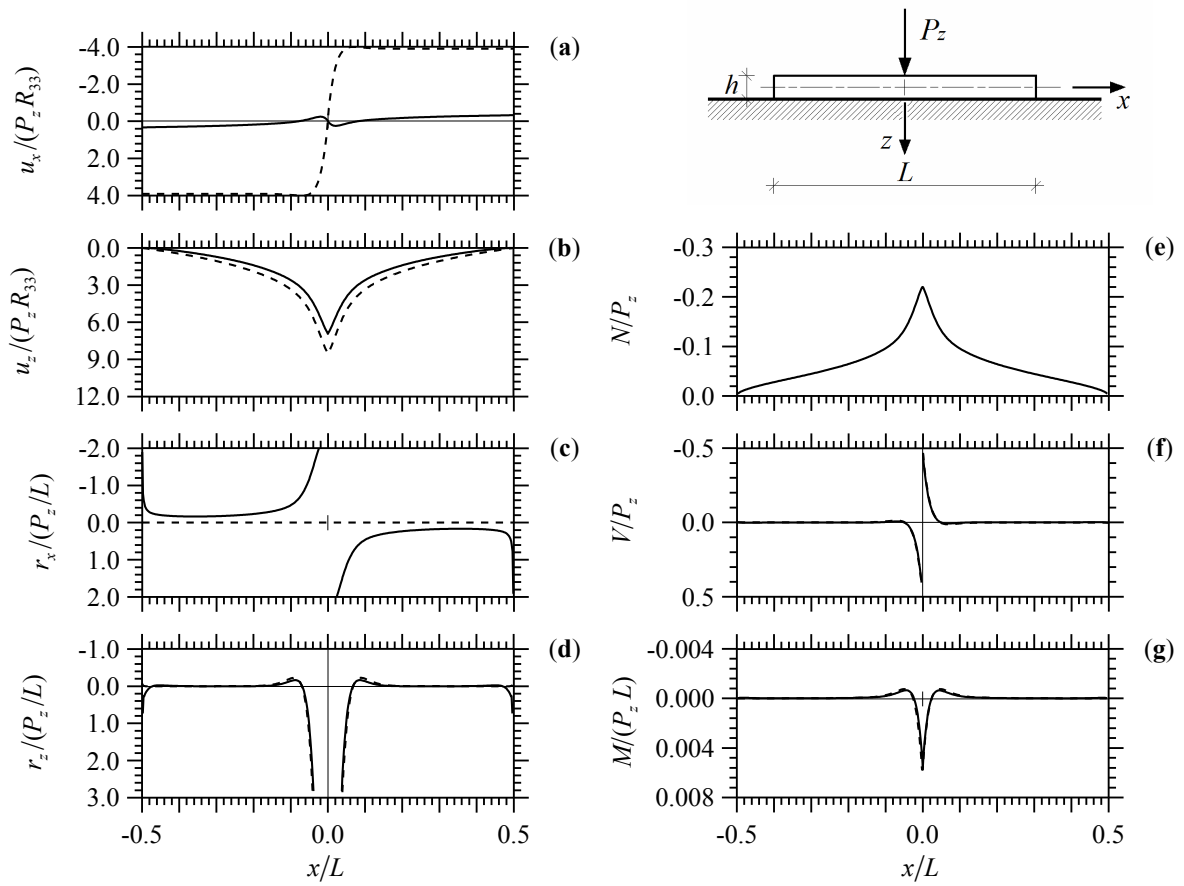
Fig. 2.10. GFRP Timoshenko beam ($L/h = 100$, $\alpha L = 106.4$ and $\phi = 0.001$) loaded by vertical force P_z at the midpoint and bonded to Balsa orthotropic half-plane in plane strain state ($c_1 = 2.91$; $c_2 = 2.24$; $c_3 = 7.81$) in perfect adhesion (solid line) and in frictionless contact (dashed line). Dimensionless values of u_x (**a**), u_z (**b**), r_x (**c**), r_z (**d**), N (**e**), V (**f**), M (**g**) versus x/L.
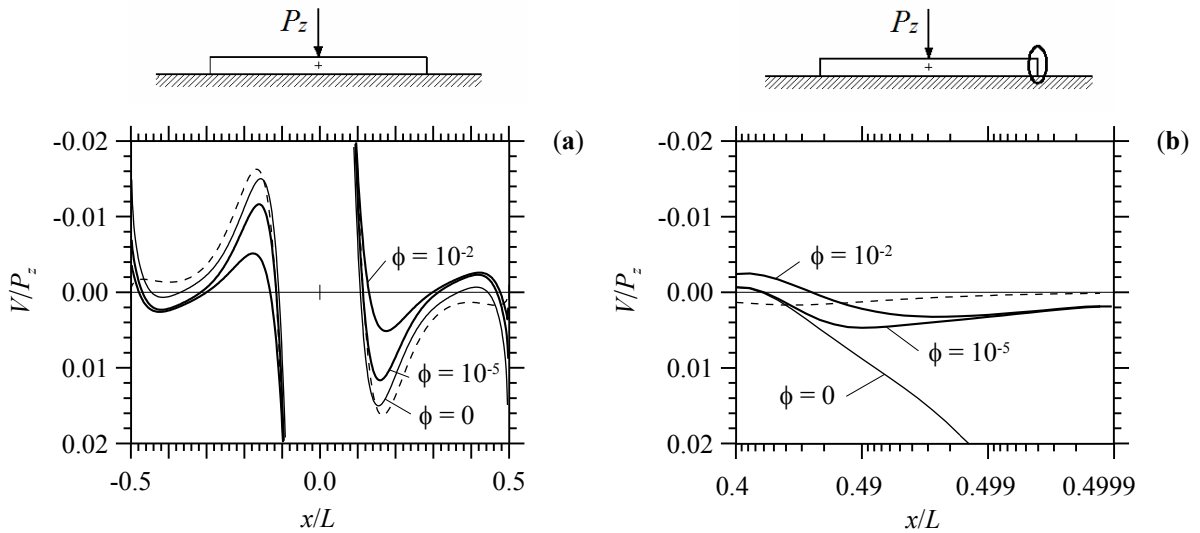
Fig. 2.11. GFRP Euler-Bernoulli ($\phi = 0$) and Timoshenko beam ($\phi = 10^{-2}$ and 10^{-5}) with $L/h = 40$ loaded by a vertical force P_z at the midpoint and bonded to Balsa orthotropic half-plane in plane strain state ($c_1 = 2.91$; $c_2 = 2.24$; $c_3 = 7.81$) in perfect adhesion $\alpha L = 42.5$ (solid line) and in frictionless for a GFRP Euler-Bernoulli beam (dashed line). Shear force V along length of beam along the beam (**a**) and at the beam end (**b**).

In particular, a singularity of the shear force for the Euler-Bernoulli beam is observed (see Fig. 2.11b). Conversely, for beams in the frictionless contact with the half-plane, the shear force does not depend significantly on the kind of beam adopted, and it assumes vanishing values at the beam ends.

2.4.2.2 Maximum bending moment of foundations loaded by P_z at midspan and resting on soils

The maximum bending moment of concrete beams resting on an elastic medium is a key issue in the framework of civil engineering, with particular reference to the design of shallow foundation of buildings. A Euler-Bernoulli ($\phi = 0.0$) or Timoshenko ($\phi = 0.03$) concrete foundation beam, loaded by a vertical point force P_z at the midspan, and resting on an isotropic or orthotropic soil is considered. Dimensionless maximum bending moment at $x/L = 0$ versus αL is reported for a beam in frictionless contact (Figs. 2.12a, b) and in perfect adhesion (Figs. 2.12 c, d), respectively. The elastic parameters $c_1 = 0.84$, $c_2 = 2.15$, $c_3 = 0.62$, and $E_3 = 0.12$ MPa are taken for the orthotropic soil (solid line), while the same Young's modulus is assumed (dash-dot line) for the isotropic soil. Table 2.1 shows the elastic modulus and Poisson's coefficients of the adopted beam T2 and soil S2.

The results are compared with some analytic solutions, as previously mentioned. The maximum bending moment of a rigid indentation loaded by a vertical point force and resting isotropic or orthotropic soil is about $M_{\max} = 0.1592\ P_z\ L$ in frictionless contact and about $M_{\max} \approx 0.1443\ P_z\ L$ in perfect contact. While the maximum bending moment of an infinite Euler-Bernoulli beam resting on isotropic substrate in frictionless contact is given by Biot [43], $M_{\max} \approx 0.4849\ P_z\ L/\alpha L$, assuming $\kappa = 2.44$ that is $\kappa = (3 - \nu_s)/(1 + \nu_s)$ or $\kappa = 3 - 4\nu_s$ for a generalized plane stress or strain state with the Poisson coefficient of isotropic substrate ν_s equal to 0.16 or 0.14 respectively. Note that for $\alpha L > 5$, the maximum bending moment obtained by considering the orthotropic half-plane results about 5% or 10% lower than that obtained for an isotropic substrate, respectively in frictionless or perfect contact. Whereas the analytic solution could be applied for rigid and short beam having $\alpha L \leq 1$.
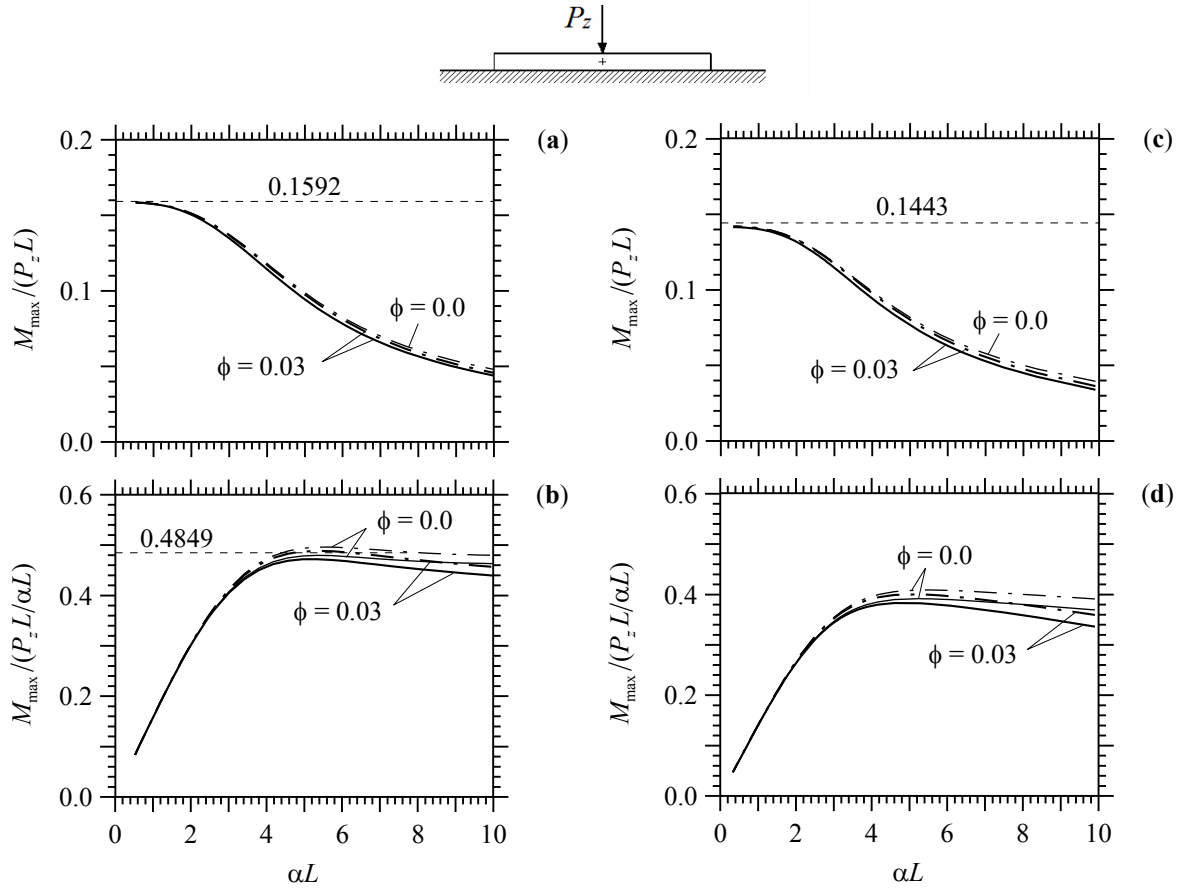
Fig. 2.12. Concrete beam loaded by a vertical force P_z at the midpoint, bonded to an orthotropic soil with $c_1 = 0.84$; $c_2 = 2.15$; $c_3 = 0.62$; $E_3 = 0.12$MPa (solid line) and isotropic soil (dash-dot line). Bending moment M at the midspan versus αL in frictionless contact (**a,b**) and in perfect adhesion (**c,d**) for $\phi = 0.0$ and $\phi = 0.03$ (thin and thick line respectively).

2.4.2.3 Foundation loaded by a vertical pressure p_z over length L/4 at midspan

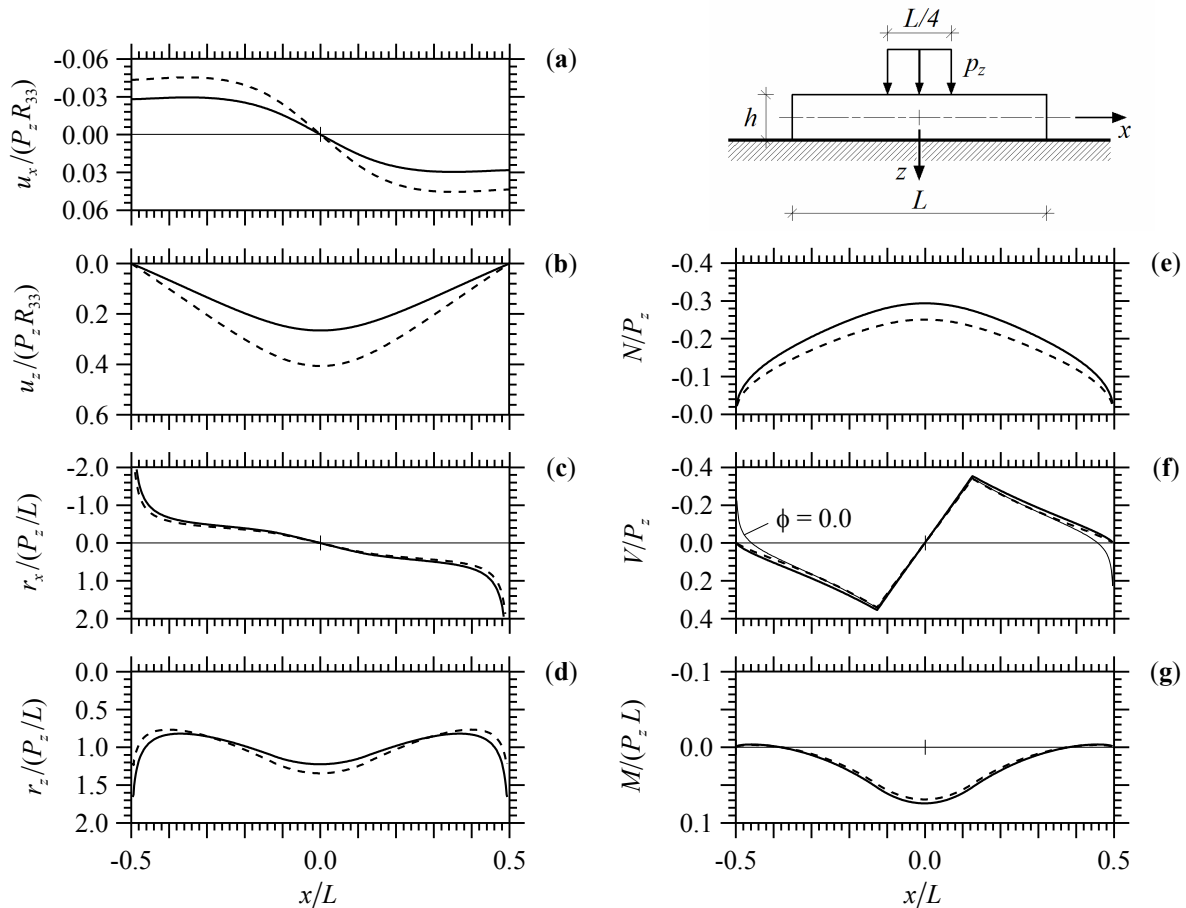In this Section, the case of a Timoshenko beam subjected to a uniform vertical load distribution p_z acting over a length $L/4$ centered with respect to the midspan is analysed. Dimensionless interface displacements, soil reactions, and axial force, shear force, and bending moment along the beam, are reported in Fig. 2.13. Two kinds of orthotropic soil in perfect adhesion with the beam are studied, assuming the elastic modulus and Poisson's coefficient of concrete beam T2, and clay S2 or sand soil S3 listed in Tab. 2.1. The soil coefficients are $c_1 = 0.84$, $c_2 = 2.15$, $c_3 = 0.62$ for clay soil or $c_1 = 1.06$, $c_2 = 2.15$, $c_3 = 0.93$ for sand soil. Thus, assuming a ratio $L/h = 10$ for the beam, the parameter αL becomes equals 3.65 or 4.54, respectively.

Displacement u_x and u_z at the substrate boundary for perfect adhesion condition are reported in Fig. 2.13a and b respectively, for both soils. It is worth noting that for a beam resting on a relatively rigid soil, (i.e. $\alpha L = 4.54$, dashed line), the horizontal interface

displacement at the beam end and vertical interface displacement at $x/L = 0$ are 30% and 60% higher, respectively, than those calculated for a beam bonded to a relatively soft soil (i.e. $\alpha L = 3.65$, solid line), whereas both substrate reactions are quite similar, as shown in Fig. 2.13c and d. Conversely, axial force of the beam resting on the relatively rigid soil (Fig. 2.13e, dashed line) is about 15% lower than that obtained by considering a soft soil. However, almost the same values for the shear force and bending moment along the beam are found for both the orthotropic soils. The shear force obtained by considering the Euler-Bernoulli beam ($\phi = 0.0$) with $\alpha L = 3.65$ in perfect adhesion with the soil is also displayed in Fig. 2.13f (thin solid line). It is worth noting that, in this case, a completely different behaviour of the shear force is observed going toward the beam ends, with respect to that found for the Timoshenko beam. In particular, the shear force for an Euler-Bernoulli beam takes non zero values, having opposite sign with respect those obtained by considering a Timoshenko beam.

Fig. 2.13. Concrete beam subjected to a uniform vertical load distribution p_z acting over a length $L/4$ centered with respect to the midspan, resting on an orthotropic soil. Timoshenko beam ($L/h = 10$, $\phi = 0.03$) bonded to two kinds orthotropic half-planes in perfect adhesion, $c_1 = 0.84$; $c_2 = 2.15$; $c_3 = 0.62$; $\alpha L = 3.65$ (solid line) and $c_1 = 1.06$; $c_2 = 2.15$; $c_3 = 0.93$; $\alpha L = 4.54$ (dashed line). Shear force V of an Euler-Bernoulli beam bonded to a half-plane with $c_1 = 0.84$; $c_2 = 2.15$; $c_3 = 0.62$; $\alpha L = 3.65$ (thin solid line in **f**).

2.4.2.4 Detached GFRP stiffener loaded by P_z at one end

A glass fibre reinforcement polymer (GFRP) subjected to vertical point force P_z applied at one end upward directed, bonded to a Balsa orthotropic substrate in perfect adhesion is investigated. Elastic modulus and Poisson's coefficients are reported in Tab. 2.1 for the beam (T1) and substrate (S1).

Dimensionless interfacial displacements and substrate reactions are show in Figs. 2.14a-d, whereas the axial force, shear force and bending moment are displayed in Fig. 2.14e-g, for a beam detached from the substrate between $x/L = 0.3$ and $x/L = 0.40$ (solid line) and a fully bonded beam (dashed line). For the detached beam, a number of 297 logarithmically spaced FEs are used, and the length of the beam has been subdivided in 4 intervals to capture straightforwardly the stress singularity. Thus a number of 84 logarithmically spaced points are generated in the intervals $[-0.5+10^{-8}, -0.1]/L$, 85 points into $[-0.1, 0.3]/L$, 65 points into $[0.4, 0.45]/L$, and 64 points into $[0.45, 0.5-10^{-8}]/L$.
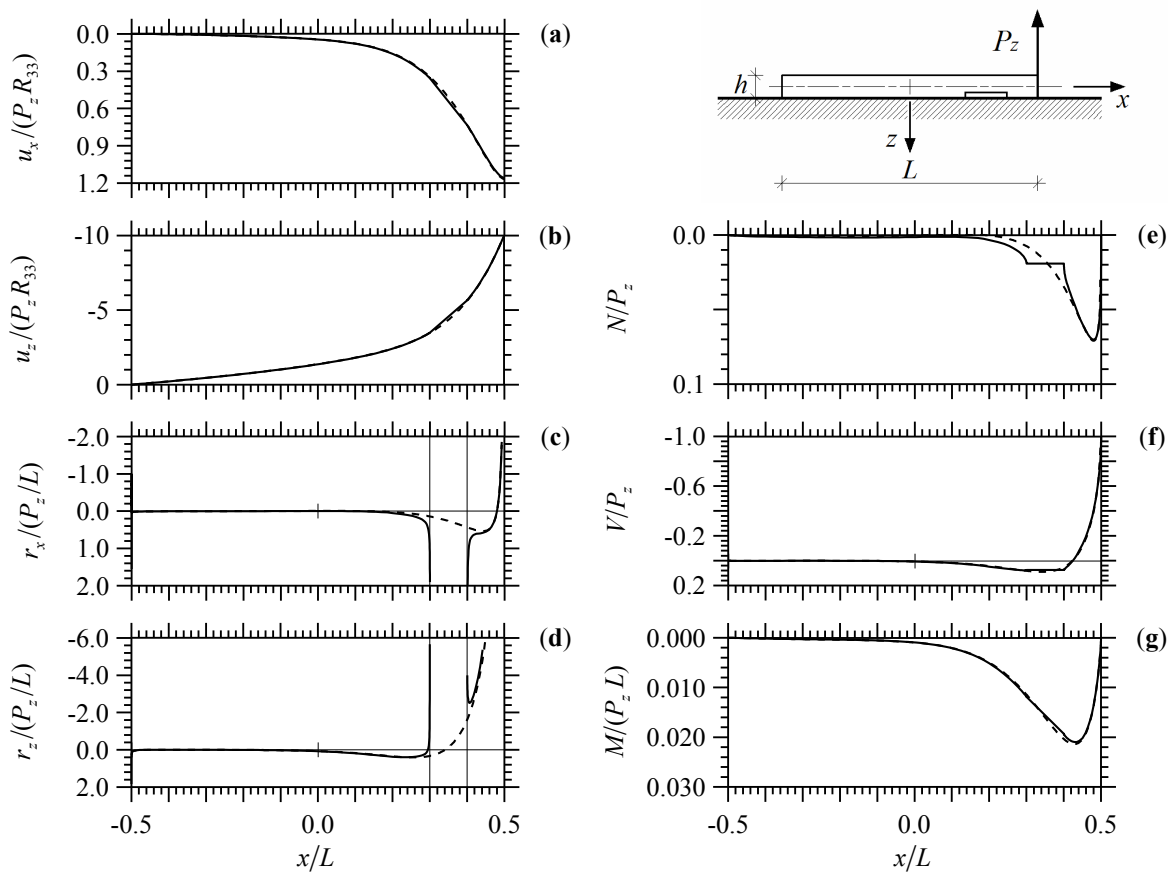
Fig. 2.14. GFRP Timoshenko beam ($L/h = 20$, $\alpha L = 21.3$ and $\phi = 0.02$) loaded by a vertical force P_z acting at a beam end and detached between $x/L=0.3$ and $x/L = 0.4$ (solid line) and perfect bonded (dashed line) to Balsa orthotropic half-plane in plane strain state ($c_1 = 2.91$; $c_2 = 2.24$; $c_3 = 7.81$). Dimensionless values of u_x (a), u_z (b), r_x (c), r_z (d), N (e), V (f), M (g) versus x/L.

The result of the detached beam is almost identical to those obtained for the fully bonded beam, except in the neighbourhood of the detached region. In particular, at the ends of the detached region both the shear and peel stresses appear to be singular. As expected, zero substrate reaction and constant axial force are found within the detached region.

2.4.2.5 GFRP stiffener loaded by P_x at one end and bonded to wood substrate

The case of an elastic Timoshenko beam T1 loaded by a horizontal concentrated force acting at one end, perfectly bonded to a wood substrate S4 is analysed and compared with a beam having a vanishing bending rigidity (thin film assumption) in Fig. 2.15. Plane stress state is assumed with ratio $L/h = 60$. The governing parameter for the beam is $\alpha L = 40.2$ (solid line), whereas $\beta L = 1.50$ (dashed line) holds for the membrane assumption. Dimensionless interface displacements or substrate reactions for both cases are similar, except the normal component of the interfacial stress field, which is zero within the whole contact region for the case of a thin film. It is worth noting that the normal component of the displacement quickly grows going toward the ends of the stiffener, particularly for the case of the Timoshenko beam. Note also that the peel stress changes its sign in the neighbourhoods of the beam ends, similarly to the case of a beam loaded by a vertical pointwise force acting at the midspan (see Fig. 2.10d). Moreover, a peak value for the peel stress occurs in the neighbouring of the load section, as shown in Fig. 2.15d. Besides, the shear force and the bending moment could be found for the beam case only. However, the solution of the beam-substrate interaction problem where only horizontal forces act on the system do not appreciably depend on the parameter ϕ [32]. Hence, concerning this loading condition, the choice of Euler-Bernoulli or Timoshenko beam model leads to almost the same results.

Conversely, the shear force is significantly affected by the shear deformation of the beam. This fact has been found by investigating a Timoshenko beam loaded by a horizontal pointwise force acting at one end of the beam varying the parameter ϕ. In particular, an Euler-Bernoulli beam ($\phi = 0$) and a Timoshenko beam with $\phi = 10^{-2}$ and 10^{-5} have been studied in detail. Fig. 2.16 shows the shear force along the beam and in the neighbourhood of the external force. As expected, the shear force of a Timoshenko beam with small ϕ tends to that of an Euler-Bernoulli beam. However, the main differences occur in the neighbourhood of the loaded section, where the shear force of the Euler-Bernoulli beam takes opposite sign and does not vanish at the beam ends.
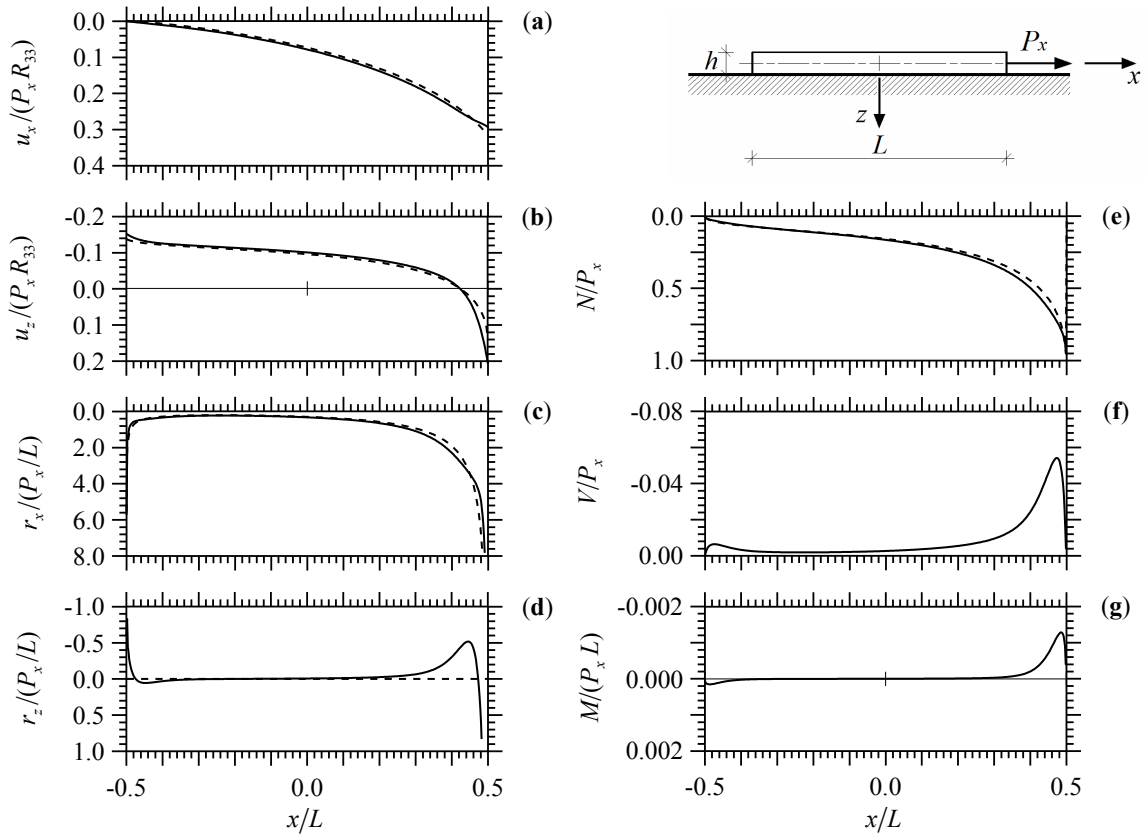
Fig. 2.15. GFRP Timoshenko beam ($L/h = 60$ and $\phi = 0.003$ with $c_1 = 0.70$; $c_2 = 2.40$; $c_3 = 0.44$) loaded by a horizontal force P_x acting at one end and bonded to wood orthotropic half-plane in plane stress state ($c_1 = 0.56$; $c_2 = 2.22$; $c_3 = 0.28$) with $\alpha L = 40.2$ (solid line), and thin film assumption with $\beta L = 1.50$ (dashed line). Dimensionless values of u_x (a), u_z (b), r_x (c), r_z (d), N (e), V (f), M (g) versus x/L.
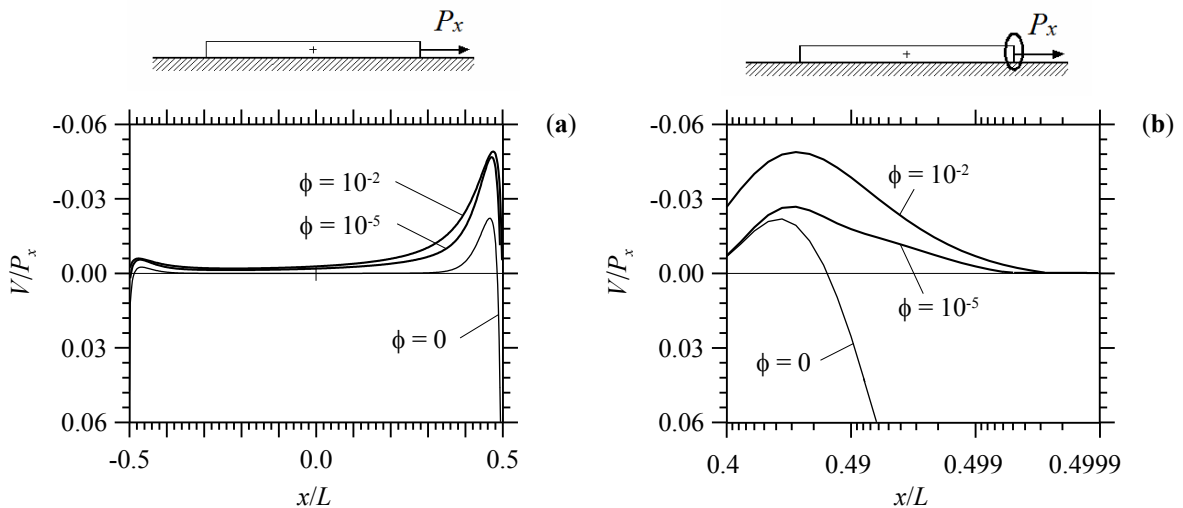

Fig. 2.16. GFRP Euler-Bernoulli ($\phi = 0$) and Timoshenko beams ($\phi = 10^{-2}$ and 10^{-5}) with $L/h = 60$ loaded by horizontal force P_x acting at one end and bonded to a wood orthotropic half-plane in plane stress state ($c_1 = 0.56$; $c_2 = 2.22$; $c_3 = 0.28$) with $\alpha L = 40.2$. Shear force V along the beam (a) and at the beam end (b).

On the other hand, the shear force of a Timoshenko beam at the loaded section vanishes, and going toward the inner part of the contact region, it increases in magnitude as the parameter ϕ increases. Note also that the maximum value achieved by the shear force of a Timoshenko beam occurs at about $0.47 \div 0.48\ x/L$, whereas in an Euler-Bernoulli beam it occurs in the range $0.46 \div 0.47\ x/L$.

2.4.2.6 Aluminium stiffener subject to uniform thermal load ΔT and bonded wood substrate
The behaviour of a beam resting on an elastic substrate and subjected to a uniform thermal variation ΔT, resembles that of a beam symmetrically loaded by two opposite axial forces applied at the beam ends, as shown for the bar-substrate problem [33]. The interaction between an aluminium stiffener and a wood substrate is investigated. The Euler-Bernoulli beam theory is assumed and two kinds of orthotropic half-plane are studied, as shown in Fig. 2.17. The elastic moduli and Poisson's coefficients of the beam T3 and the substrates S5 or S6 are listed in Table 2.1. In particular, two kinds of half-plane having the same Young modulus in z-direction and characterised by $c_1 = 0.45$, $c_2 = 1.95$, $c_3 = 0.20$ (S5, solid line), and $c_1 = 0.65$, $c_2 = 2.90$, $c_3 = 0.40$ (S6, dashed line) are considered. Therefore, by taking a length-to-height ratio $L/h = 10$, both cases are characterized by $\alpha L = 60$.

Dimensionless interface displacements and substrate reactions versus x/L are plotted in Fig. 2.17a, b and c, d, respectively. The axial force, shear force and bending moment of the beam are shown in Fig. 2.17e, f and g. It is worth remarking that the substrate S5 having a high elastic stiffness in x-direction higher (solid line) exhibits a horizontal component of the interfacial displacement 25% lower than that found for the substrate S6 (dashed line). Conversely, the vertical component of the interfacial displacement is 60% higher with respect that exhibited by the wood substrate S6. On the other hand, shear and normal components of the interfacial stress field for a substrate having a low value of Young modulus in x-direction (namely, the substrate S6), are quite uniform along the beam, with relatively low peak values attained at the beam ends, see Fig. 2.17c, d. This circumstance holds for the axial force, shear force and bending moment also, which magnitude decrease by assuming the wood substrate S6. Note also that the peel tractions change sign in the range $0.3 \div 0.4\ x/L$ for both the substrates. For comparison, in Fig. 2.17f is plotted the shear force of a Timoshenko beam ($\phi = 0.03$) also, which vanishes at the end sections, as expected. Similarly to the previous loading condition, also for the case of a uniform thermal variation, the shear force of an Euler-Bernoulli beam in the neighbourhoods of the beam ends change its sign with respect that found for a Timoshenko beam.
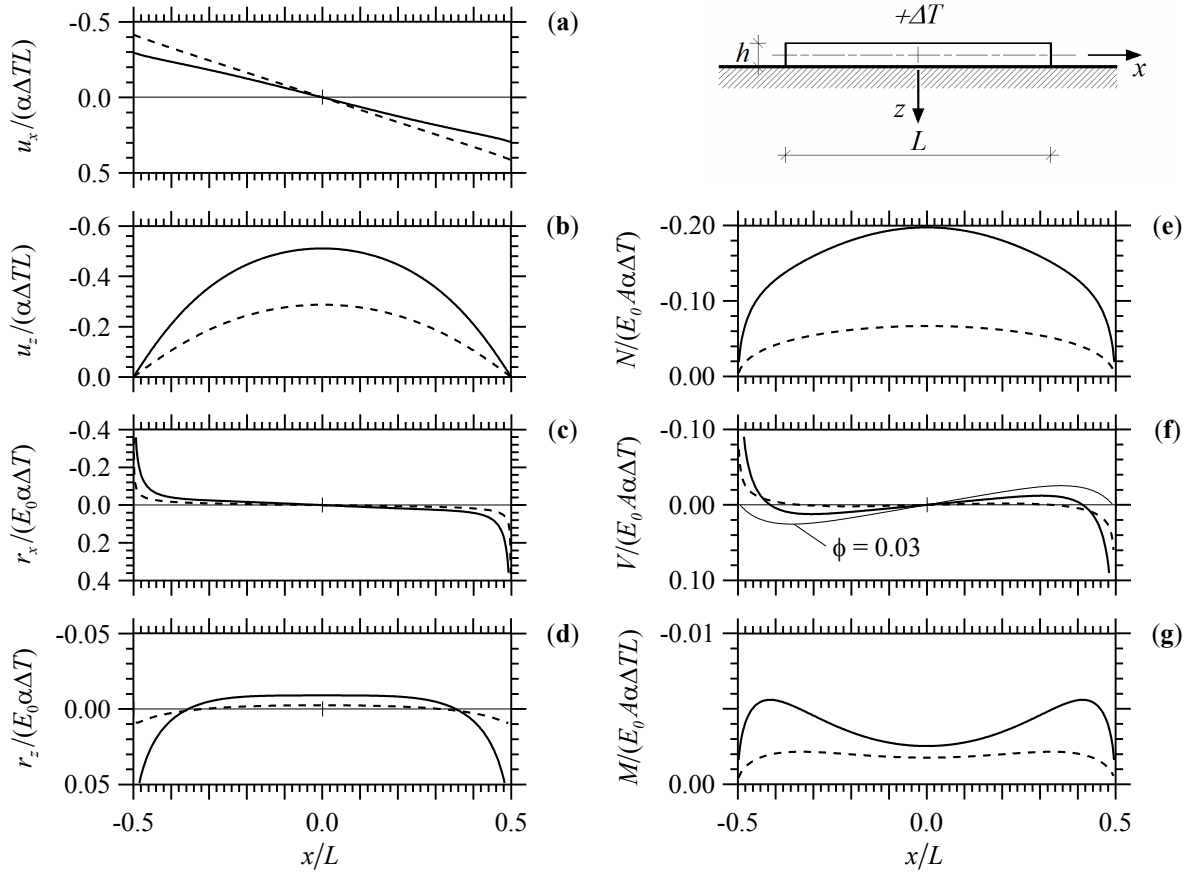
Fig. 2.17. Aluminium stiffener subjected to a uniform thermal variation $+\Delta T$ bonded to a wooden substrate. Euler-Bernoulli beam ($L/h = 10$, $\alpha L = 60$) resting on two kinds of orthotropic half-plane with $c_1 = 0.45$; $c_2 = 1.95$; $c_3 = 0.20$ (solid line) and $c_1 = 0.65$; $c_2 = 2.90$; $c_3 = 0.40$ (dashed line) in perfect adhesion. Dimensionless values of u_x (**a**), u_z (**b**), r_x (**c**), r_z (**d**), N (**e**), V (**f**), M (**g**) versus x/L. Shear force V of a Timoshenko beam ($\phi = 0.03$) bonded to half-plane with $c_1 = 0.45$; $c_2 = 1.95$; $c_3 = 0.20$ (thin solid line in **f**).

2.4.2.7 Foundation loaded by C at midspan and bonded to soil

A concrete foundation loaded by a counter-clockwise couple C acting at midspan and resting on orthotropic soil is investigated in this Section. Fig. 2.18 shows the results of a Timoshenko beam T2 with $L/h = 10$, $\phi = 0.03$ in perfect adhesion (solid line) and in frictionless contact (dashed line) with an orthotropic soil S5 having $c_1 = 0.84$, $c_2 = 2.15$, $c_3 = 0.62$.

The horizontal component of the interfacial displacement of a Timoshenko beam perfectly welded to the half-plane assumes an opposite sign and values lower (in modulus) than those found for a beam in frictionless contact, as displayed in Fig. 2.18a. In the same figure is plotted the displacement at the centreline $u_{bx,0}$ of of a beam perfectly bonded to the substrate, thus confirming the relevance of the term $\varphi \, h/2$ affecting the horizontal component of the displacement field. The vertical component of the interfacial

displacement of a beam in perfect adhesion is almost the same of that of a beam in frictionless contact, as shown in Fig. 2.18b. The same circumstance holds for the peel traction except at the loaded section, where the peel traction of a Timoshenko beam in perfect adhesion with the half-plane exhibits a discontinuity. As expected, the shear reaction and, in turn, the normal force along the beam are zero when frictionless contact is supposed. It is worth noting that the shear traction of a Timoshenko beam in perfect adhesion with the half-plane is singular across the loaded section. The axial force, shear force and bending moment of the beam are shown in Fig. 2.18e, f and g, respectively. Note that the axial force attains the maximum value at about 0.3 x/L and, owing to symmetry, it vanishes at $x = 0$. Moreover, the shear force and bending moment are not significantly affected by the contact condition. For both the contact conditions here considered, the maximum value achieved by the shear force turns out to be 1.5 C/L and it occurs at $x = 0$. Moreover, $|M(0^{+})| = |M(0^{-})| = C/2$, as expected due to symmetry.
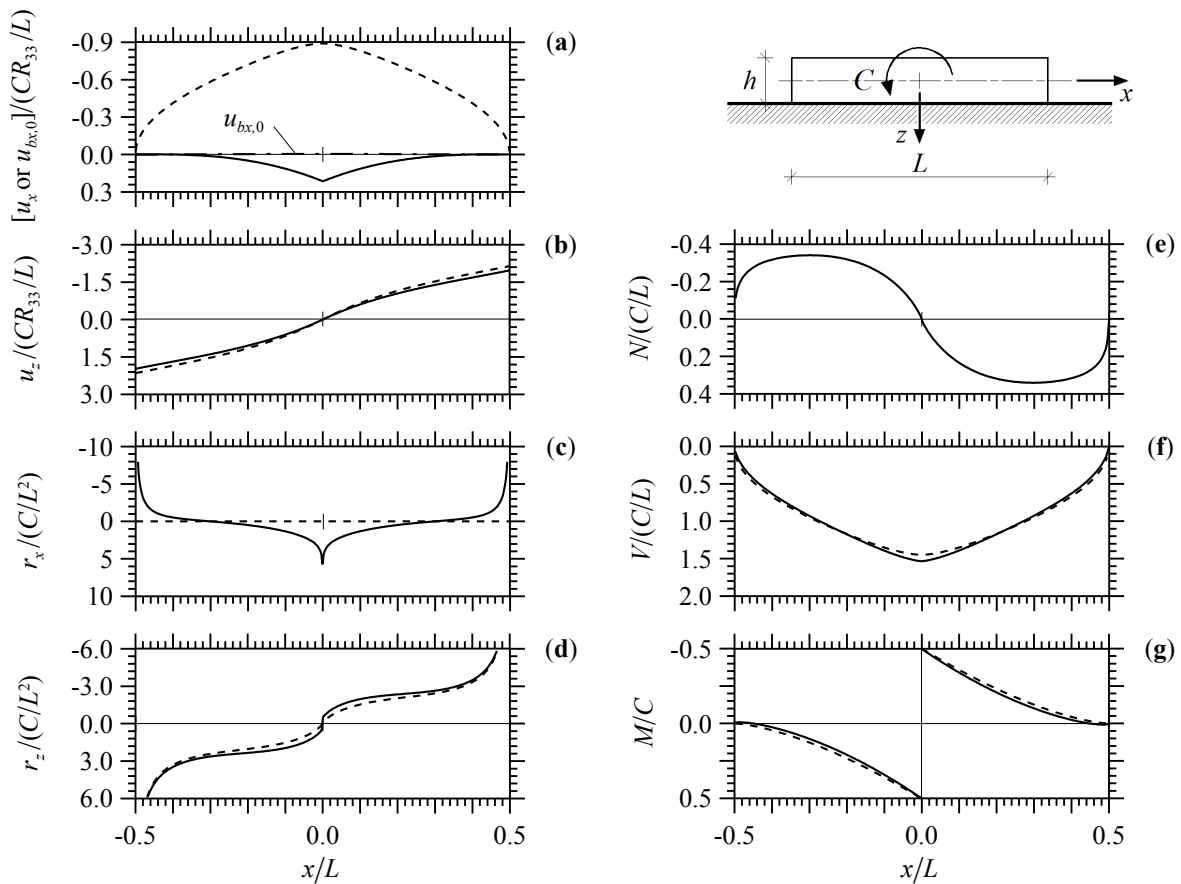
Fig. 2.18. Concrete beam modeled as a Timoshenko beam ($L/h = 10$, $\phi = 0.03$, $\alpha L = 3.65$) loaded by a counter-clockwise couple C acting at the midpoint and bonded to an orthotropic soil ($c_1 = 0.84$; $c_2 = 2.15$; $c_3 = 0.62$) in perfect adhesion (solid line) and in frictionless contact (dashed line). Dimensionless values of u_x (**a**), u_z (**b**), r_x (**c**), r_z (**d**), N (**e**), V (**f**), M (**g**) versus x/L. Horizontal displacement $u_{bx,0}$ (dash-dot line in **a**) refers to the centreline of the beam in perfect adhesion.

2.5   Conclusions

A coupled FE-BIE method for the analysis of a prismatic beam bonded to an elastic orthotropic half-plane is considered in plane stress and plane strain state. The mixed variational formulation is obtained through the theorem of work and energy for exterior domain. Unknown functions are represented by beam displacements and surface tractions by means of classical FE method and BIE approach respectively. A generalised Green function of orthotropic half-plane, characterised by three substrate coefficients, has been used, providing the relationship between displacements and interface reactions. Linear shape function is selected to approximate axial displacement, whereas cubic and quadratic shape functions are used to interpolate transverse deflection and rotation, respectively. Shear and normal surface tractions are described by piecewise constant shape functions.

The proposed method is utilised to study in detail the contact problem of a finite elastic Timoshenko beam bonded to an orthotropic half-plane in perfect adhesion as well as in frictionless contact. The case of a beam having a vanishing bending rigidity has been investigated also. In particular, when shear tractions and external horizontal forces are set to zero, the proposed formulation resembles a frictionless contact. The thin film problem can be properly handled by neglecting the beam bending rigidity. Moreover, through post-processing analysis, the axial force, shear force and bending moment of the beam are determined. The use of the Timoshenko beam theory to analyse the effects of the shear deformation leads to values for the internal shear force sensibly different than that calculated by assuming the Euler-Bernoulli theory.

A variety of examples are presented and discussed considering a beam loaded by a horizontal or vertical force and a couple. In the case of a beam subjected to a vertical point force it is shown that the relative stiffness of beam-substrate significantly affects the maximum bending moment. Moreover, for such a loading condition, the peel traction displays a singular behaviour just across the loaded section for both the contact conditions considered in the analysis. The analytic solutions available in the literature for the problem of the rigid punch and the maximum bending moment of an infinite Euler-Bernoulli beam resting on an isotropic substrate are retrieved. Furthermore, the present model can be used in forthcoming studies in the framework of contact mechanics. As an example, peel or shear tests of a glass fibre reinforcement polymer or aluminium stiffener bonded to wood substrate are analysed. The case of a detached or fully bonded beam has been investigated also, finding almost the same results, except in the region close to the detachment. Furthermore, a stiffener subjected to a uniform thermal variation has been studied, showing

a decrease in the stress response for orthotropic substrates having the same elastic modulus in *z*-direction and lower in *x*-direction. Finally, in the last application regarding the soil-foundation interaction when a concentrated couple acts at the beam midspan, the contact condition (i.e., perfect adhesion or frictionless contact) does not effect the response of the system, except for the horizontal displacement. It must be remarked that, for a beam perfectly welded to the substrate subjected to a such a loading condition, the shear traction appears to be singular whereas the peel stress displays a finite jump across the loaded section.

References

[1]   Teng JG, Chen JF, Smith ST, Lam L. FRP strengthened RC structures. Chichester: John Wiley & Sons; 2001.

[2]   Zhao X-L. FRP-strengthened metallic structures. Boca Raton: CRC Press; 2014.

[3]   Schobera K-U, Harteb AM, Kligerc R, Jockwerd R, Xue Q, Chenf J-F. FRP reinforcement of timber structures. Constr Build Mater 2015; 97:106–118.

[4]   Galin LA. Contact Problems. The legacy of L.A. Galin. Netherlands: Springer; 2008.

[5]   Johnson KL. Contact mechanics. Cambridge. Cambridge University Press; 1985.

[6]   Kachanov ML, Shafiro B, Tsukrov I. Handbook of elasticity solutions. Dordrecht: Kluwer Academic Publishers; 2003.

[7]   Lekhnitskii SG. Theory of elasticity of an anisotropic body. MIR Publishers, Moscow 1977.

[8]   Gladwell GML. Contact problems in the classical theory of elasticity. The Netherlands: Sijthoff & Noordhoff; 1980.

[9]   Willis JR. The elastic interaction energy of dislocation loops in anisotropic media. Q. J. Mech. Appl. Math. 1965; 18(4): 419–433.

[10]   Pan YC, Chou TW. Point force solution for an infinite transversely isotropic solid. J. Appl. Mech. 1976; 43(4): 608–612.

[11]   Pan YC, Chou TW. Green's functions for two-phase transversely isotropic materials. J. Appl. Mech. 1979; 46(3): 551–556.

[12]   Wu RS, Chou YT. Line force in a two-phase orthotropic medium. J. Appl Mech ASME 1982; 49: 55–61.

[13]   Lin W, Kuo CH, Keer LM. Analysis of a transversely isotropic half space under normal and tangential loadings, J. Tribol ASME 1991; 113(4): 335–338.

[14]   Bjarnehed H L. Rigid punch on stressed orthotropic half-plane with partial slip. Journal of Applied Mechanics 1991; 58: 128–133.

[15]   Bjarnehed H L. Multiply loaded rigid punch on a stressed orthotropic half-plane via a thin elastic layer. Journal of Applied Mechanics 1992; 59: 115–122.

[16]   Bjarnehed H L. Multiply loaded Timoshenko beam on a stress orthotropic half-plane via thin elastic layer. Journal of Applied Mechanics 1993; 60: 541–546.

[17]   Lanzoni L, Radi E. Thermally induced deformations in a partially coated elastic layer. Int J Solids Struct 2009; 46(6):1402–1412.

[18]   Lanzoni L. Analysis of stress singularities in thin coatings bonded to a semi-infinite elastic substrate. Int J Solids Struct 2011; 48(13):1915–1926.

[19] Gallagher AP. Bending of a free beam on an elastic foundation. J Appl Mech ASME 1983; 50(2):463–465.

[20] Shield TW, Kim KS. Beam theory models for thin film segments cohesively bonded to an elastic half space. Int J Solids Struct 1992; 29(9):1085–1103.

[21] Li H, Dempsey JP. Unbonded contact of finite Timoshenko beam on elastic layer. J Eng Mech 1988; 114(8): 1265–1284.

[22] Zhang Y-M, Gu Y, Chen J-T. Internal stress analysis for single and multilayered coating systems using the boundary element method. Eng Anal Boundary Elem 2011; 35(4):708–717.

[23] Freund LB, Suresh S. Thin film materials. Stress, defect formation and surface evolution. Cambridge: Cambridge University Press; 2008.

[24] Bush MB. Simulation of contact-induced fracture. Eng Anal Bound Elem 1999; 23(1):59–66.

[25] Rudas M, Bush MB, Reimanis IE. The kinking behaviour of a bimaterial interface crack under indentation loading. Eng Anal Bound Elem 2004; 28(12): 1455–1462.

[26] Ribeiro DB, Paiva JB. An alternative BE–FE formulation for a raft resting on a finite soil layer. Eng Anal Bound Elem 2015; 50:352–359.

[27] Luo JF, Liu YJ, Berger EJ. Analysis of two-dimensional thin structures (from micro- to nano-scales) using the boundary element method, Comput Mech 1998; 22(5):404–412.

[28] Gu Y, Chen W, Zhang B. Stress analysis for two-dimensional thin structural problems using the meshless singular boundary method. Eng Anal Boundary Elem 2015; 59:1–7.

[29] Cheung YK, Zienkiewicz OC. Plates and tanks on elastic foundations - an application of finite element method. Int J Solids Structure 1965; 1(4):451–461.

[30] Cheung YK, Nag DK. Plates and beams on elastic foundation - linear and non-linear behaviour. Geotechnique 1968; 18(2):250–260.

[31] Tullini N, Tralli A. Static analysis of Timoshenko beam resting on elastic half-plane based on the coupling of locking-free finite elements and boundary integral. Comput Mech 2010; 45(2–3): 211–225.

[32] Tezzon E, Tullini N, Minghini M. Static analysis of shear flexible beams and frames in adhesive contact with an isotropic elastic half-plane using a coupled FE-BIE model. Eng. Struct. 2015; 104: 32–50.

[33] Tullini N, Tralli A, Lanzoni L. Interfacial shear stress analysis of bar and thin film bonded to 2D elastic substrate using a coupled FE-BIE method. Finite Elem Anal Des 2012; 55: 42–51.

[34] Tullini N, Tralli A, Baraldi D. Stability of slender beams and frames resting on 2D elastic half-space. Arch Appl Mech 2013; 83(3): 467–482.

[35] Tullini N, Tralli A, Baraldi D. Buckling of Timoshenko beams in frictionless contact with an elastic half-plane. J Eng Mech 2013; 139(7): 824–831.

[36] Cowper GR. The shear coefficient in Timoshenko's beam theory. J. Appl. Mech. ASME 1966; 33: 335–340.

[37] Tullini N, Savoia M. Elasticity interior solution for orthotropic strips and the accuracy of beam theories. J Appl Mech ASME 1999; 66(2): 368–373.

[38] Gurtin ME, Sternberg E. Theorems in linear elastostatics for exterior domains. Arch Ration Mech Anal 1961; 8: 99–119.

[39] Narayanaswami R, Adelman HM. Inclusion of transverse shear deformation in finite element displacement formulations. AIAA J 1974; 12(11): 1613–1614.

[40] Friedman Z, Kosmatka JB. An improved two-node Timoshenko beam finite element. Comput Struct 1993; 47(3): 473–481.

[41] Reddy JN. On locking-free shear deformable beam finite elements. Comput Meth Appl Mech Eng 1997; 149(1-4): 113–132.

[42] Minghini F, Tullini N, Laudiero F. Locking-free finite elements for shear deformable orthotropic thin-walled beams. Int J. Numer Methods Eng 2007; 72(7): 808–834.

[43] Biot MA. Bending of an infinite beam on an elastic foundation. J. Appl. Mech. 1937; 4: A1–A7.

[44] Vesic AB. Bending of beams on isotropic elastic medium. J. Eng. Mech. Div ASCE 1961; 87(EM2): 35–53.

[45] Grigolyuk EI, Tolkachev VM. Contact problems in the theory of plates and shells, Moscow: Mir Publishers; 1987.

[46] Forest Products Laboratory. Wood handbook. Wood as an engineering material. General Technical Report FPL-GTR-190. Madison, WI: U.S. Department of Agriculture, Forest Service, Forest Products Laboratory; 2010.

[47] Kolar V, Nemec I. Modelling of soil-structure interaction. Developments in geotechnical engineering 58, Czechoslovakia 1989.

[48] Thomsen L. Weak elastic anisotropy. Geophysics 1986; 51(10): 1954–1966.

[49] Yimsiri S, Soga K. Cross-anisotropic elastic parameters of two natural stiff clays. Geotechnique 2011; 61(9): 809–814.

[50] Ratananikom W, Likitlersuang S, Yimsiri S. An investigation of anisotropic elastic parameters of Bangkok Clay from vertical and horizontal cut specimens. Geomechanics and Geoengineering: An International Journal 2013; 8(1): 15–27.

[51] Bellotti R, Jamiolkowski M, Lo Presti DCF, O'Neill D A. Anisotropy of small strain stiffness in Ticino sand. Geotechnique 1996; 46(1): 115–131.

[52] Schadlich B, Schweiger HF. Influence of Anisotropic Small Strain Stiffness on the Deformation Behavior of Geotechnical Structures. Int. J. Geomech. 2013; 13: 861–868.

3   Static analysis of layer bonded to elastic half-plane

3.1   Introduction

In solid mechanics, the contact problem that involves an elastic layer lying on an elastic half-plane, has been very widely studied. In geotechnical engineering, some applications have interested important structures, such as foundation grillages, pavements in roads and runways, railway ballast, and other structures consisting of layered media.

The interaction of a foundation beam resting on soil is a problem that has been studied by several investigators by using different models for the soil. The simplest model that has been used for the soil medium is the Winkler model [1]. This model assumes that the surface displacement of the soil medium at every point is directly proportional to the stress applied to it at that point and completely independent of stresses or displacements, implies there is a lack of continuity in the medium which is physically unrealistic. To overcome this deficiency, a two-parametric model has been developed which accounts for the continuity of displacements. Several continuum models have been developed ranging from homogeneous, isotropic and linearity elastic soils to more complex inhomogeneous anisotropic and non-linear soils. The implications and difficulties in solving soil-structure interaction problems using the various continuum models have been discussed by Selvadurai [2] and Feda [3]. Moreover, the soil-structure interaction has been studied using not only theoretical approach but also photoelastic methods [4].

The problem of contact between a layer and a substrate are treated by some researchers: Keer et al. [5] examined the smooth receding contact problem between an elastic layer and a half space formulated under the assumption of plane stress, plane strain and axisymmetric conditions. The same problem was accounted by Borgi et al. [6] for the functionally graded layer. Ratwani et al. [7] considered the plane smooth contact problem for an elastic layer lying on an elastic half space with a compressive load applied to the layer through a frictionless rigid stamp. Civelek et al. [8] investigated the general axisymmetric double frictionless contact problem for an elastic layer pressed against a half-space by an elastic stamp under the assumptions that the three materials have different elastic properties. Gecit [9] studied the frictionless contact problem of a semi-infinite cylinder compressed against a half-space. Comez et al. [10] investigated the plane double receding frictionless contact problem for a loaded rigid stamp in contact with two different elastic layers. Furthermore, a rigid indenter (so called punch) has been investigated,

involving circular flat or conical punch in frictionless contact with elastic layer on a rigid base [11, 12], as well as square rigid punch pressing normally onto an elastic layer, itself attached to an elastically half-plane [13]. These mentioned contacts between layers bonded to homogeneous substrate are considered according to the theory of elasticity neglecting friction forces. In actual practice, the footing may experience a certain amount of interface friction that appears to be no way of finding the actual amount. However, the effect of friction normally tends to reduce the foundation pressure and surface displacement and hence often, for the purpose of analysis, the condition of smooth interface (frictionless) or perfectly bonding could be assumed.

In the present Chapter, interactions of finite layer bonded to semi-infinite plane are studied using a coupled Finite Element-Boundary Integral Equation (FE-BIE) in perfect adhesion. The model makes use of standard formulation of two-dimensional finite element (plate) for the layer in plane strain or plane stress state [14], coupling boundary substrate with integral equation which involves the Green's function [15]. The analysis of a layer-substrate system involves the same basic steps as those described for the beam-substrate interaction problem in Chapters 1 and 2. The layer region could be described by two-dimensional finite elements, such as triangles, rectangles or quadrilaterals, which are connected to each other at nodal points of the elements. The plane elements could be dealt with isotropic or anisotropic materials, where the material properties are specified by supplying the constitutive matrix as input variable to the element functions. The representation of a given layer region by a set of elements, called discretization or mesh generation, is an important choice for the analysis. Moreover, the interpolation functions of 2D finite element depend on the number of nodes in the element, the number of unknowns per node, and the shape of the element. For the sake of simplicity, the domain of layer is subdivided into rectangle elements, though the simplest geometric shape is triangle. The coupling of 2D finite elements with the boundary integral equation of elastic half-plane is briefly described, adopting traditional quadrilateral isoparametric elements in plane stress or strain state. The model makes use of displacements based on numerical formulation of the 2D finite element (plate), coupled with integral equations for the substrate boundary, including the Green's function. Thus, the independent variables of the mixed formulation proposed are plate nodal displacements of the plate and boundary substrate tractions in tangential and normal directions.

Some examples of plate-substrate interaction are compared with an analogous beam-substrate model, though the model in this Section does not enforce the nodal rotation.

Finally, the last example of this Chapter deals with the interaction of embankment-soil that could be aimed to assess the choice and location of reinforcement constituted by geosynthetic, such as geotextile or geogrid. The reinforced embankment has been broadly employed in the construction of high-speed railways over soft soils. This technique has the merits of rapid construction, controllable deformation and global stability [16]. It has been proven that the geogrid can help facilitate in controlling the lateral displacement of the embankment and the settlement of the subsoil [17, 18]. Therefore, the aim of this last analysis could help to determine the distribution of the tensile force necessary for a geogrid design which has raised great concerns in the past decade [19, 20, 21]. A presumed interaction of an embankment loaded by a foundation beam and resting on subsoil, has been investigated using the present coupled FE-BIE model. Assuming unidimensional finite element for the foundation structure, bidimensional finite element for the embankment and boundary integral equation for the semi-infinite subsoil.

3.2 Variational formulation

A layer in plane state, length L, height h and width b, resting on semi-infinite isotropic homogeneous and elastic material is investigated, Fig. 3.1. The problem is referred to a Cartesian coordinate system (O; x, z), where x coincides with the boundary between layer and half-plane while z is chosen in the downward transverse direction. The layer is defined in a domain Ω bounded by Γ

$$\Omega(x,z) \begin{cases} -L/2 \leq x \leq L/2 \\ \quad 0 \leq z \leq h \end{cases} \tag{3.1}$$

in particular two displacement are represented in $\Omega(x,z)$ domain, defined in global direction x and z, respectively by

$$\mathbf{u}(x,z) = \left[u_x(x,z),\ u_z(x,z) \right]^{\mathrm{T}}. \tag{3.2}$$

The infinitesimal strain displacements are obtained by derivation of displacements as:

$$\boldsymbol{\varepsilon}(x,z) = \left[\varepsilon_x,\ \varepsilon_z,\ \gamma_{xz} \right]^{\mathrm{T}} = \left[\frac{\partial u_x}{\partial x},\ \frac{\partial u_z}{\partial z},\ \frac{\partial u_x}{\partial z} + \frac{\partial u_z}{\partial x} \right]^{\mathrm{T}}. \tag{3.3}$$

The stress-strain relationship of the layer, which depend on the constitutive matrix (called with the letter $\mathbf{C}$), is given by $\boldsymbol{\sigma}(x,z) = \mathbf{C}\,\boldsymbol{\varepsilon}$, where for plane stress is

$$\begin{bmatrix} \sigma_{xx} \\ \sigma_{zz} \\ \tau_{xz} \end{bmatrix} = \frac{E_p}{1-\nu_p} \begin{bmatrix} 1 & \nu_p & 0 \\ \nu_p & 1 & 0 \\ 0 & 0 & (1-\nu_p)/2 \end{bmatrix} \begin{bmatrix} \varepsilon_x \\ \varepsilon_z \\ \gamma_{xz} \end{bmatrix}, \tag{3.4}$$

while for plane strain is

$$\begin{bmatrix} \sigma_{xx} \\ \sigma_{zz} \\ \tau_{xz} \end{bmatrix} = \frac{E_p}{(1+\nu_p)(1-2\nu_p)} \begin{bmatrix} 1-\nu_p & -\nu_p & 0 \\ -\nu_p & 1-\nu_p & 0 \\ 0 & 0 & (1-2\nu_p)/2 \end{bmatrix} \begin{bmatrix} \varepsilon_x \\ \varepsilon_z \\ \gamma_{xz} \end{bmatrix}, \tag{3.5}$$

defined E_p the elastic modulus and ν_p the Poisson's coefficient of the layer.
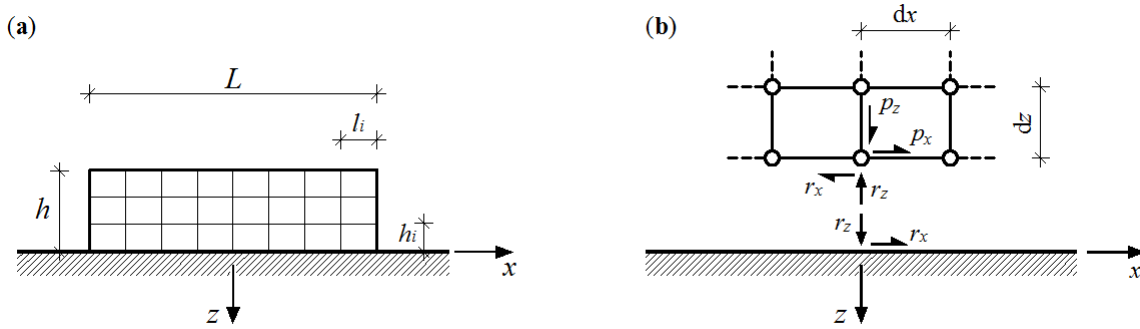
Fig. 3.1. A layer bonded to a half-plane (**a**), and free-body diagram (**b**).

3.2.1 Total potential energy for the layer-substrate system

The total potential energy for the layer-substrate system is given by

$$\Pi = \Pi_{\text{plate}} + \Pi_{\text{soil}} \tag{3.6}$$

which is a mixed variational formulation with variational functions represented by nodal displacements of layer (u_x, u_z) as well as interfacial shear and normal tractions (r_x, r_z) along contact region.

The potential energy of the layer is defined as $\Pi_{\text{plate}} = U_p - W_p$ where U_p is the elastic strain deformation given by

$$U_p = \frac{1}{2} b \int_\Omega \sigma^T \varepsilon \, d\Omega = \frac{1}{2} b \int_\Omega \varepsilon^T C \varepsilon \, d\Omega, \tag{3.7}$$

and W_p is the energy produced by the external forces:

$$W_b = b \int_\Omega \mathbf{u}^T \mathbf{f}_b \, d\Omega + b \int_\Gamma \mathbf{u}^T \mathbf{f}_s \, d\Gamma, \tag{3.8}$$

with $\mathbf{f}_b$ and $\mathbf{f}_s$ the body forces and surface loads, respectively. Finally, the total potential energy for the half-plane Π_{soil} in perfect adhesion is mentioned in the Chapter 1.

3.3   Finite element model

Given domain of a layer denoted by Ω and a boundary denoted by Γ, the *n*-noded finite element displacement vector is definite by $2n$ degrees of freedom

$$\mathbf{u}^e = [u_{x1},\ u_{x2}, ..., u_{xn},\ u_{z1},\ u_{z2}, ..., u_{zn}]^{\mathrm{T}}. \tag{3.9}$$

The unknown displacement vector in each element is interpolated by the nodal displacements as

$$u_x = \sum_{i=1}^{n} N_i^e\, u_{xi} = N_1\, u_{x1} + N_2\, u_{x2} + ... + N_n\, u_{xn} \tag{3.10a}$$

$$u_z = \sum_{i=1}^{n} N_i^e\, u_{zi} = N_1\, u_{z1} + N_2\, u_{z2} + ... + N_n\, u_{zn} \tag{3.10b}$$

where N_i^e denotes the element shape functions. The displacements can also be expressed in matrix form as

$$\mathbf{u} = \begin{bmatrix} N_1^e & N_2^e & ... & N_n^e & 0 & 0 & ... & 0 \\ 0 & 0 & ... & 0 & N_1^e & N_2^e & ... & N_n^e \end{bmatrix} \mathbf{u}^e = \mathbf{N}\, \mathbf{u}^e \tag{3.11}$$

and the strain vector can be obtained by derivation of the displacements as

$$\mathbf{\varepsilon} = \begin{bmatrix} \dfrac{\partial N_1^e}{\partial x} & \dfrac{\partial N_2^e}{\partial x} & ... & \dfrac{\partial N_n^e}{\partial x} & 0 & 0 & ... & 0 \\[2mm] 0 & 0 & ... & 0 & \dfrac{\partial N_1^e}{\partial z} & \dfrac{\partial N_2^e}{\partial z} & ... & \dfrac{\partial N_n^e}{\partial z} \\[2mm] \dfrac{\partial N_1^e}{\partial z} & \dfrac{\partial N_2^e}{\partial z} & ... & \dfrac{\partial N_n^e}{\partial z} & \dfrac{\partial N_1^e}{\partial x} & \dfrac{\partial N_2^e}{\partial x} & ... & \dfrac{\partial N_n^e}{\partial x} \end{bmatrix} \mathbf{u}^e = \mathbf{B}\, \mathbf{u}^e \tag{3.12}$$

The strain-displacement matrix $\mathbf{B}$ is needed for computation of the stiffness matrix and the stress vector at the each element. The derivatives with respect to the global coordinates can be found as $\partial ... / \partial x = \mathbf{J}^{-1}\, \partial ... / \partial \xi$ where $\mathbf{J}$ is the Jacobian operator, relating natural and global coordinates.

Soil reactions for the *i*th element can be approximated by the expressions:

$$r_x(\xi) = [\mathbf{\rho}_a(\xi)]^{\mathrm{T}}\, \mathbf{r}_{xi}, \qquad r_z(\xi) = [\mathbf{\rho}_b(\xi)]^{\mathrm{T}}\, \mathbf{r}_{zi}, \tag{3.13}$$

where $\mathbf{r}_{xi}$, $\mathbf{r}_{zi}$ denote nodal interfacial shear and normal tractions, respectively, and vectors $\mathbf{\rho}_a$, $\mathbf{\rho}_b$ collect constant or linear shape functions.

Substituting Eqs. (3.9) and (3.13) into variational principle and assembling over all elements, the total potential energy of the whole system assumes the following generalized expression:

$$\Pi(\mathbf{u},\mathbf{r}) = \frac{1}{2}\mathbf{u}^{\mathrm{T}}\mathbf{K}_p\,\mathbf{u} - \mathbf{u}^{\mathrm{T}}\mathbf{F} + \mathbf{u}^{\mathrm{T}}\mathbf{H}\mathbf{r} - \frac{1}{2}\mathbf{r}^{\mathrm{T}}\mathbf{G}\,\mathbf{r} \qquad (3.14)$$

Requiring the total potential energy in Eq. (3.14) to be stationary, the following system of equations is obtained

$$\begin{bmatrix} \mathbf{K}_{p11} & \mathbf{K}_{p12} & \mathbf{0} \\ \mathbf{K}_{p21} & \mathbf{K}_{p22} & \mathbf{H} \\ \mathbf{0} & \mathbf{H}^{\mathrm{T}} & -\mathbf{G} \end{bmatrix} \begin{Bmatrix} \mathbf{u}_1 \\ \mathbf{u}_2 \\ \mathbf{r} \end{Bmatrix} = \begin{Bmatrix} \mathbf{f}_1 \\ \mathbf{f}_2 \\ \mathbf{0} \end{Bmatrix} \qquad (3.15)$$

denoting with $\mathbf{u}_1$ and $\mathbf{u}_2$ the vectors of nodal displacements referred to the layer, unshared and shared with the substrate elements respectively, and $\mathbf{f}_1$, $\mathbf{f}_2$ the corresponding load vectors. The vector of nodal force $\mathbf{f}$ is obtained as

$$\mathbf{f} = b\int_{\Omega}\mathbf{N}^{\mathrm{T}}\mathbf{f}_b\,\mathrm{d}\Omega + b\int_{\Gamma}\mathbf{N}^{\mathrm{T}}\mathbf{f}_s\,\mathrm{d}\Gamma \qquad (3.16)$$

3.3.1 Layer subdivided to quadrilateral element plate

A quadrilateral element with four nodes in natural coordinates (ξ, η) is considered [22]. The coordinates (x, z) are interpolated as

$$x = \sum_{i=1}^{4} N_i\, x_i, \qquad z = \sum_{i=1}^{4} N_i\, z_i \qquad (3.17)$$

where N_i are the Lagrange shape functions as given

$$N_1(\xi,\eta) = l_1(\xi)\, l_1(\eta) = (1-\xi)(1-\eta)/4, \qquad (3.18a)$$

$$N_2(\xi,\eta) = l_2(\xi)\, l_1(\eta) = (1+\xi)(1-\eta)/4, \qquad (3.18b)$$

$$N_3(\xi,\eta) = l_2(\xi)\, l_2(\eta) = (1+\xi)(1+\eta)/4, \qquad (3.18c)$$

$$N_4(\xi,\eta) = l_1(\xi)\, l_2(\eta) = (1-\xi)(1+\eta)/4, \qquad (3.18d)$$

Hence displacements u_x, u_z are interpolated as Eq. (10) at any point in the element with the nodal displacements u_{xi}, u_{zi}, $i = 1, ..., 4$.

The stiffness matrix of the layer $\mathbf{K}_p$ is obtained as

$$\mathbf{K}_p = b \int_{\Omega} \mathbf{B}^{\mathrm{T}} \mathbf{C} \mathbf{B} \, d\Omega \tag{3.19}$$

which dependent on the number of integration points in the ξ, η directions and the corresponding weights ω

$$\mathbf{K}_p^e = b \int_{\Omega^e} \mathbf{B}^{\mathrm{T}} \mathbf{C} \mathbf{B} \, d\Omega^e = b \int_{-1}^{1} \int_{-1}^{1} \mathbf{B}^{\mathrm{T}} \mathbf{C} \mathbf{B} \det \mathbf{J} \, d\xi \, d\eta = b \sum_{i=1}^{2} \sum_{j=1}^{2} \mathbf{B}^{\mathrm{T}} \mathbf{C} \mathbf{B} \det \mathbf{J} \, \omega_i \, \omega_j \tag{3.20}$$

The stiffness matrix of the layer is computed using 2x2 Gauss points having unit weight.

3.3.2 Piecewise constant substrate tractions

A piecewise constant functions are used to interpolate tractions $\mathbf{r}_x$ and $\mathbf{r}_z$, hence the matrix $\mathbf{G}$ does not vary with respect to the case shown in Chapter 1. With regard to matrix $\mathbf{H} = b \widetilde{\mathbf{H}}$, if piecewise constant tractions r_x and r_z are assumed, the components bonded to semi-infinite substrate for the ith FE are

$$\widetilde{\mathbf{h}}_{xx,i} = l_i / 2 \, [1, 1]^{\mathrm{T}}, \tag{3.21a}$$

$$\widetilde{\mathbf{h}}_{zz,i} = l_i / 2 \, [1, 1]^{\mathrm{T}}. \tag{3.21b}$$

In conclusion, Fig. 3.2 shows a representation of the matrix system of Eq. (3.15). The layer is subdivided into two plates, where only one of them is bonded to one substrate element (s_1). Two point forces P_x, P_z are applied at the top right of the layer.
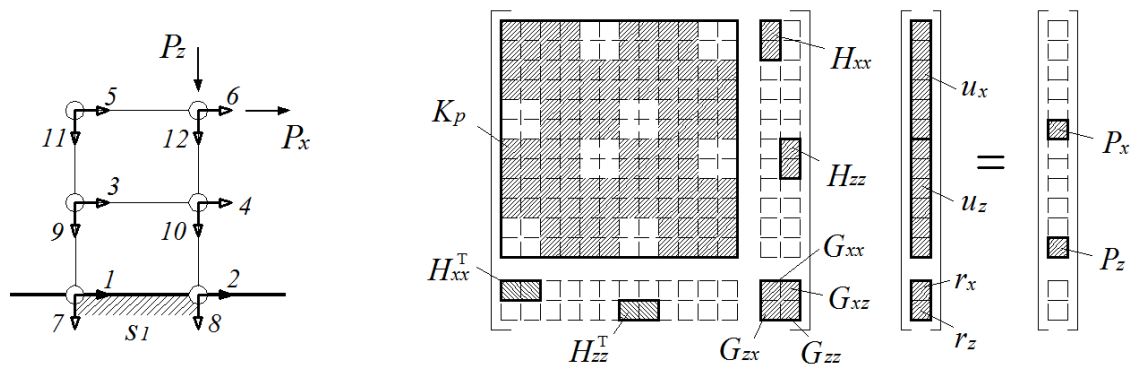
Fig. 3.2. Matrix system of a layer subdivided in two plate elements where only one of them is bonded to one substrate element (s_1). External point loads P_x, P_z are applied at the top right.

3.4   Numerical example

The domain of a layer, length L and height h, is discretized by horizontal and vertical subdivision $n_{el,x}$ and $n_{el,z}$, obtaining a mesh of $n_{el} = n_{el,x} \times n_{el,z}$ quadrilateral elements having length l_i and height h_i. The perfect adhesion interface between layer and half-plane is considered. The horizontal and vertical interface displacements (u_x, u_z), through FE method, as well as tangential and normal tractions (r_x, r_z), through BIE approach, are determined by the equation system (Eq. 3.15). The values of interfacial displacements and substrate reactions are plotted non-dimensionally along the boundary contact. Moreover, stresses in x and z direction (σ_{xx}, σ_{zz}) of the layer are post-calculated and plotted into plane finite elements.

The solutions which are obtained by the static response of the beam-substrate system, calculated in Chapter 1 with parameter $\alpha L = 10$, are proposed again and compared with the contact of an analogous layer (same mechanical characteristics and geometry of beam) bonded in perfect adherent to the half-plane. In all examples presented, unless otherwise specified, a plane stress state is used.

3.4.1   Layer loaded by pressure at central

In this Section, a layer with ratio $L/h = 10$ and resting on an elastic isotropic half-plane having $c = 0.8$ is investigated. The layer is subdivided by rectangular mesh, using a number of elements $n_{el,x} = 16$ in the x-direction and $n_{el,z} = 2$ in the z-direction, hence comprehensively a number of plate elements $n_{el} = 32$. The isotropic substrate is discretized using the same number elements of the layer in x-direction ($n_{el,x}$). Three cases, having a pressure applied at central, are following examined.

3.4.1.1 Layer loaded by uniform vertical pressure p_z

The case of a layer bonded to elastic half-plane and loaded by a uniform vertical pressure p_z at central cross section is considered first. Dimensionless displacements and reactions along the substrate boundary are reported in Fig. 3.3 for layer-substrate system (thick solid line) and for the analogous beam-substrate problem (thick dashed line). In particular, a Timoshenko with the same number elements of x-direction $n_{el,x}$ ($n_{el} = 16$) and subjected to point force $P_z = p_z A_b$ at midspan is compared. The value of ϕ has been determined considering the shear modulus $G_b = E_b/[2(1+\nu_b^2)]$ and the shear correction factor $k_b =$

$5/(6-\nu_b G_b/E_b)$, hence obtained $\phi = 12/5(1-\nu_b/12)/(1-\nu_b)(L/h)^2 = 0.024$. A good agreement of results between the two models is illustrated. The evolution of dimensionless layer displacements and layer stresses are plotted in Fig. 3.4.

The horizontal displacements evaluated along centroidal axis of layer are in contraction (Fig. 3.3a and Fig. 3.4a). They tend to stretch in the area of the contact region close to the load section. That behaviour is also proved in the beam-substrate model that is influenced by the contribution of term $\phi\, h/2$. The shear reactions of substrate (r_x) show a discontinuity at the midspan, Fig. 3.3b, having a correlation with the plate stresses in x-direction (σ_{xx}). The latter stresses, Fig. 3.4b, identify a compression zone at the top and a tense zone at the bottom of the layer. With regard to vertical displacements of the substrate boundary, the same values appeared along the cross-section, showing maximum deflection at central (Fig. 3.3c and Fig. 3.4c). The normal reactions of substrate (r_z) of the two models are plotted in Fig 3.3d, where its maximum value is at $x/L = 0$, the highlighted peak is also reported in the normal plate stresses (σ_{zz}), Fig. 3.4d.

3.4.1.2 Layer loaded by uniform horizontal pressure p_x

A layer bonded to an elastic isotropic substrate, is loaded by a uniform horizontal pressure p_x at central cross-section. The value of pressure is chosen such that the resultant become equal to $P_x = p_x\, A_b$ with target to compare the solutions with those of an analogous beam-substrate interaction problem.

Dimensionless results of the system, and plate stresses calculated by the post-processing analysis, are plotted in Figs. 3.5 and 3.6. Horizontal displacements, along boundary surface or centroidal axis of layer, are in good conformity with the analogous Euler-Bernoulli beam resting on the same substrate (dashed line in Figs. 3.5a). Notice that, the horizontal displacements, which are relative to the value found at the bottom end point, increase toward the top of the layer, as shown Fig. 3.6a. With regard to tangential reactions (r_x), Fig 3.5b, the influence of the two interaction systems (layer-substrate and beam-substrate) are not particularly significant. In the central zone where a peak reaction comes up by presence of pressure, plate stresses in x-direction provide opposite sign, distinguishing compression and tension zone, Fig. 3.6b. Antisymmetric vertical displacements are observed in Fig 3.5c, where negative values occur in the interval $[-0.5, 0)/L$ and positive one into $(0, 0.5]/L$, providing a clockwise rotation. Same displacements turn out along the cross-section of the layer, showing in Fig. 3.6c. A quite insignificant difference between normal substrate reactions obtained by the two kinds of systems (layer-substrate and beam-substrate), is

illustrated in Fig. 3.5c. In particular, a peak value occurs at the ends which could be compared with the maximum plate stress in z-direction reported in Fig. 3.6d.

3.4.1.3 Layer loaded by varying horizontal pressure p_x

The case of a layer loaded by a couple is not possible to investigate, because of the neglected nodal rotation in the formulation of two-dimensional finite element. To overcome that, a varying horizontal pressure is applied along the cross-section with the purpose of simulating a moment given by an analogous couple C at the midspan. The dimensionless interfacial displacements and substrate reactions are plotted in Fig. 3.7 Analogous beam-substrate system (in dashed line) has been compared using a Timoshenko beam with ϕ = 0.024, loaded by the couple C at midpoint. Furthermore, layer displacements and layer stresses are reported in dimensionless, Fig. 3.8.

The horizontal displacements along centroidal axis of the layer ($u_{x,0}$) take absolute values lower and opposite sign with respect to interfacial horizontal displacements (u_x), shown in Fig. 3.7a. That is highlighted in the layer displacements, Fig. 3.8a, near the central cross-section, where positive values are found at the bottom and those negative at the top of layer. Shear reactions of the substrate coincide almost everywhere between two kinds of systems, Fig. 3.7b. Besides, the stress in x-direction shows the difference between compression zone with negative values and zone of the layer with tension fibres through positive values, Fig. 3.8b. With regard to vertical displacements, in the interval [−0.5, 0)/L they have down-direction, whereas up-direction into (0, 0.5]/L (Figs. 3.7c and 3.8c), providing so a counter-clockwise movement. The response of the interaction layer-substrate with analogous beam-substrate system, in term of normal interfacial reaction, is plotted in Fig. 3.7d, showing an expected discontinuity at the central. The stresses in z-direction reported in the layer, Fig. 3.8d, confirm the values higher at the midspan and toward the contact region .
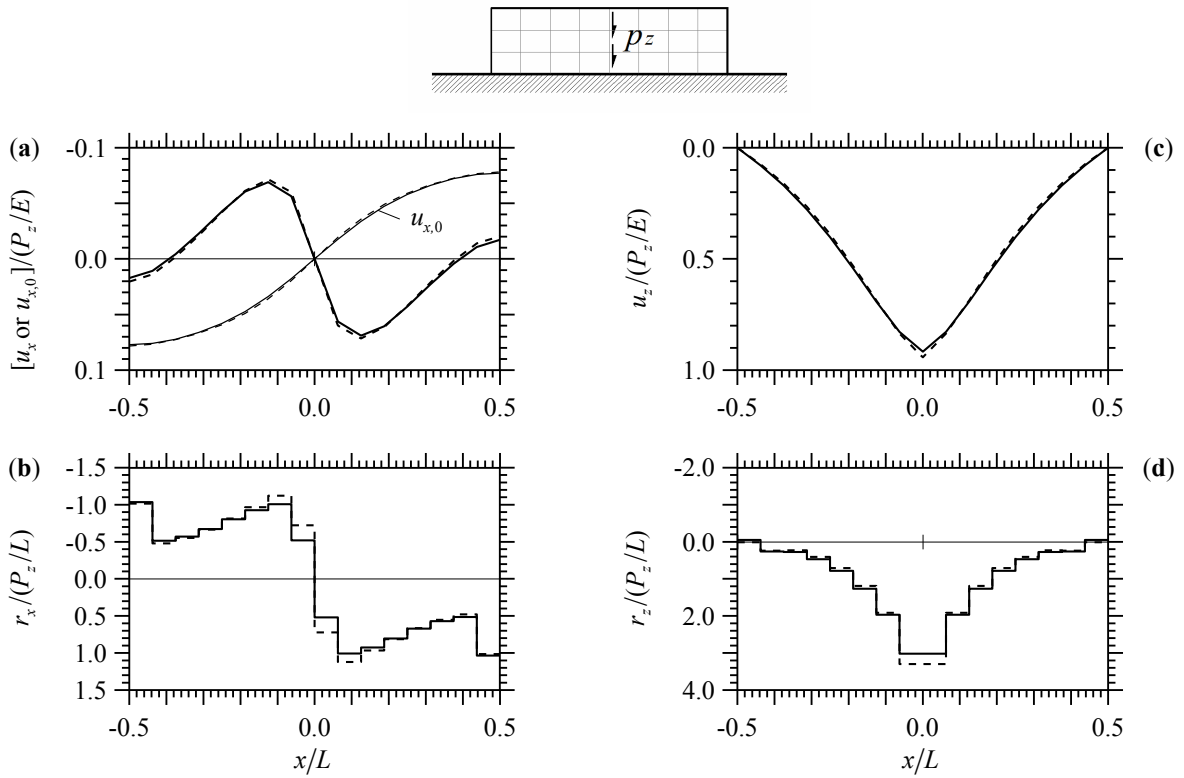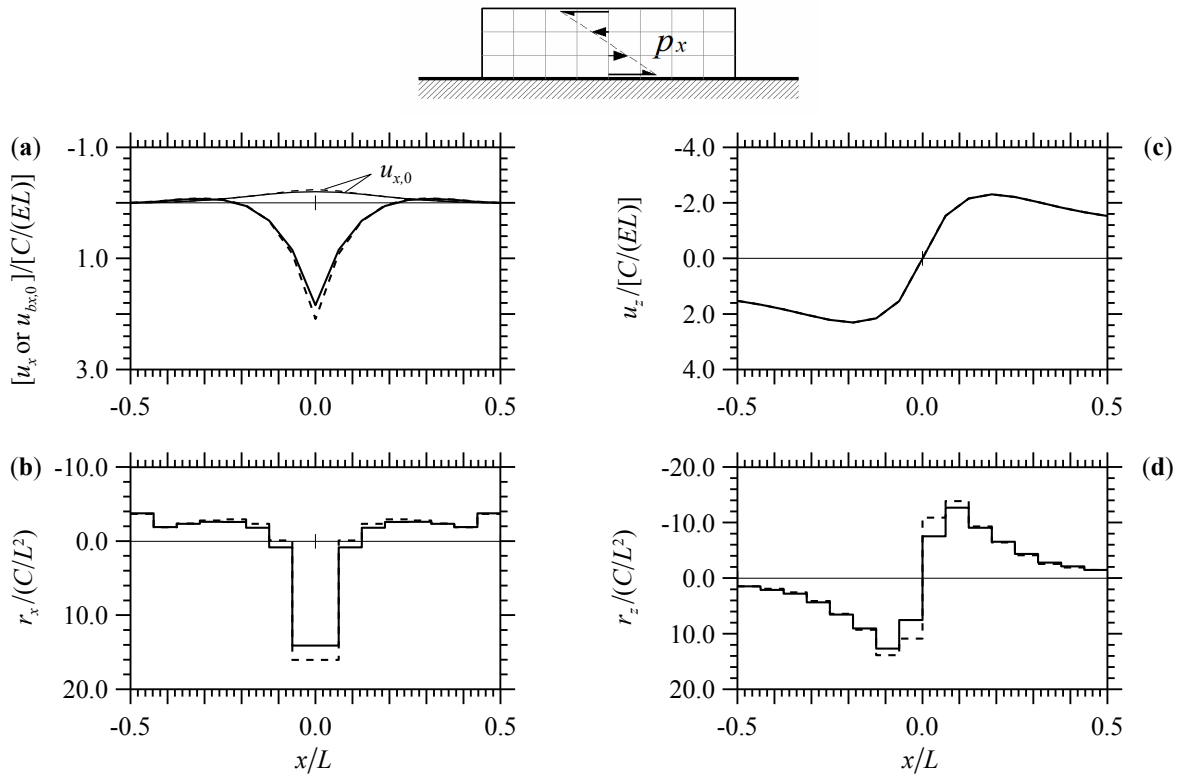
Fig. 3.3. Layer loaded by uniform vertical pressure p_z at central (solid line) and analogous Timoshenko beam ($L/h = 10$, $\alpha L = 10$, $\phi = 0.024$) subjected to point P_z at midspan (dashed line). Nondimensional values of u_x (**a**), r_x (**b**), u_z (**c**), and r_z (**d**) in perfect adhesion. Horizontal displacement $u_{bx,0}$ is referred to the centreline of layer or beam (respectively thin solid or thin dashed line in (**a**)).
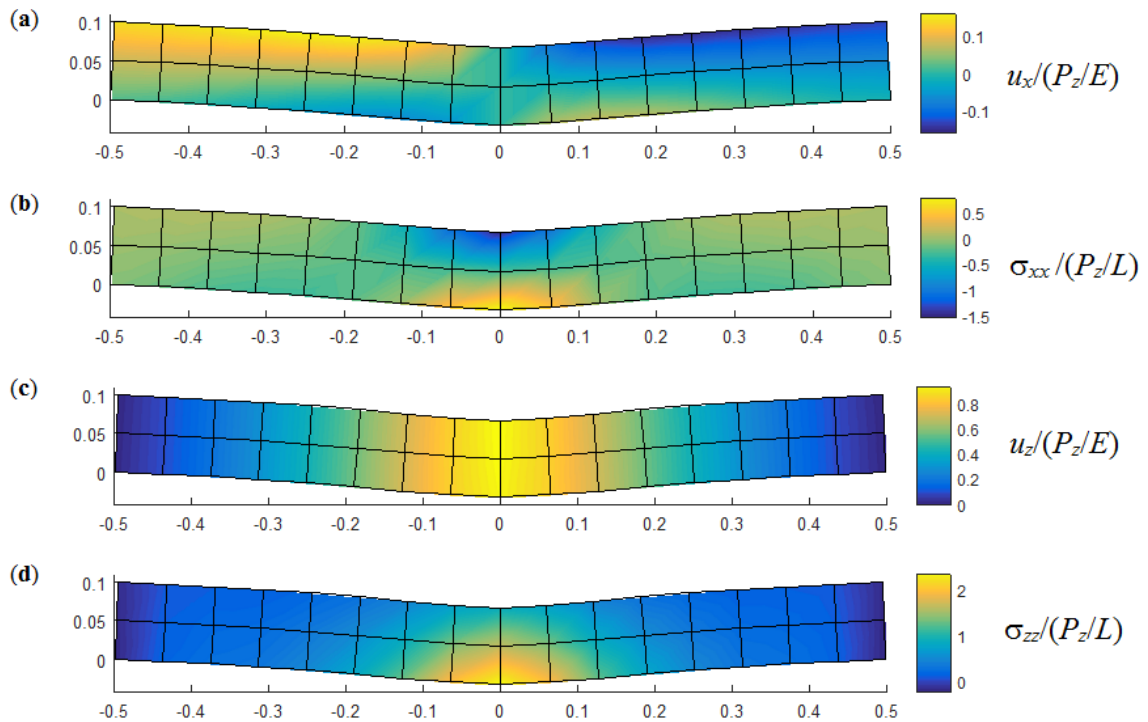

Fig. 3.4. Layer loaded by uniform vertical pressure p_z at central. Nondimensional values of u_x (**a**), σ_{xx} (**b**), u_z (**c**), and σ_{zz} (**d**) in perfect adhesion.
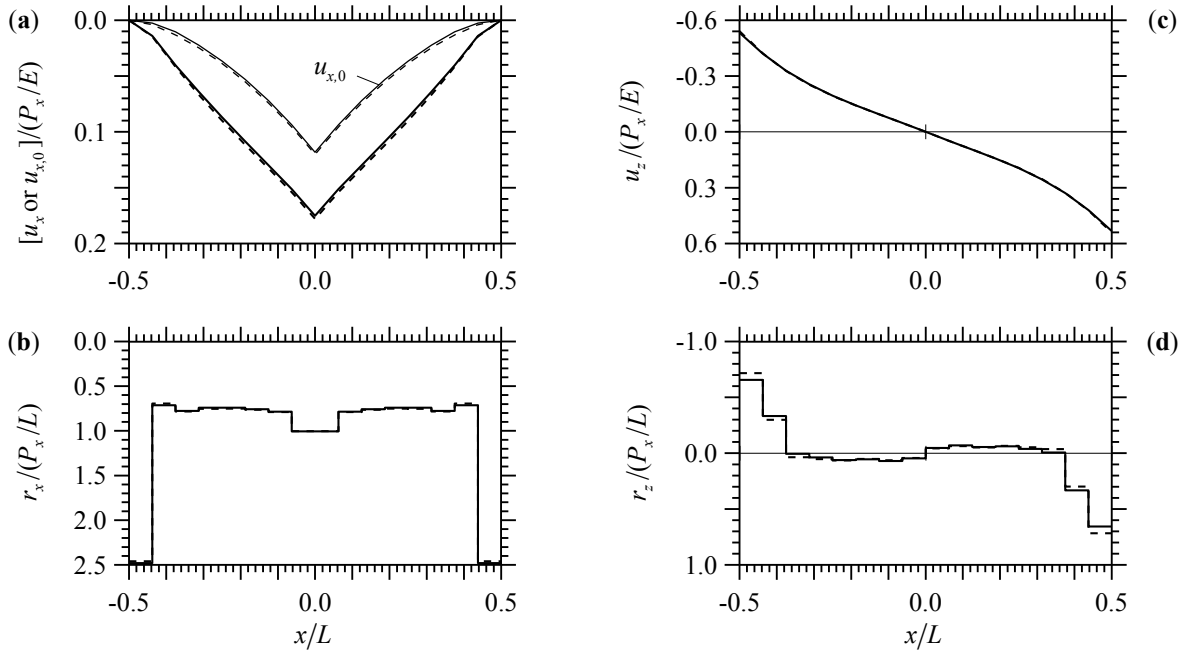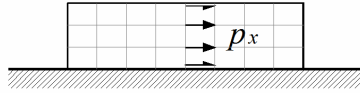
Fig. 3.5. Layer loaded by uniform horizontal pressure p_x at central (solid line) and analogous Euler-Bernoulli beam ($L/h = 10$, $\alpha L = 10$) subjected to point P_x at midspan (dashed line). Nondimensional values of u_x (**a**), r_x (**b**), u_z (**c**), and r_z (**d**) in perfect adhesion. Horizontal displacement $u_{bx,0}$ is referred to the centreline of layer or beam (respectively thin solid or thin dashed line in (**a**)).
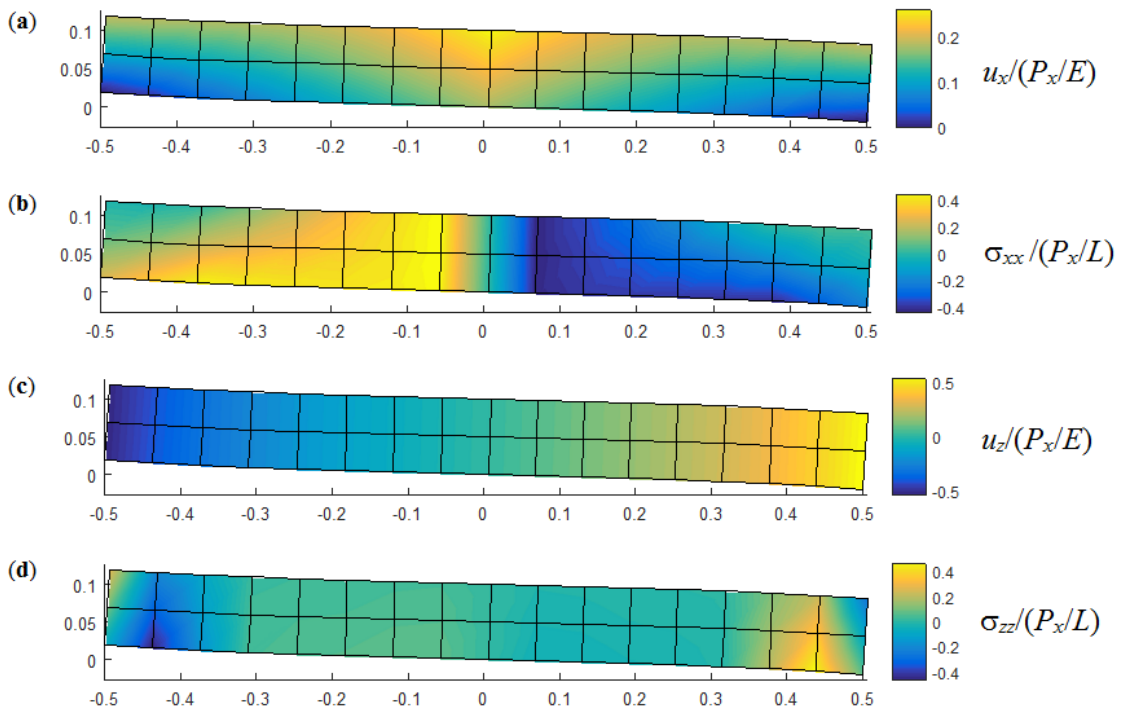
Fig. 3.6. Layer loaded by uniform horizontal pressure p_x at central. Nondimensional values of u_x (**a**), σ_{xx} (**b**), u_z (**c**), and σ_{zz} (**d**) in perfect adhesion.

Fig. 3.7. Layer loaded by varying horizontal pressure p_x at central (solid line) and analogous Timoshenko beam ($L/h = 10$, $\alpha L = 10$, $\phi = 0.024$) subjected to couple C at same section (dashed line). Nondimensional values of u_x (**a**), r_x (**b**), u_z (**c**), and r_z (**d**) in perfect adhesion. Horizontal displacement $u_{bx,0}$ is referred to the centreline of layer or beam (respectively thin solid or thin dashed line in (**a**)).
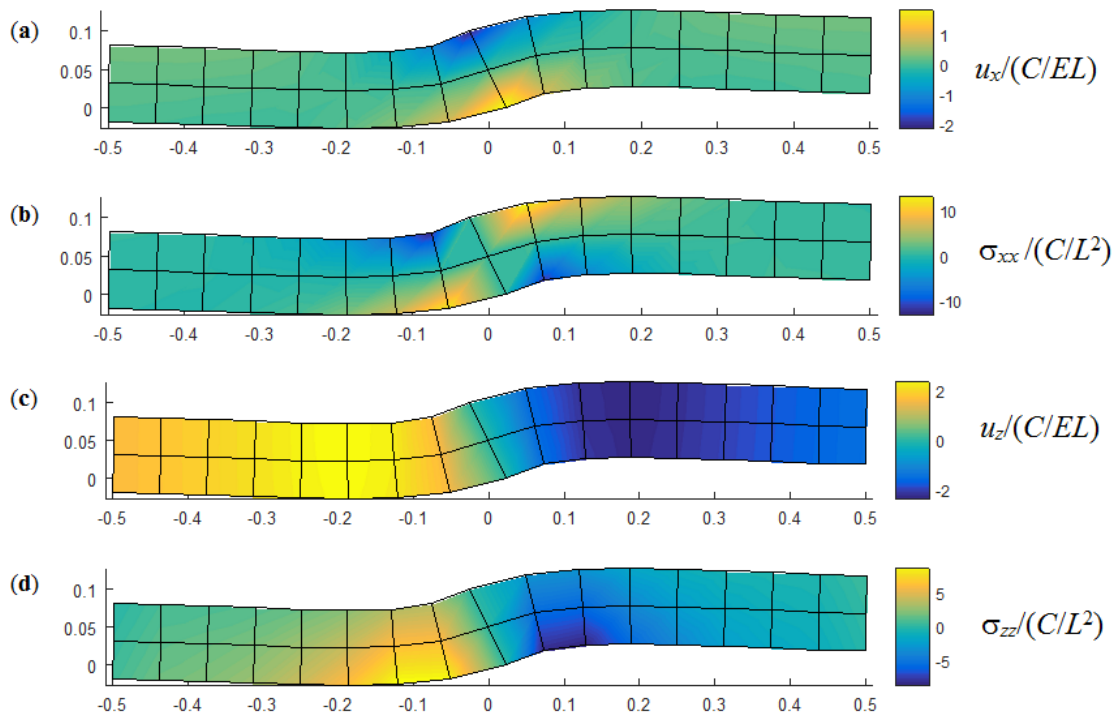
Fig. 3.8. Layer loaded by varying horizontal pressure p_x at central. Nondimensional values of u_x (**a**), σ_{xx} (**b**), u_z (**c**), and σ_{zz} (**d**) in perfect adhesion.

111

3.4.2 Layer loaded by pressure at one end

The same interaction layer-substrate problem has been investigated in this Section applying pressure at one end. Vertical or horizontal uniform pressure and horizontal varying pressure are considered. Dimensionless relative displacements, substrate reactions and plate stresses are reported using a mesh with 32 uniform rectangle elements. Moreover, an analogous beam-substrate problem assuming Euler-Bernoulli or Timoshenko beam theory bonded in perfect adhesion with 512 uniform elements is compared.

3.4.2.1 Layer loaded by uniform vertical pressure p_z

When the layer is subjected to a uniform vertical pressure p_z at one end, the highest displacement, substrate reaction or stress is located at the area of the load section. The following results are reported when the pressure is applied toward up-direction.

Relative horizontal displacements, assessed along the substrate boundary, are positive, indeed tend to stretch the layer-substrate system. Contrarily, the horizontal displacements at centroidal axis of layer show negative sign with absolute values lower, Fig. 3.9a. In particular, the negative horizontal displacements indicate that layer-substrate systems tend to contract. This feature is shown in the plot of layer displacements, Fig. 3.10a, with values relative to unloaded edge end. In Fig. 3.9b, shear substrate reactions show negative value at the ends with an opposite sign peak near the load section. The zone of layer with compression and tension fibre is reported in Fig. 3.10b by means of plate stress in *x*-direction. As expected, the relative vertical displacements are all negative, Fig. 3.9c and 3.10c, as well as the normal substrate reaction, Fig. 3.9d. These effects make an uplift, highlighted even by stresses in *z*-direction of the layer, Fig. 3.10d.

3.4.1.2 Layer loaded by uniform horizontal pressure p_x

A layer loaded by a uniform horizontal pressure, having resultant $P_x = p_x A_b$, toward positive direction of *x*-axis and applied at one end, is studied consequently.

Dimensionless displacements and reactions along the boundary substrate are reported in Fig. 3.11. Moreover, the horizontal displacements assess at the centroidal axis of layer, $u_{x,0}$, are shown in Fig. 3.11a. Two remarkable peaks appear in the shear substrate reaction, Fig. 3.11b. The effect of stretch is highlighted by horizontal displacement, while the uplift in the left zone or the lowering in the right zone of layer could be noted by vertical displacements, Fig. 3.11c. The normal substrate reaction values turn out with opposite

peaks at the two ends, Fig. 3.11d. Nondimensional displacements and stresses into the layer are illustrated in Fig. 3.12. The positive horizontal displacements are affirmed in Fig. 3.12a, indeed all fibres of the layer are in tension, Fig. 3.12b. The vertical displacement of the layer, Fig. 3.12c, describes the uplift and lowering effect as mentioned. Finally, two peaks of stress in z-direction at the contact of edge ends of the layer are shown in Fig. 3.12d.

3.4.1.3 Layer loaded by varying horizontal pressure p_x

A varying horizontal pressure is applied at one end of the layer such that simulates a moment described by a counter-clockwise couple. Dimensionless displacements and substrate reactions are shown in Fig. 3.13, where displacements are relative to the value at unload edge end ($x/L = -0.5$). In particular, the stretch behaviour of layer is shown by positive value of horizontal interfacial displacements reported between the interval [0.3, 0.5]/L, instead elsewhere negative values are found, Fig. 3.13a. Moreover, the horizontal displacements are reported in the layer, Fig. 3.14a. The maximum peak of shear substrate reactions is shown in Fig. 3.13b, provides tension at the bottom fibres and compression at the top fibres of layer, Fig. 3.14b. An uplift of layer occurs at the end where the pressure is applied. This behaviour is shown by the negative value of relative vertical displacements, Figs 3.13c and 3.14c. Finally, normal substrate reaction, Fig. 3.13d, and stresses in z-direction of the layer, Fig. 3.14d, put in evidence a peak at the load region and close to the contact.
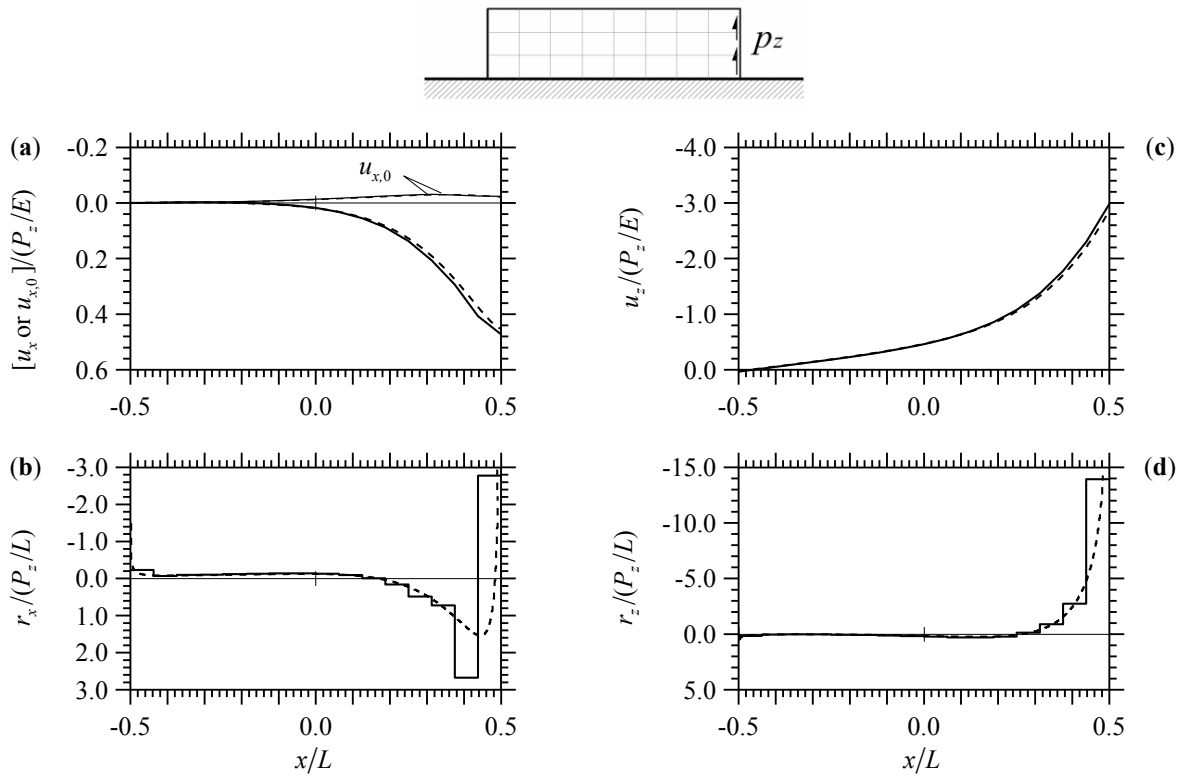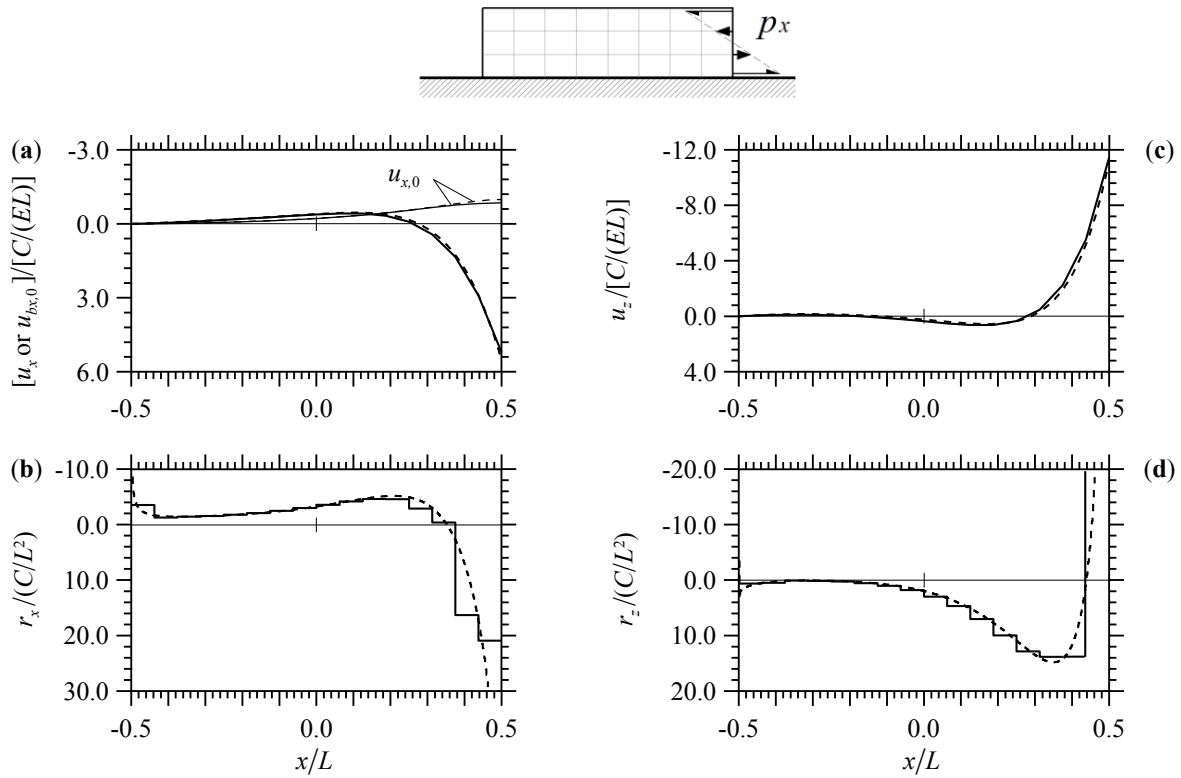
Fig. 3.9. Layer loaded by uniform vertical pressure p_z at one end (solid line) and analogous Timoshenko beam ($L/h = 10$, $\alpha L = 10$, $\phi = 0.024$) subjected to point P_z at same end section (dashed line). Nondimensional values of u_x (**a**), r_x (**b**), u_z (**c**), and r_z (**d**) in perfect adhesion. Horizontal displacement $u_{bx,0}$ is referred to the centreline of layer or beam (respectively thin solid or thin dashed line in (**a**)).
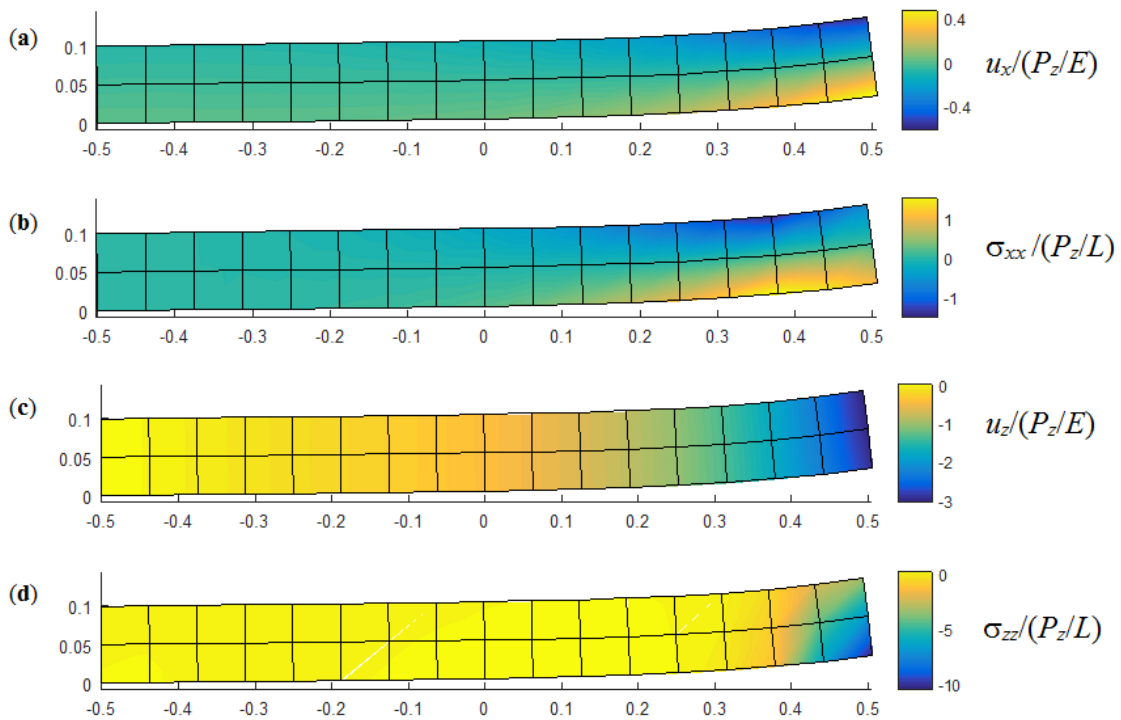

Fig. 3.10. Layer loaded by uniform vertical pressure p_z at one end. Nondimensional values of u_x (**a**), σ_{xx} (**b**), u_z (**c**), and σ_{zz} (**d**) in perfect adhesion.
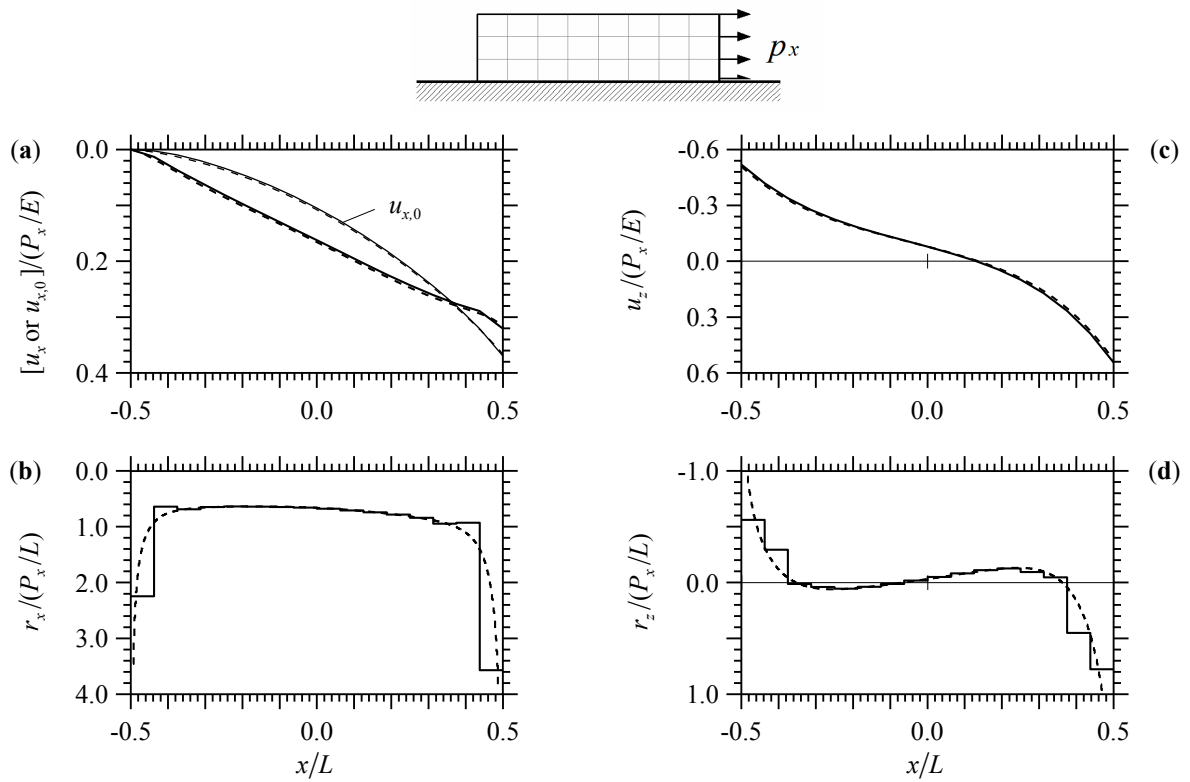
Fig. 3.11. Layer loaded by uniform horizontal pressure p_x at one end (solid line) and analogous Euler-Bernoulli beam ($L/h = 10$, $\alpha L = 10$) subjected to point P_x at same end section (dashed line). Nondimensional values of u_x (**a**), r_x (**b**), u_z (**c**), and r_z (**d**) in perfect adhesion. Horizontal displacement $u_{bx,0}$ is referred to the centreline of layer or beam (respectively thin solid or thin dashed line in (**a**)).
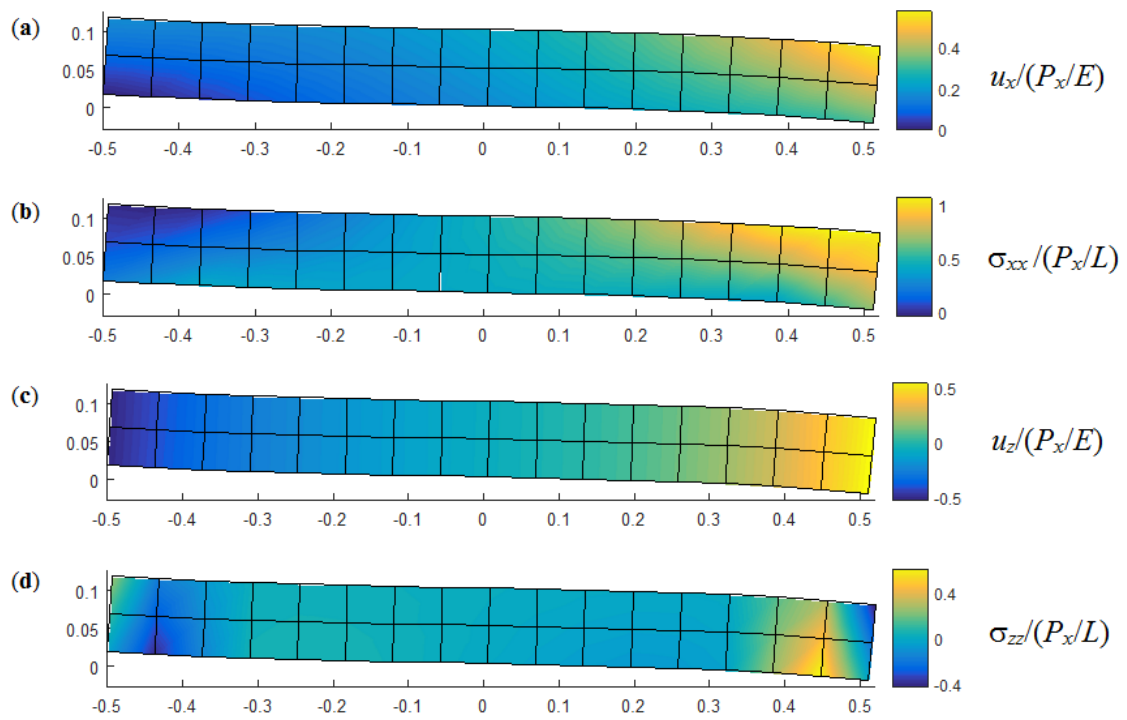
Fig. 3.12. Layer loaded by uniform horizontal pressure p_x at one end. Nondimensional values of u_x (**a**), σ_{xx} (**b**), u_z (**c**), and σ_{zz} (**d**) in perfect adhesion.

Fig. 3.13. Layer loaded by varying horizontal pressure p_x at one end (solid line) and analogous Timoshenko beam ($L/h = 10$, $\alpha L = 10$, $\phi = 0.024$) subjected to couple C at same end section (dashed line). Nondimensional values of u_x (**a**), r_x (**b**), u_z (**c**), and r_z (**d**) in perfect adhesion. Horizontal displacement $u_{bx,0}$ is referred to the centreline of layer or beam (respectively thin solid or thin dashed line in (**a**)).
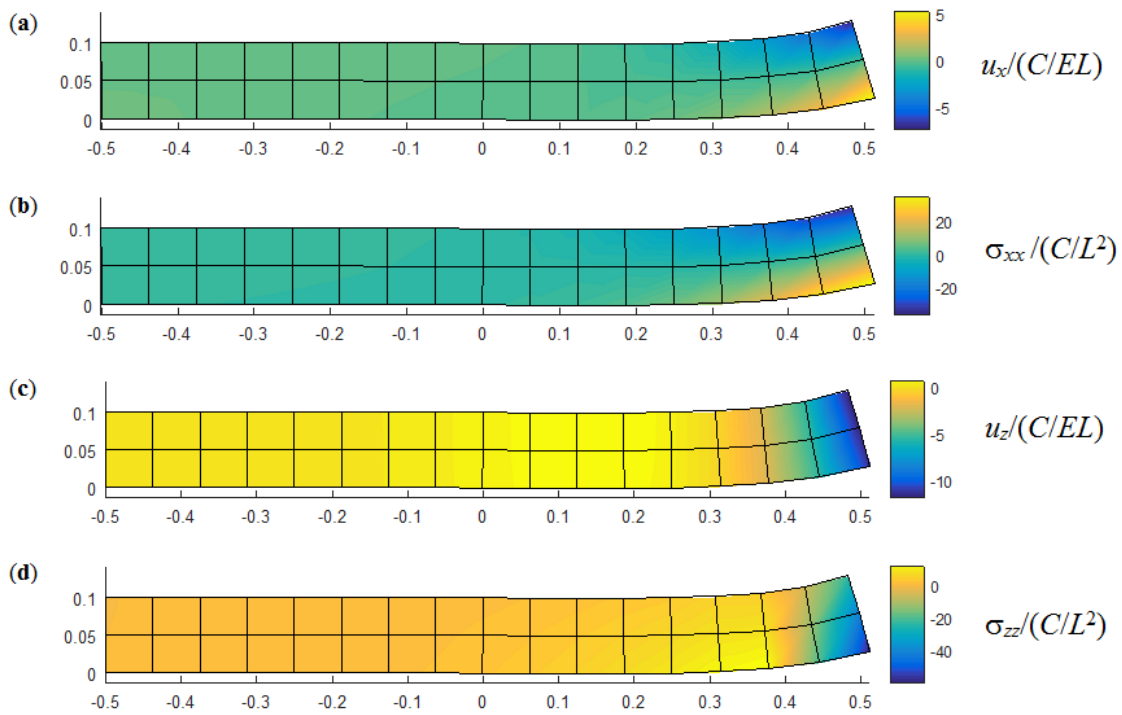
Fig. 3.14. Layer loaded by varying horizontal pressure p_x at one end. Nondimensional values of u_x (**a**), σ_{xx} (**b**), u_z (**c**), and σ_{zz} (**d**) in perfect adhesion.

116

3.4.3 Layer loaded by two pressures at ends

The goal of examples in this Section is to investigate the contact behaviour with symmetric or antisymmetric load condition, where two pressures at the edge ends of layer are applied.

An elastic isotropic layer, with ratio $L/h = 10$ and $\alpha L = 10$, bonded to a half-plane is examined. For the layer, a rectangular mesh refinement of $n_{el} = 128$, having in the x-direction $n_{el,x} = 32$ and in the z-direction $n_{el,z} = 4$ is used. The same number of subdivision along the x-direction is assumed for the half-plane. Dimensionless results of the displacements and substrate reactions are reported. Furthermore, dimensionless stresses in x and z direction of the layer are calculated through the post-processing analysis. Finally, results obtained by the interaction of an analogous beam-substrate system, assuming the Euler-Bernoulli beam theory, and using a uniform mesh of $n_{el} = 512$, has been reported for comparison.

3.4.3.1 Layer loaded by symmetric uniform vertical pressure p_z

The contact layer-substrate problem with two uniform vertical pressure p_z at the edge ends of layer and both are applied toward up-direction, is illustrated in Figs. 3.15 and 3.16.

An antisymmetric behaviour of the horizontal displacement is found, where values become opposite sign reaching the top layer, Fig. 3.15a and Fig. 3.16a. The same antisymmetric behaviour is shown in the shear substrate reaction, Fig. 3.15b, having opposite peaks at the two ends. The effect provides a tension stress at the bottom and a compression stress at the top of layer, as shown the stress in x-direction (σ_{xx}), Fig. 3.16b. The vertical displacement turns out to be symmetric, Fig. 3.15c, with the maximum value at $x = 0$ and constant along the cross-section, Fig. 3.16c. In particular, both figures show relative displacements with respect to its end value. With regard to normal substrate reaction, the magnitude is almost constant in the interval $[-0.25, 0.25]/L$, and increase at the ends, Fig, 3.15d. Nevertheless, stresses in z-direction of the layer show peak values at the contact ends, which decrease toward the top of layer, Fig. 3.16d.

3.4.3.2 Layer loaded by antisymmetric uniform vertical pressure p_z

Results in figures 3.17 and 3.18 show the case of the layer subject to two antisymmetric and uniform vertical pressures p_z applied at the ends.

Relative horizontal displacements (u_x, and $u_{x,0}$) are plotted with regard to their end values. In particular, the maximum interfacial horizontal displacement u_x occurs at the

midspan, Fig. 3.17a. While, the horizontal displacements reported in the layer are relative to the end value at centroidal axis, Fig. 3.18a. and obviously are not zero at the ends of the contact. A symmetric shear substrate reaction occurs, showing two negative peaks before to reach the edge ends, Fig. 3.17b. The stress of layer in x-direction changes sign along the cross-section, showing at the right side of layer a tension zone at the bottom and a compression zone at the top of fibres, vice versa happens in the other side, Fig. 3.18b. With regard to vertical displacements, negative values appear in the interval $[-0.5, 0)/L$ while those positive into $(0, 0.5]/L$, giving a clockwise rotation, Figs. 3.17c and 3.18c. Normal substrate reaction turns out antisymmetric with the maximum values occur at the ends, Figs. 3.17d. The same remark is shown in Fig. 3.18d with peaks of stress in z-direction at the ends of contact.

3.4.3.3 Layer loaded by symmetric uniform horizontal pressure p_x

A layer subjected to tension load generated by two opposite and uniform horizontal pressure p_x is analysed.

The solutions in terms of horizontal displacement are reported in Figs. 3.19a and 3.20a, where the values in the contact region (u_x) and along centroidal axis of layer ($u_{x,0}$) are quite similar. An antisymmetric behaviour of shear substrate reactions (r_x) are shown in Fig. 3.19b. The stresses in x-direction (σ_{xx}) are all positive, Fig 3.20b, and are not constant along the cross-section. The lifting effect could be observed by negative values of the vertical displacement with maximum at the midspan, Figs. 3.19c and 3.20c. Finally, constant normal substrate reactions, Fig. 3.19d, and constant stresses in z-direction, Fig. 3.20d, are found into $[-0.25, 0.25]/L$, while the peak values are reached at the ends.

3.4.3.4 Layer loaded by antisymmetric uniform horizontal pressure p_x

Considering the same layer subjected to two uniform horizontal pressure p_x at ends but toward the positive direction of x-axis. The effect of antisymmetric load condition provides symmetric horizontal displacement and shear substrate reaction. While vertical displacement and normal substrate reaction turn out to be antisymmetric.

The horizontal displacements (u_x and $u_{x,0}$), plotted in Fig. 3.21a, are either relative to their end value. The interfacial displacements u_x have absolute relative values lower than $u_{x,0}$. Difference reference is taken for the Fig. 3.22a, where the value is zero at half-height of the edge ends. With regard to shear substrate reactions, a good agreement between

layer-substrate and beam-substrate is delineated, showing positive values throughout the contact, Fig. 3.21b. The compression and tension zone are shown through σ_{xx}, Fig. 3.22b. The two pressures provide a clockwise rotation, clearly evident by vertical displacements, Figs. 3.21c and 3.22c. Normal substrate reactions and stresses in z-direction emphasize peak values occur at ends of the contact, Figs 3.21d and 3.22d.

3.4.3.5 Layer loaded by symmetric varying horizontal pressure p_x

The simulation of two couple at ends could be produced by a varying horizontal pressure p_x along the cross-section. The direction of pressure depend on couple direction which, in this Section, provide tension at the top fibres of layer.

The interfacial horizontal displacements u_x tend to contract throughout the contact, while stretched behaviour is observed along centroidal-axis of the layer, Fig 3.23a. This effect is also marked in Fig. 3.24a. Antisymmetric behaviour of shear substrate reaction is reported in Fig. 3.23b. Besides the tense zone at the top and compression region at the bottom of layer are confirmed in Fig. 3.24b. The vertical displacements result negative and are constant along the cross-section, Figs. 3.23c and 3.24c. Finally, two peaks of the normal reactions (r_z) are found before to reach the edge ends where maximum values occur, Figs. 3.23d. Moreover, the behaviour of stress in z-direction (σ_{zz}) is reported in Fig. 3.24d, showing high values at the ends, as expected.

3.4.3.6 Layer loaded by antisymmetric varying horizontal pressure p_x

A layer loaded by two horizontal pressure p_x which vary along cross-section such that have the purpose to simulate two antisymmetric couples in clockwise direction, is analysed.

The antisymmetric load condition provides symmetric behaviour of the horizontal displacement and shear reaction, while the vertical displacement and normal reaction turn out antisymmetric. The relative horizontal displacements u_x and $u_{x,0}$ are reported in Fig. 3.25a, showing opposite sign each other, Fig. 3.26a. Constant and positive shear substrate reactions occur in the interval $[-0.25, 0.25]/L$, which become negative with peak value at the two ends, Fig. 3.25b. Tension fibres at the bottom and compression fibres at the top are on the left side of layer, while vice versa happen on the right side, Fig. 3.26b. The spin of layer in the clockwise direction could be noticed by the vertical displacements Fig. 3.25c and 3.26c. Finally, normal substrate reaction and layer stresses in z-direction show in Fig. 3.25d and 3.26d report both high values at ends of the contact.
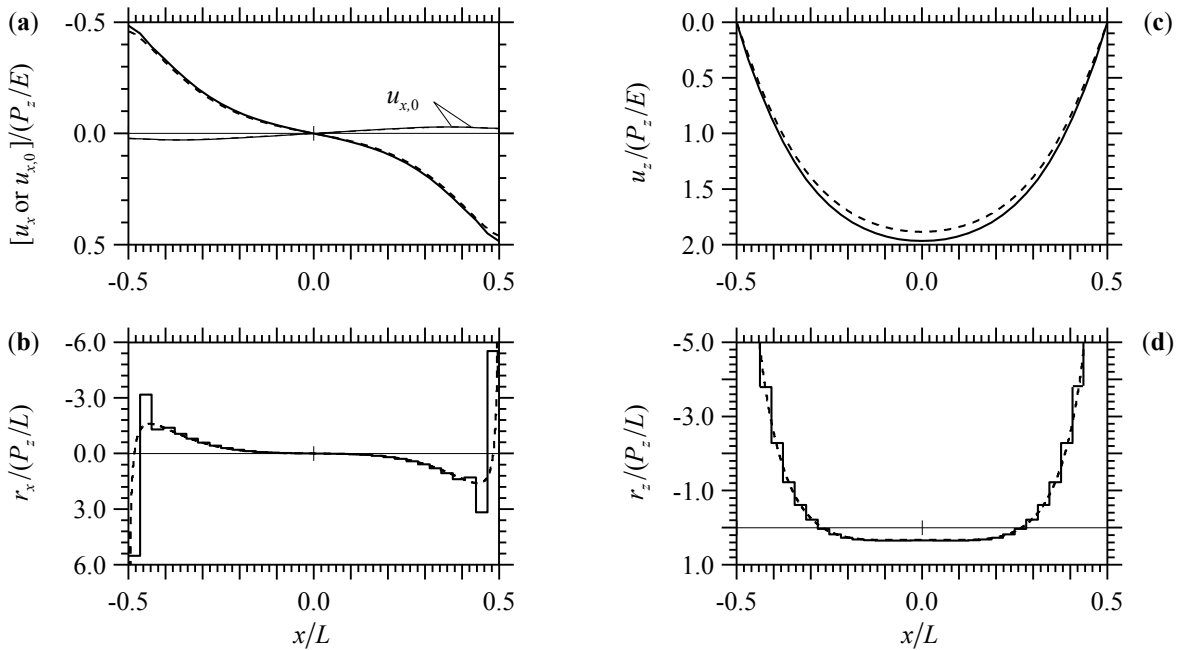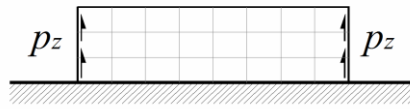
Fig. 3.15. Layer loaded by symmetric uniform vertical pressure p_z at ends (solid line) and analogous Euler-Bernoulli beam ($L/h = 10$, $\alpha L = 10$) subjected to point P_z at ends (dashed line). Nondimensional values of u_x (**a**), r_x (**b**), u_z (**c**), and r_z (**d**) in perfect adhesion. Horizontal displacement $u_{bx,0}$ is referred to the centreline of layer or beam (respectively thin solid or thin dashed line in (**a**)).
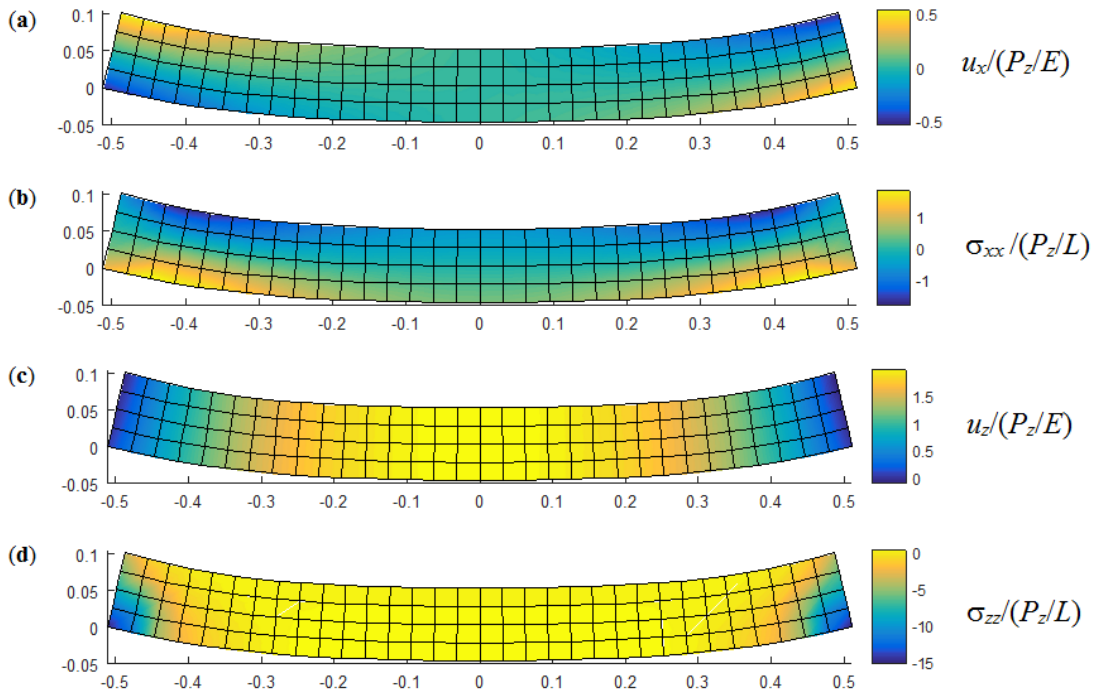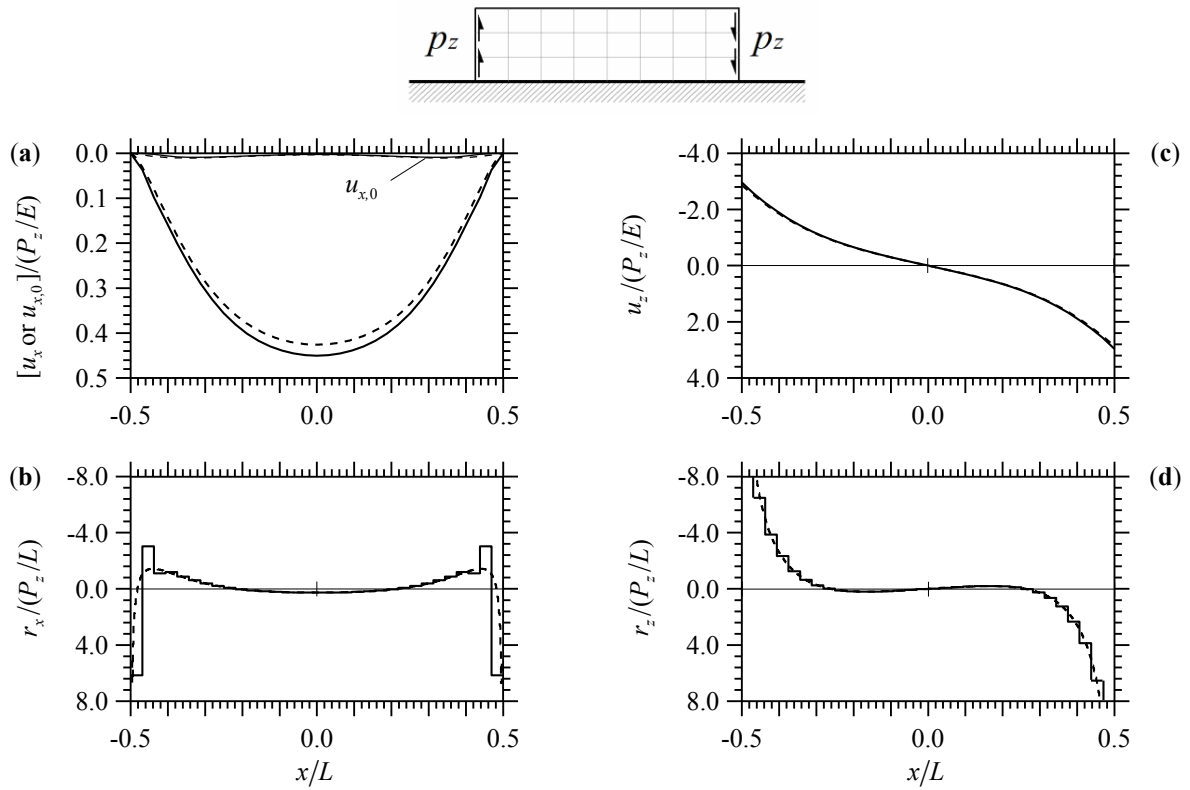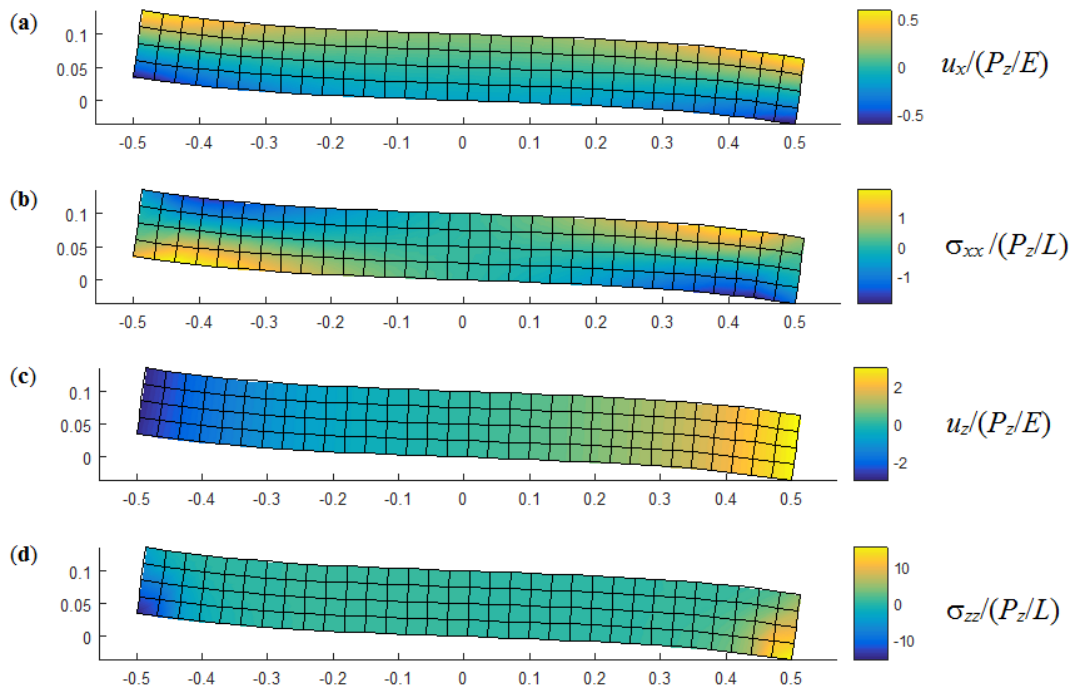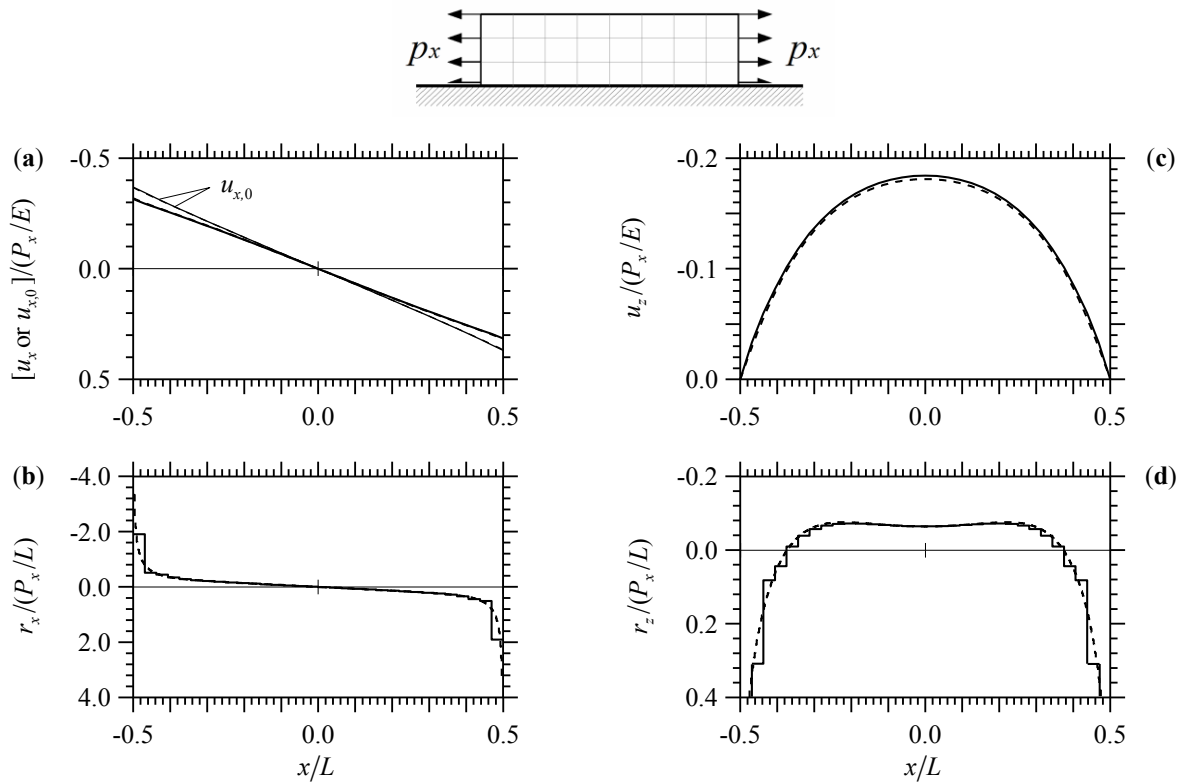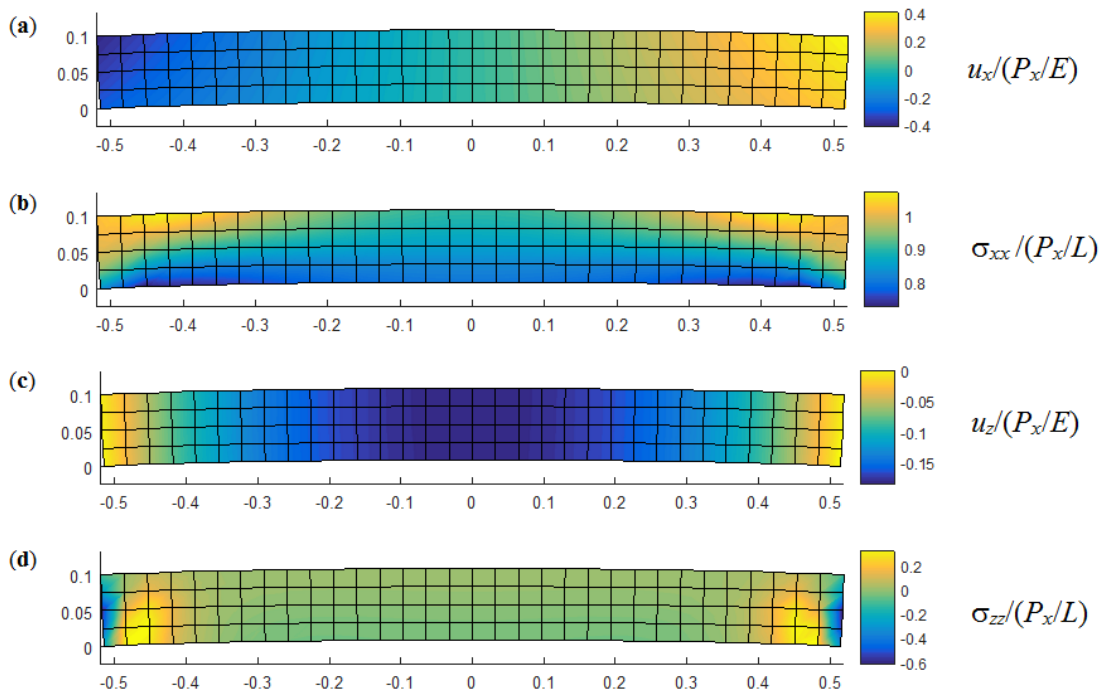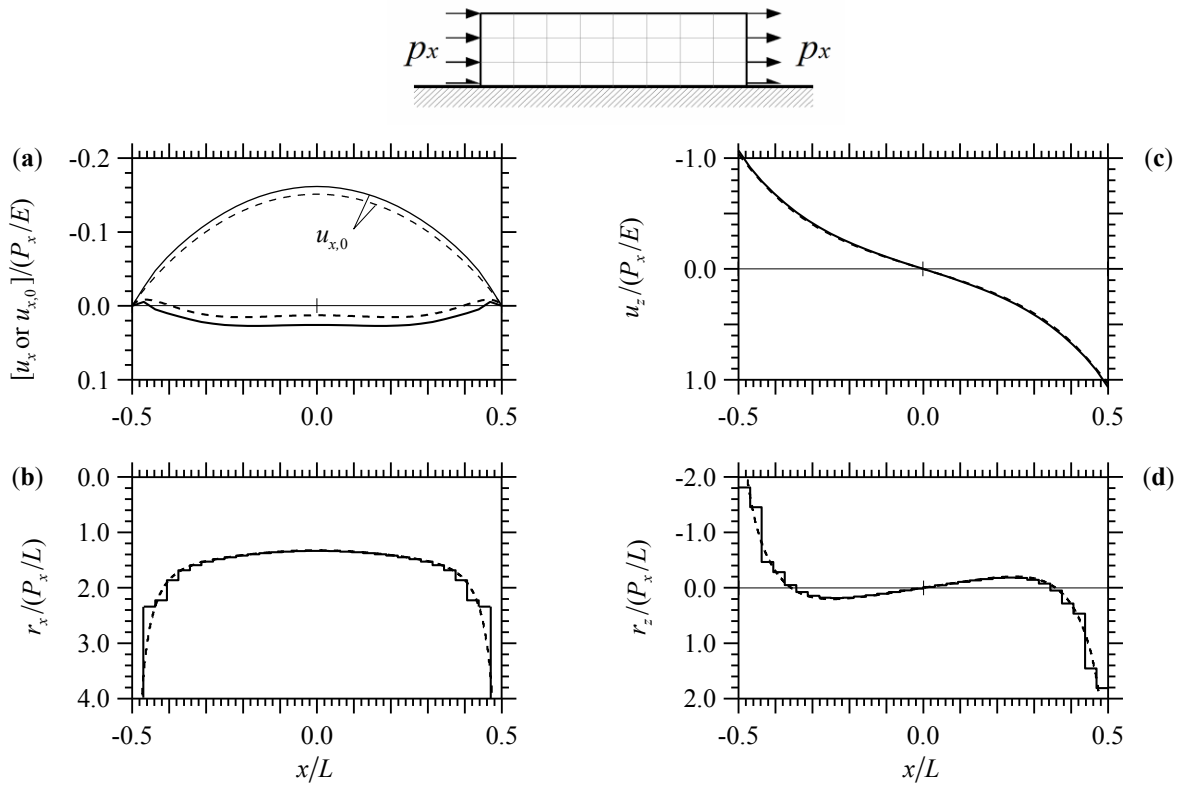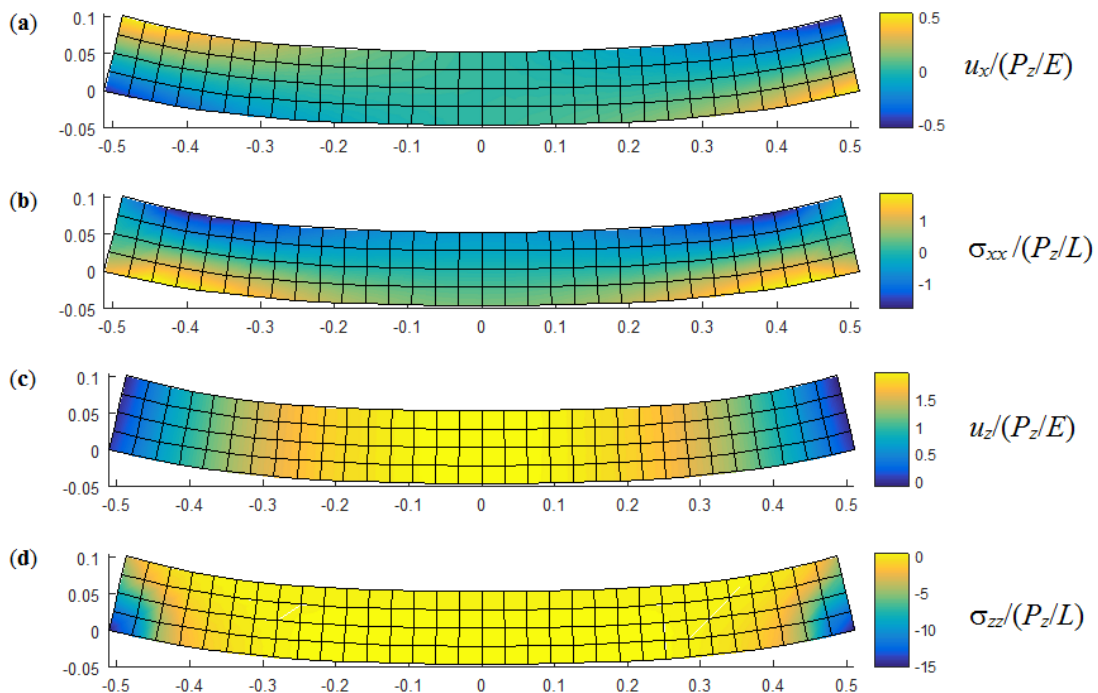

Fig. 3.16. Layer loaded by symmetric uniform vertical pressure p_z at ends. Nondimensional values of u_x (**a**), σ_{xx} (**b**), u_z (**c**), and σ_{zz} (**d**) in perfect adhesion.
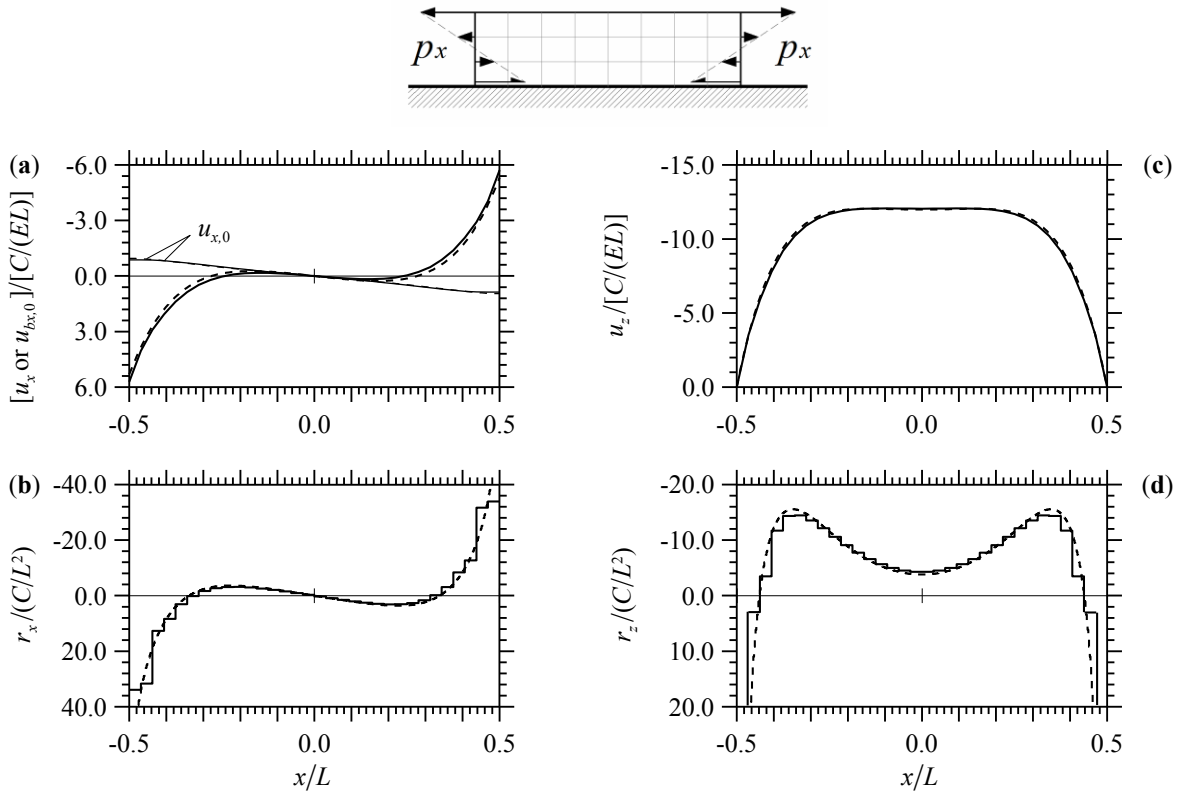
Fig. 3.17. Layer loaded by antisymmetric uniform vertical pressure p_z at ends (solid line) and analogous Euler-Bernoulli beam ($L/h = 10$, $\alpha L = 10$) subjected to point P_z at ends (dashed line). Nondimensional values of u_x (**a**), r_x (**b**), u_z (**c**), and r_z (**d**) in perfect adhesion. Horizontal displacement $u_{bx,0}$ is referred to the centreline of layer or beam (respectively thin solid or thin dashed line in (**a**)).
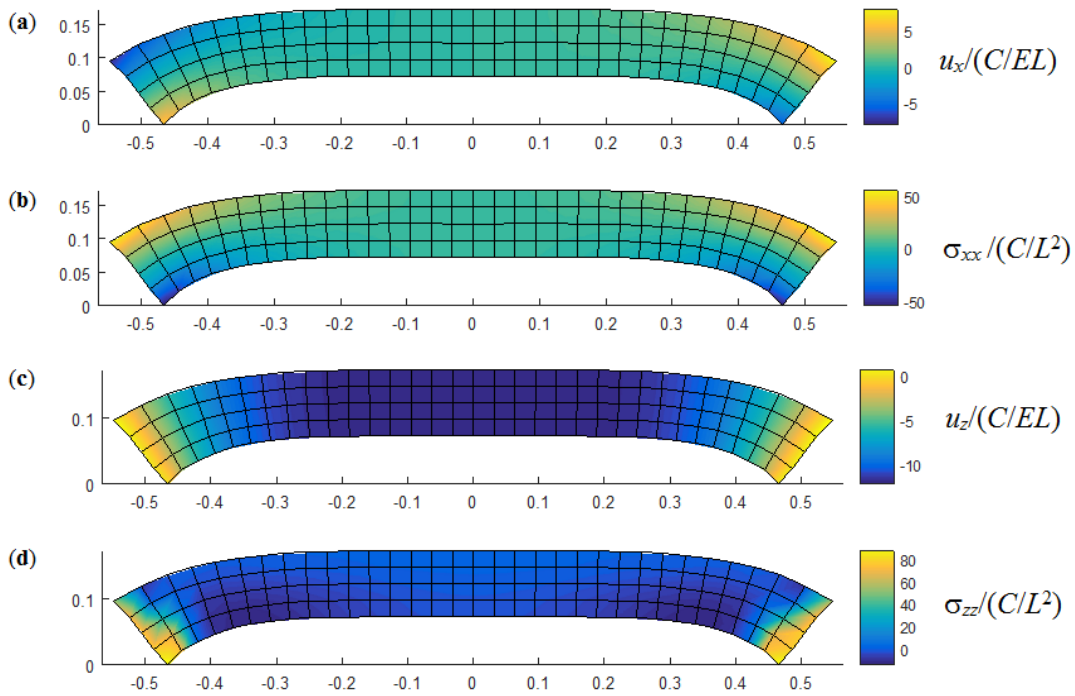

Fig. 3.18. Layer loaded by antisymmetric uniform vertical pressure p_z at ends. Nondimensional values of u_x (**a**), σ_{xx} (**b**), u_z (**c**), and σ_{zz} (**d**) in perfect adhesion.
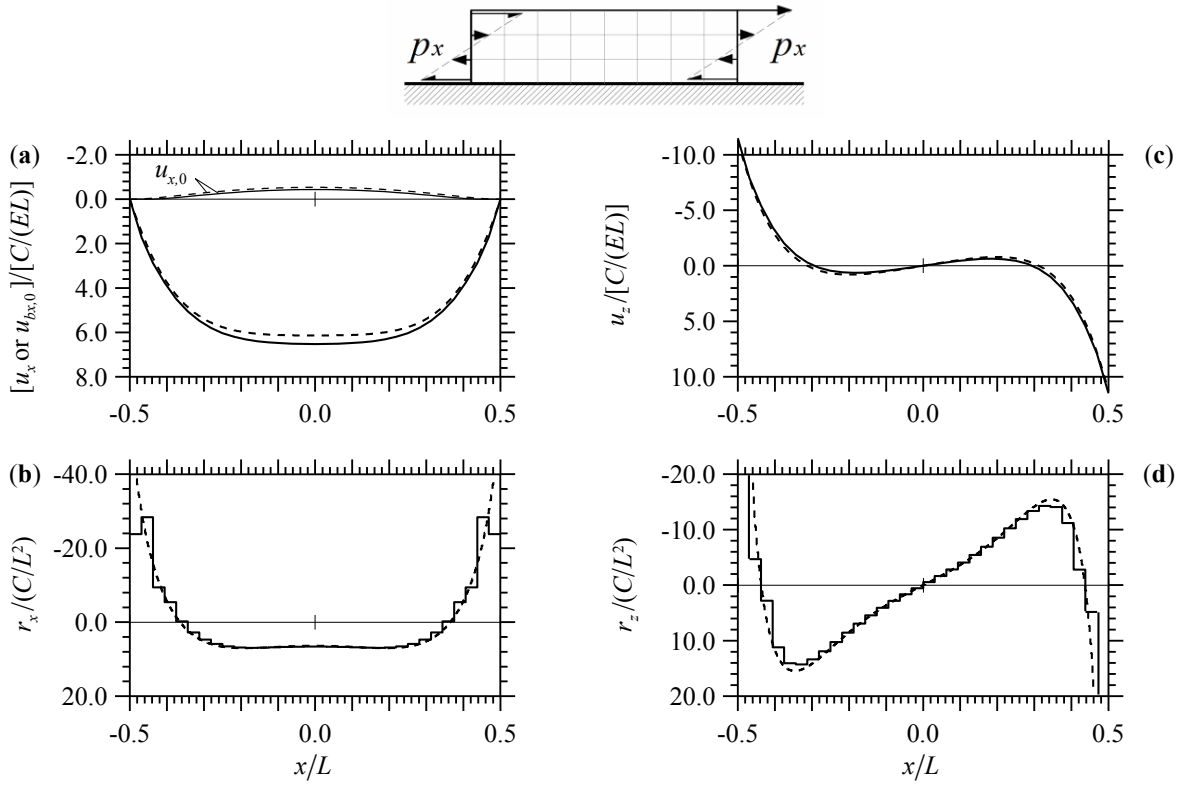
Fig. 3.19. Layer loaded by symmetric uniform horizontal pressure p_x at ends (solid line) and analogous Euler-Bernoulli beam ($L/h = 10$, $\alpha L = 10$) subjected to point P_x at ends (dashed line). Nondimensional values of u_x (**a**), r_x (**b**), u_z (**c**), and r_z (**d**) in perfect adhesion. Horizontal displacement $u_{bx,0}$ is referred to the centreline of layer or beam (respectively thin solid or thin dashed line in (**a**)).

Fig. 3.20. Layer loaded by symmetric uniform horizontal pressure p_x at ends. Nondimensional values of u_x (**a**), σ_{xx} (**b**), u_z (**c**), and σ_{zz} (**d**) in perfect adhesion.

Fig. 3.21. Layer loaded by antisymmetric uniform horizontal pressure p_x at ends (solid line) and analogous Euler-Bernoulli beam ($L/h = 10$, $\alpha L = 10$) subjected to point P_x at ends (dashed line). Nondimensional values of u_x (a), r_x (b), u_z (c), and r_z (d) in perfect adhesion. Horizontal displacement $u_{bx,0}$ is referred to the centreline of layer or beam (respectively thin solid or thin dashed line in (a)).
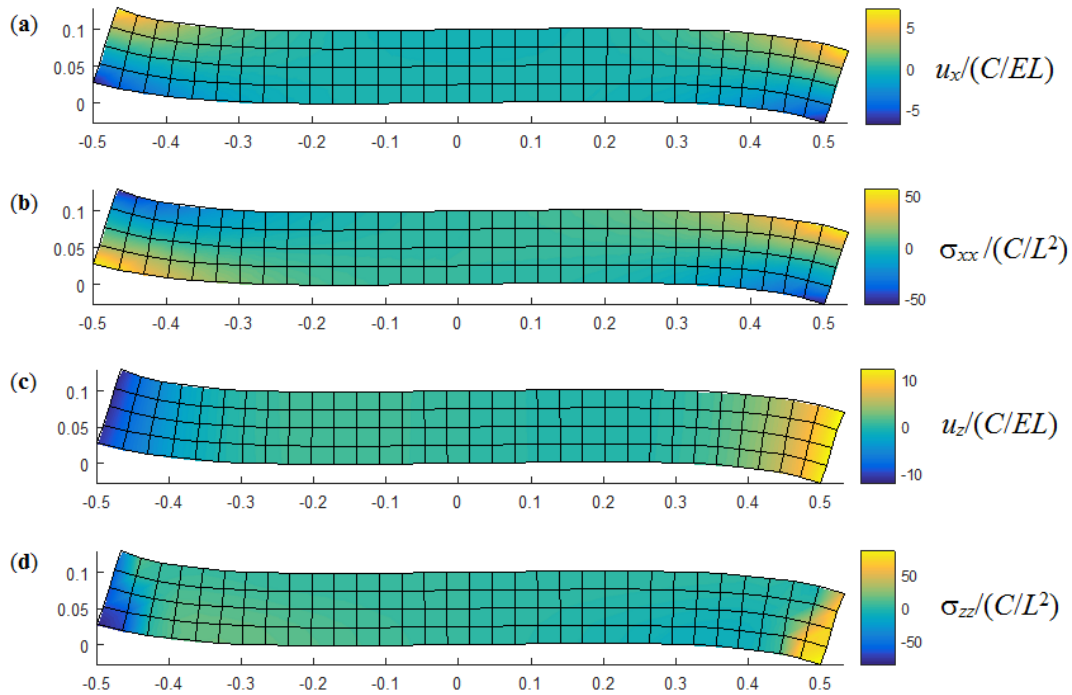

Fig. 3.22. Layer loaded by antisymmetric uniform horizontal pressure p_x at ends. Nondimensional values of u_x (a), σ_{xx} (b), u_z (c), and σ_{zz} (d) in perfect adhesion.

Fig. 3.23. Layer loaded by symmetric varying horizontal pressure p_x at ends (solid line) and analogous Euler-Bernoulli beam ($L/h = 10$, $\alpha L = 10$) subjected to couple C at same sections (dashed line). Nondimensional values of u_x (**a**), r_x (**b**), u_z (**c**), and r_z (**d**) in perfect adhesion. Horizontal displacement $u_{bx,0}$ is referred to the centreline of layer or beam (respectively thin solid or thin dashed line in (**a**)).

Fig. 3.24. Layer loaded by symmetric varying horizontal pressure p_x at ends. Nondimensional values of u_x (**a**), σ_{xx} (**b**), u_z (**c**), and σ_{zz} (**d**) in perfect adhesion.

124

Fig. 3.25. Layer loaded by antisymmetric varying horizontal pressure p_x at ends (solid line) and analogous Euler-Bernoulli beam ($L/h = 10$, $\alpha L = 10$) subjected to couple C at same sections (dashed line). Nondimensional values of u_x (**a**), r_x (**b**), u_z (**c**), and r_z (**d**) in perfect adhesion. Horizontal displacement $u_{bx,0}$ is referred to the centreline of layer or beam (respectively thin solid or thin dashed line in (**a**)).

Fig. 3.26. Layer loaded by antisymmetric varying horizontal pressure p_x at ends. Nondimensional values of u_x (**a**), σ_{xx} (**b**), u_z (**c**), and σ_{zz} (**d**) in perfect adhesion.

3.4.4 Embankment subjects to foundation beam and resting on half-plane soil

A number of researchers have examined the behaviour of reinforced embankments providing the basis for the development of design methods. The current design methods are usually based on limit equilibrium analysis which is relatively simple but can not adequately describe soil-reinforcement interaction. The tensile force of the geogrid is directly related to its service performance. When the tensile force of the geogrid is larger than the anchoring force provided by the resistance on the interface between the geogrid and soil, the geogrid will be pulled out or even be ruptured. The effect, behaviour and design of geosynthetic-reinforced embankments over soil have attracted considerable attention in the literature. Numerical analysis results and laboratory model test of cases with and without reinforcement has been discussed and compared. The results indicate that the reinforcement had a positive effect on embankment stability and did not have an obvious effect on the subsoil response. In other words, geosynthetic reinforcements within an embankment constructed on soft soils can substantially improve stability without influence on settlement, allowing construction to heights in excess of that which would be practicable without reinforcement. The analysis and design of embankments require consideration of soil-structure interaction, where the effectiveness of the reinforcement depend on the relative stress and strain of the embankment-subsoil contact.

An example of embankment, subjected to a load foundation, resting on subsoil is reported. Two embankments with same length $L = 3$ m, but different height H (1 or 0.5 m) are studied with a foundation beam at the top middle and loaded by a vertical force equal to 1000 KN/m downwards and at the midspan. Plane strain state analysis is conducted by assuming the length of the foundation beam 1 m, and ratio length-to-height equal to 10. The foundation is made of concrete having Young's modulus $E_b = 30$ GPa and Poisson's coefficient $\nu_b = 0.2$. Euler-Bernoulli theory is assumed subdividing the beam into 8 uniform FEs. An isotropic elastic material soil is supposed for the embankment and subsoil with mechanic parameter $E_s = 0.2$ GPa and $\nu_s = 0.3$. Perfect adhesion has been set between the contact of the embankment and half-plane soil. Dimensional horizontal, vertical displacements [mm] and tangential, normal reactions [MPa] underneath embankment are reported in Fig. 3.27. In particular, higher values of displacements and reactions are obtained for the lower embankment because of high load pressure near the base of embankment. Notice that, doubling the height of embankment, the maximum tangential reaction (r_x) decreases of 35%, Fig. 3.27b. While, the vertical displacement at the bottom middle of embankment decreases about 20%, Fig. 3.27c, halving the corresponding normal

boundary reaction (r_z), Fig. 3.27d. Moreover, displacements (u_x, u_z) and stresses (σ_{xx}, σ_{zz}) into the embankment are shown in Figs. 3.28 and 3.29 for the dike correspondingly high H = 0.5 m and 1 m. A contraction behaviour turns out along the length of embankment, clearly indicated by opposite sign of horizontal displacements with a strongly difference at the top side. Besides, a peak stress in x-direction occurs at the beam ends. Finally, high vertical displacement and the corresponding stresses in z-direction are reported underneath the beam foundation, where their distribution depend on the beam stiffness.
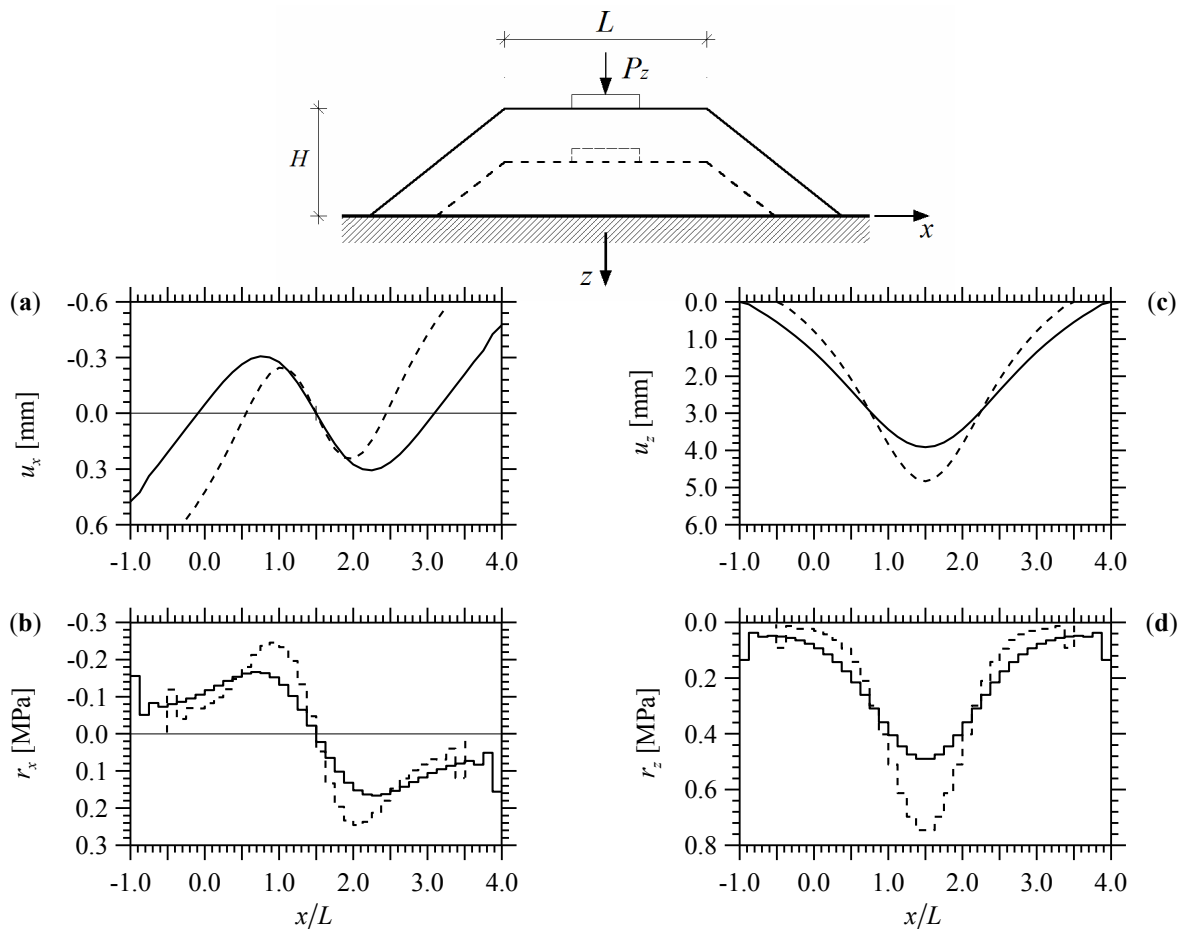
Fig. 3.27. Embankment (L = 3 m) subjected to load foundation (P_z = 1 MN/m) and resting on half-plane soil. Interfacial displacements [mm] (**a**, **c**) and boundary substrate reactions [MPa] (**b**, **d**) of an embankment having height H = 1 m (solid line) and 0.5 m (dashed line).
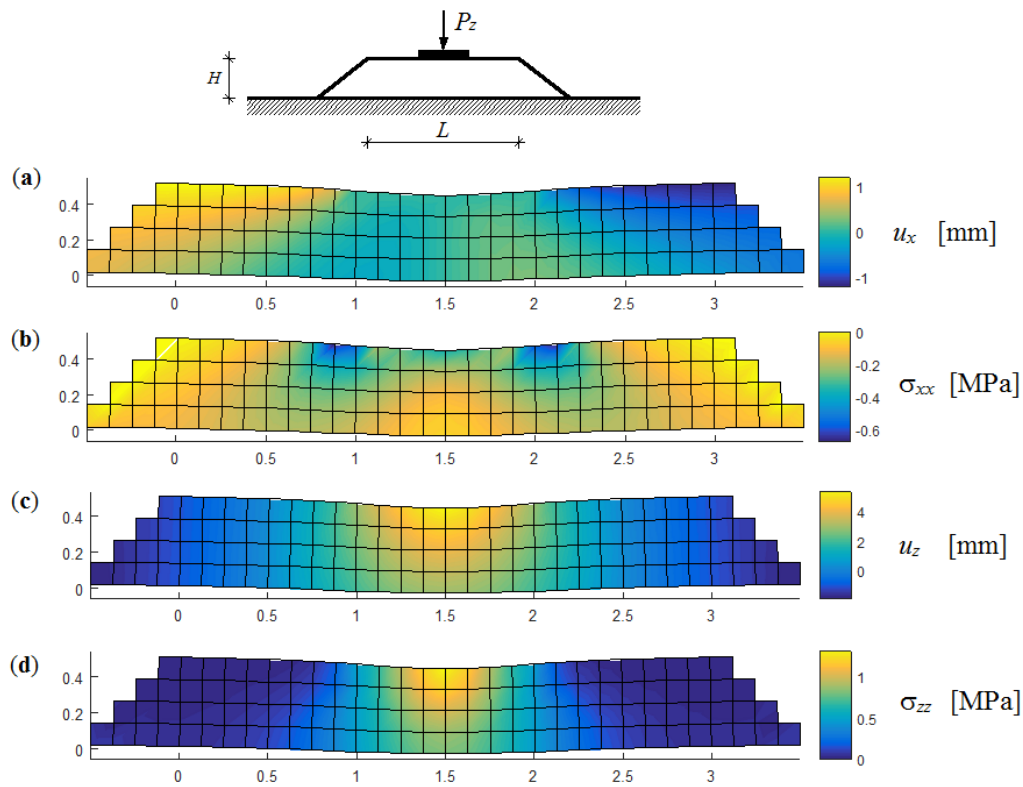
Fig. 3.28. Embankment ($L = 3$ m, $H = 0.5$ m) subjected to load foundation ($P_z = 1$ MN/m) and resting on half-plane soil. Plate displacements [mm] (**a**, **c**) and plate stress [MPa] (**b**, **d**).
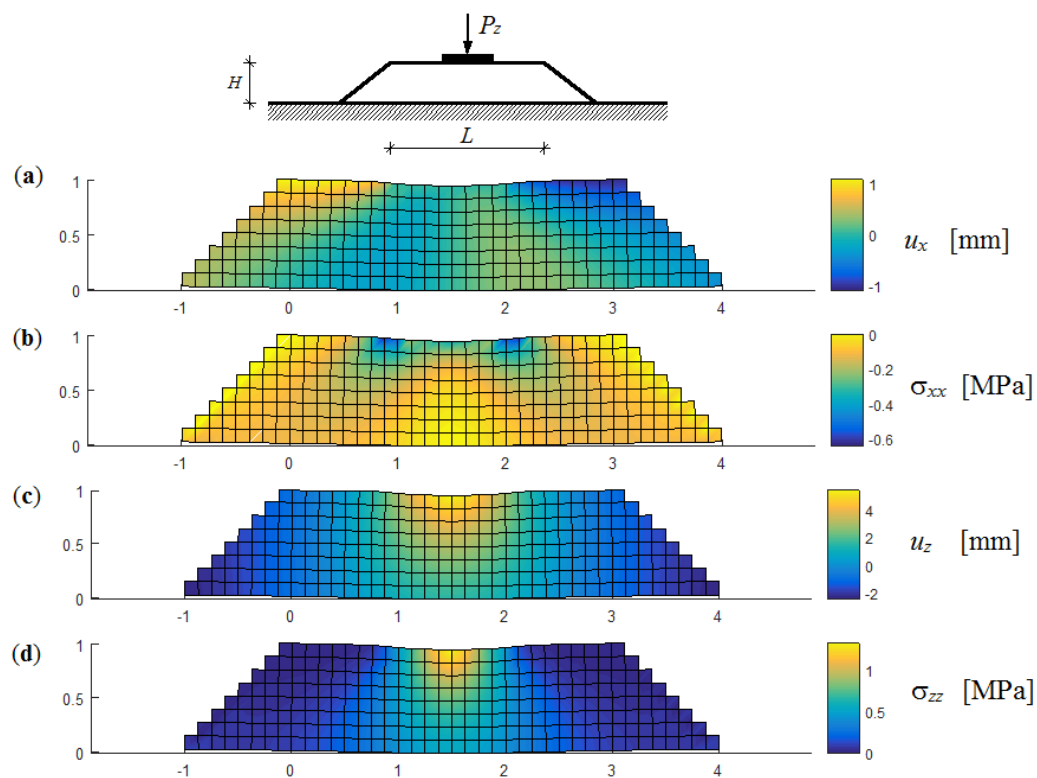
Fig. 3.29. Embankment ($L = 3$ m, $H = 1$ m) subjected to load foundation ($P_z = 1$ MN/m) and resting on half-plane soil. Plate displacements [mm] (**a**, **c**) and plate stress [MPa] (**b**, **d**).

3.5   Conclusions

The couple FE-BIE method is used to evaluate the mechanical behaviour of elastic finite layer bounded in perfect adhesion to a homogeneous half-plane under horizontal or vertical pressure. The FE method is used to describe the plane element of the layer, whereas the behaviour of the semi-infinite substrate has been represented by the BIE approach.

A mixed variational formulation involving the Green function of the half-plane, providing a proper relation between horizontal, vertical displacements and shear, normal interfacial stresses. The proposed method is used to study in detail the contact problem of an elastic quadrilateral element bonded to a half-plane. Displacement field of the quadrilateral element has been interpolated by means of the Lagrange shape function in the four nodes.

Interaction of a stiffener resting on a substrate, adopting two-dimensional finite element (layer) or one-dimensional finite element (beam) for the reinforcement, are analysed with various load condition. A good agreement, in terms of displacements and boundary substrate reactions, is obtained for the system having radio length-to-height of the stiffener $L/h = 10$ and parameter $\alpha L = 10$. Moreover, through the post-processing analysis, plane stresses in x and z direction are calculated showing the tension or compression zones of the layer.

Furthermore, a model of a foundation resting on an embankment which lying on a half-plane subsoil has been proposed. The aim of this analysis is to determine the interfacial stress for the project of geosynthetic reinforcements having mainly the purpose of improving the stability of embankment. The investigation is done with two embankments having the same mechanical properties and length L but different height H. The foundation is discretized by means of a uniform mesh of 8 beam FEs. The load are applied at midspan of the foundation which is collocated at the top middle of the embankment. A mesh with quadrilateral elements is used to descretize the embankment that is bonded in perfect adhesion to the subsoil. The proposed formulation shows to be effective to assess the deformation and soil reactions of an embankment on an elastic subsoil.

References

[1]   Hetenyi M. Beams on Elastic Foundations. University of Michigan Press, Ann Arbor. 1946.

[2]   Selvadurai A P S. Elastic Analysis of Soil-Foundation Interaction. Elsevier, Amsterdam 1979.

[3]   Feda J. Stress in subsoil and method of final settlement calculations. Developments in Geotechnical Engineering Vol. 18. Elsevier, Amsterdam 1978.

[4]   Chandrashekhara K, Antony S J. Theoretical and experimental investigation of framed structure-layered soil interaction problems. Computers and Structures 1993; 48(2): 263–271.

[5]   Keer L M, Dondurs J, Tsai K C. Problems involving a receding contact between a layer and a half space. Journal of Applied Mechanics, Transactions ASME, 1972; 39(4): 1115–1120.

[6]   El-Borgi S, Abdelmoula R, Keer L. A receding contact plane problem between a functionally graded layer and a homogeneous substrate. Int. J. Solids. Struct. 2006; 43: 658–674.

[7]   Ratwani M, Erdogan F. On the plane contact problem for a frictionless elastic layer. Int. J. Solids. Struct. 1973; 9: 921–936.

[8]   Civelek M B, Erdogan F. The axisymmetric double contact problem for a frictionless elastic layer. International Journal of Solids and Structures 1974; 10(6): 639‑659.

[9]   Gecit M R. Axisymmetric contact problem for a semi-infinite cylinder and a half space. International Journal of Engineering Science 1986; 24(8): 1245‑1256.

[10]   Comez I, Birinci A, Erdol R. Double receding contact problem for a rigid stamp and two layers. Eur. J. Mech. A/Solid 2004; 23: 301–309.

[11]   Jaffar M J. Frictionless contact between an elastic layer on a rigid base and a circular flat-ended punch with rounded edge or a conical punch with rounded tip. International Journal of Mechanical Sciences, 2002; 44(3): 545–560.

[12]   Comez I, Erdol R. Frictional contact problem of a rigid stamp and an elastic layer bonded to a homogeneous substrate. Arch Appl Mech 2013; 83:15–24.

[13]   Porter M I, Hills D A. Note on the complete contact between a flat rigid punch and an elastic layer attached to a dissimilar substrate. International Journal of Mechanical Sciences, 2002; 44(3): 509–520.

[14]   Reddy J N. An Introduction to the Finite Element Method. 3rd edn. Mcgraw Hill; Singapore 2006.

[15] Johnson KL. Contact mechanics. Cambridge: Cambridge University Press; 1985.

[16] Chai JC, Miura N, Shen SL. Performance of embankments with and without reinforcement on soft subsoil. Canadian Geotechnical Journal 2002; 39(4): 838–848.

[17] Rowe RK, Soderman KL. Stabilization of Very Soft Soils Using High Strength Geosynthetics: the Role of Finite Element Analyses. Geotextiles and Geomembranes 1987; 6: 53–80.

[18] Rowe RK, Li AL. Geosynthetic-reinforced embankments over soft foundations. Geosynthetics International 2005; 12(1): 50–85.

[19] Palmeira EM, Pereira JHF, Silva ARL. Backanalyses of geosynthetic reinforced embankments on soft soils. Geotextiles and Geomembranes, 1998; 16: 273–292.

[20] Abusharar SW, Zheng JJ, Chen BG, Yin JH. A simplified method for analysis of a piled embankment reinforced with geosynthetics. Geotext. Geomembr. 2009; 27(1): 39–52.

[21] Chen RP, Wang YW, Ye XW, Bian XC, Dong XP, Tensile force of geogrids embedded in pile-supported reinforced embankment: A full-scale experimental study. Geotextiles and Geomembranes 2016; 44: 157–169.

[22] Ferreira A J M. Matlab Codes for Finite Element Analysis, Solid mechanics and its applications. Vol. 157, Springer 2009.

4 Linear and Non-linear static analysis of bar attached to elastic half-plane

4.1 Introduction

In the last few decades, repairing and strengthening of existing structures made of concrete and masonry [1, 2], or rehabilitation of tubular steel structures [3, 4, 5] emerge as a cutting edge issue in structural engineering. The use of Fibre Reinforced Polymer (FRP) strips became more and more common as a technical solution, reducing times of installation with great advantages in terms of structural efficiency. Plenty of studies focus on the issue of strengthening Reinforced Concrete (RC) members with externally bonded FRP sheets [6]. A simply solution of a beam reinforced is presented by Taljsten, Qiao et al. [7, 8] using an elastic linear behaviour for the adhesive interface. In particular, the effect of the deformation has been studied assuming the Euler-Bernoulli theory, transferring normal and tangential stresses from the top and bottom adhered through a thin adhesive layer bonded perfectly.

In the present chapter, the problem of a reinforcement attached to an infinite substrate has been reconsidered under the hypothesis no perfect adhesion between two bodies. A couple Finite Element-Boundary Integral Equation (FE-BIE) model is implemented, assuming a jump of displacement (slip) between the two elements. The contact link between reinforcement and substrate, so-called *"weak interface"*, is firstly assumed linearly proportional to the interface reactions. Comparing some numerical results with analytic solution in the literature, results show how the interface stiffness influences the displacements and reactions solutions. The problem of transmission of stress in the case with a concentrated force acting on the middle of a reinforcement have been calculated and checked with the close-form of Melan's solution [9], who, in 1932, determined the interface tangential stress between a infinite stiffener and an infinite linear elastic sheet. Several authors have reconsidered and extended the Melan's soluction, especially in the field of reinforcing aircraft structures and, later, in the field of fibro-reinforced composites. Russian schools have also studied the previously cited work, their numerous contributions are summarized in Grigolyuk and Tolkachev [10].

A non-linear analysis of the proposed numerical model is adopted for simulating the debonding in FRP-strengthened reinforced concrete substrate. The mechanical properties

of adhesive interaction between composite strip and substrate can be obtained throughout pull-out tests, adopting different layouts such as single slipping test with fixed back side [11] or double pull-out shear schemes [12], to predict an intermediate crack (IC) [13] and critical diagonal crack (CDC) [14] debonding failure. Theoretical models are currently available to simulate the debonding failure. Closed-form solutions [15, 16], numerical models [17, 18], as well as codes and standards issues derived from simplified mechanical models calibrated by means of experimental results [19], are generally aimed at predicting the bond-slip response of FRP strips glued to substrate. These formulations are generally based on adopting "*a priori*" analytical expression for describing the interface bond-slip law, assuming a fracture process in pure "mode II", disregarding the effect of interface normal stress (peeling) and occurrence of out-of-plane displacement (uplift). Although, the interface peeling stress and uplift, experimentally observed through advanced optical systems [20], are developed by eccentricity between applied force and interface. Recently models [21, 22] have demonstrated, taking into these components which affect the ultimate bearing capacity of the adhesive joint, a negligible influence on the distribution of interface slips throughout the contact.

A comparison of the present model, with experimental results and the prediction of another model found in the literature, is made to validate the novel aspect based on assuming "*a priori*" of a bilinear bond-slip law applied into the FE-BIE method, simulating the behaviour of the adhesive interface in pure mode II.

4.2   Variational formulation

An elastic bar with length L and cross section A attached on an elastic half-plane is considered, as shown in Fig. 4.1. Reference is made to a Cartesian coordinate system (O, x, z) centred at the middle of bar, with the vertical axis z directed toward the half-plane and the x-axis placed along the interface. Both the bar and the semi-infinite substrate are made of homogeneous and isotropic solids. Where elastic constants E_b and ν_b are the Young's modulus and Poisson's coefficient of the bar, whereas E_s and ν_s characterise the substrate. Generalised plane stress or plane strain regime can be considered in the present formulation. For the later state, the width of the half-plane b will be assumed unitary. The thickness of the coating is assumed thin, so making possible to neglect its bending stiffness. Being ignored the vertical component of reactions (peeling stress), only shear

stress $r_x(x)$ occurs along the contact region. The system is subjected to a generically distributed horizontal load $p_x(x)$ or thermal variation $\Delta T(x)$.

Unlike of the contact between bar and half-plane proposed by Tullini, et al. [23], the adhesion could be considered as a third material with its mechanical characteristics. This assumption involves the development of bar and half-plane displacements, $u_{x,b}$ and $u_{x,s}$.
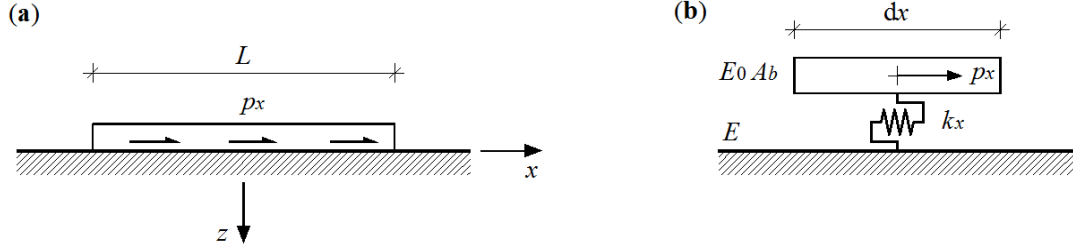

Fig. 4.1. Bar weakly attached on semi-infinite substrate (**a**), and free-body diagram (**b**).

4.2.1 Total potential energy for the bar

Using the strain components $\varepsilon_x = u'_x(x)$ and the constitutive laws $\sigma_{x,b} = E_0\,\varepsilon_x(x)$. The strain energy of a bar long L, in terms of mechanical and thermal components of axial strain [24], can be written as follows:

$$U_{\text{bar}} = \int \sigma_{x,b}\,d\varepsilon = \frac{1}{2}\int_L E_0 A(x)\,[u'_x(x) - \alpha_0 \Delta T]^2\,dx, \tag{4.1}$$

where the Young's modulus of bar and coefficient of thermal expansion are correspondently $E_0 = E_b$, $\alpha_0 = \alpha_b$ for a generalized plane stress or $E_0 = E_b/(1-v_b^2)$, $\alpha_0 = (1+v_b)\alpha_b$ for plane strain state. It is worth noting that axial force in the bar is $N(x) = E_0 A(x)[u'_x(x) - \alpha_0 \Delta T]$ and prime denotes differentiation with respect to x.

Thus, the potential energies for the bar Π_{bar} can be written as the strain energy U_{bar} minus the work related to the external loads, as following

$$\Pi_{\text{bar}} = U_{\text{bar}} - b\int_L [p_x(x) - r_x(x)]\,u_x(x)\,dx. \tag{4.2}$$

4.2.2 Total potential energy for the substrate

The solutions of the elastic problem for a homogeneous isotropic half-plane loaded by a point force to its boundary are known as Flamant or Cerruti solutions [25]. In particular,

the horizontal displacement $u(x)$ due to the interfacial tractions acting along the boundary between the half-plane and the bar can be found by integrating

$$u_x(x) = \int_L g(x,\hat{x}) r_x(\hat{x}) d\hat{x}, \tag{4.3}$$

where the Green function $g(x,\hat{x})$ can be expressed

$$g(x,\hat{x}) = -\frac{2}{\pi E} \ln \frac{|x - \hat{x}|}{d}. \tag{4.4}$$

In Eq. (4.4), $E = E_s$ or $E = E_s/(1 - v_s^2)$ in the plane stress or plane strain, respectively, and d is an arbitrary length associated with a rigid displacement.

Using the theorem of work and energy for exterior domains [26], the strain energy stored in the half-plane is

$$U_{\text{soil}} = \frac{b}{2} \int_L r_x(x) \, u_x(x) \, d\,x, \tag{4.5}$$

hence the potential energy of the half-plane Π_{soil} can be rewritten as the strain energy U_{soil} minus the work related to the external loads

$$\Pi_{\text{soil}} = U_{\text{soil}} - b \int_L r_x(x) \, u_x(x) \, d\,x, \tag{4.6}$$

replacing the Eq. (4.3) into the Eq. (4.6) is obtained

$$\Pi_{\text{soil}} = -\frac{b}{2} \int_L r_x(x) \, d\,x \int_L g(x,\hat{x}) \, r_x(\hat{x}) \, d\,\hat{x}. \tag{4.7}$$

4.2.3   Total potential energy for the adhesive

Adding the interface energy into the total potential energy of the system, it can be described also the behaviour of adhesive between the contact surface and of many kinds of not perfect bonding such as fractured and damaged. In fact, when a stiffener is glued to a support by an adhesive, there is a jump of displacement which is proportional to the transmission stress, although the continuity of the tension is maintained for equilibrium. Therefore, assuming the transmission stress linearly depends on the jump of displacement Δu_x between bar and half-plane displacement as

$$r_x = k_x(u_{x,b} - u_{x,s}) = k_x \Delta u_x, \tag{4.8}$$

where parameter k_x summarizes mechanical characteristics of the interface, and it can be resolved from elastic moduli of the interface on the basis of formulas reported [9]. The variation of displacement Δu_x between bar and half-plane can be written as

$$\Delta u_x = \frac{r_x}{k_x}.$$

(4.9)

Noting that from a physical point of view, this interface energy is like the energy of a lot of springs spreadable between bar and half-plane. Assuming the complementary energy, it may be written as

$$\Pi_{\text{spring}} = -\frac{b}{2}\int_L r_x\,\Delta u_x\,dx = -\frac{b}{2}\int_L \frac{r_x^2}{k_x}.$$

(4.10)

4.2.4 Total potential energy for the bar-adhesive-substrate system

Maxing use of Eqs. (4.2), (4.7) and (4.10), the total potential energy of the whole system turns out to be

$$\Pi(u_x, r_x) = \Pi_{\text{bar}} + \Pi_{\text{soil}} + \Pi_{\text{spring}},$$

(4.11)

which is a mixed variational formulation represented by bar displacement $u_x = u_{x,b}$ and interfacial shear tractions r_x along the contact region. Nonetheless Eq. (4.11) has been suggested to axially study, namely bar resting on elastic half-plane, similar variational formulation could also be applied for a Timoshenko beam underlying soil [27]. Useful mathematical references of contact problem are found [28, 29, 30], where the variational problem and the corresponding Galerkin solution is well-posed.

4.3   Finite element model

The bar and substrate are subdivided into FEs of length $l_i = |x_{i+1} - x_i|$ where x_{i+1} is end and x_i initial coordinates. Axial displacements field u_x are characterized in each finite element by vector $\mathbf{N}(\xi)$ which containing the shape functions, and by nodal displacements $\mathbf{u}_{xi}$, as shown

$$u_x(\xi) = [\mathbf{N}(\xi)]^T \mathbf{u}_{xi},$$

(4.12)

where $\xi = x/l_i$ represents the dimensionless local coordinate. Using a set of linear Lagrange polynomials, where the shape functions $N_i(\xi)$ are $N_1 = 1-\xi$ and $N_2 = \xi$, or quadratic Lagrange polynomials by means of $N_1 = 1-3\xi+2\xi^2$, $N_2 = 4\xi(1-\xi)$ and $N_3 = \xi(2\xi-1)$.

The mesh of the half-plane boundary can be defined independently of the bar, but similar subdivision has been adopted. The approximation soil reaction can be described as

$$\mathbf{r}_x(\xi) = [\boldsymbol{\rho}(\xi)]^T \, \mathbf{r}_{x,i}, \tag{4.13}$$

where $\mathbf{r}_{x,i}$ is the known vectors of nodal substrate reaction while $\boldsymbol{\rho}(\xi)$ assembles the shape functions.

Substituting Eqs. (4.12) and (4.13) in variational principle (4.11) and assembling over all the elements, the potential energy takes the expression

$$\Pi(\mathbf{u}_x, \mathbf{r}_x) = \frac{1}{2}\mathbf{u}_x{}^T\mathbf{K}_a\,\mathbf{u}_x - \mathbf{u}_x{}^T\mathbf{f}_x + \mathbf{u}_x{}^T\mathbf{H}_{xx}\,\mathbf{r}_x - \frac{1}{2}\mathbf{r}_x{}^T\mathbf{G}_{xx}\,\mathbf{r}_x - \frac{1}{2}\mathbf{r}_x{}^T\mathbf{G}_{kx}\,\mathbf{r}_x, \tag{4.14}$$

where $\mathbf{K}_a$ is the bar stiffness matrix and $\mathbf{f}_x$ the external load vector, whose elements take the usual form

$$k_{a,ij} = l_i \int_0^1 E_0 A_b(\xi)\, N'_{a,i}(\xi) N'_{a,j}(\xi)\, \mathrm{d}\xi, \tag{4.15}$$

$$f_{x,i} = l_i \int_0^1 \left(N_{a,i}(\xi)\, p_x(\xi)\, b + N'_{a,i}(\xi)\, E_0 A_b(\xi)\, \alpha_0 \Delta T \right) \mathrm{d}\xi. \tag{4.16}$$

The components of matrices $\mathbf{H}_{xx}$ and $\mathbf{G}_{xx}$ are given by the following expressions

$$h_{xx,ij} = b l_i \int_0^1 N_{a,i}(\xi)\,\rho_{a,j}(\xi)\,\mathrm{d}\xi, \tag{4.17}$$

$$g_{xx,ij} = b \int_{x_i}^{x_{i+1}} \rho_{a,i}(x)\,\mathrm{d}x \int_{x_j}^{x_{j+1}} g(x,\hat{x})\,\rho_{a,j}(\hat{x})\,\mathrm{d}\hat{x}. \tag{4.18}$$

Imposing the potential energy functional to be stationary, the solution of the problem is given by

$$\frac{\mathrm{d}\Pi}{\mathrm{d}\mathbf{u}_x} = \mathbf{K}_a\mathbf{u}_x - \mathbf{f}_x + \mathbf{H}_{xx}\,\mathbf{r}_x = 0, \qquad \frac{\mathrm{d}\Pi}{\mathrm{d}\mathbf{r}_x} = \mathbf{H}_{xx}{}^T\mathbf{u}_x - \mathbf{G}_{xx}\,\mathbf{r}_x - \mathbf{G}_{kx}\,\mathbf{r}_x = 0, \tag{4.19a,b}$$

it can be written in matrix form as following

$$\begin{bmatrix} \mathbf{K}_a & \mathbf{H}_{xx} \\ \mathbf{H}_{xx}{}^T & -(\mathbf{G}_{xx}+\mathbf{G}_{kx}) \end{bmatrix} \begin{Bmatrix} \mathbf{u}_x \\ \mathbf{r}_x \end{Bmatrix} = \begin{Bmatrix} \mathbf{f}_x \\ \mathbf{0} \end{Bmatrix}. \tag{4.20}$$

The solution of Eq. (4.20) provides the nodal displacements and tractions

$$\mathbf{r}_x = (\mathbf{G}_{xx} + \mathbf{G}_{kx})^{-1} \mathbf{H}_{xx}^{\mathrm{T}} \mathbf{u}_x, \tag{4.21}$$

$$(\mathbf{K}_a + \mathbf{K}_{\text{soil}}) \mathbf{u}_x = \mathbf{f}_x, \tag{4.22}$$

where $\mathbf{K}_{\text{soil}}$ is the stiffness matrix for the substrate in the weak interface condition, defined as:

$$\mathbf{K}_{\text{soil}} = \mathbf{H}_{xx} (\mathbf{G}_{xx} + \mathbf{G}_{kx})^{-1} \mathbf{H}_{xx}^{\mathrm{T}}. \tag{4.23}$$

The Eq. (4.22) represents the discrete system of equations governing the response of the bar-adhesive-substrate system.

In the case of a bar detached from the substrate between the nodes d_1 and d_2, no shear stress is transmitted, the bar stiffness matrix $\mathbf{K}_a$ is assembled as usual and system (4.20) can be partitioned as follows:

$$\begin{bmatrix} & & & \mathbf{H}_{xx,L} \\ & \mathbf{K}_a & & \mathbf{0} \\ & & & \mathbf{H}_{xx,R} \\ \mathbf{H}_{xx,L}^{\mathrm{T}} & \mathbf{0} & \mathbf{H}_{xx,R}^{\mathrm{T}} & -(\mathbf{G}_{xx} + \mathbf{G}_{kx}) \end{bmatrix} \begin{Bmatrix} \mathbf{u}_{x,L} \\ \mathbf{u}_{x,d} \\ \mathbf{u}_{x,R} \\ \mathbf{r}_x \end{Bmatrix} = \begin{Bmatrix} \mathbf{f}_{x,L} \\ \mathbf{f}_{x,d} \\ \mathbf{f}_{x,R} \\ \mathbf{0} \end{Bmatrix}, \tag{4.24}$$

where $\mathbf{u}_{x,L} = [u_{x,L1}, \ldots, u_{x,Ln}]^{\mathrm{T}}$ and $\mathbf{u}_{x,R} = [u_{x,R1}, \ldots, u_{x,Rn}]^{\mathrm{T}}$ are the nodal displacements at the left and right side of the detached region having nodal displacements $\mathbf{u}_{x,d} = [u_{x,d1}, \ldots, u_{x,dn}]^{\mathrm{T}}$ and $\mathbf{f}_{x,L}$, $\mathbf{f}_{x,R}$ and $\mathbf{f}_{x,d}$ are the corresponding external load vectors. Moreover, tractions r_x as well as matrices $\mathbf{H}_{xx,L}$, $\mathbf{H}_{xx,R}$ are defined in the bar FEs attached to the substrate only. The set of the vectors $\mathbf{u}_{x,L}$, $\mathbf{u}_{x,d}$ and $\mathbf{u}_{x,R}$ give the total vector $\mathbf{u}_x$.

4.3.1 Prismatic bar subjected to uniform loads and thermal variation

As for the discrete problem, a prismatic bar element subjected to uniform loads p_x and thermal variation with one constant substrate pressure has been considered. Bar stiffness matrix $\mathbf{K}_a$, vector of equivalent external load $\mathbf{F}_x$ and matrix $\mathbf{H}_{xx}$ can be rewritten for the case of Lagrange linear functions as

$$\mathbf{K}_{a,i} = \frac{E_0 A}{l_i} \begin{bmatrix} 1 & -1 \\ -1 & 1 \end{bmatrix}, \tag{4.25a}$$

$$\mathbf{F}_{x,i} = p_x b \, l_i / 2 [1,1]^{\mathrm{T}} + E_0 A \alpha_0 \Delta T [1,1]^{\mathrm{T}}, \tag{4.25b}$$

$$\mathbf{H}_{xx,i} = b \, l_i / 2 [1,1]^{\mathrm{T}}, \tag{4.25c}$$

while for Lagrange quadratic functions as

$$\mathbf{K}_{a,i} = \frac{E_0 A}{3 l_i} \begin{bmatrix} 7 & -8 & 1 \\ -8 & 16 & -8 \\ 1 & -8 & 7 \end{bmatrix},$$

(4.26a)

$$\mathbf{F}_{x,i} = p_x b \, l_i / 6 [1, 4, 1]^{\mathrm{T}} + E_0 A \alpha_0 \Delta T [-1, 0, 1]^{\mathrm{T}},$$

(4.26b)

$$\mathbf{H}_{xx,i} = b \, l_i / 6 \, [1, 4, 1]^{\mathrm{T}}.$$

(4.26c)

Finally, components of matrix $\mathbf{G}$ are as follows

$$g_{ii} = \frac{2b}{\pi E} l_i^2 \left(\frac{3}{2} - \ln l_i \right),$$

(4.27a)

$$g_{ij} = \frac{2b}{\pi E} \left[\frac{3}{2} l_i l_j + G(x_{j+1} - x_{i+1}) - \right.$$

$$\left. G(x_{j+1} - x_i) - G(x_j - x_{i+1}) + G(x_j - x_i) \right] \quad \text{for } i \neq j,$$

(4.27b)

where $G(x) = x^2/2 \ln|x|$ and parameter d has been omitted since a rigid-body displacement.

4.3.2   Solution and post-computation

The solution of the FE-BIE analysis, Eq. (4.20), gives nodal displacement of bar $u_x = u_{x,b}$ and substrate reaction r_x. Once the nodal values of the primary variables are known, we can use their to computer the desired quantities, such as the axial force N and the displacement of the substrate $u_{x,s}$. This process of computing is termed post-computation or post-processing, these words are meant to indicate that further computations are made after obtaining the solution of the equation system. It is worth noting that the derivative du_{xi}/dx of the approximation u_{xi} based on Lagrange interpolation is discontinuous, for any order element. The error of the strain ε, therefore axial force of the bar N, decreases when increasing the number of elements and/or the degree of interpolation.

In summary, the general flow of the proposed analysis of reinforcement bar resting on elastic substrate requires that the following steps be taken:

- discretize the bar element and the underlying substrate by dividing them into FEs;

- calculate element matrices $\mathbf{K}_{ai}$, $\mathbf{H}_{xxi}$ and vectors $\mathbf{f}_{xi}$ for every element;

- assemble element matrices $\mathbf{K}_{ai}$ and vectors $\mathbf{f}_{xi}$ into the global matrix $\mathbf{K}_a$ and vector $\mathbf{f}_x$;

- assemble element matrices $\mathbf{H}_{xxi}$ into the global matrix $\mathbf{H}_{xx}$ and calculate global matrix $\mathbf{G}_{xxi}$ and $\mathbf{G}_{kxi}$;
- apply possible constraints to global matrix and vector as usual;
- solve the matrix equation Eq. (4.20) or Eq. (4.24) for the primary variables $u_{x,b}$ and r_x;
- compute secondary variable $u_{x,s}$ and N.

4.4   Numerical Examples

Several loading cases of a bar with weak interface to the underlying half-plane are considered and discussed. Moreover they are compared with cases of perfect bonding. Similarly to [10] and to [23], the parameter characterising the elastic response of the bar-substrate system is taken as

$$\beta L = \frac{E\,b\,L}{E_0 A}.$$
(4.28)

Low values of βL characterise short bar and stiffer than the substrate. The bar performs like an almost inextensible stiffener. Increase the values of βL, the bar become more flexible than the substrate. Then long bar bonded to stiff substrate, the values of βL is high.

Introducing a new parameter γL which regard the weak interface.

$$\gamma L = \sqrt{\frac{k_x L^2}{E_0 A}},$$
(4.29)

where k_x is the spring stiffness, representing the presence of third material, i.e. the layer of glue between bar and support.

4.4.1   Bar loaded by a single horizontal point force at midpan or one end

This section, a bar subject to a horizontal concentrated force P_x applied at midspan, comparing with analytic solution given by Melan, or at one end section are considered. A number of 512 uniform finite elements is used, adopting quadratic Lagrange polynomials as shape functions for bar element including one equal constant substrate element.

A simply uniform subdivision of mesh might not be able to describe a correctly behaviour at end section and close the concentrate force. In order to obtain accurate results, a power graded mesh is used, as was proposed in the Chapter 1, characterized by a grading exponent β_{exp}. It is worth noting that the refinement mesh turns out uniform using a unitary

grading exponent, while with values of $\beta_{exp} > 1$, elements close to end sections become smaller and those ones near the midpoint become bigger. Hence the results at midspan are not accurate. To get around this trouble, the graded mesh formulation [31] has been used twice along bar length, into the interval [-0.5, 0]/L and [0, +0.5]/L. So in this section, coordinate x_j of the generic jth node of the mesh is given by following expression

$$
x_j = \begin{cases} \dfrac{1}{2}\left[\dfrac{1}{2}\left(\dfrac{2j}{n_{el}/2}\right)^{\beta_{exp}}\right] & \text{if } 0 \le j \le n_{el}/4 \\[3mm] \dfrac{1}{2} - x_{n_{el}/2-j} & \text{if } n_{el}/4 < j \le n_{el}/2 \\[3mm] \dfrac{1}{2} + x_{j-n_{el}/4} & \text{if } n_{el}/2 < j \le n_{el} \end{cases}
\tag{4.30}
$$

being n_{el} the total number of FEs. Uniform mesh is obtained by assuming $\beta_{exp} = 1$.

4.4.1.1 Bar loaded by horizontal point force P_x at midspan

Dimensionless axial displacement $u_x/(P_x/E)$, axial force N/P_x and shear reaction $r_x/(P_x/L)$ are reported versus the dimensionless abscissa x/L. In particular, perfect and weak bonding are plotted in Figs. 4.2, 4.3 and 4.4, assuming value of parameter βL equal to 1, 10, 100, respectively. The weak interface cases are reported with parameter $\gamma L = 5$ (solid line), whereas the perfect bonding (dashed line, $\gamma L = \inf$.) was calculated by Tullini et al. [23].

The case with $\beta L = 1$, in Fig. 4.2, shows the behaviour of an inextensible bar. Even though value of γL is low, bar displacement $u_{x,b}$, axial force and shear reaction of the weak interface case are similar to perfect bonding results. Only substrate displacement $u_{x,s}$, appearing in the weak contact, is higher and tends to the value of bar displacement $u_{x,b}$ when the parameter γL increased.

With the same parameter γL and rising βL, bar displacements of the weak interface increase, whereas substrate displacements decrease, Figs. 4.3a and 4.4a. Axial force keeps more or less a linearly behaviour along bar, exhibiting a discontinuity in correspondence at the point of load application. Basically, this linear effect turns out when interface boundary is low, Figs. 4.3b and 4.4b. In presence of a flexible bar, shear reactions assume low values, except at bar end and around load section. The peak of stresses is reduced with the weak contact, Figs. 4.3c and 4.4c, spreading tractions along the length of contact.

Using a graded mesh with $n_{el} = 256$ and $\beta_{exp} = 3$, by means of quadratic Lagrange polynomials as shape functions of the bar element, including one equal constant substrate

element. Bar displacements and substrate reactions at the midpoint versus parameter βL and γL are reported on logarithmic scale in Fig. 4.5 and 4.6, respectively. The bar displacement behaviour is linear versus βL and quite constant versus γL, when the parameter βL is lower than 10. While, for higher values of βL, the linearity occurs reaching a enough high value of γL. Substrate reactions at the midpoint are compared with Melan's solution, given by Lenci who considered an isotropic elastic infinite sheet [9].

The general distribution of tangential reaction r_x of Melan's problem in the weak interface can be obtained from
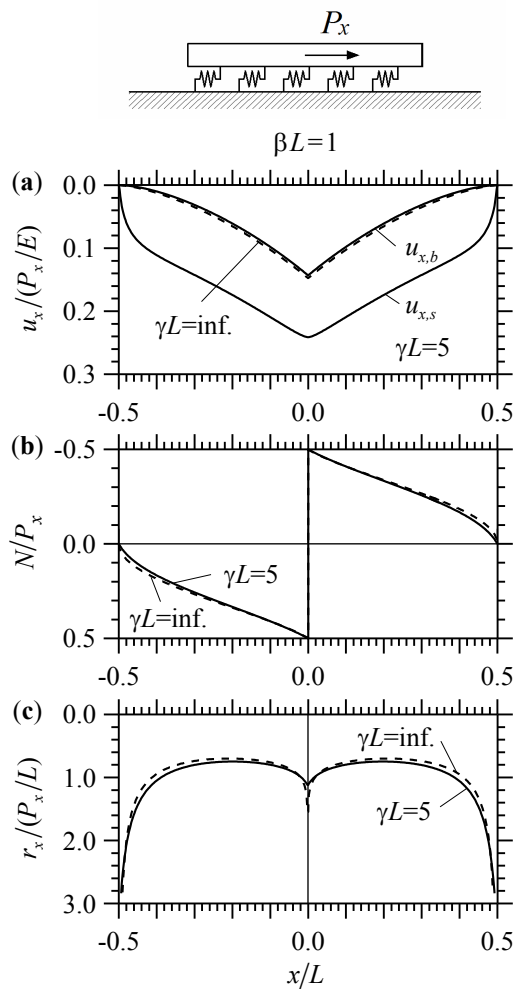
Fig. 4.2. Bar ($\beta L = 1$) loaded by a point force P_x at midspan. Nondimensional values of u_x (**a**), N (**b**) and r_x (**c**) versus x/L for weak (solid line) and perfect contact (dashed line).
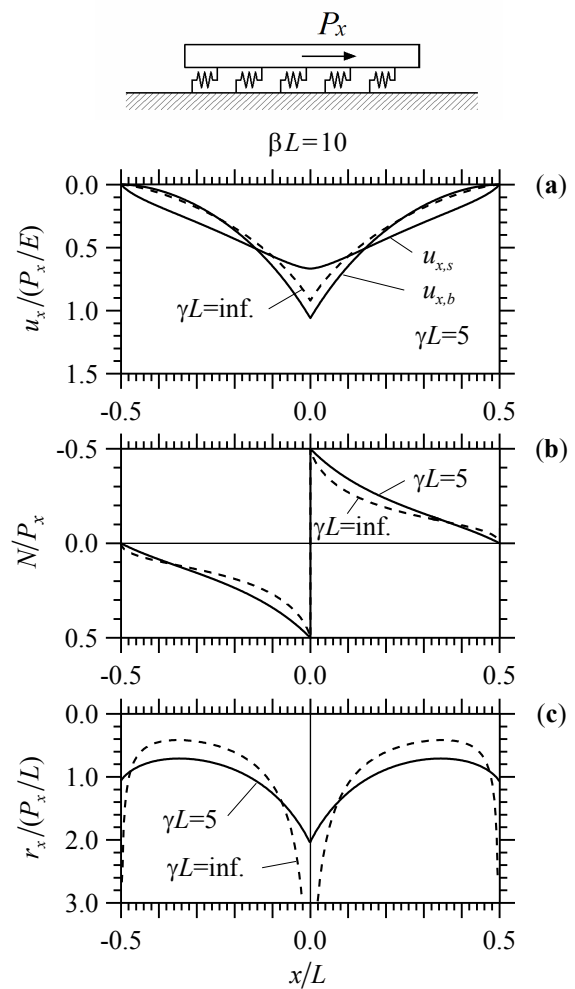
Fig. 4.3. Bar ($\beta L = 10$) loaded by a point force P_x at midspan. Nondimensional values of u_x (**a**), N (**b**) and r_x (**c**) versus x/L for weak (solid line) and perfect contact (dashed line).

$$\hat{r}_x(s) = P_x \frac{1}{\dfrac{s^2}{(\gamma L)^2} + \dfrac{2}{\beta L}|s| + 1},$$

(4.31)

using the inverse Fourier transform $\hat{f}(x) = \dfrac{1}{2\pi}\displaystyle\int_{-\infty}^{\infty}\hat{f}(s)e^{-isx}ds$, then the Eq. (31) can be

expressed in x coordinate as following

$$r_x(x) = \frac{P_x}{2L\pi}\frac{\gamma L}{\sqrt{(\gamma L / \beta L)^2 - 1}}\left[g(x\alpha_1) - g(x\alpha_2)\right],$$

(4.32)
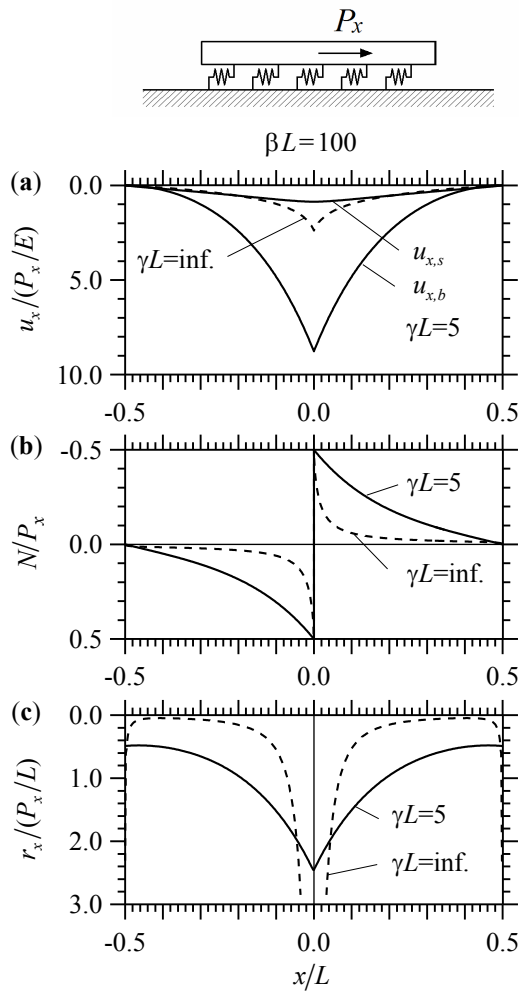
Fig. 4.4. Bar ($\beta L = 100$) loaded by a point force P_x at midspan. Nondimensional values of u_x (**a**), N (**b**) and r_x (**c**) versus x/L for weak (solid line) and perfect contact (dashed line).
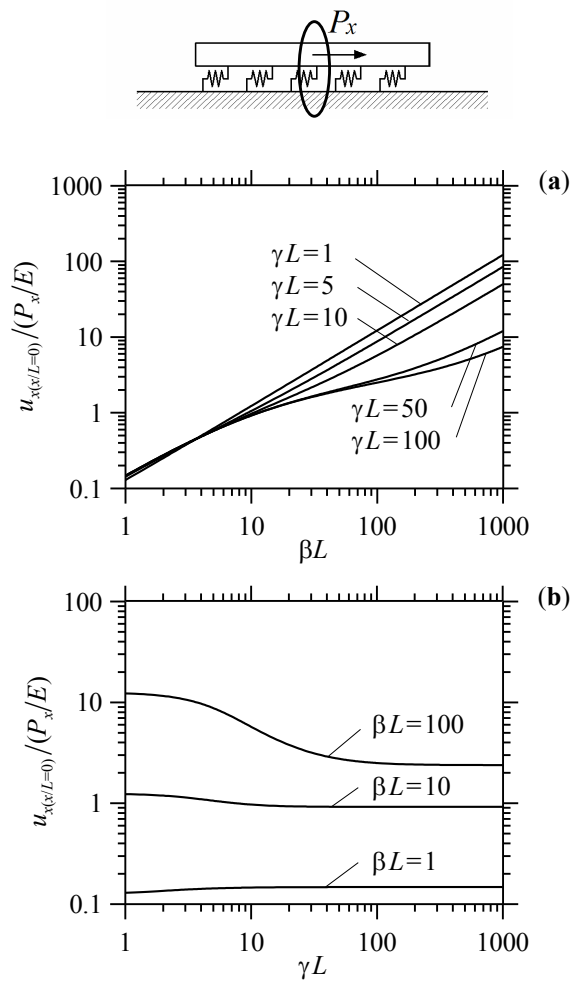
Fig. 4.5. Bar loaded by a point force P_x at midspan. Nondimensional value of u_x at the bar midpoint $x/L = 0$ versus βL (**a**) and γL (**b**).

where the constants α_1 and α_2 are

$$\alpha_1 = \frac{1}{L}\frac{(\gamma L)^2}{\beta L}\left(1-\sqrt{1-(\beta L/\gamma L)^2}\right), \qquad \alpha_2 = \frac{1}{L}\frac{(\gamma L)^2}{\beta L}\left(1+\sqrt{1-(\beta L/\gamma L)^2}\right), \qquad (4.33\text{a,b})$$

while $g(x) = -\sin(x)si(x) - \cos(x)ci(x)$, with the sine integral $si(x)$ and the cosine integral $ci(x)$ express as

$$si(x) = -\int_x^\infty \frac{\sin(z)}{z}dz, \qquad ci(x) = -\int_x^\infty \frac{\cos(z)}{z}dz. \qquad (4.34\text{a,b})$$

In the positive part of the x-axis, the transmission stress $r_x(x)$ is a decreasing function vanishing for $x \to \infty$. Therefore the maximum value is in $x = 0$ ($r_{x,max} = r_x(0)$). In the general case with k_x, the Eq. (4.32) becomes

$$\lim_{x\to 0} r_x(x) = r_{x,max} = \frac{P_x}{2L\pi}\frac{\beta L}{\sqrt{1-(\beta L/\gamma L)^2}}\ln\left[\frac{1+\sqrt{1-(\beta L/\gamma L)^2}}{1-\sqrt{1-(\beta L/\gamma L)^2}}\right]. \qquad (4.35)$$

The Eq. (4.35), that represent the value of maximum substrate reaction, is plotted by dot line in Fig. 4.6a and b versus βL and γL, respectively. In particular in Fig. 4.6a, it could be observed that shear stresses versus βL become constant when the ratio $\beta L /\gamma L > 1$.

Looking at the case of perfect bonding ($k_x \to \infty$) therefore when $\gamma L \to \infty$, the maximum shear stress $r_{x,max}$, Eq. (4.35), tends to infinite. The term $\beta L\ [1-(\beta L/\gamma L)^2]^{-0.5}$ of the Eq. (4.35) could be written in the following as $\gamma L\ [(\gamma L/\beta L)^2-1]^{-0.5}$. Notice that when the parameters βL and γL are equal, the shear reaction of the Eq. (4.35) can not be determined. The case in perfect bonding, Eq. (4.32) becomes

$$\lim_{k\to\infty} r_x(x) = \frac{P_x\overline{\alpha_1}}{\pi}g(x\overline{\alpha_1}) = \frac{P_x}{\pi}\frac{\beta L}{2L}g\left(x\frac{\beta L}{2L}\right), \qquad (4.36)$$

where $\lim_{k\to\infty}\alpha_1 = \overline{\alpha_1} = \frac{E}{2E_0 A} = \frac{\beta L}{2L}$, $\lim_{k\to\infty}\alpha_2 = \infty$, $\lim_{x\to\infty} g(x) = 0$.

Hence the Eq. (4.36) can be rewritten

$$r_x(x) = -\frac{P_x}{\pi}\frac{\beta L}{2L}\left[si\left(\frac{\beta L}{2L}x\right)\sin\left(\frac{\beta L}{2L}x\right)+ci\left(\frac{\beta L}{2L}x\right)\cos\left(\frac{\beta L}{2L}x\right)\right]. \qquad (4.37)$$

In the area of the point load ($x \to 0$), shear reaction of perfect bonding is given by

$$\lim_{x\to 0} r_x(x) = -\frac{P_x}{\pi}\frac{\beta L}{2L}\left[\gamma_{Eul} + \ln\left(\frac{\beta L}{2L}x\right)\right], \qquad (4.38)$$

where for $x \rightarrow 0$, $ci(x) \approx \gamma_{Eul} + \ln(x)$ and $\gamma_{Eul} \approx 0.577$ is the Euler constant. Equations (4.37) and (4.38) are reported in Tullini et al. [23].

In summery, the shear stress with weak interface is given by the Eq. (4.32), while the maximum value of shear stress $r_{x,max}$ is in $x = 0$, Eq.(4.35). For the perfect bonding, the shear stress is given by Eq. (4.36) or Eq. (4.37), where Eq. (4.38) is its maximum value.
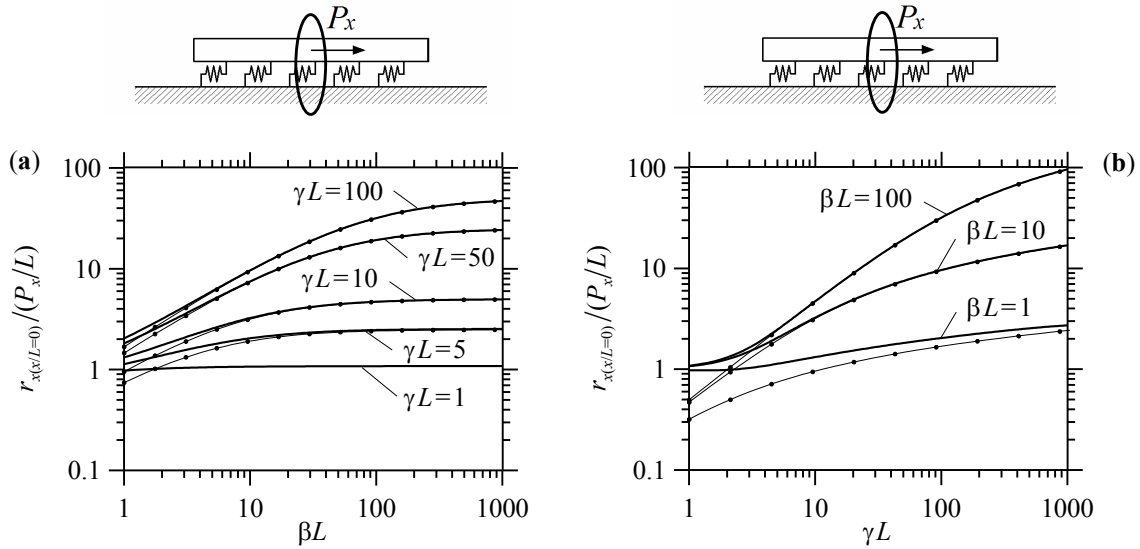

Fig. 4.6. Bar loaded by a point force P_x at midspan. Nondimensional value of r_x at the bar midpoint $x/L = 0$ versus βL (**a**) and γL (**b**), with analytic solution (thin solid line with symbol).
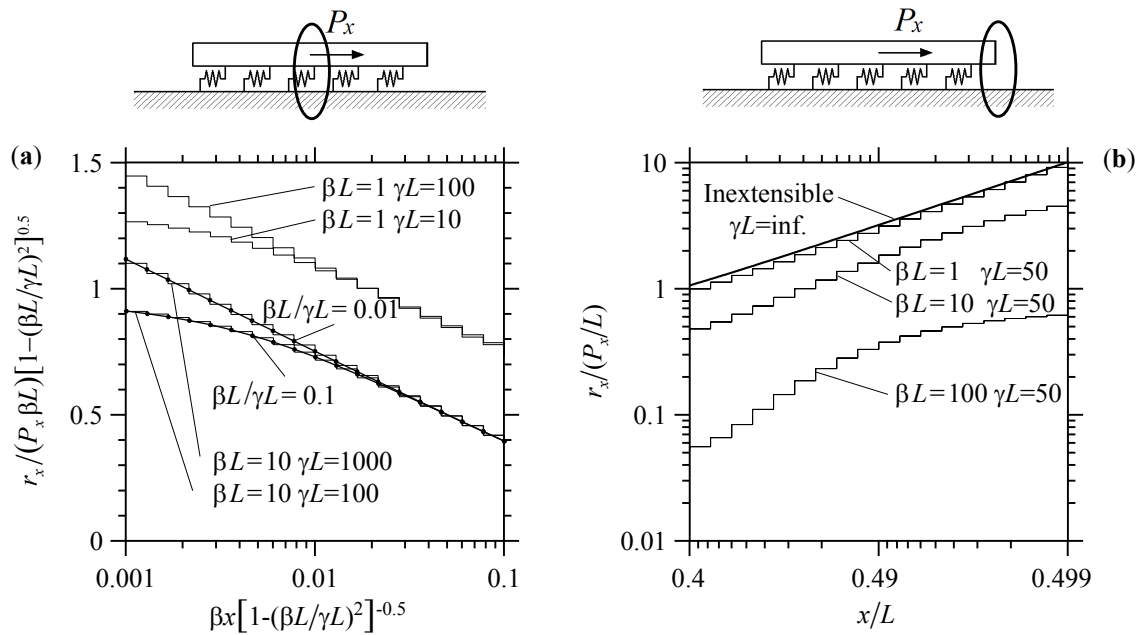
Fig. 4.7. Bar loaded by a point force P_x at midspan. Nondimensional value of r_x in the neighbourhood of the midpoint bar with analytic solution (thin solid line with symbol) (**a**) and bar end (**b**).

Dimensionless shear reactions r_x in the neighbourhood of the midpoint bar versus $\beta x[1-(\beta L/\gamma L)^2]^{-0.5}$, Fig. 4.7a, and r_x it the area of the bar end versus x/L, in Fig. 4.7b, are obtained by a mesh refinement by 202 logarithmically space, using bar elements with quadratic Lagrange polynomials as shape functions and one equal constant substrate element. Considering the substrate reaction close at the bar midpoint, in Fig. 4.7a is reported the condition using $\beta L = 1$ with $\gamma L = 10$ and 100, as well as $\beta L = 10$ with $\gamma L = 100$ and 1000. Moreover assuming value of βL bigger than 10, the substrate reactions are overlapped at the case $\beta L = 10$ with the corresponding ratio $\beta L/\gamma L$. Furthermore, analytic solution is reported for the cases with $\beta L/\gamma L = 0,1$ and $0,01$ (dashed line in Fig. 4.7a). It is worth noting that different value of βL or γL but with the same ratio $\beta L/\gamma L$, shear stresses are characterised by the same slope.

In the neighbourhood of the bar end, Fig. 4.7b, it is compared the case with $\gamma L = 50$, varying βL to 1, 10 and 100. In particular, the case with $\gamma L = 50$ and $\beta L = 1$, hence when $\beta L/\gamma L = 0.02$, could be well approximated by the analytic expression of an inextensible stiffener given by

$$r_x(x) = \frac{2P_x}{\pi L} \frac{1}{\sqrt{4(x/L)(1-x/L)}}. \tag{4.39}$$

Decreasing the ratio $\beta L/\gamma L$, the substrate reaction increases at the midpoint bar where the force is applied, and at the bar end. It is observed that the value of shear stress tends to the case in perfect contact, when the ratio $\beta L/\gamma L$ tends to zero.

4.4.1.2 Bar loaded by horizontal point force P_x at one end

The case of a bar loaded by a horizontal point force P_x at one end section is investigated, assuming the same parameters βL and γL of the previously example. Dimensionless values of displacements, axial force and substrate reaction along the bar are reported in Figs. 4.8, 4.9, 4.10.

Nevertheless for a short bar and stiffer than the substrate, case in Fig. 4.8 with $\beta L = 1$, bar displacement, axial force and shear stress of the weak contact are very similar to the perfect bonding, except substrate displacement which depend on the choice of interface parameter γL.

With the same interface condition, in particular assuming $\gamma L = 5$, the behaviour of a long bar and more flexible than the substrate is shown in Figs. 4.9 and 4.10 with the parameter $\beta L = 10$ and 100 respectively. Comparing to the perfect adhesion, bar

displacement $u_{x,b}$ increases, while substrate displacement $u_{x,s}$ decreases until it becomes about zero. Obviously, their different depend on the parameter γL assumed. Axial force tends to become almost linear along the bar, Figs. 4.9b and 4.10b, and the maximum shear reaction decreases transferring stresses everywhere along the length of contact, Figs. 4.9c and 4.10c. This is one of particular advantages of having weak bonding between reinforcement and substrate.

As previously example, maximum axial displacements versus the parameter βL and γL are investigated using a graded mesh by $n_{el} = 256$ and $\beta_{exp} = 3$ of quadratic bar elements including one equal substrate elements, Fig. 4.11. The maximum bar displacement increases when bar becomes long and flexible, whatever condition of adhesion is applied. Interesting are the maximum substrate reactions $r_x(x/L=0.5)$, Fig 4.12, which are constant varying the parameter βL and linear versus γL with the same slope.
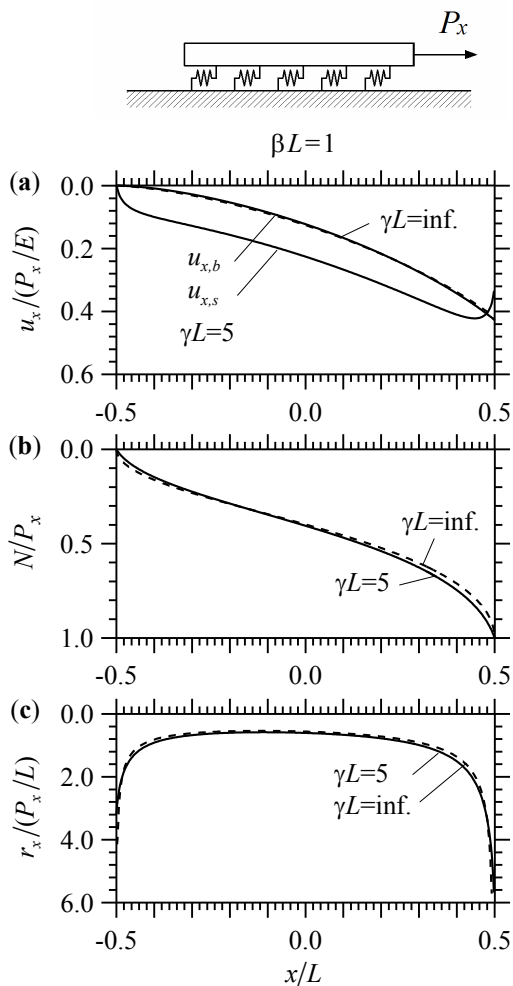
Fig. 4.8. Bar ($\beta L = 1$) loaded by a point force P_x at one end. Nondimensional values of u_x (a), N (b) and r_x (c) versus x/L for weak (solid line) and perfect contact (dashed line).
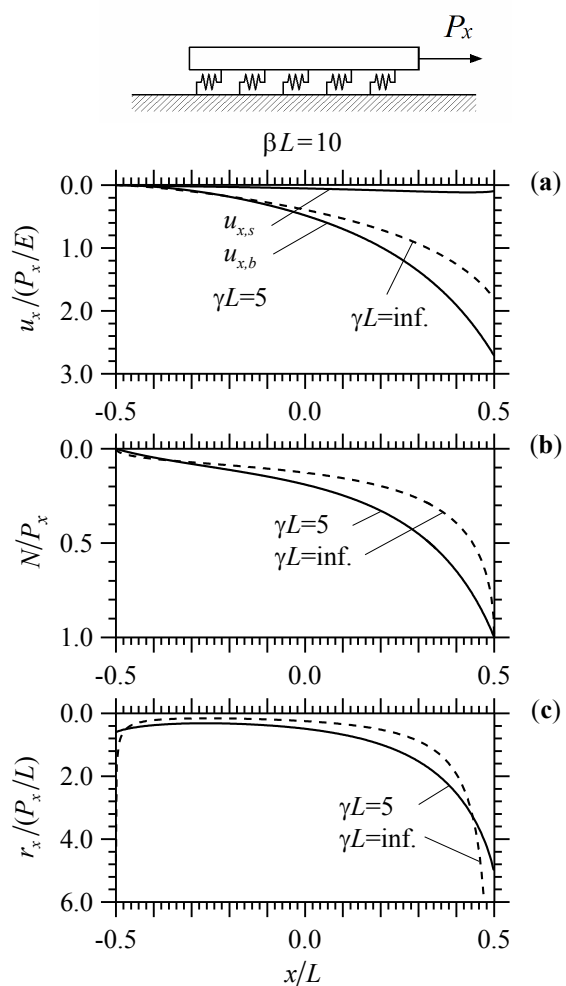
Fig. 4.9. Bar ($\beta L = 10$) loaded by a point force P_x at one end. Nondimensional values of u_x (a), N (b) and r_x (c) versus x/L for weak (solid line) and perfect contact (dashed line).
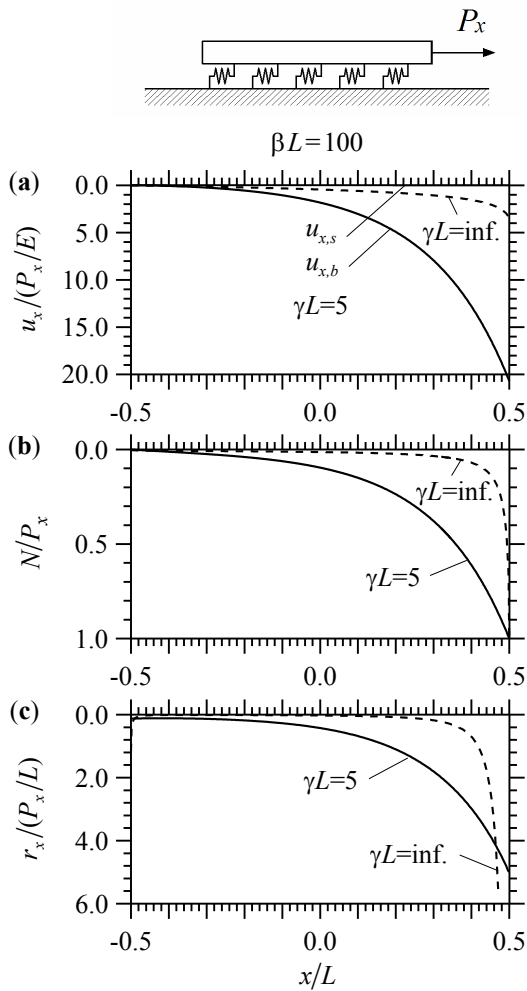
Fig. 4.10. Bar ($\beta L = 100$) loaded by a point force P_x at one end. Nondimensional values of u_x (**a**), N (**b**) and r_x (**c**) versus x/L for weak (solid line) and perfect contact (dashed line).
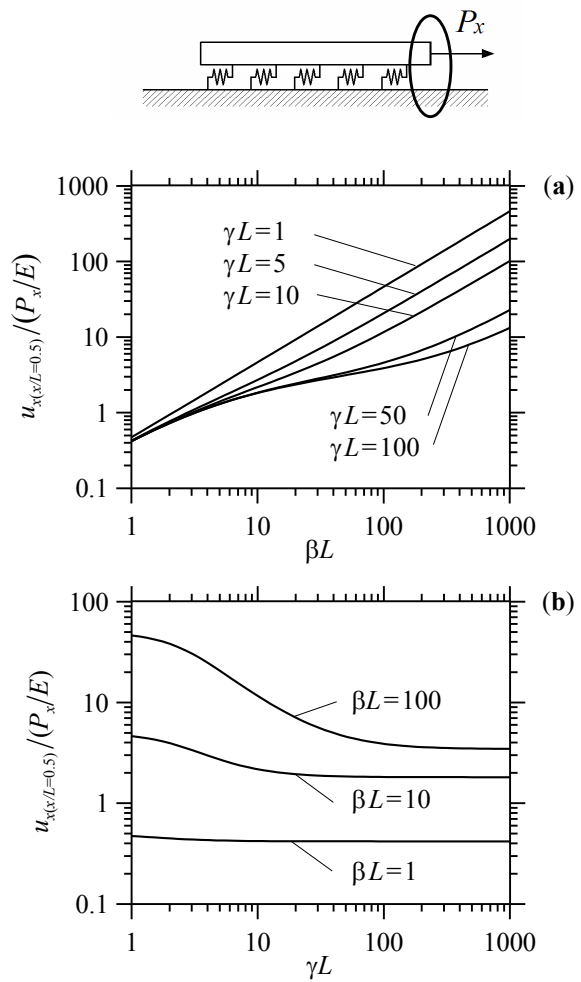
Fig. 4.11. Bar loaded by a point force P_x at one end. Nondimensional value of u_x at the bar end $x/L = 0.5$ versus βL (**a**) and γL (**b**).
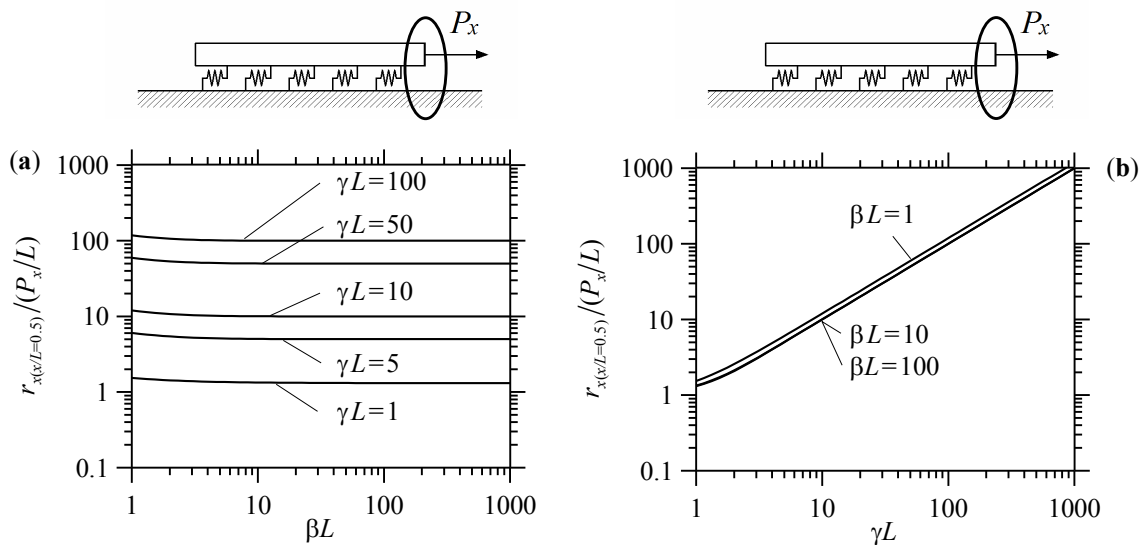
Fig. 4.12. Bar loaded by a point force P_x at one end. Nondimensional value of r_x at the bar end $x/L = 0.5$ versus βL (**a**) and γL (**b**).

4.4.1.3 Axial force of the bar loaded by P_x at midspan or at one end

As mentioned, axial forces and substrate displacements are calculated by means of post-processing analysis. In particular, dimensionless axial force of the bar ($\beta L = 10$) loaded by P_x at midpsan or at one end are reported in Fig. 4.13, versus βx or $\beta L/2 - \beta x$ respectively, and assuming two weak adhesion condition $\gamma L = 10$ and 100.

Moreover, the case with concentrated force, acting at midspan, is compared with axial force that is computed integrating the $r_x(x)$ of the Eq. (4.32) given by Melan's solution, permitting to conclude

$$N(x) = \frac{P_x}{2L\pi} \frac{\gamma L}{\sqrt{(\gamma L/\beta L)^2 - 1}} \left[-\frac{f(x\alpha_1)}{\alpha_1} + \frac{f(x\alpha_2)}{\alpha_2} \right], \qquad (4.40)$$

where α_1 and α_2 are defined by Eq. (4.33) while $f(x) = \sin(x)ci(\text{x}) - \cos(x)si(\text{x})$ with $g(x) = -df(x)/dx$. The limit of N when x tend to 0 is equal to $P_x/2$, as expect

$$\lim_{x \to 0} N(x) = \frac{P_x}{2L\pi} \frac{\gamma L}{\sqrt{(\gamma L/\beta L)^2 - 1}} \left[\frac{(\alpha_1 - \alpha_2)\pi}{2\alpha_1\alpha_2} \right] = \frac{P_x}{2}, \qquad (4.41)$$

where

$$\lim_{x \to 0} \left[-\frac{f(x\alpha_1)}{\alpha_1} + \frac{f(x\alpha_2)}{\alpha_2} \right] = \frac{(\alpha_1 - \alpha_2)\pi}{2\alpha_1\alpha_2}. \qquad (4.42)$$

The Eq. (4.40) is reported in Fig. 4.13a (line with symbol) where βL has been assumed about 9.999 for the case $\beta L = 10$ and $\gamma L = 10$, because of Natural Logarithm.
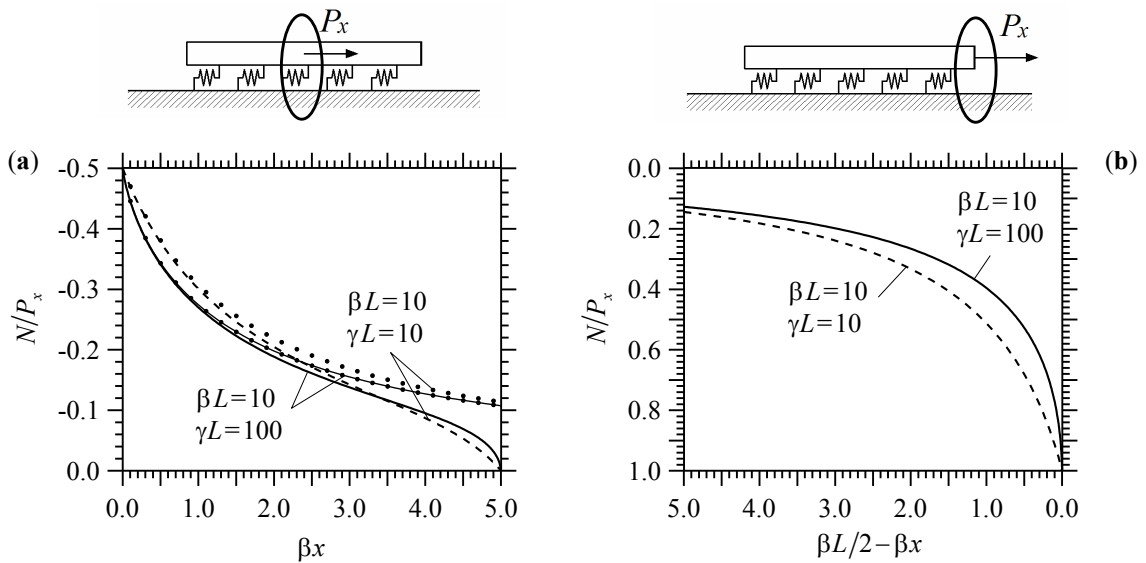
Fig. 4.13. Bar loaded by a point force P_x at midspan and one end. Nondimensional value of N in the neighbourhood of the midpoint bar with analytic solution (line with symbol) **(a)** and bar end **(b)**.

4.4.2 Bar loaded by a double horizontal point forces at ends or inside

The case of an elastic bar loaded by two opposite equal horizontal concentrate forces, each equal to $P_x/2$, is considered. The forces are applied at ends, Fig. 4.14, or inside bar at $x/L = \pm 1/4$ as shown Fig. 4.15, comparing with the analytic solution given by Melan.

A number of 512 elements are used with a uniform mesh. Quadratic Langrange polynomials and piecewise constant functions are used to interpolate the bar displacements $u_{x,b}$ and shear tractions r_x. A post-processing analysis is used to determine substrate displacements $u_{x,s}$ and axial force N. Nondimensional value of u_x, N and r_x versus x/L are reported for the weak adhesion with $\beta L = 10$ and $\gamma L = 5$ and in perfect bonding ($\gamma L \to \infty$).

Noting that, for the weak interface condition, bar displacements increase, while substrate ones decrease. Besides their different become lower with the raise of γL. Nevertheless the magnitude of axial forces diminish and shear reactions are more distributed along the bar, reducing the peak close the force zones. Furthermore, the Melan's solution of an infinite stiffener shows that the interaction depends strongly on the properties of the interface, and on the distance between the forces. The shear traction of two equal and opposite forces $P = P_x/2$, acting on the x-axis at the points $x = -d$ and $x = +d$ is given by

$$\hat{r}_x(s) = \frac{2iPk_x}{EA} \frac{\sin(sd)}{s^2 + 2a|s| + b}.$$

(4.43)

Inverting Eq. (4.43) by using the inverse Fourier transform, one could be obtained

$$r_x(x) = \frac{P}{2L\pi} \alpha_3 \left[g(|x-d|\alpha_1) - g(|x-d|\alpha_2) - g((x+d)\alpha_1) + g((x+d)\alpha_2) \right].$$

(4.44)

The expression of axial force $N(x)$ is obtained integrating Eq. (4.44), when $x < d$

$$N(x) = -\frac{P}{2L\pi} \alpha_3 \left\{ \frac{f[(d-x)\alpha_2]}{\alpha_2} - \frac{f[(d-x)\alpha_1]}{\alpha_1} + \frac{f[(x+d)\alpha_2]}{\alpha_2} - \frac{f[(x+d)\alpha_1]}{\alpha_1} \right\},$$

(4.45a)

while if $x > d$

$$N(x) = -\frac{P}{2L\pi} \alpha_3 \left\{ \frac{f[(x-d)\alpha_2]}{\alpha_2} - \frac{f[(x-d)\alpha_1]}{\alpha_1} - \frac{f[(x+d)\alpha_2]}{\alpha_2} + \frac{f[(x+d)\alpha_1]}{\alpha_1} \right\},$$

(4.45b)

where α_1, α_2 are defined by Eq. (4.33), $\alpha_3 = \gamma L[(\gamma L/\beta L)^2 - 1]^{-0.5}$, while

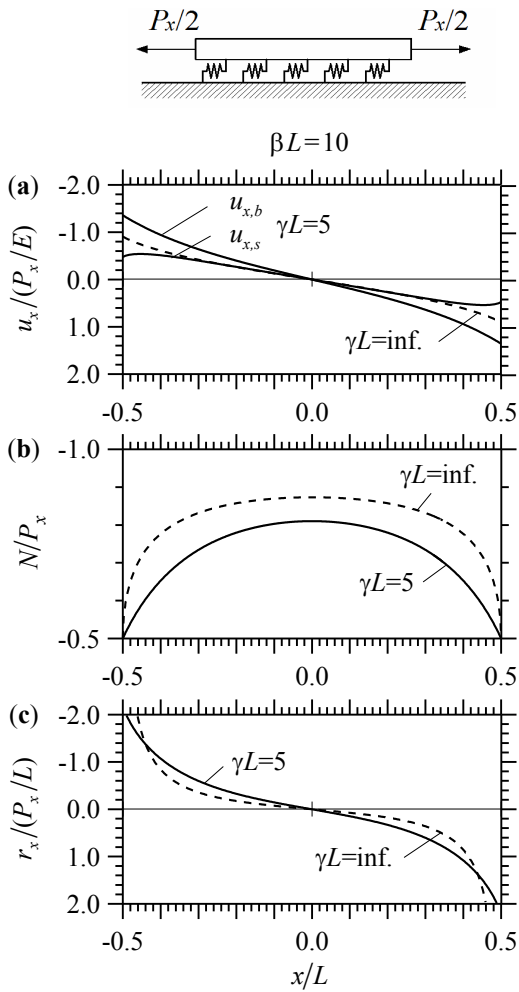$g(x) = -\sin(x)si(x) - \cos(x)ci(x)$ and $f(x) = \sin(x)ci(x) - \cos(x)si(x)$.

Fig. 4.14. Bar ($\beta L = 10$) loaded by two opposite equal point force $P_x/2$ at end. Nondimensional values of u_x (**a**), N (**b**) and r_x (**c**) versus x/L for weak (solid line) and perfect contact (dashed line).
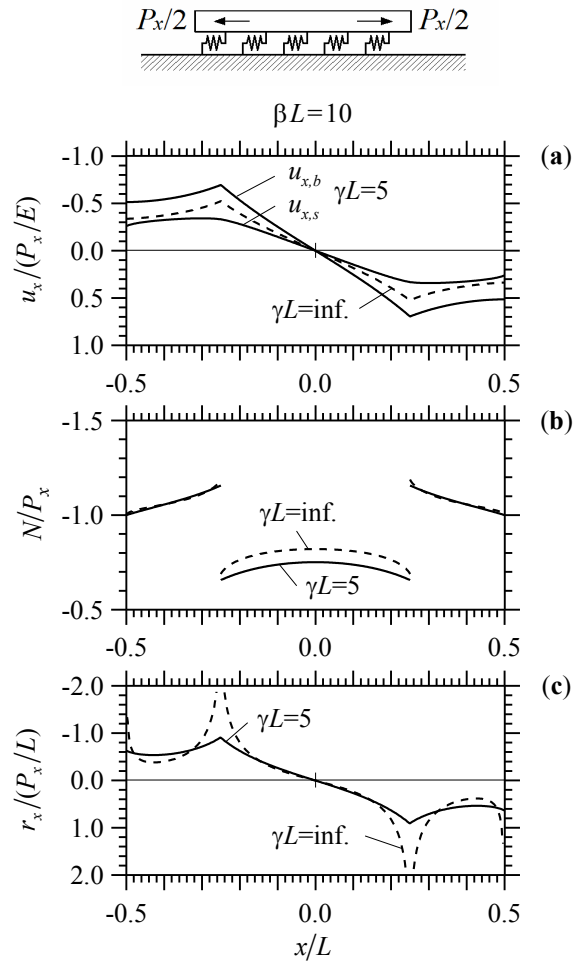
Fig. 4.15. Bar ($\beta L = 10$) loaded by two opposite equal point force $P_x/2$ at $x/L = \pm 1/4$. Nondimensional values of u_x (**a**), N (**b**) and r_x (**c**) versus x/L for weak (solid line) and perfect contact (dashed line).
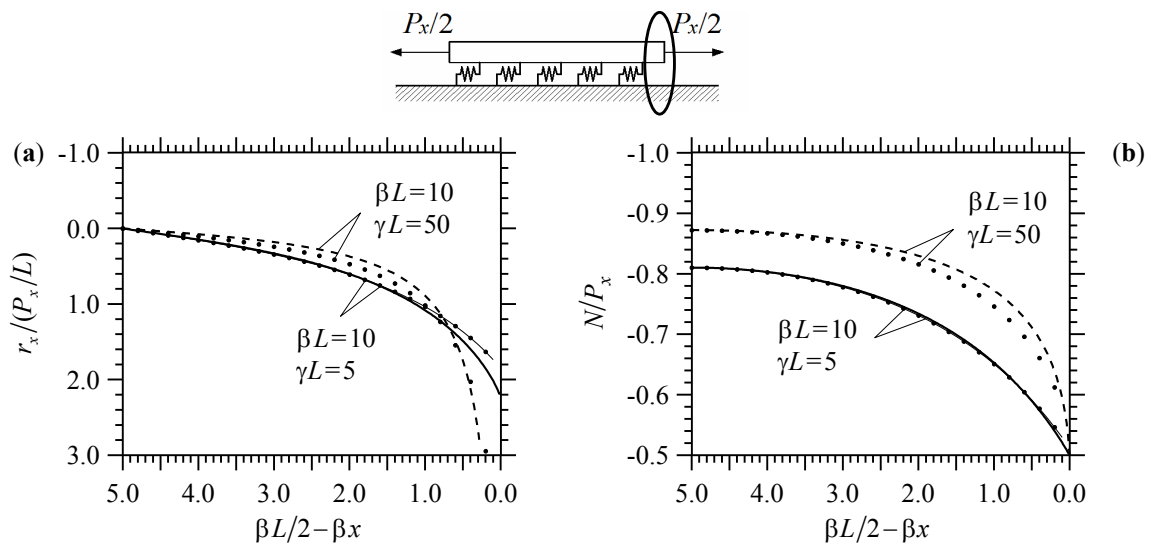
Fig. 4.16. Bar loaded by two opposite equal point force $P_x/2$ at end. Nondimensional value of r_x (**a**) and N (**b**) in the neighbourhood of bar end with analytic solution (line with symbol).

152

In particular, shear tractions and axial force of the bar ($\beta L = 10$) loaded at end ($d = 0.5$), with two weak interface condition ($\gamma L = 5$ and 50), are reported in Fig. 4.16a and b, respectively.

Although, the Melan's solution, Eqs. (4.44) and (4.45), could not be compared with the result of the present analysis (FE-BIE) because a finite bar is considerate in the present problem. Results of shear reaction and axial forces of both analysis are quite equivalent.
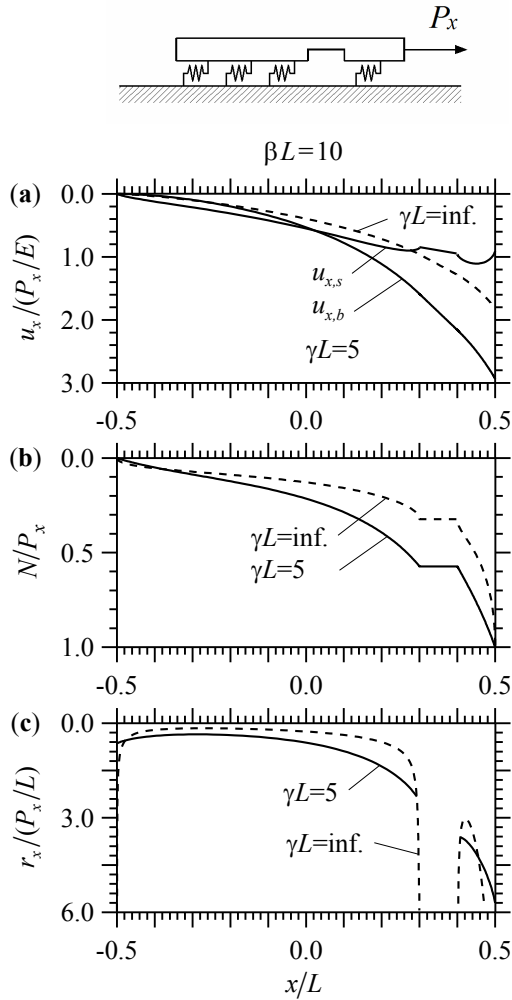
Fig. 4.17. Bar ($\beta L = 10$) loaded by a point force P_x at one end and detached between $x/L = 0.30$ and 0.40. Nondimensional values of u_x (a), N (b) and r_x (c) versus x/L for weak (solid line) and perfect contact (dashed line).
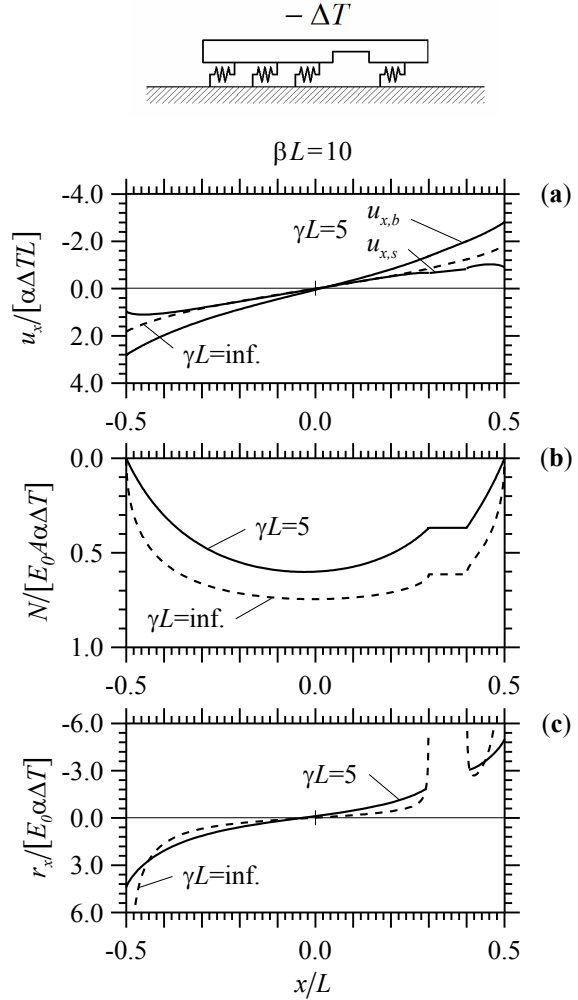
Fig. 4.18. Bar ($\beta L = 10$) subjected to a thermal variation $-\Delta T$ and detached between $x/L = 0.30$ and 0.40. Nondimensional values of u_x (a), N (b) and r_x (c) versus x/L for weak (solid line) and perfect contact (dashed line).

4.4.3 Detached bar subjected to horizontal point force at one end or thermal load

In this section, a bar with $\beta L = 10$ and resting partially on an elastic substrate in weak adhesion $\gamma L = 5$ and in perfect bonding ($\gamma L \rightarrow \infty$), is considered. Bar displacements and substrate reactions for detached case are obtained by solving the Eq. (4.24). Dimensionless displacement, stress reaction and axial force of the bar loaded by horizontal point force P_x at one end, Fig. 4.17, or subject to uniform compression thermal load $-\Delta T$, Fig. 4.18, are studied assuming a detached between $x/L = 0.30$ and 0.40.

A set of quadratic Langrange polynomials for bar elements and piecewise constant functions for substrate are used, subdividing the bar in three zone and applying each one a graded mesh with $\beta_{exp} = 3$. The accuracy of refinement in the neighbourhood of detachment depend on type of adhesion contact, therefore γL parameter. Consequently, a number of 192 finite elements are used, where 128 of them are generated in the intervals [-0.5, 0.3]/L, 32 elements into [0.3, 0.4]/L and other 32 ones into [0.4, 0.5]/L.

The case of an elastic bar subject to uniform compression thermal variation $(-\Delta T)$ is analogous at the case of a bar loaded by two opposite forces applied at the end, see Fig. 4.14, assuming as magnitude of force $\Theta = E_0 A \alpha_0 \Delta T$.

As expected, along the detached region, constant axial force and no substrate reaction are found. Nevertheless, in presence of the weak contact, axial forces decrease and the peak of shear reaction vanishes at the edges of detachment and bar ends.

4.5 Non-linear analysis of shear test

This paragraph presents the solution of an adhesive interface, simulating the delamination of a strip bonded to a general material. The debonding occurs when the slip between the strip and substrate reaches a critical value that causes separation. The shear test could be used to determine not only the ultimate load but even the local bond-slip behaviour of the interface [32, 33, 34, 35] where a reliable estimation is of fundamental importance to understanding the debonding failures. The local bond-slip curves from shear test is commonly determined in two ways:

- from axial strains of the reinforcement measured with strain gauges;
- from load-displacement curves (slip at the loaded end).

The first method, apparently simple, does not produce accurate local bond-slip curves because the axial strains, measured on the thin FRP plate on concrete, generally show violent variations due to the heterogeneity and presence of crack into the substrate.

Consequently, the bond-slip curves found from different tests could be substantially. The second method is an indirect method, where the local bond-slip curve is determined indirectly from the load-displacement curve, but as results that different local bond-slip curves may lead to similar load-displacement curves.

In the scientific literature there are plenty of experimental results available of shear-out tests especially carried out on FRP plates bonded on concrete blocks, such as Yao et al. [36]. The bilinear elastic-softening bond-slip relationship is among the most commonly adopted [37], where other proposals are based on exponential [15] or rational [17] bond-slip law. A closed-form analytical solution is presented by Caggiano et al. [38], modelling the mechanical behaviour of FRP plates adhesively bonded to a rigid supporting material. In particular a globally softening behaviour is observed in shear-out tests for "*short*" anchorage, and a snap-back behaviour for "*long*" anchorage length. This latter computational behaviour can be considered as a further evolution of Yuan et al. [39].

4.5.1 Interface relationship

The debonding process in shear-out test due to the applied axial force P_{xi} is analysed in this section, Fig. 4.19a. For the sake of simplicity, the fracture behaviour of Mode II is introduced throughout the interface, which is based on a general assumption of a bilinear elastic-softening r_x - Δu_x relationship. The evolution of the mechanical response of the adhesive interface throughout the bonded length is simulated using a step-by-step approach. Global load-displacement response P_{xi} - Δu_{xi} of the pull-out test, axial strain distributions of FPR and shear reaction distributions r_x along the contact length, are investigated.
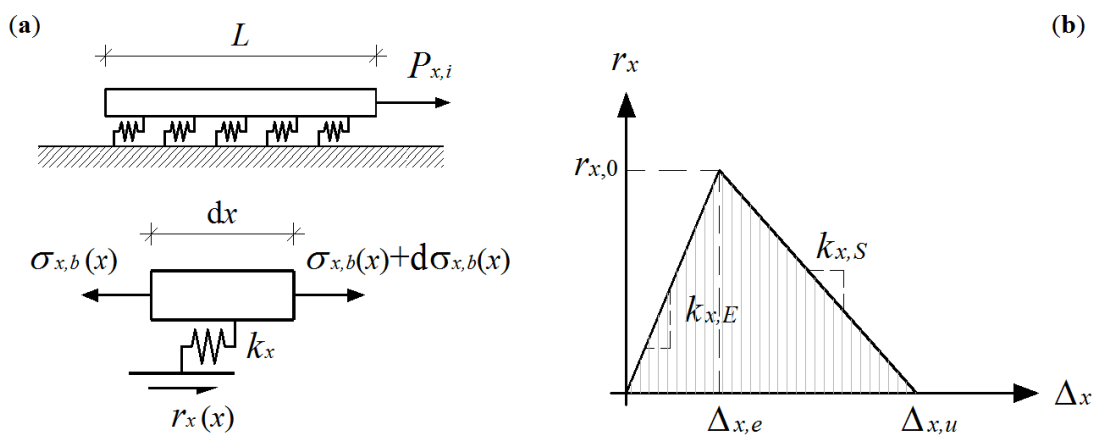
Fig. 4.19. Shear test on a bar to semi-infinite substrate with weak interface (**a**), bond-slip r_x - Δu_x law for nonlinear analysis (**b**).

The bilinear bond law r_x - Δu_x, plotted in Fig. 4.19b, simulates the relationship between the shear stresses and interface slips throughout the adhesive interface. An linear ascending branch is described by the stiffness parameter $k_{x,E}$ until reach the elastic limit $r_{x,0}$, then followed by a linear softening with descending slope $k_{x,S}$. Beyond the ultimate slip $\Delta u_{x,u} = r_{x,0}/k_{x,E} + r_{x,0}/k_{x,S}$, no bond stresses can be transferred on the interface. Based on the assumption that area of the bar keeps unchanged throughout the bonded length, the centroidal bar is coincident with substrate, namely assuming thickness of the reinforcement negligible. Besides, considering a unique bond-slip law r_x - Δu_x, the following infinitesimal equilibrium condition can be written

$$\mathrm{d}\sigma_{x,b}(x)/\mathrm{d}x = \mathrm{d}(E_0 A u'_x(x))/\mathrm{d}x = -r_x(x), \tag{4.46}$$

where r_x is the bond shear stress transferred at the interface and $\sigma_{x,b}(x) = E_0 A u'x(x)$ the axial stress on the bar section, being E_0 the elastic modulus and A cross-section area of the bar. The constitutive equations for the adhesive behaviour can be expressed as

$$
\begin{aligned}
r_x(x) &= -k_{x,E}\, \Delta u_x(x) & &\text{if } \Delta u_x(x) \le \Delta u_{x,e} \\
r_x(x) &= -r_{x,0} + k_{x,S}\,(\Delta u_x(x) - \Delta u_{x,e}) & &\text{if } \Delta u_{x,e} < \Delta u_x(x) \le \Delta u_{x,u} \\
r_x(x) &= 0 & &\text{if } \Delta u_x(x) > \Delta u_{x,u}
\end{aligned} \tag{4.47}
$$

where $k_{x,E}$ and $k_{x,S}$ are the bond stiffness of the interface shear-slip relationship and $\Delta u_{x,e} = r_{x,0}/k_{x,E}$ is the elastic slip limit. The three different expressions of Eq. (4.47) describe the elastic, softening and debonding branch, respectively. The area under the bon-slip curve, G_f, is the fracture energy:

$$G_f = \int_0^{\Delta u_{x,u}} r_x\, \Delta u_x\, \mathrm{d}\Delta u_x = r_{x,0}\, \Delta u_{x,u}\, / 2. \tag{4.48}$$

All substrate reactions are in elastic stage for low loads. The elastic-softening stage starts once the slip reach the elastic limit $\Delta u_{x,e} = r_{x,0}/k_{x,E}$. Two possible alternative evolutions of beyond the elastic-softening can occur:

- The slip Δu_x at $x = L$ reaches the ultimate slip value, $\Delta u_x(L) = \Delta u_{x,u}$, with the minimum slip (Δu_x at $x = 0$) inferior to elastic limit slip, $\Delta u_x(0) < \Delta u_{x,e}$. Leading to the transition to the new elastic-softening-debonding stage (ESD).

- The slip Δu_x at $x = 0$, reaches the elastic limit slip $\Delta u_x(0) = \Delta u_{x,e}$, with $\Delta u_x < \Delta u_{x,u}$ following the new only softening stage (S).

The evolution depends on the parameters of the interface bond-slip law. Any given interface relationship (namely for every triplet of $r_{x,0}$, $\Delta u_{x,e}$, $\Delta u_{x,u}$) a particular length value

L^* (called critical bond length) exists for which the two mentioned conditions $\Delta u_x(L) = \Delta u_{x,u}$ and $\Delta u_x(0) = \Delta u_{x,e}$ are achieved at the same time.

The reinforcement with bonding length $L > L^*$ follows the first evolution, such case will be associated to "*long*" anchorage length. On the contrary, when $L < L^*$, the mechanical system follows the second one, which characterises "*short*" anchorage length. A conceptual map, reported in Fig. 4.20, delineates the two possible mechanical behaviour, depending on the bonding length L, namely on interface law of FRP glued on substrate. In case of "*long*" anchorage ($L > L^*$), the bond-slip process following the previously (ES) stage is characterised by a debonding zone in the neighbours of the loaded end. For finite lengths, the behaviour in terms of shear-out force versus slip shows an unstable snap-back branch. While for ideal infinite anchorages the shear-out curve develops an indefinite plateau. In case of "*short*" anchorage ($L < L^*$), the mechanical stage of the adhesive interface that follows the Elastic-Softening (ES) stage is wholly described by the Softening (S) branch.
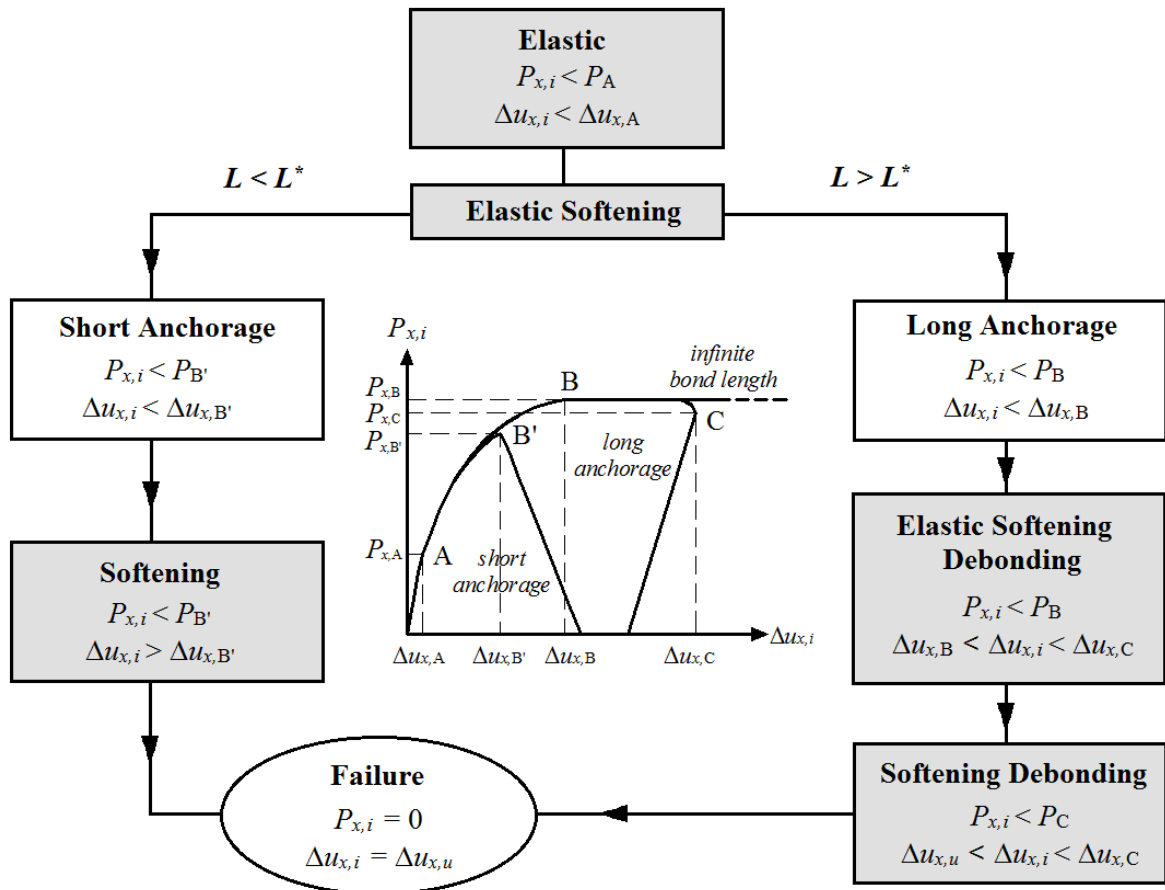
Fig. 4.20. Schematic representation of the debonding process.

4.5.2 Results of the numerical model

In this section, the response of a CFRP bonded to a concrete substrate has been investigated, using the proposed formulation FE-BIE. The interface proprieties have been calibrated by Faella et al. [37, 38] on experimental results reported in Chajes et al. [40]. The calibration procedure of each specimen in Faella has different interface properties, that assumption derives from the randomness of the mechanical properties of the concrete substrate. In particular, the numerical analysis is carried out on two specimens characterised by bond lengths, about 50 and 200 mm. The CFRP is modelled by means of bar FEs having $E_0 = 100$ GPa and $A = 25$ mm^2, while the substrate through BIE assuming Young's modulus $E = 30$ GPa.

The difference evolution of the axial strain and interface shear stress throughout the bonding length emphasize deeply the cases of "*short*" and "*long*" anchorages, Figs. 4.21 and 4.22. For the "*short*" one is assumed a stress limit $r_{x,0} = 6.9$ MPa with stiffness $k_{x,E} = 135$ N/ mm^3 and $k_{x,S} = 25$ N/mm^3, while for long anchorage $r_{x,0} = 5$ MPa with $k_{x,E} = 5000$ N/ mm^3 and $k_{x,S} = 100$ N/ mm^3. A good agreement between the numerical predictions and experimental results have been found, as shown in Fig. 4.21b in terms of axial strain.

The force-slip response of "*short*" anchorage is shown in Fig. 4.21a where the closed-form analysis of Caggiano et al. [38] is reported (dashed line with symbol). The corresponding values of axial strains of FRP in Fig. 4.21b, and substrate reaction in Fig. 4.21c, are illustrated in elastic state (solid line) and softening state (dashed line) throughout bond length. An exponential shape of axial strain, $\varepsilon_{x,FRP}$, turns out until to reach the maximum load P_x (i.e. D point in Fig. 4.21a). Afterwards, the trend of $\varepsilon_{x,FRP}$ becomes linear and decreases achieved the complete detachment. The evolution in terms of the corresponding interface shear stress, r_x, is clearly reported in Fig. 4.21c. Showing an exponential shape in early stages, a transition starts from the achievement $r_x(L) = r_{x,0}$ (i.e. B line in Fig. 4.21c) until it reaches the condition when every points have overcome the stress limit $r_x(0) = r_{x,0}$ (i.e. D line in Fig. 4.21c). Finally a progressive decline of the reactions up to failure, corresponding to maximum displacement $\Delta u_{x,u}$.

A different global behaviour of the force-slip response is observed in the "*long*" anchorages, showing a snap-back in Fig. 4.22a. The axial strains of FRP and substrate reaction are reported in elastic state (solid line) and softening stage (dashed line) along the bonding length, Figs. 4.22b and 4.22c respectively. The behaviour is similar to the previously specimen in early stages (i.e. B point in Fig. 4.22a), after that an elastic-softening-debonding stage occurs. In the zone of detachment, the axial strain of FRP

remains constant and does not increase. While, the shear stress moves to the softening-debonding stage (i.e. G line in Fig. 4.22c). In the end, a decline of strength appears with reduction of slip Δu_x.

It is worth noting that the maximum slip Δu_x is equal to $\Delta u_{x,u}$ when the bonding length L is lower than the limit value L^*, while it is bigger than $\Delta u_{x,u}$ as the bonding length L longer than L^*. It is demonstrated that in case of " *long* " anchorage, increasing the bond length ($L > L^*$), does not have significant effect on the maximum load. While for "*short*" one, the length parameter L affects the maximum debonding load.
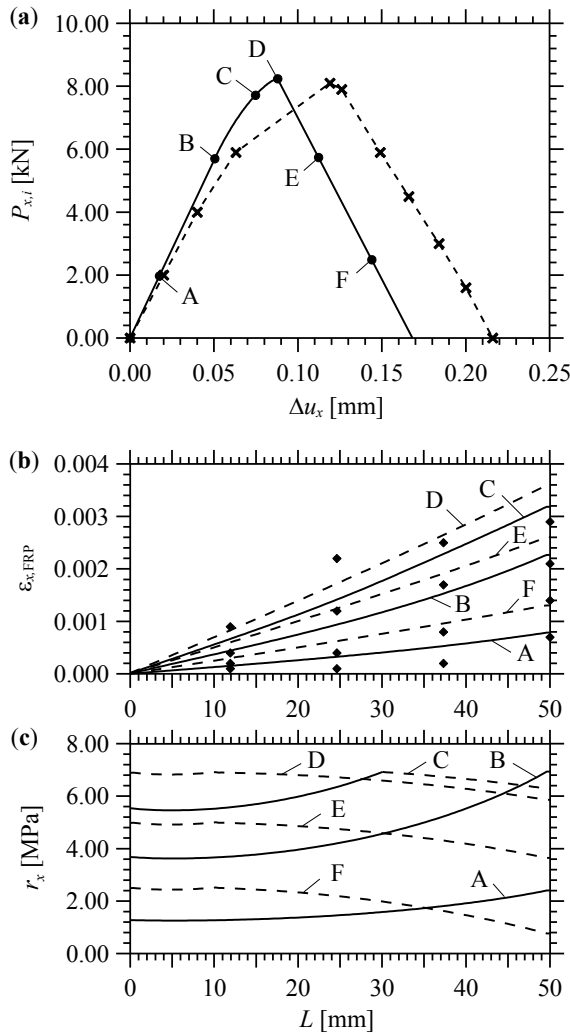
Fig. 4.21. Complete bond-slip process considering "short" anchorage ($L = 50$ mm). Shear-out curve (**a**), $\varepsilon_{x,\mathrm{FRP}}$ versus x (**b**) and r_x versus x (**c**). Results by Caggiano (linea with symbol in (**a**)) and experiment tests by Chajes (dots in (**b**)).
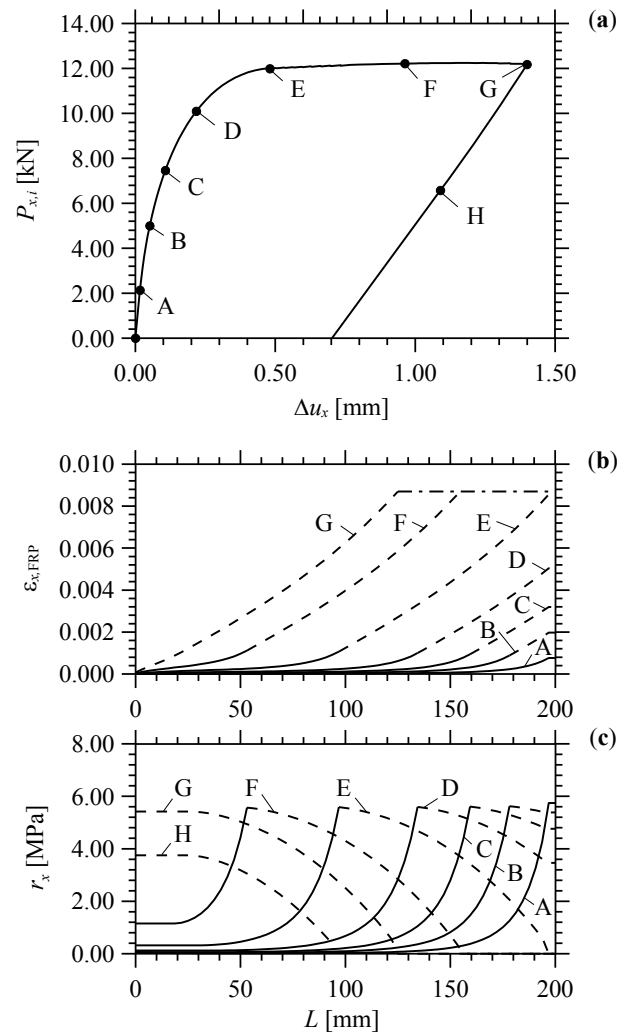
Fig. 4.22. Complete bond-slip process considering "long" anchorage ($L = 200$ mm). Shear-out curve (**a**), $\varepsilon_{x,\mathrm{FRP}}$ versus x (**b**) and r_x versus x (**c**).

4.6 Conclusions

The simple and effective FE-BIE method is proposed to investigate the problem of axially loaded thin structures weakly attached to a homogeneous elastic substrate. Bar FEs have been used to simulate the thin structure, while the behaviour of the semi-infinite substrate has been represented through BIE. Making use of a mixed variational formulation including the Green function of the half-plane, the axial displacement of the bar is interpolated using Lagrange polynomial of first or second order. Whereas, the interfacial shear stress is approximated by piecewise constant functions. A third element is interposed between the bar and substrate to simulate the weak bond of adhesive. Transmission stress of the weak interface is considered proportional to the relative bar-substrate displacement through a parameter γL, which reproduces the case of perfect bonding with value tends to infinite. Moreover, the response of system is handled by another parameter βL that characterises short or long bar on rigid or flexible substrate.

A number of numerical examples are presented to show the effectiveness of the proposed formulation. In particular, shear reaction and axial force of a bar subjected to point force at midspan or two opposite force at ends are compared with analytical solutions available in the literature. Moreover, the behaviour of displacement or reaction close to the force applied at midspan or one end is discussed with regard to two parameters βL and γL. Furthermore, a detached bar loaded by an axial force at one end or by a thermal load is reported.

Finally, non-linear analysis through step-by-step approach is used to simulated delamination of a bar stiffener glued to a substrate, assuming "*a priori*" the behaviour of adhesive by means of a constitutive law between interfacial shear reaction and slip. This model can be generally considered for investigating the adhesion behaviour of composite reinforcement glued on rigid or flexible substrate such as concrete, steel, wood, masonry or any other material which can be strengthened by externally gluing FRP. In this Chapter, the present formulation reports clearly the concepts of "*long*" and "*short*" anchorage, showing the difference in terms of shear stresses, axial strains throughout the bonded length and global shear force-displacement relationship. A comparison of the present model with experimental measures in term of axial strains and analytical formulation of global force-displacement present in the literature are reported with a good agreement.

References

[1]   Bakis C, Bank L, Brown V, Cosenza E, Davalos J, Lesko J, Machida A, Rizkalla S, Triantafillou T. Fiber-Reinforced Polymer Composites for Construction - State of the Art Review. J. Compos. Constr. 2002; 6(2): 73–87.

[2]   Kim Y, Heffernan P. Fatigue Behavior of Externally Strengthened Concrete Beams with Fiber-Reinforced Polymers: State of the Art. J. Compos. Constr. 2008; 12(3): 246–256.

[3]   Jiao H, Zhao X L. Strengthening of butt-welded very high strength (VHS) circular tubes. In: Proceedings of the international workshop on tubular connections, Kumamoto, Japan, 2002; 97–106.

[4]   Seica M V, Packer J A. FRP materials for the rehabilitation of tubular steel structures, for underwater applications. Compos Struct 2007; 80(3): 440–50.

[5]   Zhao X L, Zhang L. State of the art review on FRP strengthened steel structures. Eng Struct 2007; 29(8): 1808–23.

[6]   Carloni C, Subramaniam KV, Savoia M, Mazzotti C. Experimental determination of FRP-concrete cohesive interface properties under fatigue loading. Compos Struct 2012; 94(4): 1288–96.

[7]   Taljsten B. Strenghtening of concrete prism using the plate-bonding technique. Int. J. Fract. 1996; 82: 253–266.

[8]   Qiao P, Chen F. An improved adhesively bonded bi-material beam model for plated beams. Engineering Structures, 2008; 30: 1949–1957.

[9]   Lenci S. Melan's Problem with weak Interface, ASME Journal of Applied Mechanics, 2000.

[10]   Grigolyuk E I, Tolkachev V M. Contact problems in the theory of plates and shells, Mir Publishers, Moscow 1987.

[11]   Ferracuti B, Mazzotti C, Savoia M. A new single-shear set-up for stable delamination tests on FRP-concrete joints. Constr Buil Mater 2008; 23: 1529–37.

[12]   Panigrahi S, Pradhan B. Onset and growth of adhesion failure and delamination induced damages in double lap joint of laminated FRP composites. Compos Struct 2008; 85(4): 326–36.

[13]   Ombres L. Prediction of intermediate crack debonding failure in FRP strengthened reinforced concrete beams. Compos Struct 2010; 92(2): 322–9.

[14] Oehlers D, Park S, Ali M M. A structural engineering approach to adhesive bonding longitudinal plates to RC beams and slabs. Compos Part A: Appl Sci Manuf 2003; 34(9): 887–97.

[15] Cornetti P, Carpinteri A. Modelling the FRP-concrete delamination by means of an exponential softening law. Eng Struct 2011; 33: 1988–2001.

[16] Faella C, Martinelli E, Nigro E. Interface behaviour in FRP plates bonded to concrete: experimental tests and theoretical analyses. In: Proceedings of the international conference on advanced materials for construction of bridges, buildings and other structures III. 2003.

[17] Ferracuti B, Savoia M, Mazzotti C. A numerical model for FRP-concrete delamination. Compos Part B: Eng 2006; 37: 356–64.

[18] Faella C, Martinelli E, Nigro E. Formulation and validation of a theoretical model for intermediate debonding in FRP strengthened RC beams. Composites Part B: Eng 2008; 39(4): 645–55.

[19] CNR DT 200. Instructions for design, execution and control of strengthening interventions by means of fibre-reinforced composites. Italian National Research Council 2004; [in Italian].

[20] Czaderski C, Soudki K, Motavalli M. Front and side view image correlation measurements on FRP to concrete pull-off bond tests. ASCE – J. Compos. Constr. 2010; 14(4): 451–64.

[21] Martinelli E, Czaderski C, Motavalli M. Modeling in-plane and out-of-plane displacement fields in pull-off tests on FRP strips. Eng Struct 2011; 33(12): 3715–25.

[22] Caggiano A, Martinelli E. Fracture based model for mixed mode cracking of FRP strips glued on concrete. In: Cairns JW, Metelli G, Plizzari GA, editors. Bond in concrete 2012 – bond in new materials and under severe conditions; 2012. ISBN: 978-88-907078-3-4: 1055–1062.

[23] Tullini N, Tralli A, Lanzoni L. Interfacial shear stress analysis of bar and thin film bonded to 2D elastic substrate using a couple FE-BIE method, Finite Elements in Analysis and Design 2012: 55: 42–45.

[24] Chernin L, Volokh K Y. Simulation of thin film delamination under thermal loading, Tech Science Press 2004; 1: 259–273.

[25] Johnson K L. Contact Mechanics, University Press, Cambridge, 1985.

[26] Gurtin M E, Sternberg E. Theorems in linear elastostatics for exterior domains, Arch Ration Mech Anal 1961; 8(1): 99–119.

[27] Geymonat G, Krasucki F, Lenci S. Mathematical Analysis of a Bonded Joint With Soft Thin Adhesive, Math. Mech. Sol. 1999; 4: 201–225.

[28] Kikuchi N. Beam bending problems on a Pasternak foundation using reciprocal variational-inequalities, Q Appl Math 1980; 38 (1): 91–108.

[29] Kikuchi N, Oden J. Contact problems in elasticity: A study of variational inequalities and finite element methods, SIAM, Philadelphia, 1988.

[30] Bielak J, Stephan E. A modified Galerkin procedure for bending of beams on elastic foundations, SIAM J. Sci. Stat. Comput. 1983; 4(2): 340–352.

[31] Graham I G, McLean W. Anisotropic mesh refinement: the conditioning of Galerkin Boundary element matrices and simple preconditioners, Journal on Numerical Analysis, 2006; 44(4): 1487–1513.

[32] Taljsten B. Defining anchor lengths of steel and CFRP plates bonded to concrete. International Journal of Adhesion and Adhesives 1997; 17(4): 319–27.

[33] Nakaba K, Toshiyuki K, Tomoki F, Hiroyuki Y. Bond behavior between fiber-reinforced polymer laminates and concrete. ACI Struct Journal 2001; 98(3): 359–67.

[34] Lu X Z, Teng J G, Ye L P, Jiang J J. Bond–slip models for FRP sheets/plates bonded to concrete, Engineering Structures 2005; 27: 920–937.

[35] Akbar I, Oehlers D J, Mohamed Ali M S. Derivation of the bond-slip characteristics for FRP plated steel members. Journal of Constructional Steel Research 2010; 66(8–9): 1047–1056.

[36] Yao J, Teng J, Chen J. Experimental study on FRP to concrete bonded joints. Composites Part B 2005; 36: 99–113.

[37] Faella C, Martinelli E, Nigro E. Direct versus indirect method for identifying FRP to concrete interface relationships. ASCE - Journal of Composites for Construction 2009; 13: 226–233.

[38] Caggiano A, Martinelli E, Faella C. A fully-analytical approach for modelling the response of FRP plates bonded to a brittle substrate. International Journal of Solids and Structures 2012; 49: 2291–2300.

[39] Yuan H, Teng J, Seracino R, Wu Z, Yao J. Full-range behaviour of FRP to concrete bonded joints. Engineering Structures 2004; 26: 553–565.

[40] Chajes M, Finch W, Januska T, Thomson T. Bond and force transfer of composite material plates bonded to concrete. ACI - Structural Journal 1996; 93: 208–217.

5 Zero thickness analysis of a layer bonded to traditional boundary condition or to an elastic half-plane

5.1 Introduction

Crack and fracture behaviour of brittle materials such as concrete, rock or ceramics [1] have been proposed in the literature through a number of methods and techniques [2]. Several applications cover a wide range of cases, such as simulation of mechanical behaviour of joints, bounding surfaces and fracture propagation.

An example of a modern technique of analysis is the extended finite element method (XFEM) [3]. That requires the identification of a crack path line using the so-called "tracking algorithm", completely independent of the mesh. The XFEM is based on local enrichment functions incorporated into a finite element approximation [4], allowing the simulation of the crack growth without remeshing.

Another approach develops efficiently since the 90s, is the zero-thickness interface elements, considering each line in the 2D mesh or surface in the 3D mesh as a potential crack, evaluating inter-element forces and stresses. Although the crack can only be developed along the mesh lines or mesh surface, this technique describes crack propagation in an automatic way without the need of tracking or remeshing and without any limitation on how many times the crack opens, closes and reopens. The interface elements are treated as finite elements characterized by zero thickness, connected and detached in deformation configuration. When a given cracking criterion is exceeded, a fracture-based interface constitutive law is activated, leading to crack opening predictions. The approach has led to realistic predictions of cracking and fracture mechanisms under complex stresses in 2D [5, 6] and recently in 3D [7, 8], involving multiple cracks which start, get connected, arrested with other cracks. The opening crack at corner node of the mesh from several lines which are potential cracks, has been examined [9] assuming rigid-plastic cracking laws for each potential crack line. Nevertheless, sometimes, the opening of an interface element may be ruled by cohesive laws that allows for the transmission of cohesive stress after the opening. Moreover, the simulation of mortar joints or filled rock joints has also been studied by means of finite thickness interface elements with interface stiffness obtained by the ratio of the Young's modulus of the joint material and thickness of the joint [10], but that case has not been treated in this thesis.

In this work, the zero-thickness interface elements are implemented into the coupling FE-BIE model in order to model contact surfaces and potential cracks of the layer. The relative displacement in the mesh of layer is interpolated through shape functions and nodal displacement values. A constitutive law in terms of stress-displacement relationship defines the behaviour of interface element. This means that in the deformed configuration, the interface element generates detachment and separation of the continuum elements. The discontinuity reproduces the formation of a crack or debonding. In particular, linear elastic or rigid brittle fracture interface are considered. The interface allows transmission of stresses in the material, remaining close for the rigid behaviour or simulating an opening based on elastic proprieties, as long as a certain failure condition is reached developing an interfacial detachment. The interface elements are inserted, after defining the geometry of the problem, along the mesh layer where certain failure conditions could be satisfied. The negative side of this implementation requires a large number of node, limiting the maximum problem size that can be analysed for given computer resources.

5.2 Variational formulation

A layer bonded to traditional boundary conditions at the bottom edge, is referred to a Cartesian coordinate system (O; x, z), where x coincides with the bottom of the layer, and z is chosen in the downward transverse direction. The layer is subdivided into two-dimensional finite elements. A two-dimensional linear zero-thickness interface element is inserted between the plane elements. In particular, the interface element is characterised by two lines, indicated as S^+ and S^-, where the displacement field is interpolated from nodal values using shape functions and nodal displacements. The interface local reference system is represented by the vectors (n, s), while the global reference system is (x, z), Fig. 5.1.
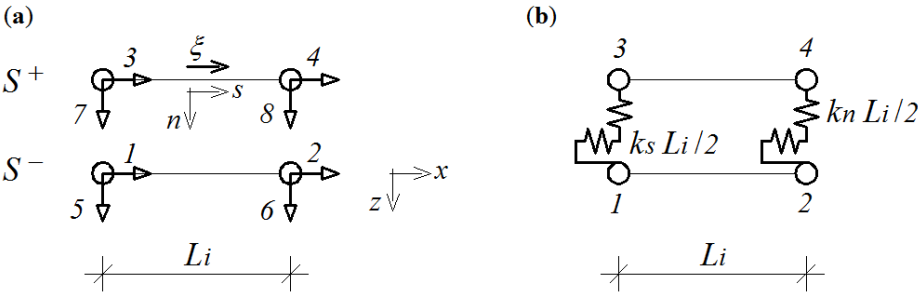
Fig. 5.1. A two-dimensional linear four-node interface element. Local (n, s) and global (x, z) reference system (**a**), equivalent spring system using the Lobatto integration rule for the element stiffness matrix $\mathbf{K}^e$ (**b**).

The potential energy of the layer with interface elements turns out to be $\Pi = \Pi_{layer} + \Pi_{interface}$, where the total potential energy of the layer (Π_{layer}) has been treated in Chapter 3, whereas the total potential energy of the interface ($\Pi_{interface}$) is discussed and studied in the following Section according to the Principle of Virtual Work states.

5.3   Finite element model

The constitutive law at any point of the interface is defined as a relation between stress σ and relative displacement u^*, where the notation (*) denotes variables in terms of local coordinates, as defined in [11]. The relative displacement field $\mathbf{u}^* = (u_n, u_s)$ is a function of the internal coordinate variable ξ, and can be written as

$$\mathbf{u}^*(\xi) = \mathbf{u}^*_+(\xi) - \mathbf{u}^*_-(\xi) = [u_n(\xi),\ u_s(\xi)]^{\mathrm{T}}, \tag{5.1}$$

in which $\mathbf{u}^*_+$ and $\mathbf{u}^*_-$ represent absolute displacement field on the surface S^+ and S^- respectively, in local coordinates. The relative displacement field in global coordinates $\mathbf{u} = (u_x, u_z)$ are obtained considering the nodal relative displacement vector δ^e in the (x, z) coordinates system:

$$\boldsymbol{\delta}^e = \left[\delta^e_{x(1,3)},\ \delta^e_{x(2,4)},\ \delta^e_{z(5,7)},\ \delta^e_{z(6,8)}\right]^{\mathrm{T}}. \tag{5.2}$$

The approximation of relative displacement field in (x, z) component is interpolated by means of linear shape function:

$$\mathbf{u}(\xi) = \mathbf{N}(\xi)\,\boldsymbol{\delta}^e \tag{5.3}$$

where $\mathbf{N} = [N_1, \ldots, N_{np}]$ with np is equal to the pair of nodes of the interface.

Assuming a linear elastic constant interface along its length, it could be obtained

$$\boldsymbol{\sigma}(\xi) = [\sigma_s,\ \sigma_n]^{\mathrm{T}} = \mathbf{D}\,\mathbf{u}^*(\xi) \tag{5.4}$$

being $\mathbf{D}$ the constitutive parameter matrix with the decoupled form

$$\mathbf{D} = \begin{bmatrix} K_s & 0 \\ 0 & K_n \end{bmatrix} \tag{5.5}$$

with K_n and K_s the elastic interface parameters.

Thus, the internal virtual work (W_{int}) can be expressed as

$$W_{int} = \int_0^{L_i} \sigma^{\mathrm{T}}(\xi) \ \mathbf{u}*(\xi) \, \mathrm{d}\xi = \int_0^{L_i} \sigma^{\mathrm{T}}(\xi) \ \mathbf{N}(\xi) \boldsymbol{\delta}^e \, \mathrm{d}\xi, \tag{5.6}$$

being L_i the length of the interface, while the external work (W_{ext}) can be defined as

$$W_{ext} = \mathbf{f}^{e^{\mathrm{T}}} \boldsymbol{\delta}^e, \tag{5.7}$$

where $\mathbf{f}^e$ is a vector conjugated to $\boldsymbol{\delta}^e$.

By equality Eqs. (5.6) and (5.7), the weak form of equilibrium is obtained

$$\mathbf{f}^e = \int_0^{L_i} \mathbf{N}^{\mathrm{T}}(\xi) \ \sigma(\xi) \, \mathrm{d}\xi. \tag{5.8}$$

Replacing in the elastic constitutive equation Eq. (5.4), the Eq. (5.8) becomes $\mathbf{f}^e = \mathbf{K}^e \, \boldsymbol{\delta}^e$. Being $\mathbf{K}^e$ the stiffness element matrix associating relative displacements to pair of forces, defined as follows

$$\mathbf{K}^e = \int_0^{L_i} \mathbf{N}^{\mathrm{T}}(\xi) \ \mathbf{D} \ \mathbf{N}(\xi) \, \mathrm{d}\xi. \tag{5.9}$$

The interface stiffness matrix $\mathbf{K}^e$ may be integrated using the Lobatto integration rule [12]. This numerical integration rule includes two end-points of the interface length L_i, defining as

$$\int_0^1 f(x) \, \mathrm{d}x = \sum_{i=1}^{nq} \omega_i \ f(x_i) \tag{5.10}$$

where the weights of the Lobatto integration rule for the linear interface elements ($nq = 2$) are all equal to $\omega_i = 0.5$ for an interface of unit length.

Although, the Gauss rule may be more accurate for polynomial functions, results through the Lobatto rule is more appropriate, avoiding spurious oscillations. A decouple scheme is provided, where the forces at each pair of nodes are proportional only to the displacements at the same pair of nodes, as shown in Fig. 5.1b for the case of a 2D linear interface element. The Lobatto rule for $nq = 2$ is know as trapezoidal integration. Using this rule for the 2D linear interface, the equation $\mathbf{f}^e = \mathbf{K}^e \, \boldsymbol{\delta}^e$ of Fig. 5.1a becomes

$$\begin{bmatrix} f_{x(1,3)}^e \\ f_{x(2,4)}^e \\ f_{z(5,7)}^e \\ f_{z(6,8)}^e \end{bmatrix} = \frac{L_i}{2} \begin{bmatrix} K_s & 0 & 0 & 0 \\ 0 & K_s & 0 & 0 \\ 0 & 0 & K_n & 0 \\ 0 & 0 & 0 & K_n \end{bmatrix} \begin{bmatrix} \delta_{x(1,3)}^e \\ \delta_{x(2,4)}^e \\ \delta_{z(5,7)}^e \\ \delta_{z(6,8)}^e \end{bmatrix} \tag{5.11}$$

where matrix $\mathbf{K}^e$ is a diagonal form when the global reference system (x, z) coincide with the local system (n, s)

$$\mathbf{K}^e = \frac{L_i}{2} \begin{bmatrix} K_S & 0 & 0 & 0 \\ 0 & K_S & 0 & 0 \\ 0 & 0 & K_n & 0 \\ 0 & 0 & 0 & K_n \end{bmatrix} \qquad (5.12)$$

Whereas the case in which the global reference system (x, z) does not coincide with the local system (n, s), the Eq. (5.4) must be multiplied by a rotation matrix. That expression is shown in [11].

It is worth noting that according to the expression of Eqs. (5.11), the insertion between two continuum elements of an interface integrated with the trapezoidal rule corresponds, from a physical point of view, to insert tangential and normal springs at the nodes of the continuum elements, Fig. 5.1b. In conclusion, the elastic interface used in an FE mesh does not correspond to physical interfaces, but is used as means to compute the inter-element forces and stresses.
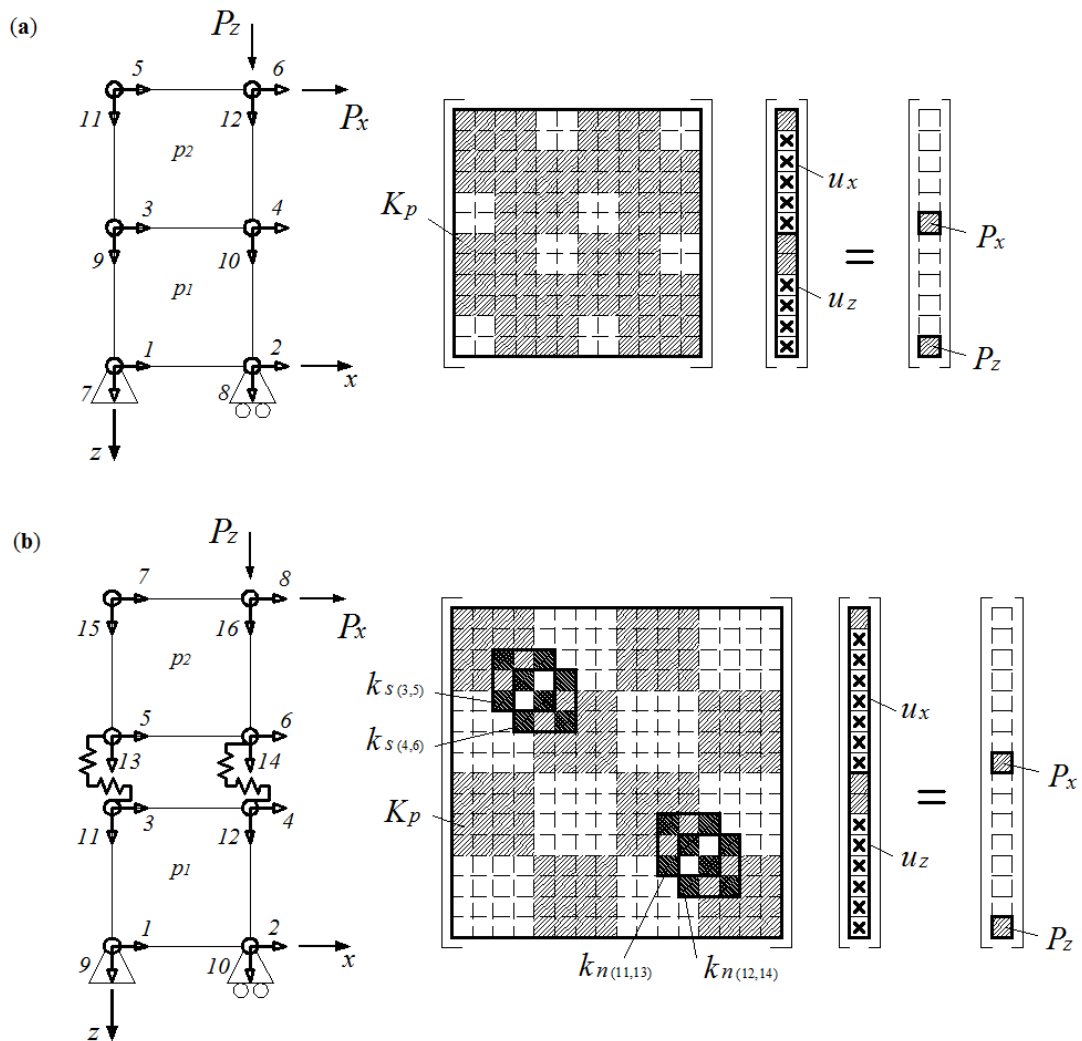
Fig. 5.2. Matrix system of two-dimensional finite element subjects to horizontal and vertical point force at right top, in the classic FEM (**a**) and applying zero-thickness interface element (**b**).

The matrix system of a layer, subdivided by two quadrilateral finite elements (p_1, p_2) and subjected to horizontal and vertical point force (P_x, P_z) at right top, is shown in Fig. 5.2. In particular, classic element analysis which does not assume interface element (Fig. 5.2a), and the model that include zero-thickness element between the two plane elements (Fig. 5.2b). The unknowns of the system are represented by x symbol, while the filling spaces are the known values.

5.4   Numerical example

Crack opening or sliding of brittle materials are studied supposing constant the mechanical parameters of the continuum elements and the stiffness parameters k_s and k_n of the interface until a limit stress imposed "*a priori*". The interface elements are implemented duplicating nodes along mesh lines which are considered a potential crack. The failure surface or cracking surface is assumed in terms of the normal and shear components of the corresponding stress.

A layer subjected to loads or displacements and bonded to classic boundary condition has been analysed firstly, using linear elastic, rigid/plastic or elastic/plastic interface. In particular, the bond is sufficiently rigid when the interfacial stiffness $k > k^*E_p/\mathrm{d}l$ with $k^* = 10^3$, as cited in [11]. A bilinear stress-displacement relationship of interface is supposed for the hardening and softening branch. Moreover, opening crack of a cantilever, subjected to two opposite displacements at end, is investigated applying several brittle interface elements. Finally, the zero-thickness method is implemented in the FE-BIE model, studying the mode I and II crack of a stiffener or beam (one-dimensional finite element) bonded to a substrate which is subdivided in two part by a layer or plate (two-dimensional finite element) and a half-plane defined through boundary integral equation (BIE). The depth of the part of substrate described by plate elements, where interface elements could be applied, is chosen such to predict a possible fracture pattern.

5.4.1   A layer subjected to a uniform vertical displacements at the top

A layer of length $L = 1$ m and height $H = 2$ m is subdivided into two quadrilateral plate elements ($\mathrm{d}l = \mathrm{d}x = \mathrm{d}z = 1$ m), having wholly 6 nodes which two of them are in common. Each node has two degrees of freedom, horizontal and vertical displacement. The plate element is made of homogeneous linearly isotropic elastic material, with elastic modulus $E_p = 30$ MPa and Poisson's coefficient $v_p = 0.3$. Assuming plane stress state with unitary

thickness (t = 1 m) of the plate element, two vertical displacements $\bar{v}$ = 0.1 m are applied at the top toward up. Boundary conditions are applied to the bottom layer in order to block the vertical move, and at the left side stopping the horizontal move, as shown Fig. 5.3a. An interface element is applied between contact of the square finite elements, adding 2 nodes, hence increase the number degrees of freedom from 12 to 16. The matrix of the global system is reported in Fig. 5.3b, highlighting the matrixes of the two quadrilateral elements (K_{p1}, K_{p2}) and an interface element with nodal stiffness k_1 and k_2. The latter element links the two plate elements through nodes 3-5 and 4-6. Nevertheless, it is not shown in Fig. 5.3b, each force, each stiffness and each displacement has horizontal and vertical component. In other words, force f_1 has f_{1x}, f_{1z}, stiffness k_1 has k_{1x}, k_{1z}, and displacement u_1 has u_{1x} and u_{1z}.
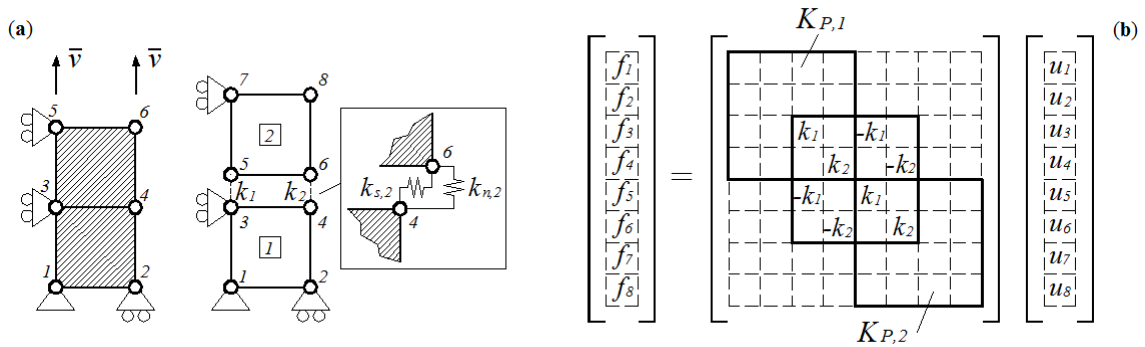
Fig. 5.3. Isotropic element subdivided into 2 quadrilateral FE, subjected to a uniform displacements $\bar{v}$ at the top, and bonded to boundary condition at left and bottom edges (**a**). Matrix of the global system with stiffness of the interface element (**b**).

5.4.1.1 Comparison deformation between FEM and ZTM

A comparison is made between the classic finite element method (FEM) and the zero-thickness method (ZTM). The first method does not have interface elements, while the second one has been assumed a tangential and a normal interface stiffness (k_s, k_n) enough rigidity (high) to not have detachment. The value of the single stiffness is equal to $tdl/2(kE_p/dl)$ [kN/m]. Deformation of the plate element for FEM and ZTM is reported in Fig. 5.4a and 5.4b, respectively. It is noted that the same deformation and stress are calculated when $k = k^* = 10^3$. In particular in the FEM, the stress in z-direction (σ_{zz}) is 1500 kN/m^2, while in the ZTM is equal to 1499 kN/m^2. Furthermore, two cases with low normal interface stiffness (k_n) and setting a rigid tangential stiffness ($k_s = k^*$) is analysed assuming the same material, load and boundary condition. The detachment between the two plate elements is equal to du_z = 33 mm or 83 mm assuming respectively $k_n = k^*/10^3$ or $k_n = k^*/10^4$. Stress in

z-direction is found low when displacement of the detachment (du_z) is high, consequently equal to 1000 kN/m² and 250 kN/m², as shown in Fig. 5.4c-d. In conclusion, with the same value of the external displacements $\bar{v}$, the vertical interface slip (du_z) increase when the normal stiffness of interface (k_n) decrease. The plate elements become less deformed with low value of plane stress in z-direction. Instead, when constant external vertical forces are applied at the top, the stress in z-direction results always same, independent from the interface, and obviously equal to the external force divided by the area of its cross-sections.
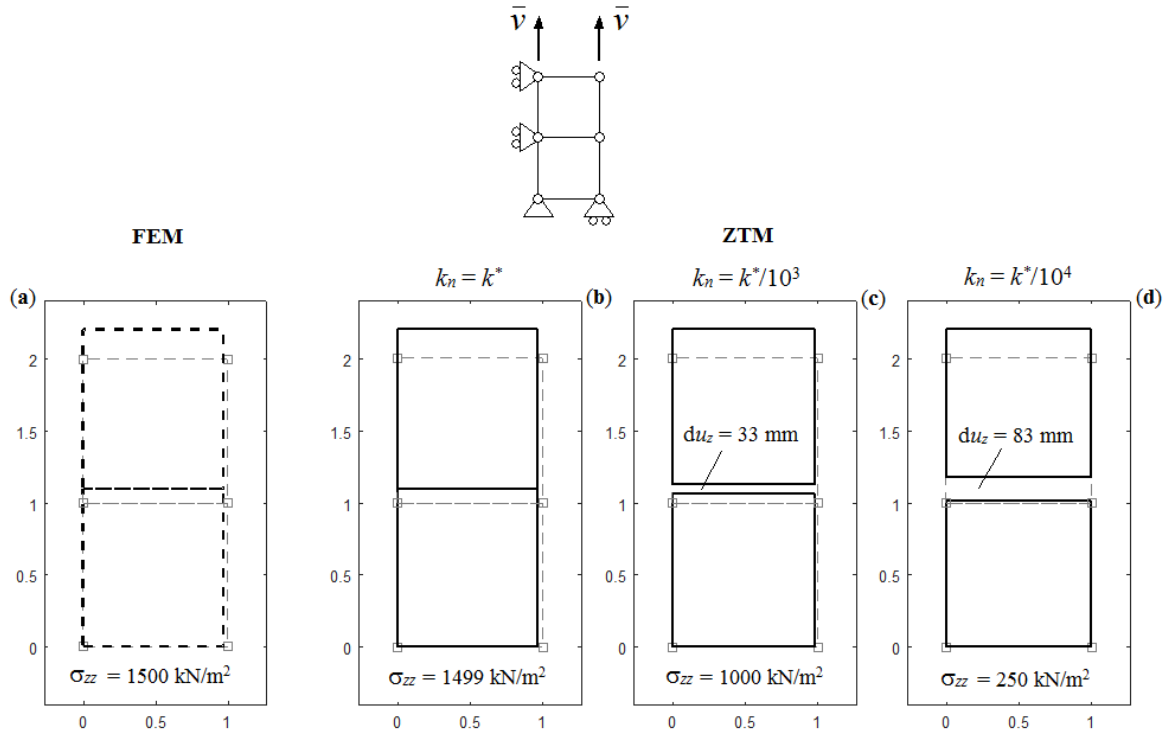
Fig. 5.4. Deformation of the plane element subjected to a uniform displacements $\bar{v}$. Classic analysis FEM (**a**), as well as assuming an interface element (ZTM) with tangential stiffness $k_s = k^*$ and different normal stiffness $k_n = k^*$ (**b**), $k_n = k^*/10^3$ (**c**) and $k_n = k^*/10^4$ (**d**).

5.4.1.2 Interface element with a rigid-plastic behaviour

In this section, a rigid-plastic relationship between stress and displacement of the interface element is considered. The analysis is executed through step-by-step approach at displacement control with increment displacement of d$\bar{v}$ = 0.1 mm. A bilinear curve is assumed, having rigid stiffness $k_s = k_n = k^*$ until an yield or ultimate plate stress $\sigma_{zz,\mathrm{B}}$ = 1000 kN/m². Overcoming this step, two different behaviours are studied: hardening or softening branch, as shown in Fig. 5.5, in the normal direction of interface. The stiffness of the hardening branch is $k_n = k^*/10^4$, with rupture stress $\sigma_{zz,\mathrm{D}}$ = 1.1 $\sigma_{zz,\mathrm{B}}$. While, stiffness of the softening one is $k_n = k^*/10^3$, until to reach the step immediately before zero stress.

The deformation of the layer, achieving the point A and B of the effective stress-separation relationship (Fig. 5.5), is reported in Fig. 5.6. The interface displacement obtained may be disregarded because of very small value equal to $du_z = 0.017$ mm with $\sigma_{zz,A} = 510$ kN/m^2 and $du_z = 0.033$ mm with $\sigma_{zz,B} = 990$ kN/m^2. The point A or B of stress-slip curve is reached applying external displacement $\bar{v} = 34$ or 66 mm, respectively.

For the hardening branch, the deformation of the layer becomes as shown in Fig. 5.7. The increase of the external displacement, until $\bar{v} = 86$ mm, reaches the point C of the stress-slip curve (Fig. 5.5a) obtaining plate stress $\sigma_{zz,C} = 1054$ kN/m^2 and interface displacement $du_z = 16.7$ mm. Finally, the rupture is achieved applying external displacement $\bar{v} = 104$ mm, where $\sigma_{zz,D} = 1099$ kN/m^2 and $du_z = 31.7$ mm occur.

Conversely, the raise of the external displacement ($\bar{v}$) in the softening branch shows a decrease of the plate stress (σ_{zz}) and an increase of the interface displacement (du_z). That is remarked in the deformation of the two plate elements, Fig. 5.8. Assuming an external displacement $\bar{v} = 83$ mm, the point C of the rigid-softening curve (Fig. 5.5b) is reached ($\sigma_{zz,C} = 494$ kN/m^2 and $du_z = 17.0$ mm). Whereas, the ultimate point D is obtained at $\bar{v} = 98$ mm ($\sigma_{zz,D} = 44$ kN/m^2 and $du_z = 32.0$ mm).

It is worth noting that the deformation of the layer turns out extension for the beginning and hardening branch, while starts to be in contraction when interface contact reaches the softening branch until an initial state of deformation characterised by null stress and ultimate interfacial displacement.
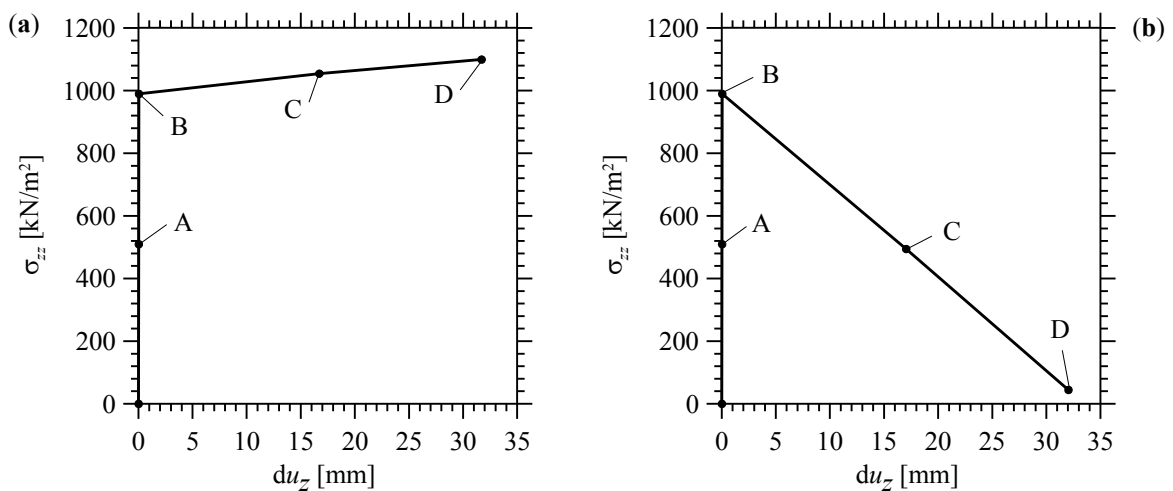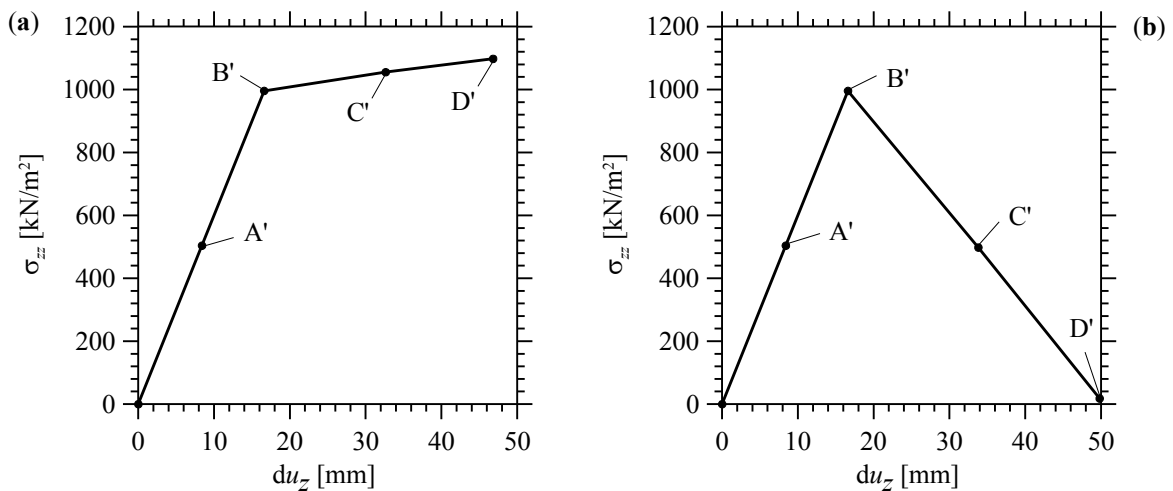

Fig. 5.5. Effective stress-slip relationships: bilinear rigid-hardening (**a**) and rigid-softening (**b**) behaviour.
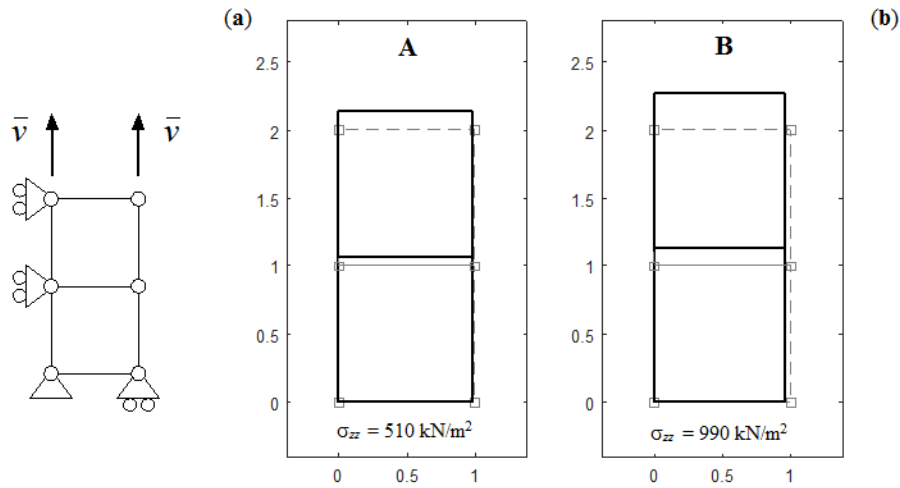
Fig. 5.6. Deformation of the layer at the point A ($\sigma_{zz} = 510$ kN/m^2, d$u_z = 0.017$ mm in (**a**)) and B ($\sigma_{zz} = 990$ kN/m^2, d$u_z = 0.033$ mm in (**b**)) of the rigid-plastic curve.
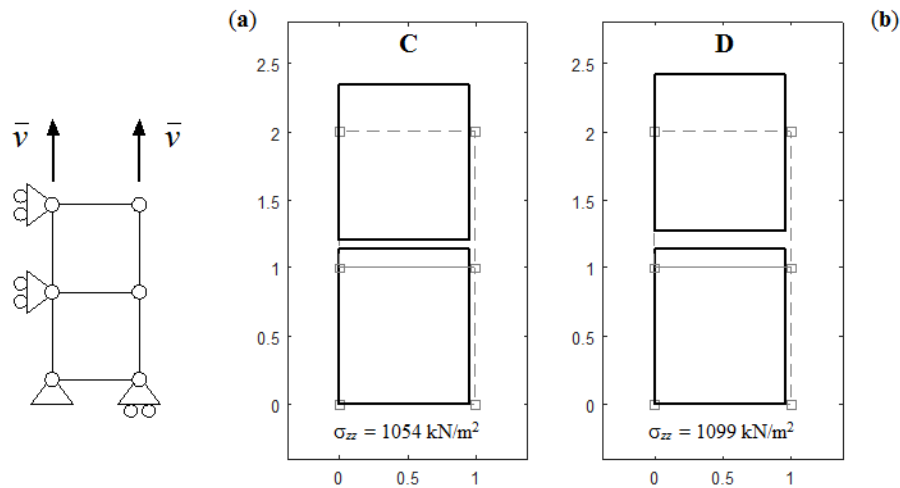
Fig. 5.7. Deformation of the layer with hardening behaviour at the point C ($\sigma_{zz} = 1054$ kN/m^2, d$u_z = 16.7$ mm in (**a**)) and D ($\sigma_{zz} = 1099$ kN/m^2, d$u_z = 31.7$ mm in (**b**)) of the rigid-plastic curve.
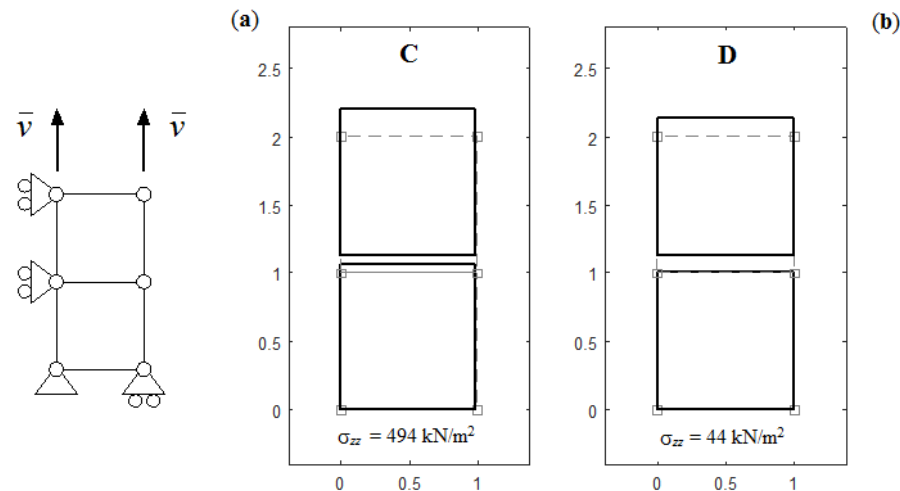
Fig. 5.8. Deformation of the layer with softening behaviour at the point C ($\sigma_{zz} = 494$ kN/m^2, d$u_z = 17.0$ mm in (**a**)) and D ($\sigma_{zz} = 44$ kN/m^2, d$u_z = 32.0$ mm in (**b**)) of the rigid-plastic curve.

5.4.1.3 Interface element with a general bilinear curve

The same layer is also studied applying interface elements having a bilinear curve of stress-slip shown in Fig. 5.9. In the first elastic branch, interface normal stiffness is assumed equal to $k_n = 2k^*/10^3$, while interface shear stiffness is always considered rigid ($k_s = k^*$). In particular, the point A is reached with external displacement $\bar{v} = 42$ mm, while the yield or maximum stress ($\sigma_{zz,B} = 1000$ kN/m^2) with $\bar{v} = 83$ mm. The deformation of layer is reported in Fig. 5.10 for the state obtained by A or B point, showing more shift between the two plates (du_z) than the previously case having an interfacial rigid-plastic behaviour. The plate stress $\sigma_{zz,A} = 504$ kN/m^2 and $du_z = 8.4$ mm are obtained in the point A, whereas $\sigma_{zz,B} = 996$ kN/m^2 and $du_z = 16.6$ mm in the point B.

For the hardening behaviour with normal stiffness $k_n = k^*/10^4$, a raise of the interfacial displacement and an expansion of the layer are shown in Fig. 5.11, as expected. In the stress-slip curve, point C of the elastic-hardening behaviour ($\sigma_{zz,C} = 1056$ kN/m^2 and $du_z = 32.6$ mm in Fig. 5.9a), is achieved applying $\bar{v} = 102$ mm. Whereas, rupture occurs at the point D ($\sigma_{zz,D} = 1098$ kN/m^2 and $du_z = 46.8$ mm) applying $\bar{v} = 119$ mm.

According to the interfacial softening behaviour, plate stress decreases and interface displacement increases when external displacement rises. Fig. 5.12 shows a reduction of plate deformation with value of external displacement $\bar{v}$ higher than the case with rigid-softening interface. The point C of the stress-slip curve (Fig. 5.9b) is reached applying $\bar{v} = 100$ mm, obtaining plate stress $\sigma_{zz,C} = 498$ kN/m^2 and interfacial displacement $du_z = 33.8$ mm. While, the ultimate point D, $\sigma_{zz,D} = 18$ kN/m^2 and $du_z = 49.8$ mm, are achieved with external displacement $\bar{v} = 116$ mm.

Fig. 5.9. Effective stress-slip relationships: bilinear elastic-hardening (**a**) and elastic-softening (**b**) behaviour.
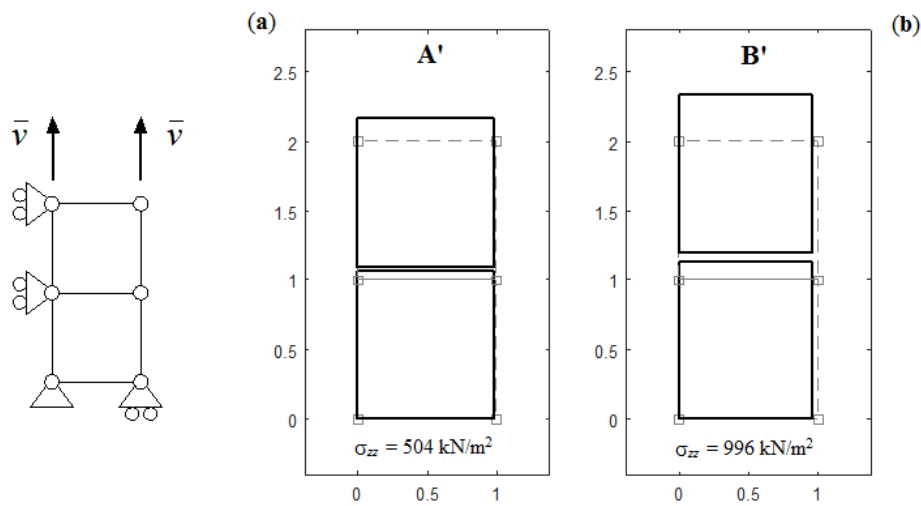
Fig. 5.10. Deformation of the layer at the point A' (σ_{zz} = 504 kN/m^2, du_z = 8.4 mm) and B' (σ_{zz} = 996 kN/m^2, du_z = 16.6 mm) of the bilinear elastic-plastic curve.
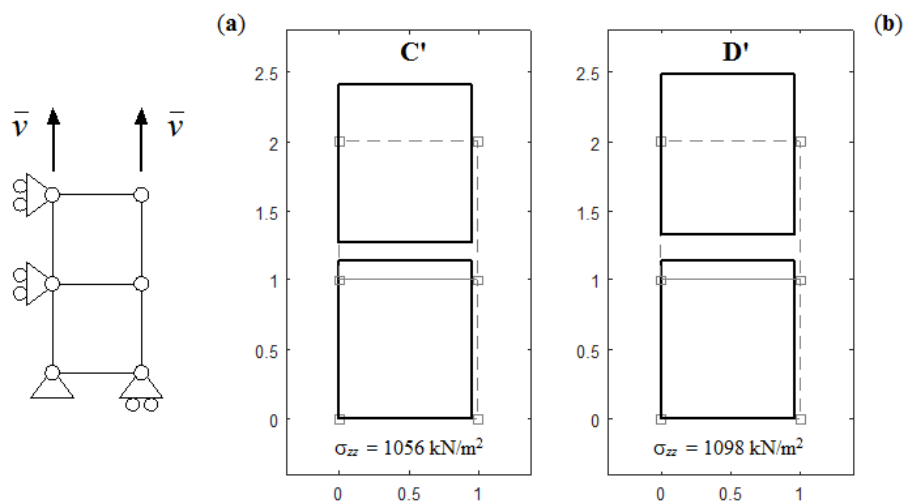
Fig. 5.11. Deformation of the layer with hardening behaviour at the point C' (σ_{zz} = 1056 kN/m^2, du_z = 32.6 mm) and D' (σ_{zz} = 1098 kN/m^2, du_z = 46.8 mm) of the bilinear elastic-plastic curve.
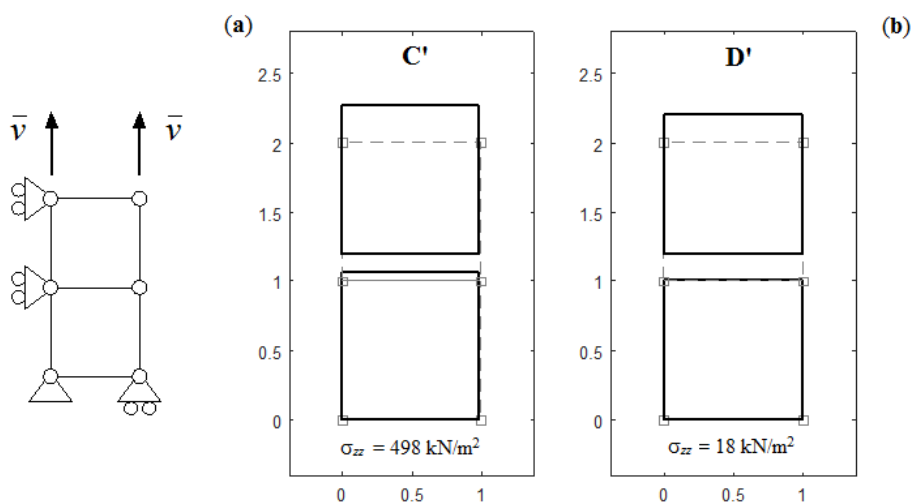
Fig. 5.12. Deformation of the layer with softening behaviour at the point C' (σ_{zz} = 498 kN/m^2, du_z = 33.8 mm) and D' (σ_{zz} = 18 kN/m^2, du_z = 49.8 mm) of the bilinear elastic-plastic curve.

In conclusion, the deformation of the plate element goes on to expand with an increase of stress when interface element has a hardening behaviour. Whereas, a contraction deformation of the layer with a decrease of stress is exhibited for interfacial softening behaviour.

5.4.2   A layer subjected to uniform load at the top and right edges

A plate element of length $L = 2$ m and height $H = 2$ m, subjected to uniform vertical load at the top and uniform horizontal load at the right edge $P = 1000$ kN/m, bonded to supports in z-direction at the bottom and to supports in x-direction at the left edge, is investigated in this Section. Assuming an isotropic elastic material with $E_p = 30$ and $v_p = 0.3$, the layer is subdivided into four homogenous quadrilateral finite elements. Plane stress state is supposed with unitary thickness. Four interface elements are introduced, where two of them are horizontal (HI_1, HI_2) and other two vertical (VI_1, VI_2), see Fig. 5.13a. Cases with several values of interface stiffness are analysed. These examples are presented just to show the quality of the displacement field when interface stiffness values are or are not rigid.

The first case, supposing all rigid stiffnesses (k_{HI} and $k_{VI} = k^*$) shows the same deformation obtained by the traditional FE analysis without interface elements, Fig. 5.13b.

Then, three cases are analysed assuming all rigid shear stiffnesses ($k_s = k^*$), and low values of the normal stiffness ($k_n = k^*/1000$) in vertical and/or horizontal interface elements. In particular, a shift turns out in z-direction when low normal stiffness is applied only in the horizontal interface elements Fig. 5.13c. Instead, toward x-direction when only low normal stiffness is presented in the vertical interface elements, Fig. 5.13d. Whereas, an opening occurs in both directions when all interface elements have low values of the normal stiffness, Fig. 5.13e.

Furthermore, two cases are studied applying rigid normal stiffness for all interface elements and low values for the shear stiffness into horizontal interface, Fig. 5.13f, or into vertical interface, Fig. 5.13g.

Finally, the deformation of layer using low stiffness in shear and normal component for all interface elements ($k_{HI} = k_{VI} = k^*/1000$) is reported in Fig. 5.13h.
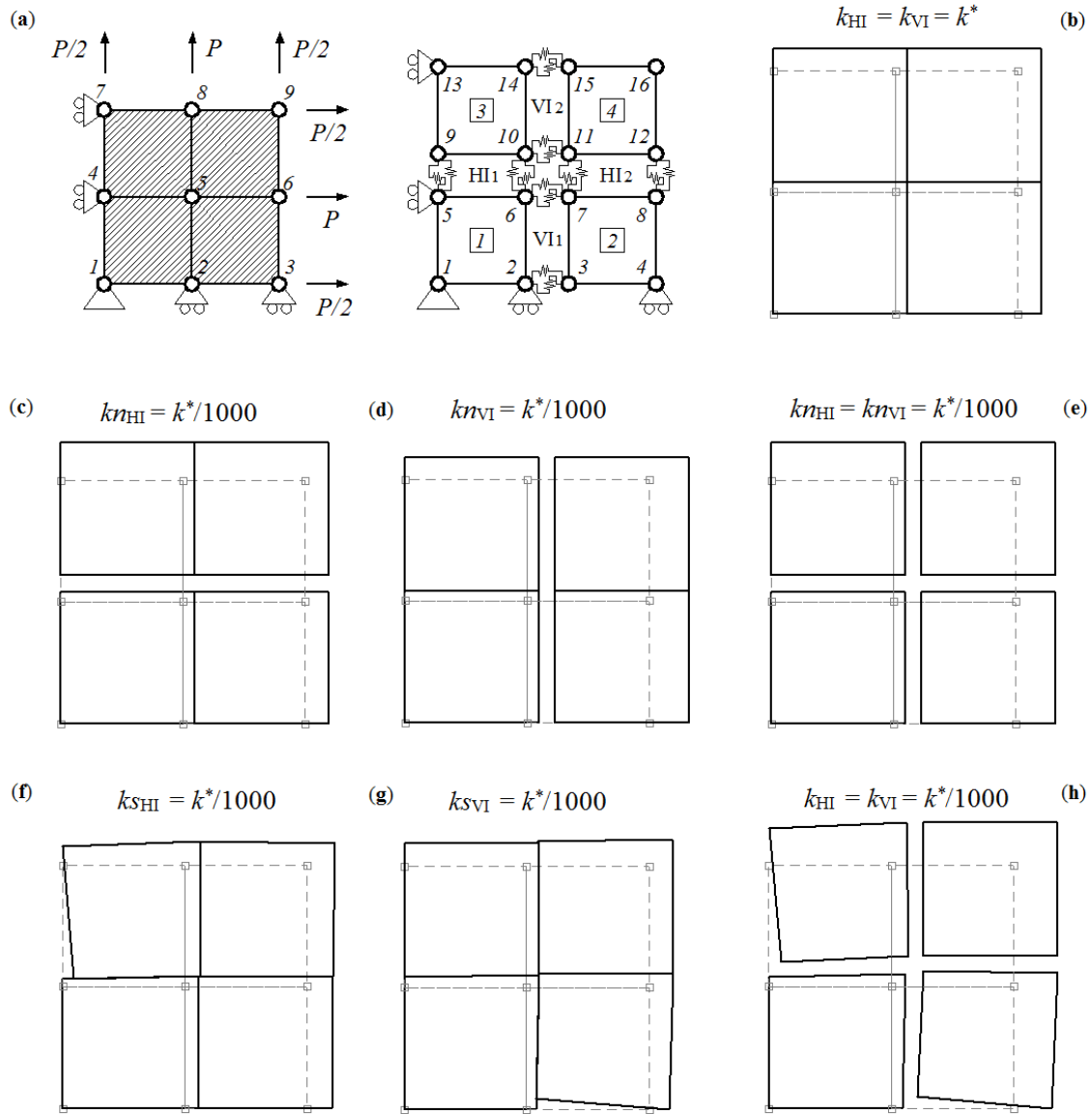
Fig. 5.13. Isotropic plate element, subdivided into 4 quadrilateral FE, bonded to boundary condition at left and bottom edges, and subjected to uniform load p at the top and right edges. Sketch of the horizontal (HI) and vertical (VI) zero-thickness interface (**a**) and deformation of the layer with: all rigid interfaces k^* (**b**), normal (**c,d,e**) or shear (**f,g**) stiffness interface equal to $k^*/10^3$, and all interfacial stiffnesses $k^*/10^3$ (**h**).

5.4.3 A cantilever subjected to two opposite displacements at the end

The double cantilever beam (DCB) is the simplest example used to understand and determined pure "mode I" of fracture. The generalized Griffth energy criterion and the linear elastic fracture mechanics (LEFM) are used to characterise crack propagation, providing a foundation for development of interfacial failure simulation in a finite element model at analysing of complex problems. Moreover, some examples are presented in the literature based on (CZM) cohesive zone model [14, 15, 16].

In this Section, deformation of the structure is limed to a linear elastic (LEFM) behaviour with only fracture interface has the ability to fail. The surface between adjoining material constrains them together with zero ductility until it fails. The failure at this point dissipates a finite amount of energy (G_c) per unity growth of the crack. However, if the bond material is extremely thin relative to the adjoining components, it may be assumed to be infinitely thin and its behaviour is lumped into the behaviour of the fracture interface. Under these conditions, the compliance of the structure C (reverse of the stiffness) can be defined in terms of the applied load F_z and opening displacement du_z as $C = du_z/F_z$. The elastic internal energy can be obtained $G_c = (F_z^2/2t)dC/da_0$, where dC/da_0 represents the change in compliance of the structure as the crack length changes a_0. That equation is valid provided that no inelastic deformation occurs in the structure, excluding the bond material, and that the fracture interface and bond material behaves with zero ductility until it fails. In other words, brittle material behaviour is characterised by the fact that no significant inelastic deformation occur prior to fracture. The brittle interfacial failure, is one of the major sources of failure in devices that consist of multiple thin and stacked layers, where delamination is a failure phenomenon that occurs frequently. It may arise under various circumstances, such as low velocity impacts, mechanical loading, temperature fluctuations, etc.
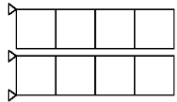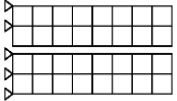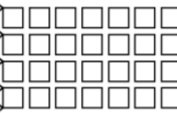
Model		Series	dl	Int.	k_s	k_n	Fig.
1		1	1.0	H	k^*	k^*	5.17
		2	1.0	H	k^*	$k^*/10^4$	5.18
		3	0.5	H	k^*	$k^*/10^4$	5.19
2		1	0.5	H	$k^*/10^3$	$k^*/10^3$	5.20
		2	0.25	H	$k^*/10^3$	$k^*/10^3$	5.21
3		1	0.5	H	$k^*/10^3$	$k^*/10^3$	5.22
				V	k^*	k^*	
		2	0.5	H	$k^*/10^3$	$k^*/10^3$	5.23
				V	k^*	$2k^*/10^3$	

Table 5.1. Meshes and interfaces adopted for a cantilever.

A cantilever of length L = 4 m, height H = 2 m, and unitary thickness (t = 1 m), characterized by brittle interface failure through zero-thickness elements, has been investigated. The structure is bonded with hinges at left side, and subjected to two opposite displacement $\bar{v}$ at the other end, Fig. 5.14a. Plane stress state is used adopting a material with E_p = 10 MPa and ν_p = 0.3. The cantilever is subdivided into quadrilateral plane elements with length mesh dl = dx = dz. A step-by-step analysis is made with increment of external displacement d$\bar{v}$ = 0.1 mm. Several cases, applying horizontal and vertical interface elements, are investigated with different values of interfacial stiffness and, for the sake of simplicity, constant in each step. Linear elastic brittle behaviour has been supposed into the interfacial contact, where the failure of the zero-thickness element occurs at one limit stress, which is assumed "*a priori*" and equal to σ_{lim} = 10 kPa. Overtaking the limit stress at one point, the contact link of this point is separated. Three models are studied where their sketches are reported in Table 5.1, showing the length of finite element (dl) and the stiffness (k_s, k_n) of horizontal or vertical interface element assumed $k^* = 10^3$ kN/m.
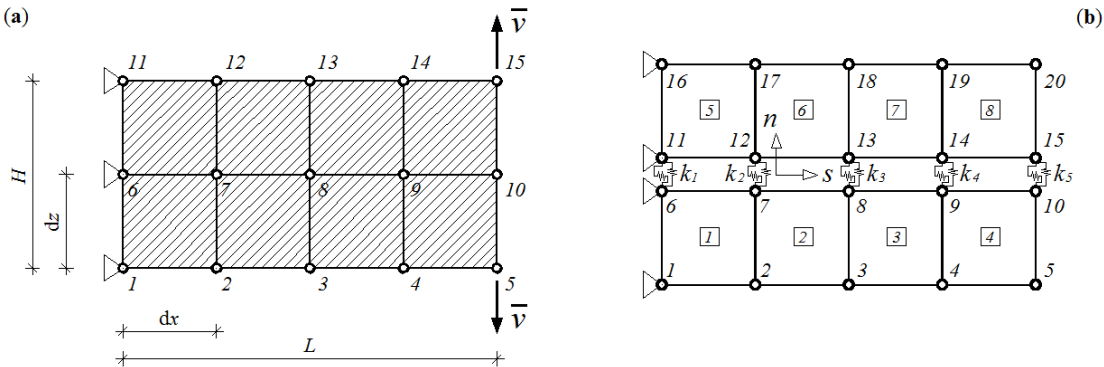
Fig. 5.14. Cantilever subject to two opposite displacements $\bar{v}$ at the end (**a**), sketch of horizontal zero-thickness interface elements (**b**).
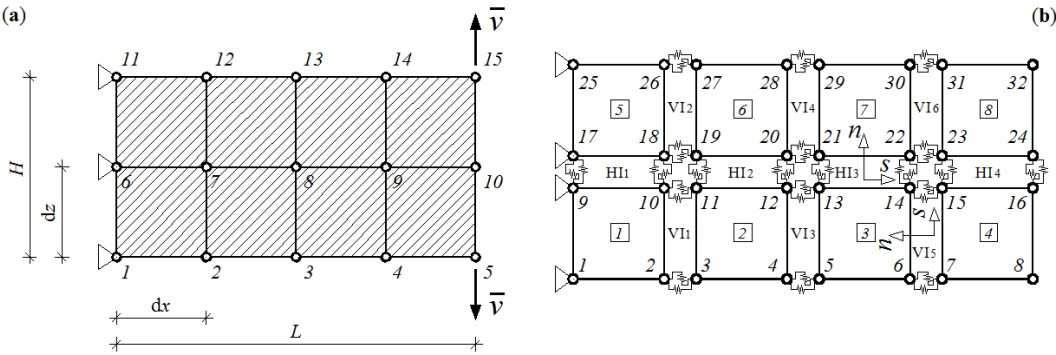
Fig. 5.15. Cantilever subject to two opposite displacements $\bar{v}$ at the end (**a**), sketch of horizontal and vertical zero-thickness interface elements (**b**).

The first model of cantilever assumes horizontal interface at the half-height (z = 1 m). The structure is subdivided with a number of plane square elements n_{el} = 8 having unitary length (dl = 1 m) and with 4 horizontal interface elements, Fig. 5.14. The stiffness of bond material is supposed rigid (high) for both shear and normal components (Model 1 Series 1 in Tab. 5.1), as well as rigid shear stiffness and low normal stiffness (Model 1 Series 2, in Tab. 5.1). In particular, the latter Series has also been studied using a mesh refinement with length of plate element dl = 0.5 (Model 1 Series 3 in Tab. 5.1), hence with n_{el} = 32 plate elements and 8 horizontal interface elements. Plane stress in z-direction and normal stress of the horizontal interface is reported for the opening crack at coordinate x = 4.0; 3.0 and 2.0 m. For the Series 1 of Model 1, the first crack (x = 4.0) occurs applying an external displacements $\bar{v}$ = 1.5 mm. Figs. 5.17a and b show stress in z-direction into the plate element (σ_{zz}) and normal stress of the horizontal interface (σ_n), respectively. Notice that, the maximum σ_{zz} is equal to 12 kPa, while the σ_n of the horizontal interface does not exceed the limit stress imposed. In this situation, the detachment does not occur, but overcoming this step, a crack turns out along horizontal direction. High value of stresses are at x = 3.0 m, before to reach the second crack obtained with $\bar{v}$ = 3.0 mm, Fig. 5.17c-d. Finally, the crack propagation is stopped at x = 2.0 with an external displacement $\bar{v}$ = 9.1 mm, showing the maximum values in Fig. 5.17e-f. Note that, the interfacial stresses in the detachment area become zero because of the rupture. The crack of the Series 2, Model 1 is shown in Fig 5.18. Owing to low value assumed in the normal stiffness, an opening crack is developed throughout interface contact before to reach the first crack with deformation higher than the case with rigid bond. Moreover, the plate stresses are not only concentrated at the failure node but they are spread along the interface line. The crack at coordinate x = 4.0; 3.0 and 2.0 m is attained respectively with $\bar{v}$ = 26.8; 45.5 and 91.1 mm. The same displacements are gotten with a more accurate mesh having length of element equal to 0.5 m, Fig. 5.19, where the same crack occurs with $\bar{v}$ = 24.7; 42.0; and 82.1 mm, respectively.

The global external load-displacement behaviour (F_z–$\bar{v}$) is obtained with several mesh refinement for the cantilever of Model 1 with rigid shear stiffness ($k_s = k^*$) and low normal stiffness ($k_n = k^*/10^4$) for the horizontal interface elements. Fig. 5.16 reports the force-displacement relationship of the cantilever with number of elements n_{el} = 8; 32; 128; 512 and 2048. Moreover, the mesh with n_{el} = 32 and 8 interface elements is checked through a software at traditional finite element (dashed line in Fig. 5.16 a). The solutions of the two analyses show a good agreement. The maximum load is reached before the first crack and converges at a value with the rise of number of elements (Fig. 5.16 b).
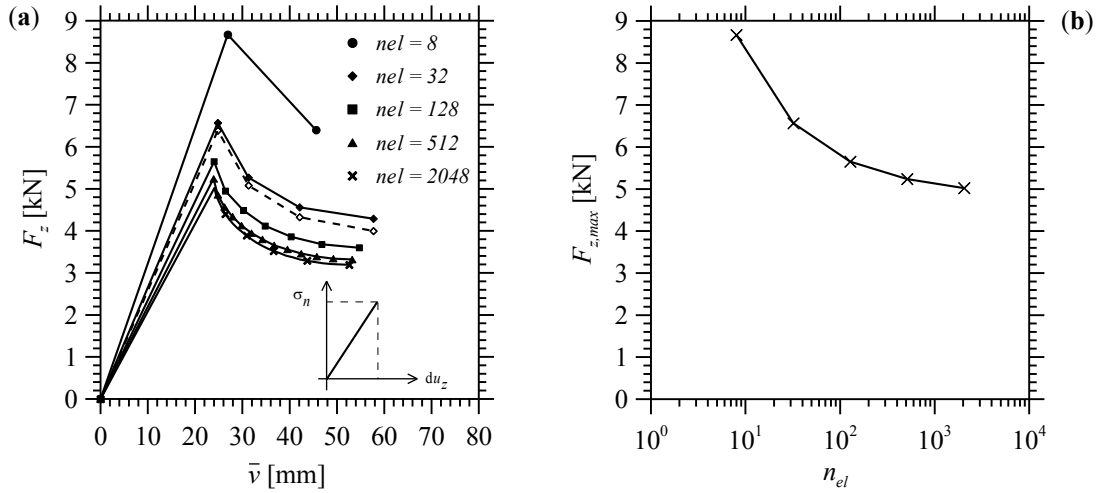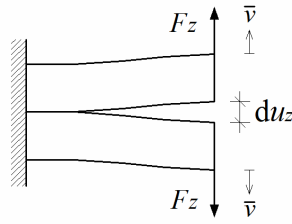
Fig. 5.16. Cantilever with horizontal interface $k_s = k^*$ and $k_n = k^*/10^4$ at half-height ($z = 1$ m). Curve of external force F_z and external displacement $\bar{v}$ of the present analysis (solid line) and FEM (dashed line), assuming several mesh refinement (**a**). Maximum external load $F_{z,max}$ versus number of plate elements n_{el} (**b**).

Furthermore, the same cantilever has been studied with more horizontal interface lines, as shown Model 2 in Tab. 5.1. The structure is subdivided with three horizontal contact lines at coordinate $z = 0.5$; 1.0 and 1.5 m (Model 2 Series 1) and with seven horizontal contact lines situated at one distant of 0.25 m from each other (Model 2 Series 2). A mesh with length of quadrilateral element equal to $dl = 0.5$ for the Series 1 and $dl = 0.25$ m for Series 2 is assumed. The cantilever is discretized with 32 or 128 plate elements, respectively for the structure having 3 or 7 contact lines. The stiffness of the glue (bond material) for both models is supposed weak and elastic-brittle in the shear and normal components along the interface line. Plate stress in z-direction (σ_{zz}) and normal stress of horizontal interface (σ_n) are reported for the cracks at coordinate $x = 4.0$ and 3.0 m. The two cracks are obtained applying external displacement $\bar{v} = 5.0$ and 14.8 mm for the Series 1, Fig. 5.20, and $\bar{v} = 7.4$ and 27.4 mm for the Series 2, Fig. 5.21. During the incremental analysis, the shear interface stresses result always lower than the normal ones, therefore the mode I crack (opening mode) is kept on along the fracture path. It is worth observing that the rupture does not occur at half height of the cantilever, but turns out simultaneously at the top and bottom level, heading to horizontal direction. Moreover, the

crack at one point for the case with more horizontal interface (Model 2 Series 2) is reached with value of external displacement higher than other case having less contact interface lines (Model 2 Series 1).

Finally, horizontal and vertical interface elements (HI, VI) are set between the edge of the plane elements, as shown the cantilever in Fig. 5.15. With regard to corner node, the detachment of the horizontal or vertical interface contact occurs when at least one of the two interfaces exceeds the limit stress σ_{lim}. In other words, looking at Fig. 5.15b, if the link between nodes 15 and 23 is disconnected, then even correspondent link between nodes 14 and 22 is interrupted. A square mesh with 32 plane elements is assumed and represented by Model 3 in Tab. 5.1. Two kinds of bond materials are investigated. In particular, a model with low stiffness in the horizontal interface elements and rigid in the vertical ones, $k_{sHI} = k_{nHI} = k^*/10^3$, $k_{sVI} = k_{nVI} = k^*$, (Model 3 Series 1); and other one with same stiffness except for the normal component of the vertical interface elements, $k_{sHI} = k_{nHI} = k^*/10^3$, $k_{sVI} = k^*$ and $k_{nVI} = 2k^*/10^3$, (Model 3 Series 2). Plate stress in z-direction and normal stress of the horizontal interface are reported for the crack at $x = 4.0$; 3.5 and 3.0 m. The solutions of the Model 3 Series 1 is shown in Fig. 5.22, and could be compared with the Model 2 Series 1 which is reported in Fig. 5.20. The three opening cracks occur applying respectively the external displacement $\bar{v} = 8.2$; 15.5 and 29.8 mm. Different deformation turns out in the Model 3 Series 2 where opening crack are higher because of the weak stiffness into vertical interface, Fig. 5.23. The external displacement applied for the respectively crack are $\bar{v} = 8.3$; 22.6 and 50.3 mm.
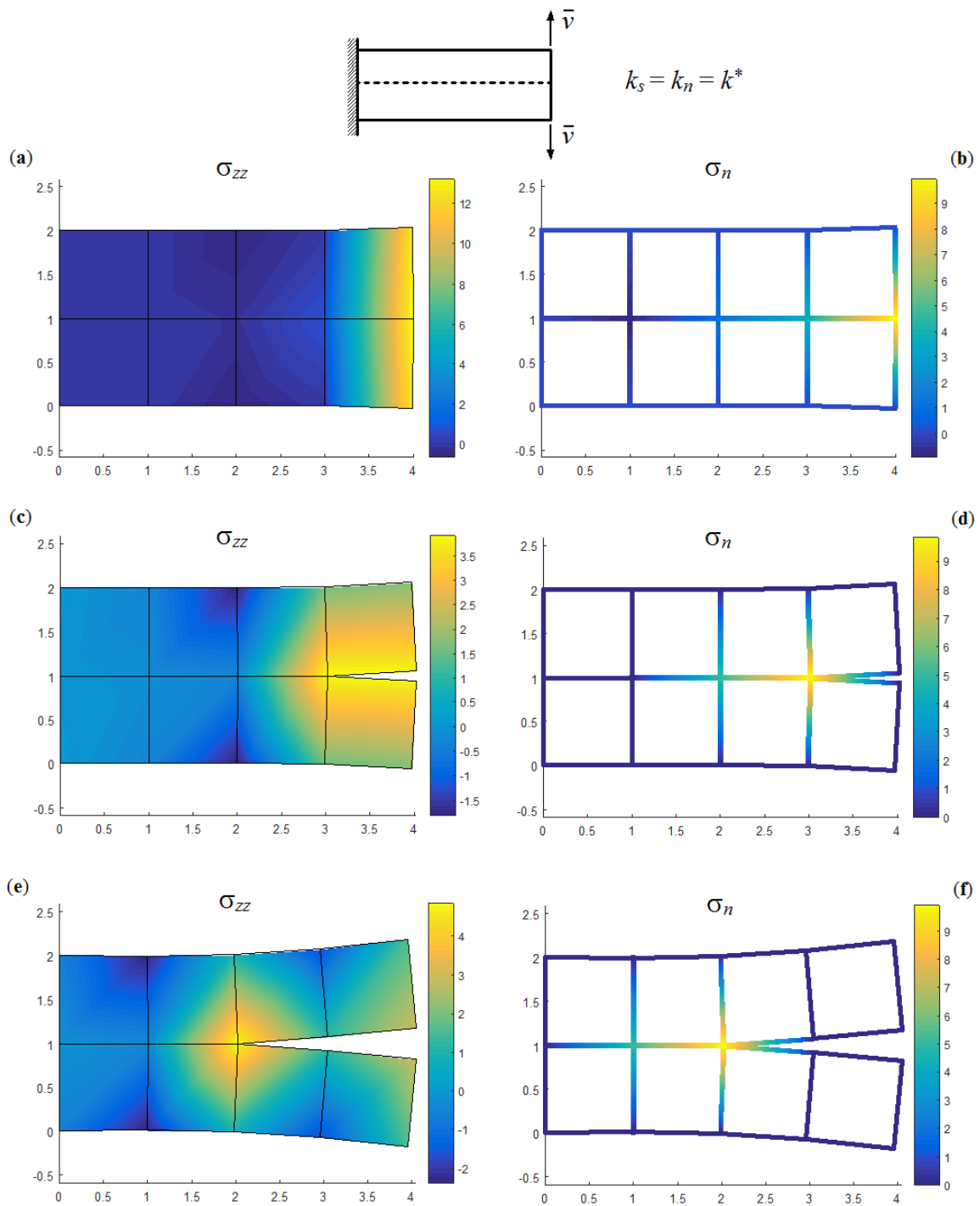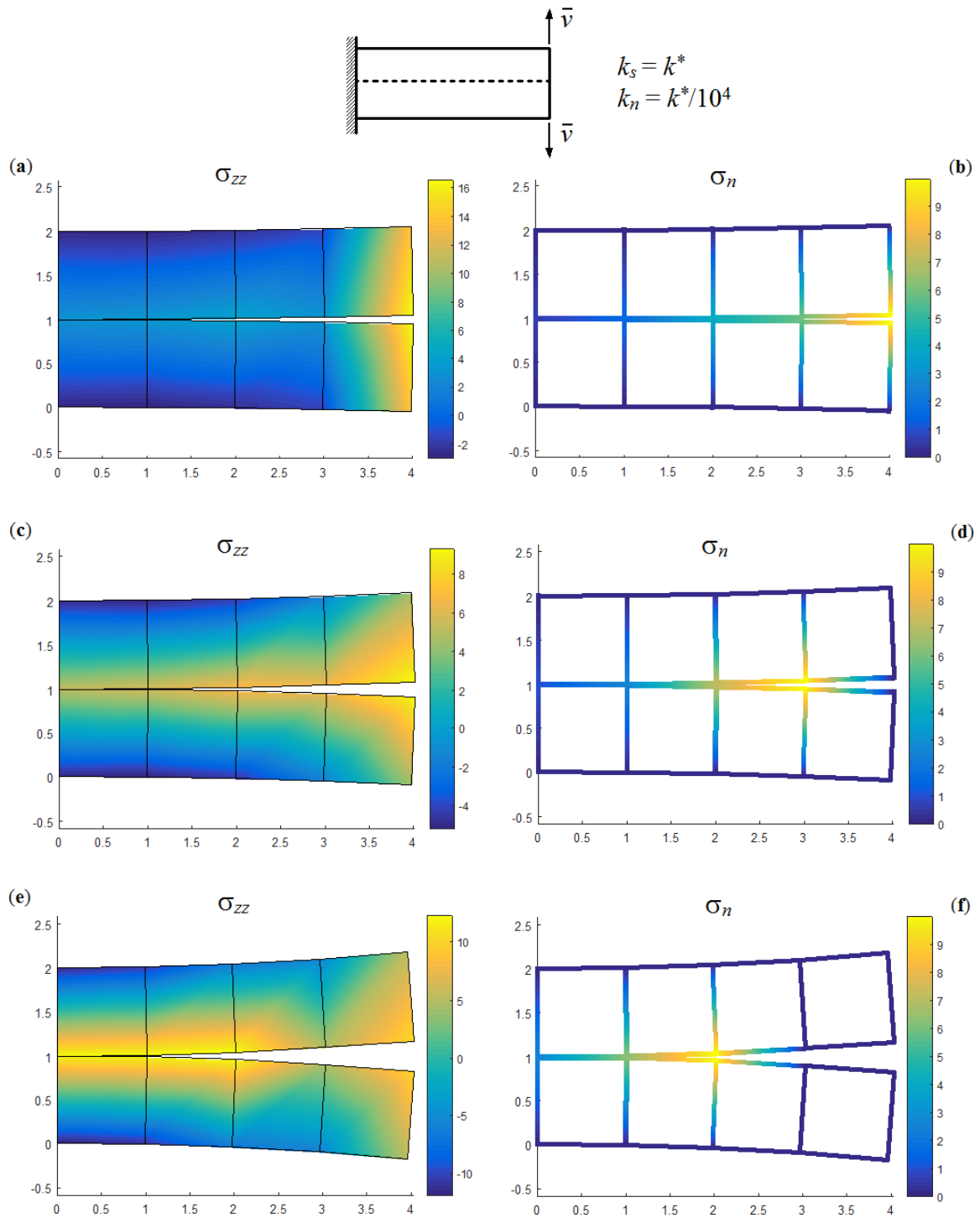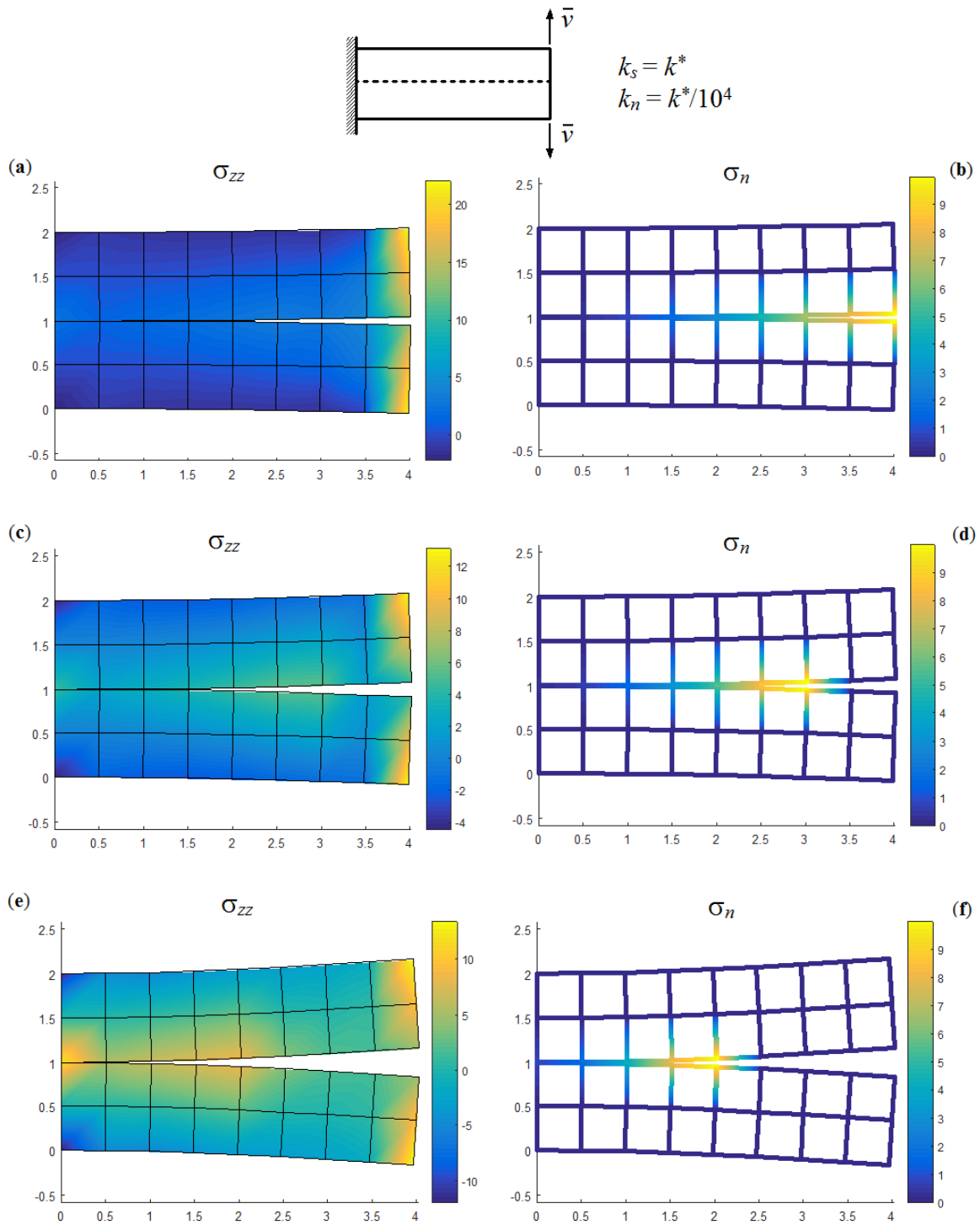
Fig. 5.17. Cantilever of the Model 1 Series 1, subjected to two opposite displacements $\bar{v}$ at the end and assuming 4 horizontal interfaces with $k_s = k_n = k^*$ at $z = 1$ m. Plate stress σ_{zz} and normal stress σ_n of the horizontal interface [kN/m²] for crack at $x = 4.0$ m with $\bar{v} = 1.5$ mm (**a**, **b**), at $x = 3.0$ m with $\bar{v} = 3.0$ mm (**c**, **d**) and at $x = 2.0$ m with $\bar{v} = 9.1$ mm (**e**, **f**).
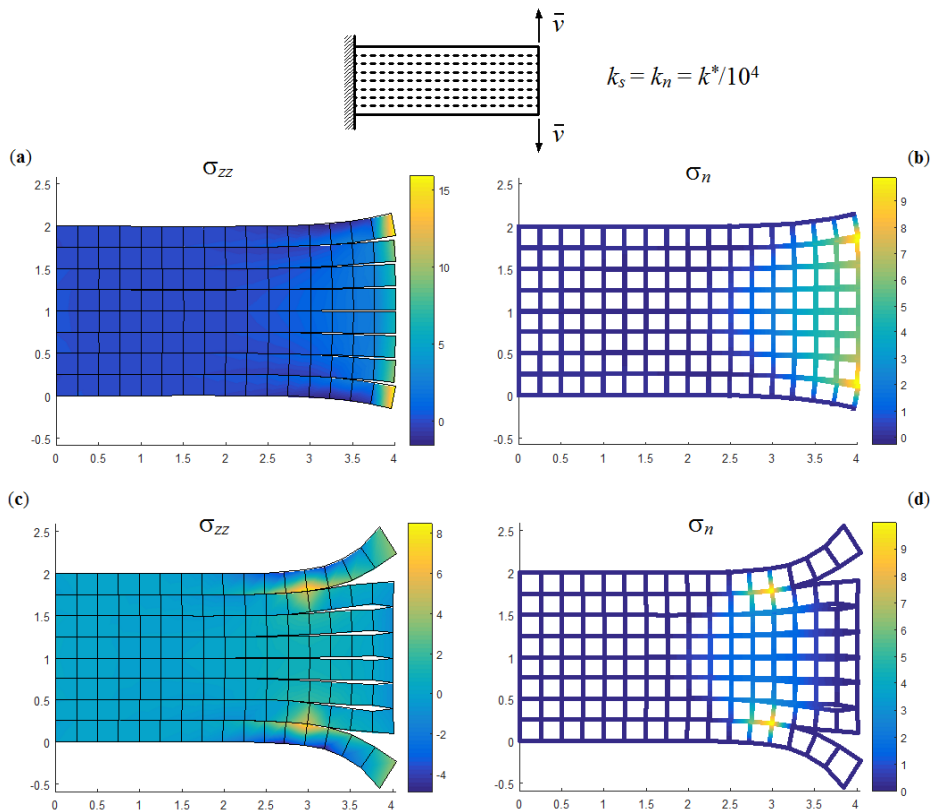
Fig. 5.18. Cantilever of the Model 1 Series 2, subjected to two opposite displacements $\bar{v}$ at the end and assuming 4 horizontal interface with $k_s = k^*$ and $k_n = k^*/10^4$ at $z = 1$ m. Plate stress σ_{zz} and normal stress σ_n of the horizontal interface [kN/m^2] for crack at $x = 4.0$ m with $\bar{v} = 26.8$ mm (**a**, **b**), at $x = 3.0$ m with $\bar{v} = 45.5$ mm (**c**, **d**) and at $x = 2.0$ m with $\bar{v} = 91.1$ mm (**e**, **f**).

Fig. 5.19. Cantilever of the Model 1 Series 3, subjected to two opposite displacements $\bar{v}$ at the end and assuming 8 horizontal interface with $k_s = k^*$ and $k_n = k^*/10^4$ at $z = 1$ m. Plate stress σ_{zz} and normal stress σ_n of the horizontal interface [kN/m^2] for crack at $x = 4.0$ m with $\bar{v} = 24.7$ mm (**a**, **b**), at $x = 3.0$ m with $\bar{v} = 42.0$ mm (**c**, **d**) and at $x = 2.0$ m with $\bar{v} = 82.1$ mm (**e**, **f**).
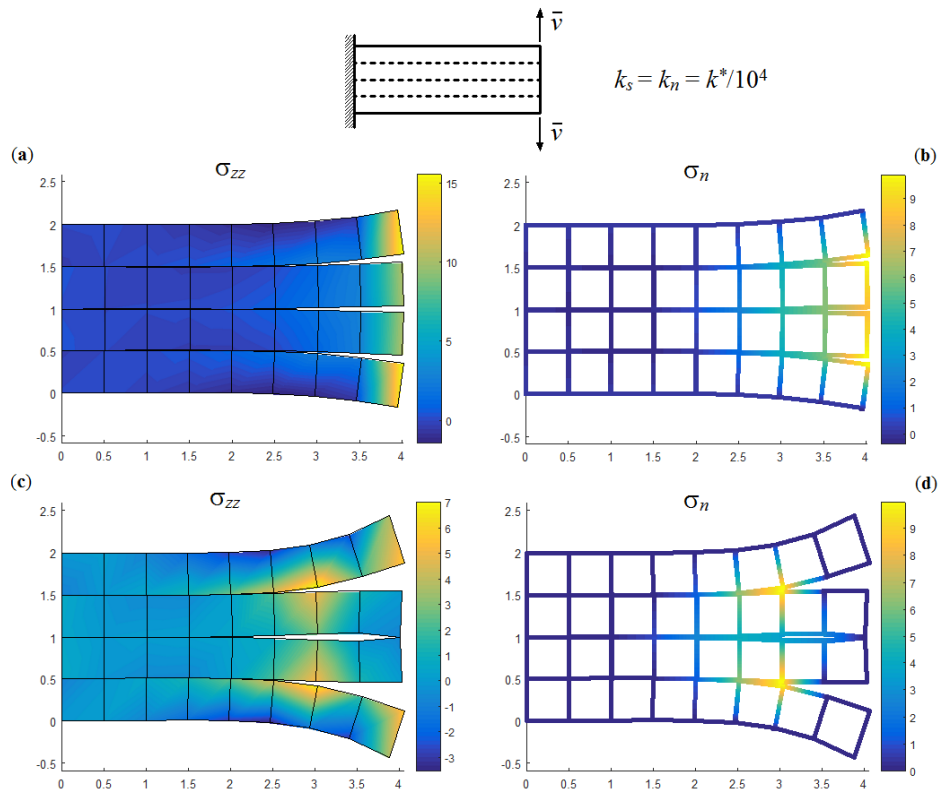
Fig. 5.20. Cantilever of Model 2 Series 1, subjected to two opposite $\bar{v}$ at the end, assuming horizontal interface $k_s = k_n = k^*/10^4$. Plate stress σ_{zz} and normal stress σ_n of the horizontal interface [kN/m²] for crack at $x = 4.0$ m with $\bar{v} = 5.0$ mm (**a**,**b**) and at $x = 3.0$ m with $\bar{v} = 14.8$ mm (**c**,**d**).
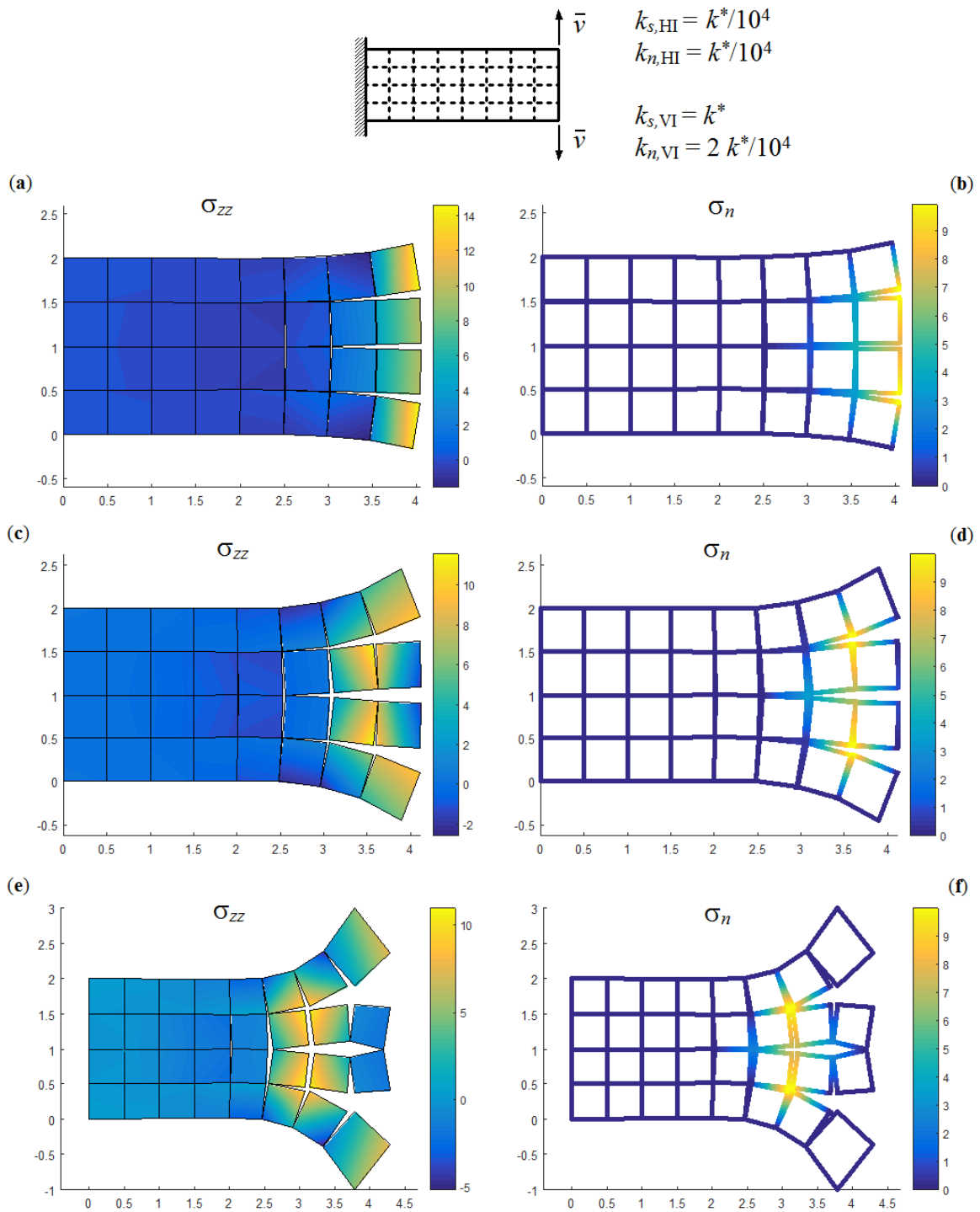

Fig. 5.21. Cantilever of Model 2 Series 2, subjected to two opposite $\bar{v}$ at the end, assuming horizontal interface $k_s = k_n = k^*/10^4$. Plate stress σ_{zz} and normal stress σ_n of the horizontal interface [kN/m²] for crack at $x = 4.0$ m with $\bar{v} = 7.4$ mm (**a**,**b**) and at $x = 3.0$ m with $\bar{v} = 27.4$ mm (**c**,**d**).
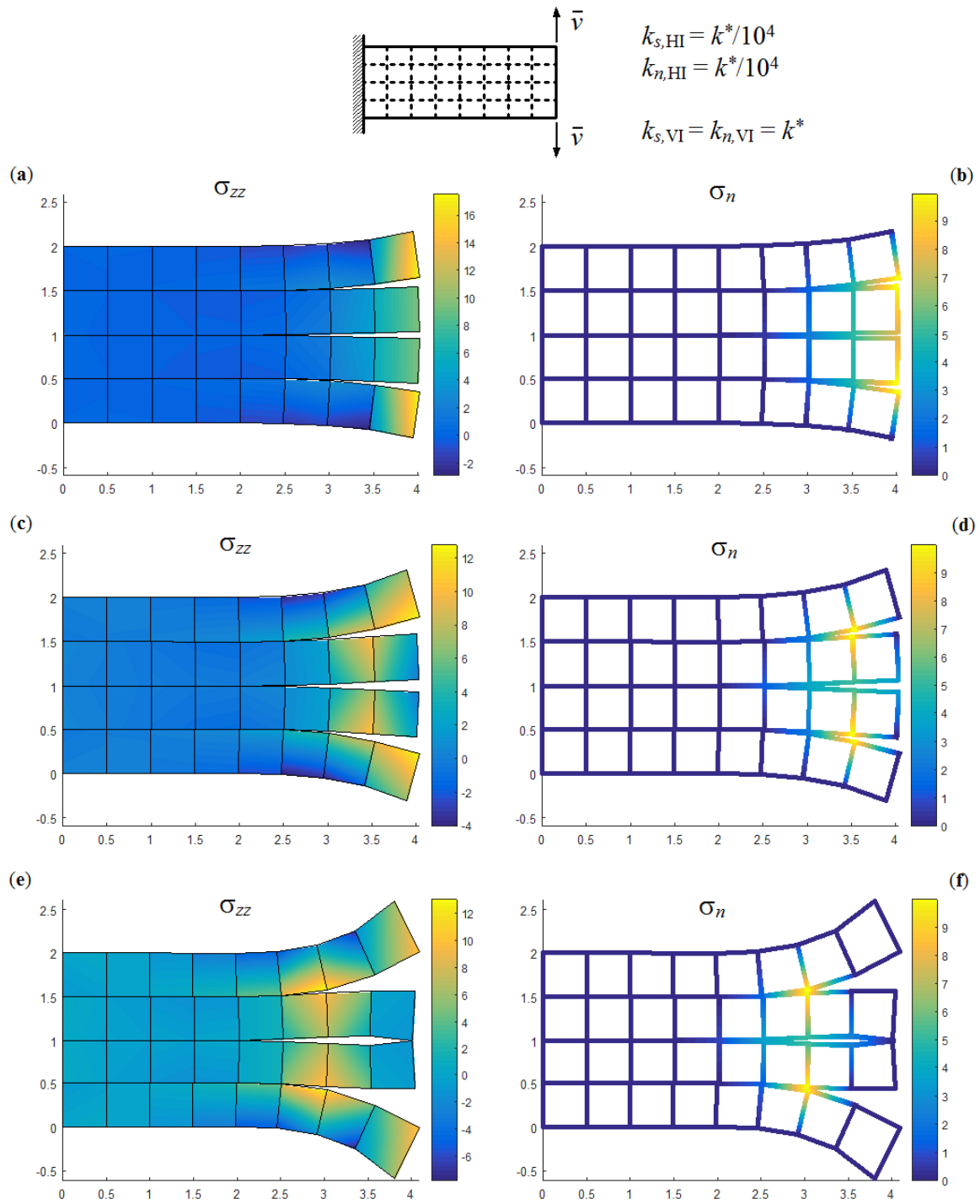
Fig. 5.22. Cantilever of Model 3 Series 1, subjected to two opposite $\bar{v}$ at the end and assuming horizontal interface $k_s = k_n = k^*/10^4$, and vertical interface $k_s = k_n = k^*$. Plate stress σ_{zz} and normal stress σ_n of the horizontal interface [kN/m^2] for crack at $x = 4.0$ m with $\bar{v} = 8.2$ mm (**a**, **b**), at $x = 3.5$ m with $\bar{v} = 15.5$ mm (**c**, **d**) and at $x = 3.0$ m with $\bar{v} = 29.8$ mm (**e**, **f**).

Fig. 5.23. Cantilever of Model 3 Series 2, subjected to two opposite $\bar{v}$ at the end and assuming horizontal interface $k_s = k_n = k^*/10^4$, and vertical interface $k_s = k^*$, $k_n = 2k^*/10^4$. Plate stress σ_{zz} and normal stress σ_n of the horizontal interface [kN/m²] for crack at $x = 4.0$ m with $\bar{v} = 8.3$ mm (**a**, **b**), at $x = 3.5$ m with $\bar{v} = 22.6$ mm (**c**, **d**) and at $x = 3.0$ m with $\bar{v} = 50.3$ mm (**e**, **f**).

5.4.4 A beam resting on layer which is lying on half-plane

In Chapter 4, the effect of the delamination due to crack propagation into the interface contact has been studied. This detachment between the surface contact of two materials does not always happen, sometimes the crack takes part into the support element, as commonly occurs in the brittle materials, such as the delamination of fibre reinforcement polymer glued to concrete substrate [13].

In this Section, a model has been realized to study the propagation of crack into the substrate. In particular, the reinforcement has been represented by a one-dimensional finite element (beam), while the support could be subdivided into two parts: a two-dimensional finite element layer and a half-plane. The mesh may be automatically generated choosing beam length L, length and height of the layer, respectively $L+2n_l L$ and H, as well as the hypothetical region affected by crack through "zero-thickness" interface elements into the layer. The sketch of present model is shown in Fig. 5.24. For the sake of simplicity, quadrilateral element ($dx = dz$) are used. The interface elements could be applied on whole substrate investigated by plate elements, except the contact between beam and plate or plate and half-plane. User might select the area subjects to fracture through the input of number of element in x and z-direction (n_x and n_z). Moreover, for an accurate solution, the number of beam elements (n_{el}) and the length of layer (n_l), Fig. 5.24b.

5.4.4.1 Peeling of beam resting on substrate with BC or lying on half-plane

An Euler-Bernoulli beam of unitary length ($L = 1$) and length-to-height ratio $L/h = 10$, resting on substrate and subjected to vertical displacement $\bar{v}$ or vertical point load Pz toward up at the midspan, is investigated. The beam is subdivided into $n_{el} = 16$, while substrate is formed by quadrilateral elements with $dx = dz = L/ n_{el} = 0.0625$ m. The substrate has length of 3 m ($n_l = 1$) and height $H = 0.25$ m. The interface elements are set underlying the beam with number of plate elements determined by $n_x = 1$ and $n_z = 3$. The limit stress of interface element (σ_{lim}) is supposed equal to 10 kPa. Every interfacial stiffness is presumed rigid, except the normal stiffness into the horizontal interface element ($k_{sHI} = k_{nVI} = k_{sVI} = k^*$, $k_{nHI} = k^*/10^4$). Plane stress state is assumed with unitary thickness. The Young's modulus and Poisson's coefficient of beam are respectively $E_b = 100$ MPa and $\nu_b = 0.3$, while for the part of substrate define by plate elements are $E_p = 5$ MPa and $\nu_p = 0.3$.
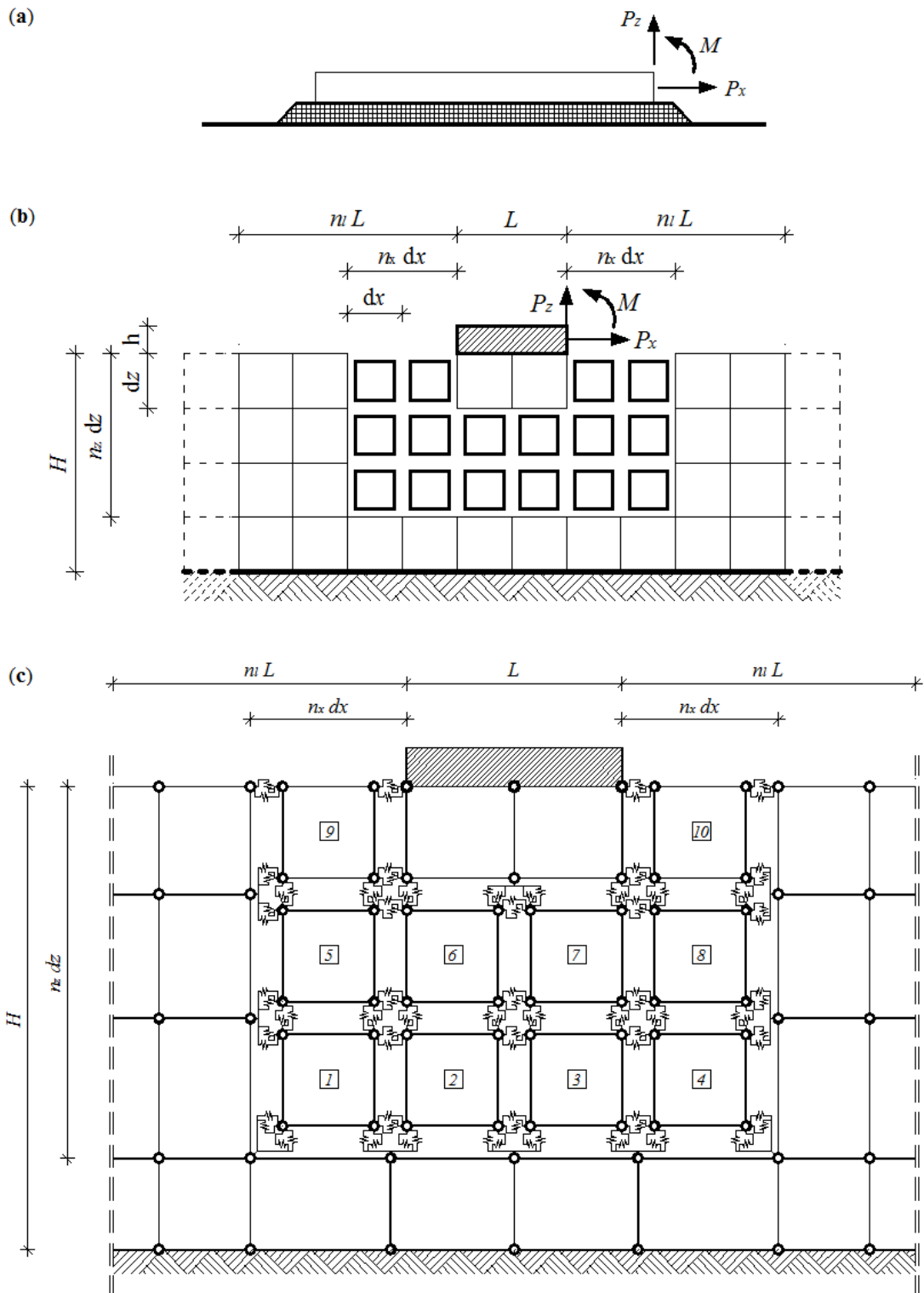
Fig. 5.24. Beam bonded by plane element which is lying on half-plane (**a**), mesh of the plate element substrate (**b**) and sketch of interface elements through "zero-thickness" analysis (**c**).
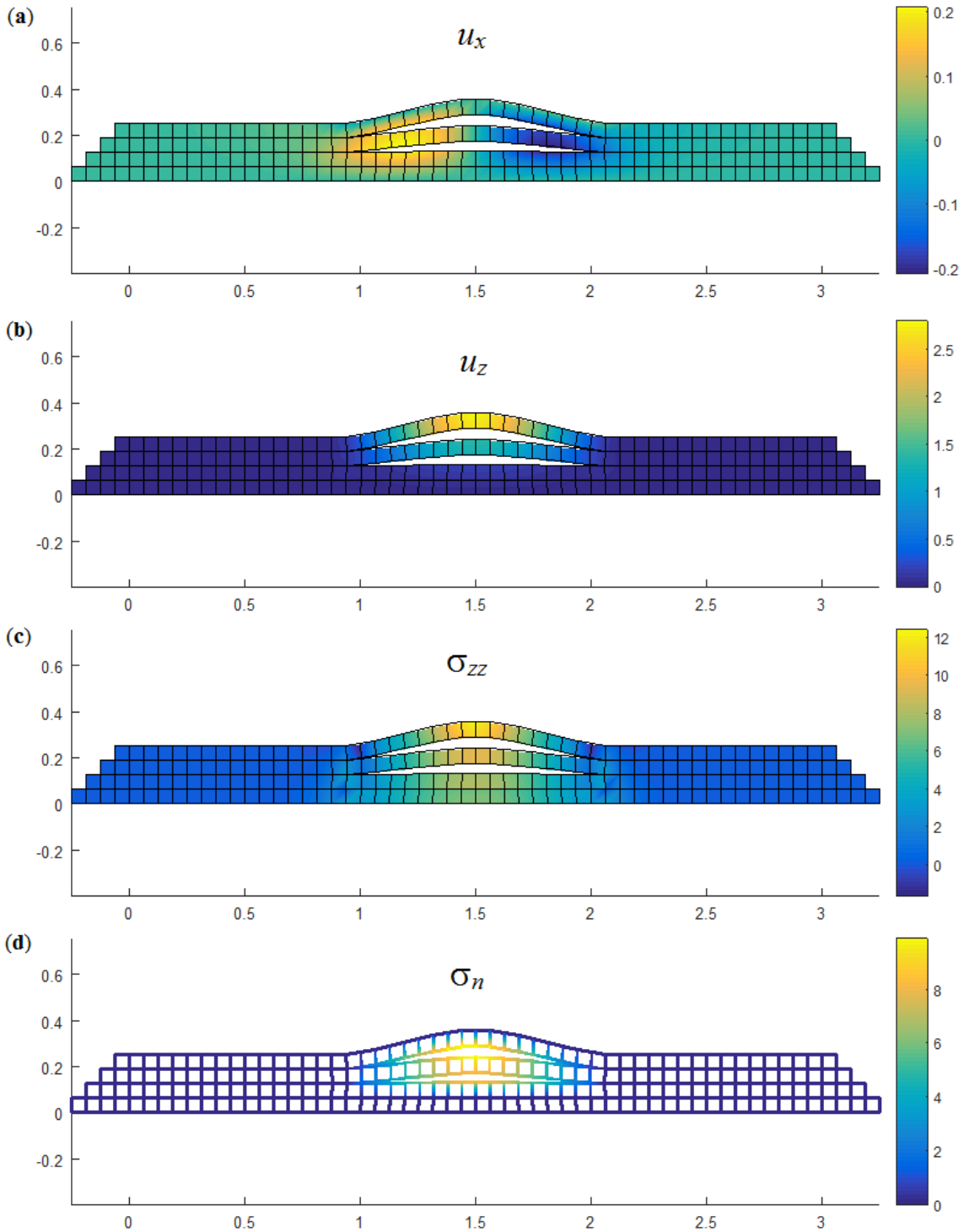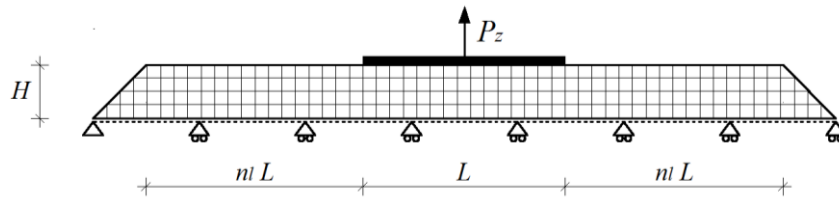
Fig. 5.25. Peeling of beam L resting on substrate with boundary conditions at the bottom edge. Horizontal (**a**) and vertical (**b**) displacements [mm], plate stresses σ_{zz} (**c**) and normal stresses of the horizontal interface σ_n (**d**) [kN/m^2].
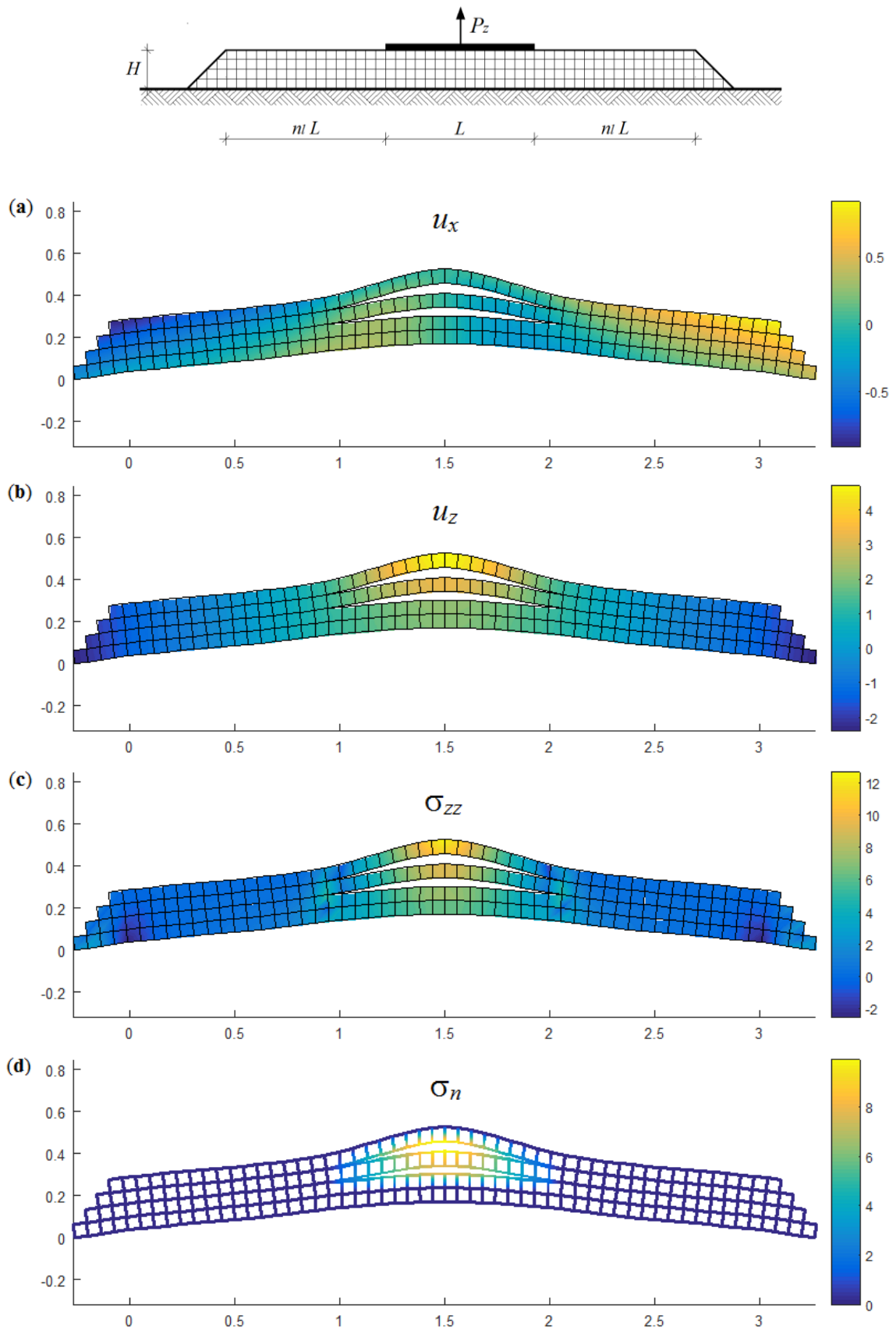
Fig. 5.26. Peeling of beam *L* resting on substrate which is lying on half-plane. Horizontal (**a**) and vertical (**b**) displacements [mm], plate stresses σ_{zz} (**c**) and normal stresses of the horizontal interface σ_n (**d**) [kN/m^2].

First, the isotropic substrate bonded to traditional boundary condition (BC) at the bottom edge is analysed. Horizontal and vertical displacement, plate stress in z-direction and normal stress of horizontal interface are plotted in Fig. 5.25. Results are obtained when the maximum interfacial stress reaches the limit stress σ_{lim}. That occurs when it is applied external displacement $\bar{v}$ = 2.7 mm or the corresponding external load Pz = 60.25 kN. The horizontal displacements turn out sign opposite, indicating a contraction along the contact of plane elements. The maximum absolute value of u_x is 0.2 mm, collocated at half-height of layer in correspondence at beam end, Fig. 5.25a. With regard to vertical displacements, maximum value is situated under the beam at the midspan as expected, Fig. 5.25b. Note that far away from the beam, the displacements are null. Consequently, maximum plate stress in z-direction (σ_{zz} = 12 kPa) and normal stress of the horizontal interface are positioned in the same zone of the highest vertical displacement, Fig. 5.25c-d.

The case with substrate bonded to an elastic homogenous isotropic half-plane is following analysed, Fig. 5.26. Assuming the Young's modulus E_s = 2 MPa and Poisson's coefficient ν_s = 0.3 of half-plane, displacements turn out higher than the previously case with boundary condition. In particular, the maximum horizontal displacement is plotted at the top end of layer with absolute value of 0.8 mm, Fig. 5.26a. While, it has been found that the maximum value of vertical displacement, plane stress σ_{zz} and normal stress of horizontal interface σ_n underneath and at the midpoint of the beam. It is worth noting that the maximum u_z is increase of 70% respect to previously case, Fig. 5.26b. Instead, the same maximum value occurs for the σ_{zz} or σ_n, Fig. 5.26c-d. The limit stress of interfacial elements is achieved applying vertical displacement equal to $\bar{v}$ = 4.6 mm, that corresponding to vertical point load Pz = 6.531 kN.

5.4.4.2 *Mode I crack of substrate lying on half-plane*

In this Section, a beam resting on substrate and subjected to vertical displacement $\bar{v}$ at beam end is investigated. The substrate is modelled with plate elements bonded to a half-plane in perfect adhesion. Elastic and isotropic material with E_p = 30 MPa and ν_p = 0.3 is used for the substrate defined by two-dimensional finite element, while E_s = 50 MPa and ν_s = 0.3 for the half-plane. The Euler-Bernoulli beam theory is assumed with Young's modulus E_b = 30 GPa, Poisson's coefficient ν_b = 0.2 and length-to-height ratio L/h = 10.

A number of 8 equal FEs are used for the discretization of beam, and zero-thickness interface elements are set in the area below the beam with $n_x = n_z$ = 3. Horizontal and vertical elements of interface are considered underneath the beam. Supposing a brittle

behaviour of the substrate, the stiffness of interfaces are assumed constant with a stress limit equal to 100 kPa. In this case, all interface elements have rigid stiffness, except the normal stiffness of the horizontal interface ($k_{sHI} = k_{nVI} = k_{sVI} = k^*$, $k_{nHI} = k^*/10^4$). Moreover, only one vertical interface, where the plate element below the beam end is linked to that immediately after the tip of beam, shear stiffness (k_{sVI}) is assumed low in order to permit shift between the two elements.

In the following figures, results in plane stress state are reported reaching opening crack at $x = 2.0$ and 1.75 m. For the first crack, displacements of substrate in horizontal and vertical component are plotted in Fig. 5.27. Highlighting, opposite sign of the horizontal displacements at the top substrate between left and right zone of the point where the external displacement $\bar{v}$ is applied, Fig. 5.27a. The high values of vertical displacements are turn out between beam-plate contact at beam end, Fig. 5.27b.
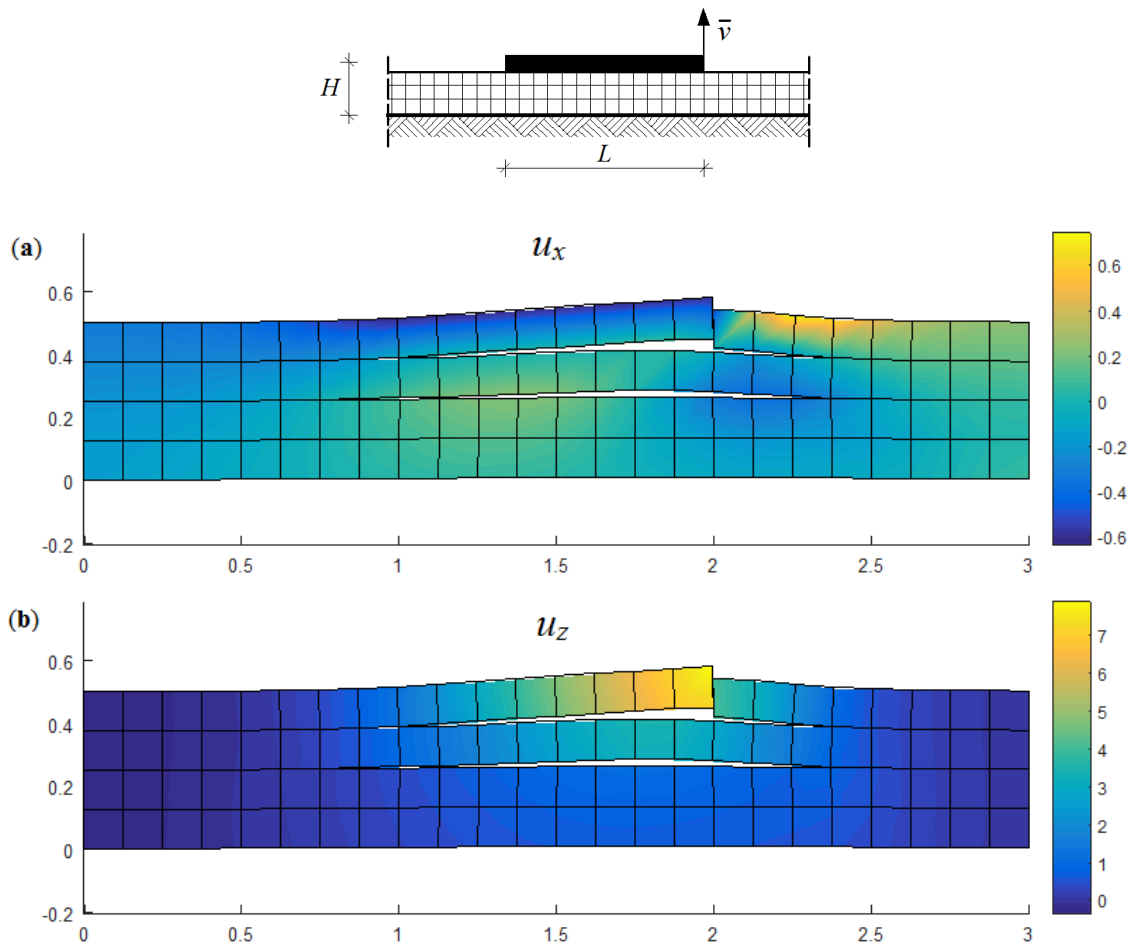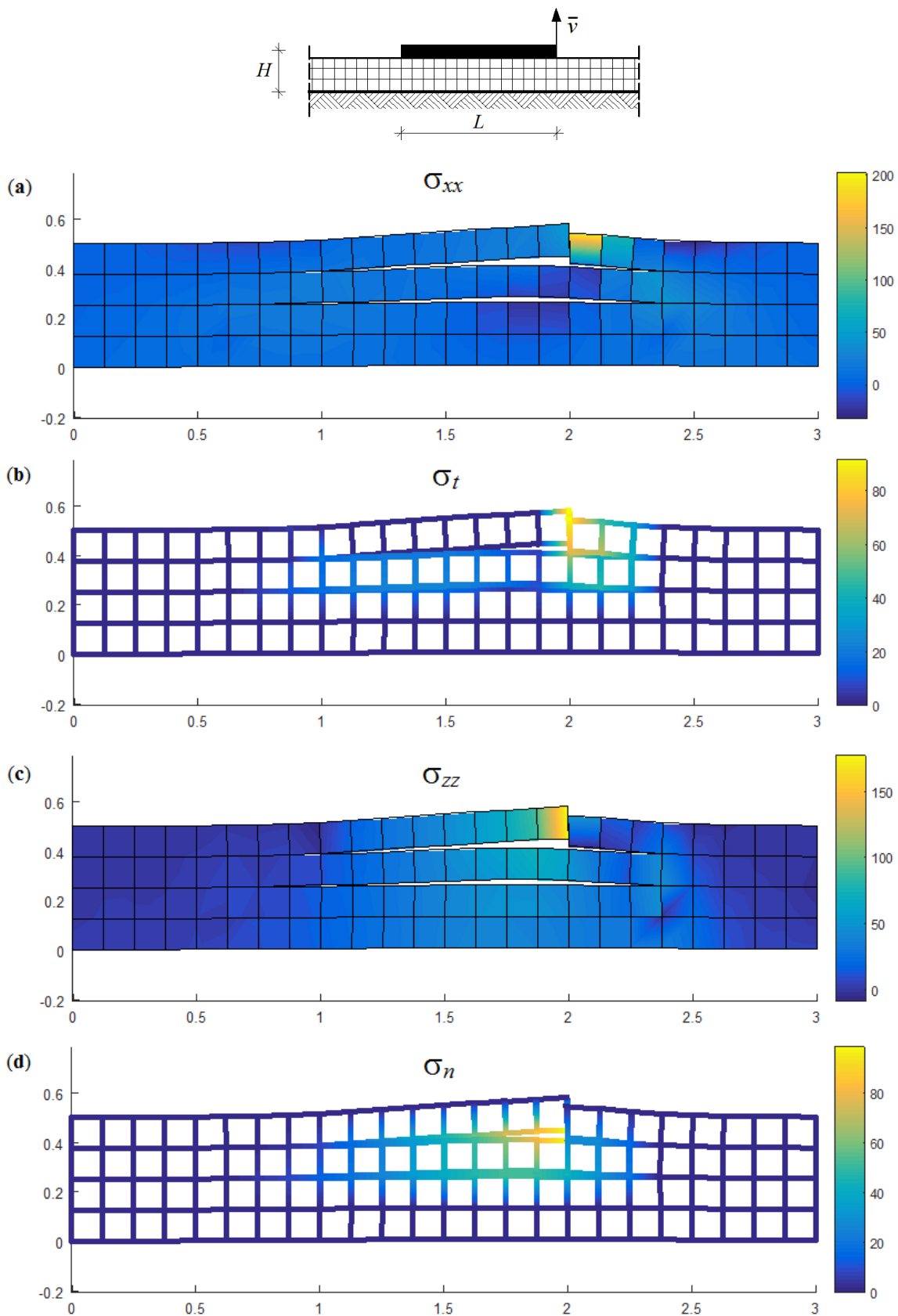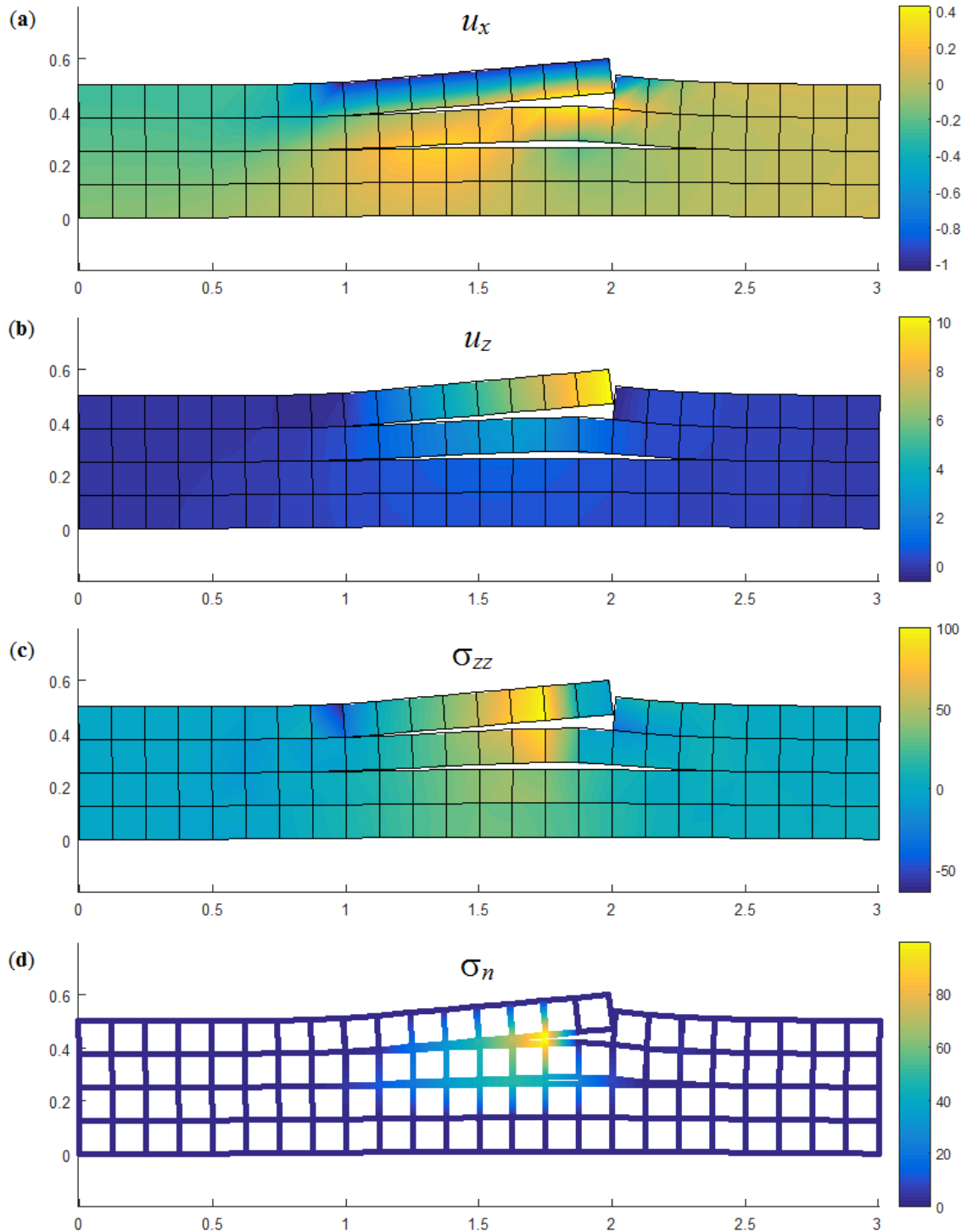

Fig. 5.27. Mode I crack at $x = 2.0$ m of a beam resting at $x = 1.0$-2.0 m ($L = 1$) with $n_{el} = 8$, resting on substrate which is lying on half-plane. Solution of the system: horizontal (**a**) and vertical displacements (**b**) [mm] into plane elements.
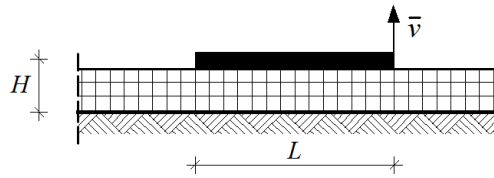
Fig. 5.28. Mode I crack at $x = 2.0$ m of a beam resting at $x = 1.0$-2.0 m ($L = 1$) with $n_{el} = 8$, resting on substrate which is lying on half-plane. Post-processing analysis: plate stress σ_{xx} (**a**), tangential stress of vertical interface σ_t (**b**), plate stress σ_{zz} (**c**), and normal stress of horizontal interface σ_n (**d**) [kN/m^2].

Fig. 5.29. Mode I crack at $x = 1.75$ m of a beam resting at $x = 1.0$-2.0 m ($L = 1$) with $n_{el} = 8$, resting on substrate which is lying on half-plane. Solution of the system: horizontal (**a**), vertical displacements (**b**) [mm] into plane elements, and post-processing analysis: plate stress σ_{zz} (**c**), normal stress of horizontal interface σ_n (**d**) [kN/m^2].

Through the post-computation, plate stress in x-direction (σ_{xx}), tangential stress of vertical interface (σ_t), plate stress in z-direction (σ_{zz}) and normal stress of horizontal interface (σ_n) are reported in Fig. 5.28a-d. Note that, the first crack ($x = 2$) occurs simultaneously in the normal component of the horizontal interfacial and the tangential component of the vertical one, Fig. 5.28b and d. Furthermore, solution of the system (u_x and u_z), plate stress σ_{zz} and normal stress of horizontal interface σ_n are reported for opening crack at $x = 1.75$ m, in Fig. 5.29a-d. Opposite signs of horizontal displacement turn out between the top and bottom edge of the plate elements underneath the beam, Fig. 5.29a. Although, the vertical displacements of Fig. 5.29b show high values close to the external displacement $\bar{v}$, the peak of plate stress in z-direction (σ_{zz}) is at the neighbourhood of the crack, Fig. 5.29c. While, the normal stress of the horizontal interface are plotted in Fig. 5.29d.

For comparison, the same example is analysed disregarding the stiffness of beam. Horizontal and vertical displacements into the plate elements are reported in Fig. 5.30 for the first crack. While, results of the post-processing analysis are plotted in Fig. 5.31.
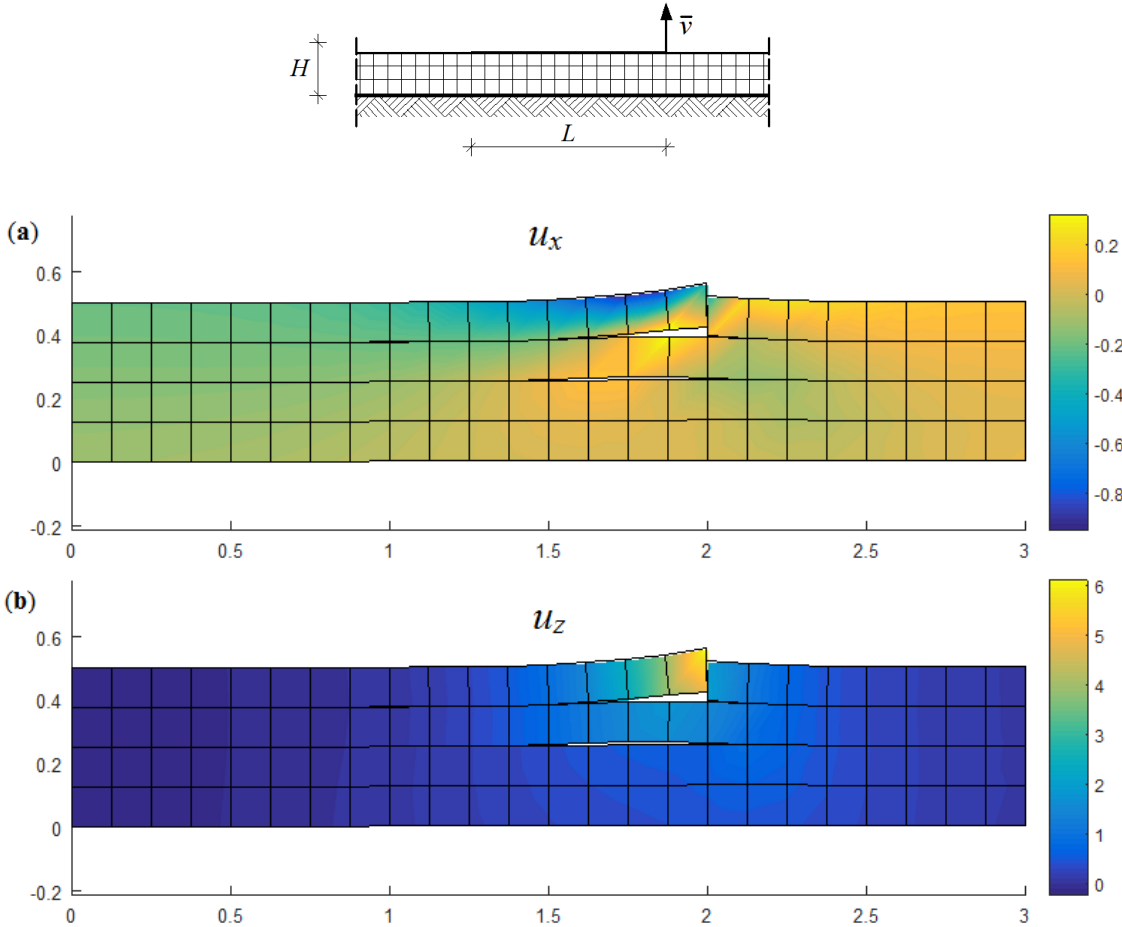

Fig. 5.30. Mode I crack at $x = 2.0$ m of substrate which is lying on half-plane and without beam. Solution of the system: horizontal (**a**) and vertical displacements (**b**) [mm] into plane elements.
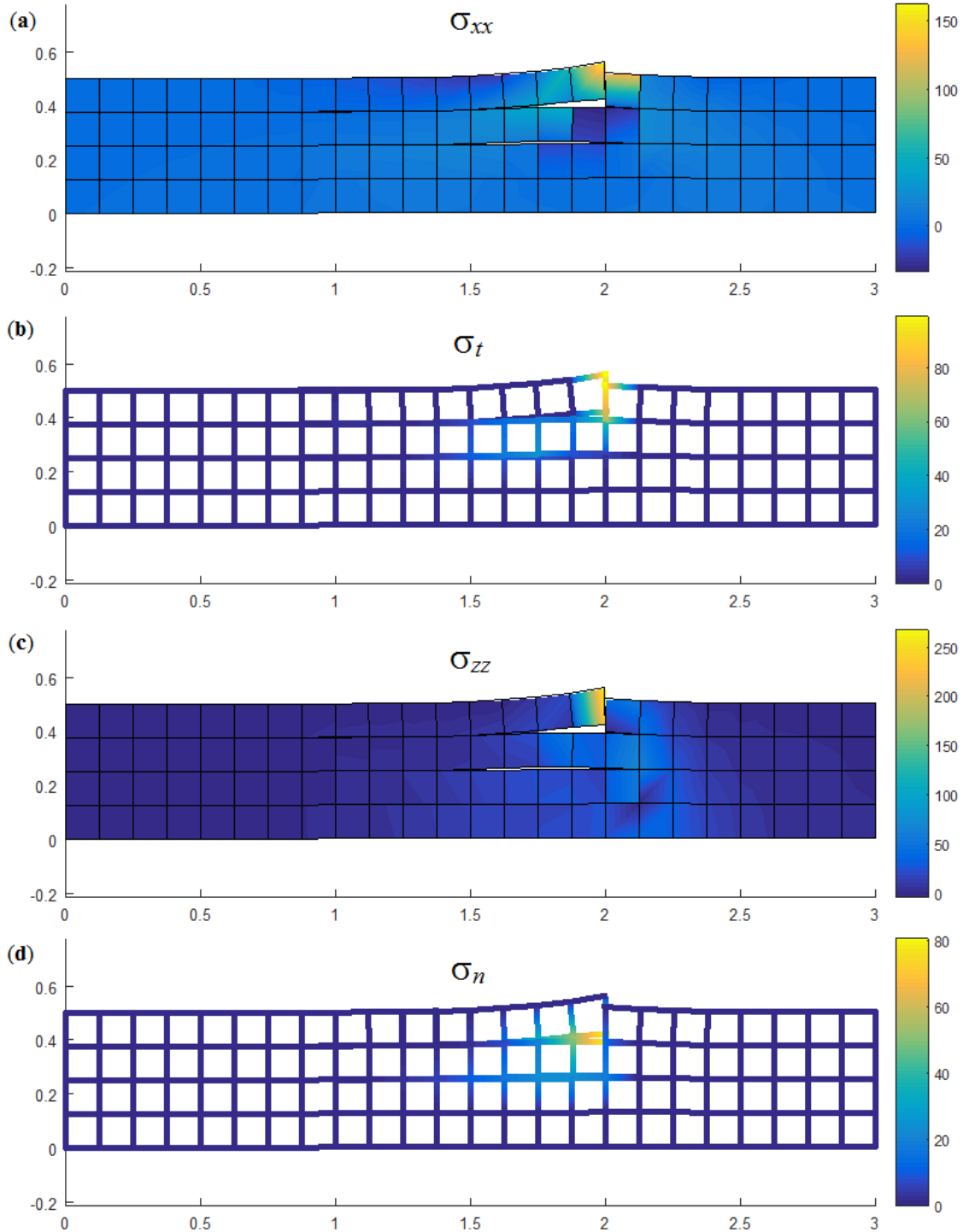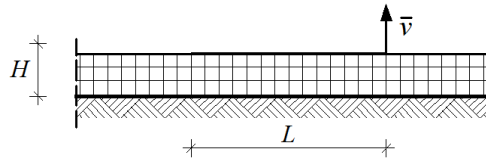
Fig. 5.31. Mode I crack at $x = 2.0$ m of substrate which is lying on half-plane and without beam. Post-processing analysis: plate stress σ_{xx} (**a**), tangential stress of vertical interface σ_t (**b**), plate stress σ_{zz} (**c**), and normal stress of horizontal interface σ_n (**d**) [kN/m^2].
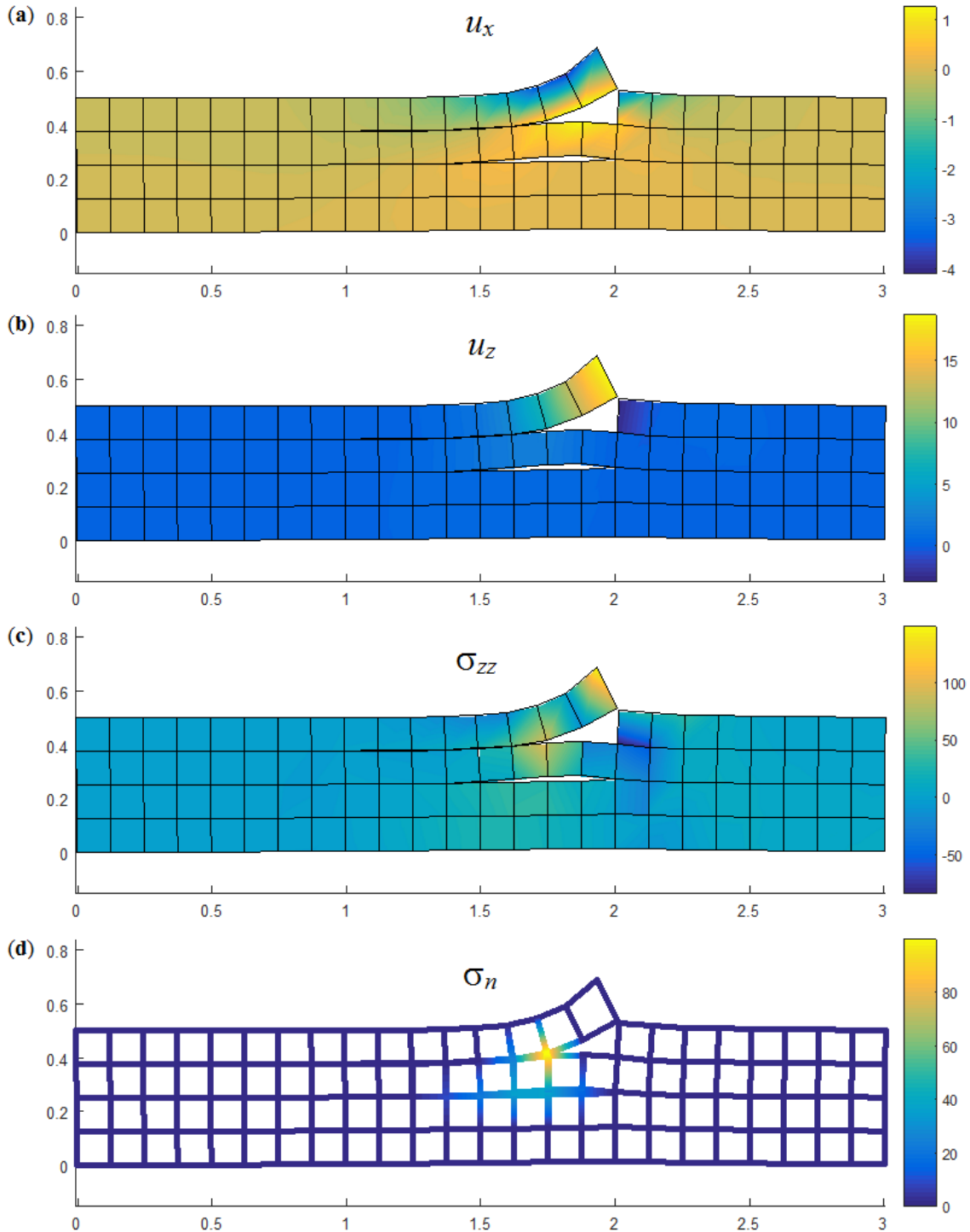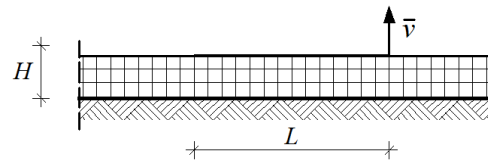
Fig. 5.32. Mode I crack at $x = 1.75$ m of substrate which is lying on half-plane and without beam. Solution of the system: horizontal (**a**), vertical displacement (**b**) [mm] into plane elements, and post-processing analysis: plate stress σ_{zz} (**c**), normal stress of horizontal interface σ_n (**d**) [kN/m^2].

The deformation of substrate shows different behaviour with regard to the previously case with the beam. That is evident above all for the opening crack at $x = 1.75$ m, where displacements of Fig. 5.32 are higher and closer to the zone subjected to the external displacement $\bar{v}$. In conclusion, the presence of a rigid beam allows more distribution of the stresses along the contact avoiding high displacement in the load zone.

5.4.4.3 Mode II crack of substrate lying on half-plane

A Euler-Bernoulli beam subjected to horizontal displacement $\bar{u}$ at one end is investigated. The beam, having length L and ratio $L/h = 10$, and resting on an isotropic substrate which could be supported by boundary condition BC or by half-plane. Plane stress state is assumed with Young's modulus and Poisson's coefficient of the beam respectively $E_b = 30$ GPa, $\nu_b = 0.2$. The material of substrate is considered elastic and isotropic with $E_p = 30$ MPa and $\nu_p = 0.3$ for the part with plate elements, while with $E_s = 10$ MPa and $\nu_s = 0.3$ in the half-plane. The discretization of beam is made with a number of 16 equal FEs. The interface elements in the layer is involved in the zone defined by $n_x = 8$ and $n_z = 3$. The interfacial stiffness is assumed rigid unless the shear component of horizontal interface ($k_{nHI} = k_{nVI} = k_{sVI} = k^*$, $k_{sHI} = k^*/10^4$). A limit stress of the interface element is supposed equal to 100 kPa.

Firstly, the layer of substrate bonded with boundary condition at the bottom is analysed, Fig. 5.33. The solution of the system in terms of displacement is reported in Fig. 5.33a and b for horizontal and vertical component, respectively. High values of the horizontal displacements turn out along the contact between beam-layer. Whereas, at the beam ends there developed a high vertical displacement. The plate stress in x-direction, Fig. 5.33c, shows a concentrated zone of compression at the top substrate after the application point of the external displacement $\bar{u}$. While, the tension zone is found at the opposite side at the beam end. It is worth observing that shear crack is along the contact surface between beam and substrate and does not involve in depth. Moreover, the tangential stress of the horizontal interface, Fig. 5.33d, shows the first crack developed throughout the length of contact beam-layer. In this contest, the model used in the Chapter 4 could be a good simplification of delamination for reinforcement subjected to horizontal load.

Secondly, the layer is supported by half-plane with mechanical parameters, previously mentioned. In this situation, relative displacements are reported in Figs. 5.34a-b. Through different deformation from the case with boundary condition, the stress σ_{xx} of the substrate and σ_t of the horizontal interface are developed in the same zone, Fig. 5.34c-d.

Finally, the shear crack is investigated neglecting the stiffness of the beam in the model where the layer is support by half-plane. The results in terms of horizontal displacement, Fig. 5.35a, show a peak at the neighbourhood of the application point of the external displacement $\bar{u}$ (or load point). On the left of that point, a lift of substrate is developed, how is reported by opposite sign of the vertical displacements in Fig. 5.35b. As expected, the plate stress σ_{xx} and σ_t of the horizontal interface are concentrated at the neighbourhood of the load point, Fig. 5.35c-d.
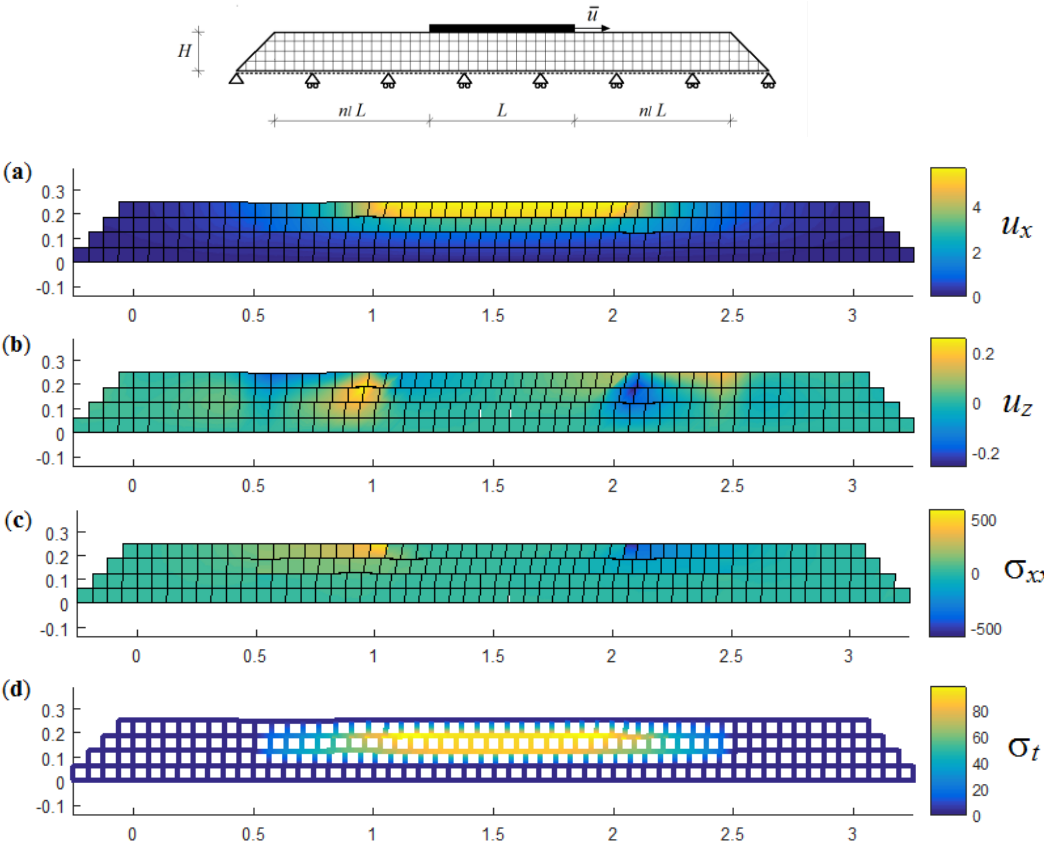

Fig. 5.33. Mode II crack of beam L subdivided into n_{el} = 16, resting on substrate with boundary conditions at the bottom edge. Values of u_x (**a**), u_z (**b**) [mm] and σ_{xx} (**c**), σ_t (**d**) [kN/m^2].
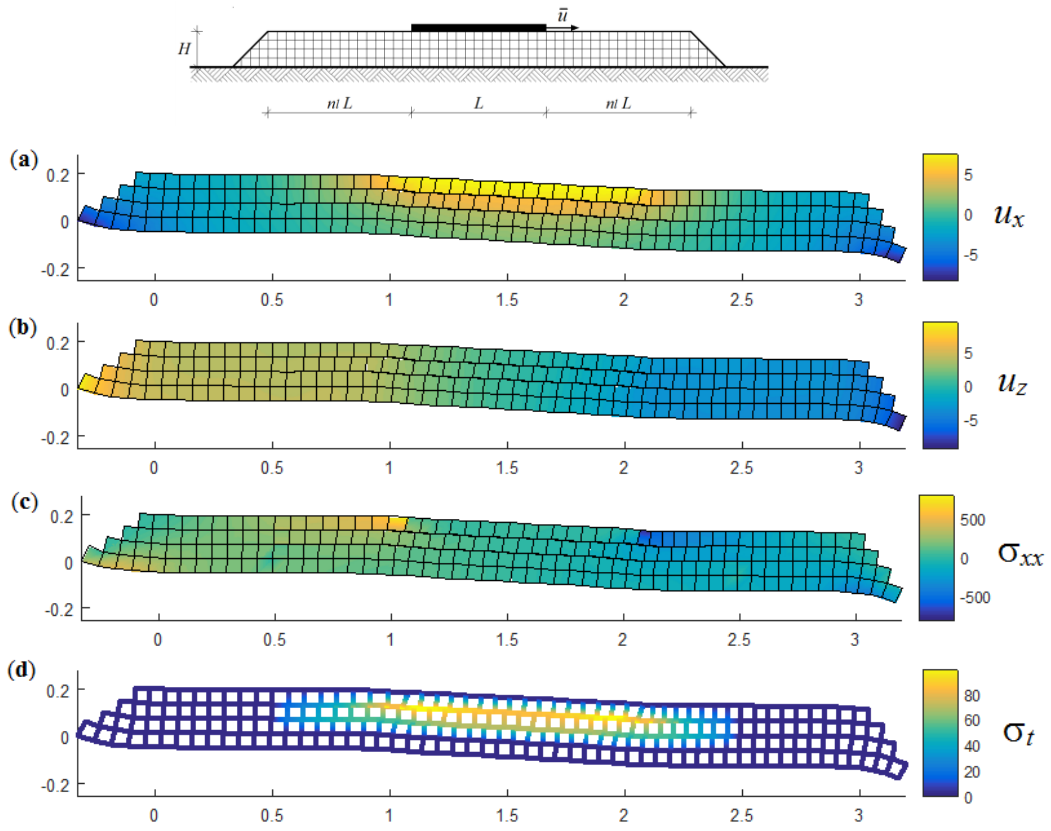
Fig. 5.34. Mode II crack of beam L subdivided into n_{el} = 16, resting on substrate which lying on half-plane. Values of u_x (**a**), u_z (**b**) [mm] and σ_{xx} (**c**), σ_t (**d**) [kN/m^2].
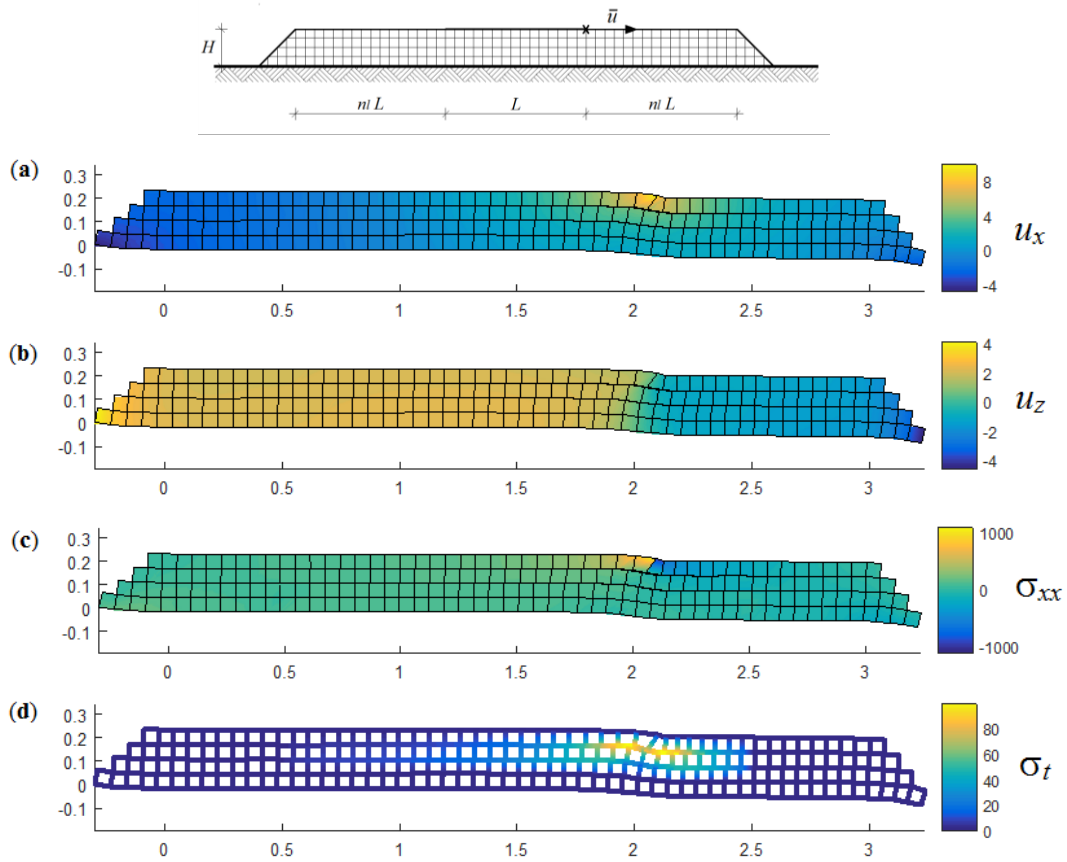

Fig. 5.35. Mode II crack of substrate which is lying on half-plane and without beam. Values of u_x (**a**), u_z (**b**) [mm] and σ_{xx} (**c**), σ_t (**d**) [kN/m^2].

5.5   Conclusion

In this Chapter, the elastic "zero-thickness" interface element has been proposed for the simulations of crack. The variational formulation is obtained through the theorem of work and energy for external domains. Using the Lobatto integration rule, the presence of the interface elements do not alter the response of the continuum elements when elastic stiffness parameters is higher than $k^*E/\mathrm{d}l$ with $k^* = 10^3$. In other words, the solution with rigid interface coincides to that of the classic FEM. A bilinear constitutive law defined in terms of stress-displacement relationship has been investigated with hardening or softening behaviour between two plate elements which are linked by an interface element. Both cases show a separation, allowing the transmission of stresses. In particular, an extension of the plate elements turns out in the case of hardening interface. While a contraction, until reaching the initial deformation, occurs following the softening branch.

The propagation of crack depend on the stiffness of interface elements, as remarked in the case of a cantilever subjected to two opposite displacements. In particular, a rigid or weak elastic brittle behaviour are inserted in the horizontal or vertical line interface of the mesh. Opening crack of the cantilever at half-height or at the top and bottom level is established by the set of the interface elements. The solution of the model with only elastic horizontal interface could be compared with that having elastic horizontal interfaces and rigid vertical interfaces. Besides, it is shown a good agreement, in terms of external force-displacement curve, between the analysis run by the present model and those calculated through a software at traditional finite element with spring elements between notes. Furthermore, a model of beam resting on substrate which is lying on half-plane is generated, inserting automatically "zero-thickness" interface elements in the area affected by the crack. A coupled FE-BIE model, for the analysis of a layer bonded in perfect adhesion to homogeneous linearity elastic half-plane, is proposed. The classic displacement based on FE method is used to describe the response of the beam and the plate element (layer). Whereas, the BIE approach is used for the substrate boundary, where surface displacements are defined by means of a suitable Green's function, as mentioned in Chapter 3. Unknown functions are represented by the beam and plate displacements and are independent from the surface tractions. A number of examples are presented to show the opening and sliding crack with the proposed formulation. Displacements and stresses are calculated and reported in some states of crack propagation. Finally, results with neglected beam stiffness or assuming the traditional boundary conditions are illustrated showing a different response in terms of deformation and stresses.

References

[1] Deng Y, Lawn BR, Lloyd IK. Characterization of damage modes in dental ceramic bilayer structures. Journal of Biomedical Materials Research 2002; 63(2): 137–145.

[2] Caballero A, William KJ, Carol I. Consistent tangent formulation for 3D interface modeling of cracking/fracture in quasi-brittle materials. Comput Methods Appl Mech Engrg 2008; 197(33-40): 2804–2822.

[3] Belytschko T, Gracie R, Ventura G. A review of the extended/generalized finite element methods for material modelling. Model Simul Mater Sci Eng 2009; 17 (24pp).

[4] Moes N, Dolbow J, Belytschko T. A finite element method for crack growth without remeshing. Int J Numer Meth Engng 1999; 46(1): 131–50.

[5] Ciancio D, Carol, Cuomo M. On inter-element forces in the FEM-displacement formulation, and implications for stress recovery. Int. J. Numer. Meth. Engng 2006; 66: 502–528.

[6] Ciancio D, Castellazzi G. Fictitious Elastic Stiffness Parameters of Zero-Thickness Finite Elements at Bi-Material Interfaces", Applied Mechanics and Materials, 2014; 553: 16–21.

[7] Caballero A, Lopez CM, Carol I. 3D meso-structural analysis of concrete specimens underuniaxial tension. Comput Meth Appl Mech Engng 2006; 195(52): 7182–7195.

[8] Ciancio D, Carol I, Cuomo M. A method for the calculation of inter-element stresses in 3D. Comput. Methods Appl. Mech. Engrg. 2013; 254: 222–237.

[9] Ciancio D, Carol I, Cuomo M. Crack opening conditions at 'corner nodes' in FE analysis with cracking along mesh lines. Engineering Fracture Mechanics, 2007; 74(13): 1963–1982.

[10] Lotfi H, Shing P. Interface Model Applied to Fracture of Masonry Structures. J. Struct. Eng. 1994; 120(1): 63–80.

[11] Ciancio D, Carol I, Castellazzi G. Optimal penalty stiffness values of concurrent 2D elastic interface elements leading to accurate stress tractions. Int. J. Numer. Meth. Engng 2004; 98: 344–370.

[12] Hughes TJR. The Finite Element Method: Linear Static and Dynamic Finite Element Analysis. Prentice-Hall: Englewood Cliffs, New Jersey, 1987.

[13] Carpinteri A. Cornetti P. Lacidogna G. Paggi M. Towards a Unified Approach for the Analysis of Failure Modes in FRP-Retrofitted Concrete Beams. Advances in Structural Engineering 2010; 1(13): 875–889.

[14] Diehl T. On using a penalty-based cohesive-zone finite element approach, Part I: Elastic solution benchmarks. Int. J. Adhesion & Adhesives 2008; 28: 237–255.

[15] Diehl T. On using a penalty-based cohesive-zone finite element approach, Part II: Inelastic peeling of an epoxy-bonded aluminum strip. Int. J. Adhesion & Adhesives 2008; 28: 256–265.

[16] Park K. Paulino GH. Cohesive Zone Models: A critical review of traction-separation relationships across fracture surfaces. Applied Mechanics Reviews 2013; 64(6).